Unidirectional freezing of soft and hard matter for biomedical applications

Unidirektionales Gefrieren von weichen und harten Materialien für biomedizinische Anwendungen

Doctoral thesis for a doctoral degree
at the Graduate School of Life Sciences,
Julius-Maximilians-Universität Würzburg,
Section: Biomedicine

submitted by

Annika Kristina Seifert

from

Würzburg

Würzburg **2022**

Unidirectional freezing of soft and hard matter for biomedical applications

Unidirektionales Gefrieren von weichen und harten Materialien für biomedizinische Anwendungen

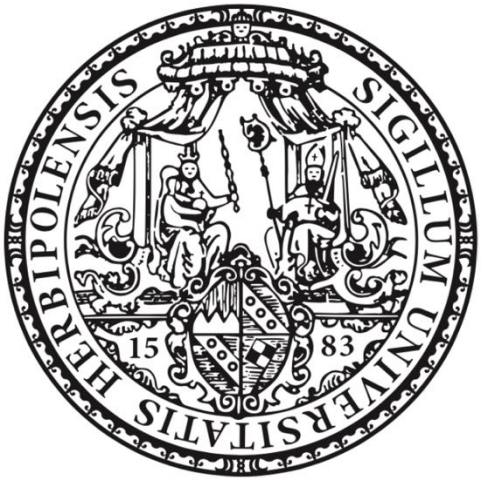

Doctoral thesis for a doctoral degree
at the Graduate School of Life Sciences,
Julius-Maximilians-Universität,
Section: Biomedicine

submitted by

Annika Kristina Seifert

from

Würzburg

Würzburg **2022**

Submitted on: ……

Members of the Thesis Committee

Chairperson: Prof. Dr. rer. nat. Carmen Villmann

Primary Supervisor: Prof. Dr. rer. nat. Jürgen Groll

Supervisor (Second): Prof. Dr. rer. nat. Jens Pflaum

Supervisor (Third): Prof. Dr. rer. nat. Torsten Blunk

Date of Public Defence: ……

Date of Receipt of Certificates: ……

This work was conducted from February 2018 to December 2021 at the Department for Functional Materials in Medicine and Dentistry (FMZ) at the Institute of Functional Materials and Biofabrication at the University of Würzburg (Würzburg, Germany) under the supervision of Prof. Dr. rer. nat. Jürgen Groll.

"The only way to do great work is to love what you do."

- Steve Jobs -

List of Publications and Conference Contributions

Publications:

As first author:

- **A. Seifert**, J. Gruber, U. Gbureck, J. Groll, Morphological Control of Freeze-Structured Scaffolds by Selective Temperature and Material Control in the Ice-Templating Process. *Advanced Engineering Materials* **2021**, 2100860.
- **A. Seifert**, J. Groll, J. Weichhold, A. V. Boehm, F. A. Müller. U. Gbureck, Phase Conversion of Ice-Templated α-Tricalcium Phosphate Scaffolds into Low-Temperature Calcium Phosphates with Anisotropic Open Porosity. *Advanced Engineering Materials* **2021**, 23(5), 2001417.
- **A. Seifert**, T. Tylek, C. Blum, N. Hemmelmann, B. Böttcher, U. Gbureck, J. Groll, Calcium Phosphate-Based Biomaterials Trigger Human Macrophages to Release Extracellular Traps*. Biomaterials* **2022**, 285, 121521.

As co-author:

- H. Joukhdar, **A. Seifert**, T. Jüngst, J. Groll, M. S. Lord, J. Rnjak-Kovacina*,* Ice Templating Soft Matter: Fundamental Principles and Fabrication Approaches to Tailor Pore Structure and Morphology and Their Biomedical Applications. *Advanced Materials* **2021**, 33(34), e2100091.

Conference contributions:

Oral presentation:

- **A. Seifert**, Controlled Cryostructuring of Reactive Inorganic Biomaterials, *Young Scientists Forum - German Society for Biomaterials (DGBM)* **2020**, Online Session.

Poster presentations:

- **A. Seifert**, T. Tylek, C. Blum, U. Gbureck J. Groll, Calcium Phosphate Scaffolds with Aligned Pore Orientation Influence Macrophage Polarization, *International Conference on Biofabrication* **2021**, Virtual Conference.

- **A. Seifert**, J. Groll, J. Weichhold, A. V. Boehm, F. A. Müller, U. Gbureck, Phase Conversion of Anisotropic Porous α-Tricalcium Phosphate Scaffolds into Various Low-Temperature Calcium Phosphates, *World Biomaterials Congress* **2020**, Virtual Conference.
- **A. Seifert**, U. Gbureck, J. Groll, Conversion of Anisotropic Porous α-Tricalcium Phosphate Scaffolds into Hydroxyapatite, Monetite and Brushite by Hydrothermal and Acidic Treatment, *Bioceramics* **2019**, New Orleans, USA.
- K. Stuckensen, **A. Seifert**, A. Schwab, M. Knauer, E. Muiños-López, F. Ehlicke, J. Reboredo, F. Granero-Moltó, U. Gbureck, F. Prósper, H. Walles, J. Groll, Tissue Mimicry in Morphology and Composition Promotes Hierarchical Matrix Remodeling of Invading Stem Cells in Osteochondral and Meniscus Scaffolds, *International Conference on Biofabrication* **2018**, Würzburg, Germany.

Awards:

- Best Presentation Award (Oral Presentation), First Prize, *Young Scientists Forum - German Society for Biomaterials (DGBM)* **2020**, Online Session.
- Best Poster Award, Third Place, *International Conference on Biofabrication* **2018**, Würzburg, Germany.

Table of Contents

Abbreviations and Symbols

Abbreviation	Meaning
α-TCP	α-tricalcium phosphate
β-TCP	β-tricalcium phosphate
2D	two-dimensional
3D	three-dimensional
Å	angstrom
a-factor	average factor
ANOVA	analysis of variance
BET	Brunauer-Emmett-Teller
CaP	calcium phosphate
CDHA	calcium deficient / nanocrystalline hydroxyapatite
cDNA	copy/complementary deoxyribonucleic acid
cm	centimeter
CPC	calcium phosphate cement
d	day
DCPA	dicalcium phosphate anhydrous - monetite
DCPD	dicalcium phosphate dihydrate - brushite
DNA	deoxyribonucleic acid
dsDNA	double stranded DNA
e.g.	exempli gratia (for example)
EM	electron microscopy
ET	extracellular trap
et al.	et alii (and others)
FBGC	foreign body giant cell
FBR	foreign body reaction
FIB	focused ion beam
g	gram
GPC	gel permeation chromatography
h	hour
HA	hydroxyapatite
hPL	human platelet lysate
Hz	Hertz
i.e.	id est (that is)
ICDD	international centre for diffraction data
ICP-MS	inductively-coupled-plasma mass-spectroscopy
ICSD	inorganic crystal structure database

IFN-γ	interferon-γ
I_h	stable hexagonal ice phase
IL	interleukin
K	Kelvin
kDa	kilodalton
kN	kilonewton
kPa	kilopascal
kV	kilovolt
L	liter
m	meter
mA	milliampere
mbar	millibar
MCPA	monocalcium phosphate anhydrous
MCPM	monocalcium phosphate monohydrate
MET	macrophage extracellular trap
min	minute
mg	milligram
mL	milliliter
mm	millimeter
mM	millimolar
M_n	number average
MPa	megapascal
MSC	mesenchymal stem cells
MW	molecular weight
M_w	weight average
M_z	centrifuge average
n.c.	not calculable
NET	neutrophil extracellular trap
nm	nanometer
OCP	octacalcium phosphate
p-HEMA	poly(2-hydroxyethyl methacrylate)
pA	picoampere
Pas	pascal second
Pen-Strep	Penicillin-Streptomycin
PBS	phosphate buffered saline
PCL	poly(ε-caprolactone)
PDMS	poly(dimethyl siloxane)
PE	Peltier element
PEEK	polyether ether ketone

pH	negative logarithm of the H^+ concentration
PLA	poly(lactic) acid
PLR	powder-to-liquid ratio
PTFE	polytetrafluoroethylene
qPCR	quantitative real-time polymerase chain reaction
rh	relative humidity
RNA	ribonucleic acid
rpm	revolutions per minute
s	second
SEM	scanning electron microscopy / scanning electron microscope
TAM	tumor-associated macrophage
TEM	transmission electron microscopy
TGF-β	transforming growth factor-β
TNF-α	tumor necrosis factor-α
TTCP	tetracalcium phosphate
UK	United Kingdom
USA	United States of America
XRD	X-ray diffractometry
µ-CT	micro-computed tomography
µL	microliter
µm	micrometer
µM	micromolar

Symbol	**Meaning**
°	degree
°C	degree Celsius
%	percent
% (v/v)	volume concentration
% (w/v)	mass concentration
% (w/w)	weight concentration
λ	wavelength

Formula symbol	**Meaning**
a_0	mean distance between two particles
c_{liquid}	solute concentration in liquid phase
c_{solid}	solute concentration in solid phase
E_i	interfacial energy
E_{pl}	interfacial energy – particle-liquid interface

E_{ps}	interfacial energy – particle-solid interface
E_{sl}	interfacial energy – solid-liquid interface
T_*	temperature frozen sample
T_0	sample temperature 0 °C
$T_L(x)$	liquidus temperature
$T_{lower\ PE}$	temperature lower Peltier element
$T_{upper\ PE}$	temperature upper Peltier element
$t(T_*)$	time point completely frozen sample
$t(T_0)$	time point sample temperature 0 °C
v_{cr}	critical ice front velocity
$\vec{x}_{lower\ PE}$	position vector lower Peltier element
$\vec{x}_{upper\ PE}$	position vector upper Peltier element
∇T	external temperature gradient
$c(x)$	solute concentration
d	distance particle - ice front
k	distribution coefficient
r	particle radius
v_c	cooling rate
η	solution viscosity
σ	compressive strength
F	force
A	surface area

List of Figures

Chapter 1

Introduction and aims of the thesis

Anisotropic structures play a major role in current research, for example in solid-state lithium battery development[1], supercapacitors[2] or thermal insulators[3]. However, besides being applied in these promising and future-oriented technologies, directed structures have been ubiquitous on earth for millions of years and are constantly present in our daily lives. They are encountered in nature, where anisotropically arranged layers are a key feature of a wide variety of materials, such as wood[4], nacre[5], or slate[6]. Highly ordered lamellae also occur in plants, such as on the underside of the cap of mushrooms.[7] Also in the human body, a multitude of tissues exhibit a hierarchical and highly ordered structure. These include, for instance, the intervertebral discs[8], articular cartilage[9], meniscus[10], heart tissue[11], skeletal muscles[12], tendons[13] and bones[14]. Several examples of anisotropic structured materials occurring in nature and the human body are shown in Figure 1.

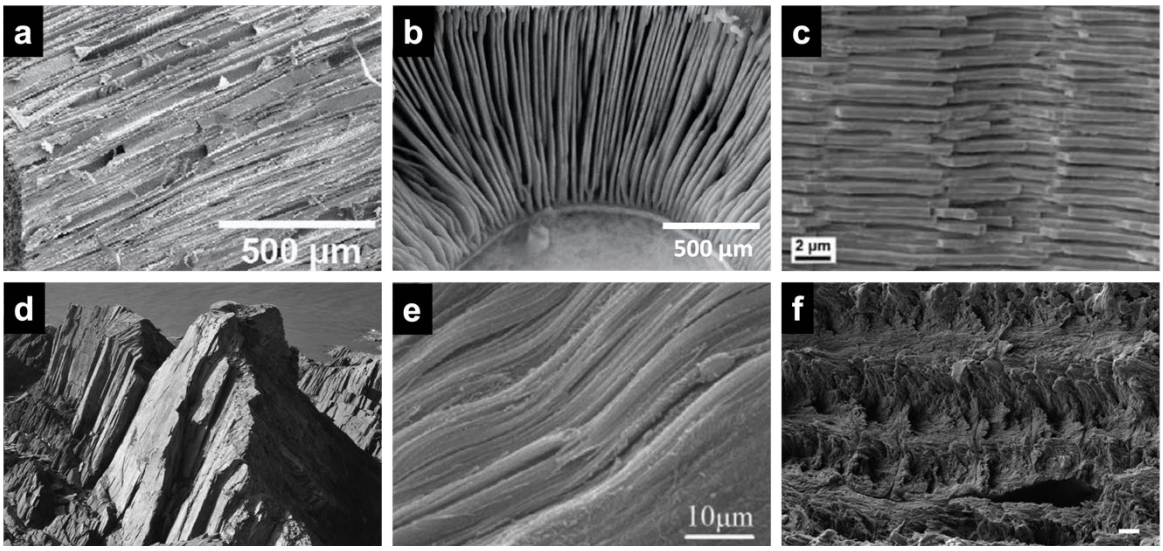

Figure 1. Directed structures occurring in nature. Highly aligned layers occur in materials such as (a) wood, (b) mushrooms (c) nacre and (d) slate, but also in biological tissues like (e) tendons or (f) circumferential lamellar bone. Scale bar in (f): 1 µm. a) Reproduced from reference [4] with permission from John Wiley and Sons. b) Own photography of the author of this thesis. c) Reprinted from reference [5], Copyright (2007), with permission from Elsevier. d) Reprinted and adapted from reference [6], Copyright (2020), with permission from Elsevier. e) Reproduced from reference [13] as open-access article distributed under the Creative Commons Attribution 4.0 International License (CC BY 4.0), which permits unrestricted use, distribution and reproduction in any medium. f) Reprinted from reference [15], Copyright (2014), with permission from Elsevier.

The loss of endogenous tissue is severe and can be caused, for instance, by diseases or accidents. Subsequently, replacement materials are needed to reconstruct the tissue in its composition and function. Current approaches include the use of synthetically produced grafts as well as the transplantation of autogenous, allogeneic or xenogeneic tissues and organs.[16-18] The obvious and major advantage of using synthetic substitutes is the circumvention of drawbacks such as a shortage of donor organs and a need for a second surgery.[19] However, although numerous tissue types are hierarchical and feature a highly ordered structure, tissue replacement materials mostly have an isotropic porosity.[20] An anisotropic porosity would not only provide the benefit of mimicking the original tissue in

structure and architecture, but would also lead to facilitated cell ingrowth, nutrient transport and vascularization.[21]

There are several approaches to prepare biomaterials with anisotropic pore structure. These include ionotropic gelation of alginate-hydroxyapatite scaffolds, allowing the generation of anisotropic tubular pores.[21] Further options involve 3D printing of polymers[22] or calcium phosphate (CaP) powders[23] and diffusion bonding of titanium meshes[24]. However, all these methods have the disadvantage that the process is either highly material-dependent with limited influence on pore orientation or requires complex and expensive equipment.

In this thesis, a unidirectional freezing approach was employed to fabricate scaffolds with highly ordered anisotropic and open porosity. This was realized by using a freeze-structuring device developed in previous works of Stuckensen *et al.*[25,26]. The core of this device consists of two superimposed Peltier elements (PEs), between which the sample solution or slurry is located. By varying the temperatures of the PEs, a temperature gradient is created that is superimposed on the sample during freezing, leading to anisotropic growth of ice lamellae. Solutes are forced between the ice crystals, which are subsequently removed by freeze-drying. The resulting scaffold thus exhibits highly ordered anisotropic porosity. The pore size and orientation can be influenced by the choice of suitable process parameters such as the cooling rate or the external temperature gradient.[25]

In addition to composition, structure, and architecture, the immune response triggered by the implantation is important for the overall success of an implanted biomaterial. This response ultimately determines whether the implant is integrated into the host tissue or encapsulated by fibrous tissue and potentially even rejected, leading to implant failure.[27] Macrophages play a crucial role in the innate immune response and are responsible for the healing success of wounds. After entering the injury site, macrophages adopt different phenotypes and can polarize into a pro- or anti-inflammatory type. While an initial pro-inflammatory state is normal and important for final tissue healing, it is essential that a transformation from the pro-inflammatory to the anti-inflammatory phenotype occurs over time. To avoid rejection and failure of the material, it is important that the inflammatory response does not persist.[28,29]

The **overall aim of this thesis** was to gain a deeper understanding of the freeze-structuring process using the previously described custom-build directional freezing device and to subsequently apply the knowledge gained to the development of anisotropically structured bone substitute materials. For this purpose, systematic investigations were first carried out using the biopolymers alginate and chitosan. Here, it was aimed to describe the anisotropic pore structure as a function of various process parameters. Based on the

obtained findings, a material platform for anisotropically porous low-temperature CaP scaffolds was developed. Since immune responses play a key role in the success of a graft after implantation, information on the immune reaction was obtained by culturing human monocyte-derived macrophages on the scaffolds *in vitro*.

Chapter 2 provides an overview of important basic information regarding this thesis and the state of the art of current research. First, the hierarchical and anisotropic structure of bone is presented and the repair mechanisms after injuries are described. Thereafter, an overview of different CaP based bone graft substitutes is given and the immune response to implanted biomaterials is elucidated. Finally, the directional freezing process used in this thesis for the preparation of anisotropically porous scaffolds is explained in more detail and an overview of applications for biomedical use is given.

For the use in biomedical applications, a fundamental understanding of the impact of process parameters during freezing on the scaffold morphology is essential. For this purpose, systematic investigations with the biopolymers alginate and chitosan were carried out in **Chapter 3**. For alginate, the focus was on the influence of different temperature regimes and temperature gradients on pore orientation and diameter. For chitosan, also material properties such as molecular weight, concentration and viscosity of the solutions and their influence on the pore structure and diameter were investigated.

The knowledge gained in the previous chapter was applied to CaPs for the use as bone substitute materials in **Chapter 4**. The material platform for anisotropically structured high-temperature CaPs presented so far in literature[30,31] was extended to low-temperature phases such as nanocrystalline hydroxyapatite (CDHA) and the secondary phosphates monetite and brushite. This has a high clinical potential due to the higher solubility of these phases[32] and was achieved by phase conversion of anisotropically structured α-tricalcium phosphate (α-TCP) scaffolds into the aforementioned phases.

In **Chapter 5**, *in vitro* cultivation of human monocyte-derived macrophages was used to obtain information on the immune response after implantation of α-TCP and CDHA scaffolds developed in the previous chapter. In addition, the influence of the pore structure on macrophage behavior was investigated. For this purpose, scaffolds with anisotropic porosity were compared with non-structured references.

A concluding discussion of the previous three chapters as well as further perspectives are presented in **Chapter 6**.

Chapter 7 provides a summary of the thesis in English and in German.

Chapter 2

State of knowledge

Parts of Chapter 2.2 and Chapter 2.4 have been published in similar form and German language in the author's master thesis.[33]

2.1 Bone as hierarchical tissue

In addition to cartilage, muscles, ligaments and tendons, an essential component of the human musculoskeletal system is bone. The musculoskeletal system protects inner organs and ensures the controlled transmission of forces within the body, with bone dictating stiffness and strength.[34] Besides dentin and enamel, bone is one of the hardest substances found in the human body and furthermore represents the main calcium reservoir. Thus, 99% of the calcium essential for numerous biological processes is bound in the mineral component of bone tissue.[35]

2.1.1 Bone structure

The complex and heterogeneous structure of bone is characterized by a hierarchical and anisotropic microstructure.[34] The extracellular bone matrix can be divided into an inorganic and organic phase.[36] The inorganic phase accounts for approximately 65% (w/w) of bone tissue, with hydroxyapatite (HA) being the major component.[37] Natural HA is impurified with ions such as carbonate (4-6%), sodium (0.9%) and magnesium (0.5%), causing low crystallinity and calcium deficiency in the HA.[38,39] The organic matrix, which makes up about 25% (w/w) of bone tissue[37], consists mainly of type I collagen, but also contains small amounts of other collagen types (III and VI)[40] as well as non-collagenous proteins. The latter ones account for only 10% of the organic phase.[37,41] Non-collagenous components include osteonectin, osteopontin, osteocalcin, phosphophoryn, bone sialoprotein, glycoprotein and proteoglycans.[35,37,39,42] Additionally, about 10% (w/w) water is contained in bone tissue.[37]

Mechanical properties of bone must meet various requirements. On the one hand, sufficient stiffness is required to enable high compressive strength, while on the other hand a certain ductility must be ensured in order to absorb shocks and prevent damage to the bone.[34] The inorganic components essentially determine the compressive strength and stiffness, while ductile properties are maintained by the organic component, thus ensuring high tensile strength. Therefore, bone tissue has the unique property of possessing high compressive as well as tensile, flexural and torsional strengths.[34,35]

Depending on the mechanical load and physiological influences on a bone, the composition and structure is adapted to the respective environment by remodeling.[34]

Microscopically, bone consists of tropocollagen molecules assembled into microfibrils. Fine HA crystals are incorporated between them, with the c-axis aligned parallel to the longitudinal axis of the collagen fibril.[14,43] The nanometer-sized fibrils are only about 300 nm long and have a diameter of 1.5 nm, while the plate-shaped HA crystals are only about 1.5 - 4 nm thick.[14,38,44] Parallel arrangement of the mineralized collagen fibers results in the formation of lamellae, which in turn are the building blocks of the cylindrically

arranged osteons.[14,43] While the fibers within a lamella are arranged parallel to each other, the orientation of the collagen fibers of two adjacent lamellae may vary.[45,46]

Bone tissue can be divided into the two subgroups of compact/cortical bone and cancellous/trabecular bone. While compact bone exhibits a porosity of only approximately 10%, trabecular bone is highly porous with a porosity of 50% to 90%.[47,48] The basic building blocks of the cortical bone are the osteons formed by collagen lamellae.[14] Vascularization of bone tissue is provided by Haversian canals located in the center of each osteon and Volkmann's canals running perpendicular to and connecting them.[14,34,35] (Figure 2)

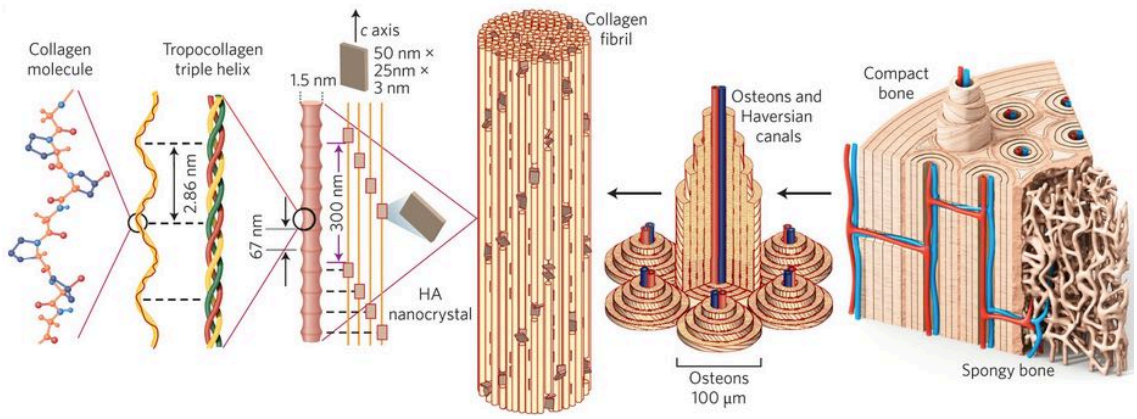

Figure 2. Hierarchical structure of bone. At the microscopic level, bone is composed of tropocollagen molecules, which are assembled into microfibrils, between which HA crystals are located. Collagen fibers arranged parallel to each other form lamellae, which are the building blocks of osteons located in the compact bone. In addition to compact bone there is highly porous cancellous bone tissue, consisting of fine trabeculae. Reprinted by permission from Springer Nature, *Nature Materials,* reference [14], Copyright (2014).

Due to the dense structure of outer cortical bone, the inner cancellous bone tissue is protected. The cancellous bone structure consists of fine trabeculae, which are also formed by lamellae. However, these are not arranged cylindrically as in cortical bone, but parallel to the trabecular surface.[46,49] The trabecular compartment consists only to a small extent of bone tissue (20%), with the major part being occupied by bone marrow and fat.[50,51] The structure of the spongiosa allows a high degree of stability, adapted to the requirements of the particular bone, while at the same time being lightweight. The distribution and arrangement of the trabeculae within the network is strongly anisotropic and depends on the mechanical loading of the bone. According to Wolff's law, the trabeculae align themselves in the direction of the acting mechanical forces.[52] In contrast to the cortical bone, trabecular bone tissue is not vascularized.[35] Osteocytes in the bone tissue must therefore be supplied with nutrients from blood vessels in the bone marrow, which occurs by diffusion. Therefore, trabeculae are usually not thicker than 300 µm.[49]

2.1.2 Bone cells and remodeling

Human bone tissue is remodeled throughout life, i.e., continuously degraded and rebuilt.[53] The aim is the repair of micrometer-sized bone cracks and the adaption to mechanical loads. In addition, material fatigue occurs over time, the negative consequences of which are avoided by renewing the material. Thus, an average of 10% of the adult human skeleton is renewed each year.[49] All four cell types of bone tissue are involved in the remodeling process: bone lining cells, osteoblasts, osteocytes and osteoclasts. Osteocytes are by far the most abundant cell type, accounting for 95% of all bone cells. While osteoblasts only survive for a few weeks and osteoclasts for several days, osteocytes are the longest-living bone cells with a lifespan of years to decades.[49,54]

Bone lining cells, osteoblasts and osteoclasts cover free surfaces of the bone, while osteocytes are located within the bone matrix. Although bone lining cells cover the bone surfaces, they are not in direct contact with the mineralized bone matrix but separated from it by a thin layer of collagen fibrils. The cells can interact with each other and with osteoblasts and osteocytes through gap junctions.[49]

Osteocytes are located in cavities or voids within the mineralized bone matrix. The cell bodies sit in the so-called lacunae, which are lenticular cavities that occur between the lamellae. Numerous bone canals (canaliculi) originate from these lacunae and run both perpendicular and parallel to the lamellae, containing the cell processes of the osteocytes. Therefore, a network of fine canals extends throughout the mineralized bone matrix.[49] The cell bodies and processes are surrounded by a thin layer of interstitial fluid as well as non-mineralized organic matrix. Due to mechanical stress on the bone, shear forces are generated in the lacuno-canalicular system. By sensing these stimuli, osteocytes act as mechanosensors. The physical signals are subsequently converted into intracellular molecular processes (mechanotransducers), which results, for example, in the secretion of proteins or other active substances.[49,55] For instance, the lower the mechanical load on the bone, the more the glycoprotein sclerostin, which inhibits bone formation, is secreted.[49]

In the bone marrow, both hematopoietic and mesenchymal stem cells exist, from which different cell types develop. While osteoclasts differentiate from hematopoietic stem cells, osteoblasts are derived from mesenchymal stem cells.[56,57]

Osteoclasts are responsible for bone resorption. These multinucleated cells are 50-100 µm in size. During the degradation of the mineralized matrix, so-called howship lacunae and tunnels are formed. Simplified, bone resorption proceeds in three steps. First, calcium compounds are dissolved by the release of acid.[49] Osteoclasts adhere to the surface via integrins and actin filaments and form a zone sealed from the surroundings into which protons are pumped by the cells. This leads to a local pH of about 4.5.[49] As the solubility of the mineral bone component increases with decreasing pH, calcium

compounds are dissolved and the mineral phase is resorbed.[58] The organic matrix is degraded by the release of lysosomal enzymes.[59] Finally, endocytosis of remaining fragments of the matrix occurs. The howship lacunae and tunnels created by osteoclastic bone resorption are subsequently refilled with new material by osteoblast activity.[49]

Osteoblasts are bone-forming cells. Their function is the collagen synthesis for the formation of new lamellae. Another task is the initiation of collagen mineralization which occurs, for instance, through the formation of alkaline phosphatase.[49]

The process of bone remodeling consists of three steps: activation, resorption and bone formation.[60,61] During remodeling, specific regions of the skeleton are renewed, with remodeling of different areas occurring independently of each other.[49,60] For a successful remodeling process, the bone lining cells detach from the surface and create the bone remodeling compartment, a protected space in which remodeling can take place, by forming a canopy.[49] After completion of the resorption by osteoclasts, the phase of new bone formation by osteoblasts begins. In this process, the osteoblasts first colonize the pits and tunnels left by the osteoclasts and deposit a first layer of non-mineralized matrix (osteoid lamella).[62] This layer is mineralized while the next one is deposited by subsequent cells. Blood serum is the major provider of ions such as calcium and phosphate. Precipitation leads to the formation of calcium deficient carbonated hydroxyapatite.[63,64]

The mineralization process proceeds in two successive phases, the primary and secondary mineralization. During the first step, mineralization of the previously formed matrix begins, while in the second stage crystal number and size increase.[65]

2.1.3 Bone fracture repair

Bone remodeling occurs not only continuously in the body, but also after fractures.[66] Bone tissue can heal without scarring and regenerate in such a way that the newly formed tissue does not differ from the original.[67] However, the success of healing is determined by several factors, such as the distance or displacement of the two bone segments and the mechanical stability.[67-70]

For primary fracture healing, certain conditions must prevail, i.e., the fracture edges must be almost perfectly positioned, in direct contact with each other and pressed together. Inter-fragmental compression and mechanical stability are usually provided by the use of plates and screws. In this healing process, which is similar to bone remodeling, bone is first resorbed at the fracture ends by osteoclasts and then rebuilt by osteoblasts, resulting in the reconstruction of the Haversian system.[67,71,72]

In many cases, these previously described conditions do not exist, since fixation with the aid of a splint or external fixators, for example, results in certain interfragmentary movements between the fracture ends.[67,69,73] Here, the reconstruction of the bone occurs

during secondary fracture healing. According to Loi *et al*., this process can be divided into five phases: injury with hematoma formation, acute inflammation, granulation tissue formation, callus formation and remodeling.[67]

A bone fracture always involves damage to surrounding blood vessels, which results in the development of a hematoma. This hematoma serves as a template for the later callus formation.[74] In this phase, immune cells such as neutrophils, platelets, macrophages, granulocytes, lymphocytes and monocytes are attracted to the fracture site.[66,75,76] The cells release pro-inflammatory cytokines and growth factors, attracting further inflammatory cells and mesenchymal stem cells (MSCs).[66,75] The hematoma is rearranged and a fibrin thrombus is formed.[74,77] Over time, vessels sprout into the clot, which is replaced by granulation tissue in the fracture gap.[67] Necrotic tissue and the fibrin matrix are phagocytized by macrophages and neutrophils. Progenitor cells derived from, for instance, the bone marrow or periosteum are in turn attracted by the factors secreted by these cells.[75,78] With the help of their immunosuppressive properties, the mesenchymal progenitor cells lead to the subsiding of the inflammation, preparing the next healing phase.[79-83]

Callus formation follows, with soft callus forming initially, transforming into mineralized hard callus or woven bone over time.[67] This stage is characterized by high osteoblast activity as well as increasing mineralization. In the last stage, the remodeling phase, the hard callus is remodeled into lamellar bone and finally assumes the shape of the original bone.[66] Until the process is fully completed, it can take months to years. After this time, the structure and function of the bone is completely restored.[67]

2.2 Calcium phosphate-based bone substitute materials

Under certain conditions, a bone fracture or defect may not heal without the use of bone graft substitutes. This is the case, for example, when a defect exceeds a critical size. Such defects can result from accidents, infections, tumor removals or congenital deformation.[48,84]

The demand for bone graft substitutes is extremely high, with over two million bone grafting procedures performed annually worldwide.[85] The requirements for an ideal bone graft material are clearly defined. Hence, the substitute material should combine the properties of osteogenesis, osteoinduction, osteoconduction and osteointegration. Therefore, the gold standard is still the use of autologous bone tissue as a substitute material, as it possesses all four of the previously mentioned properties.[86] However, drawbacks of using autologous tissue include the need for additional surgery and associated pain and complications, donor site morbidity, and limited availability.[87-89] Another option is the use of allografts. These materials come from a donor of the same species but carry the risk of

disease transmission. In addition, reduced mechanical properties compared to the original bone or the lack of donor organs are among the disadvantages here.[87,90] These problems can be circumvented by using synthetic substitutes. In the clinical use of synthetic materials, it is crucial that they are biocompatible, similar in mechanical properties to those of natural bone, and that they remodel into natural bone tissue over time. One approach is the use of CaPs. Materials of this family show the properties of osteointegration and osteoconduction.[91] CaPs are the most important component of the inorganic phase of hard tissues in the human body and of mammals in general. They are found in bones, teeth and tendons, but also in pathological calcifications, such as dental calculus or bladder stone.[44] Due to their inherent biocompatibility, they are used clinically where CaPs are applied in the form of blocks, granules or *in situ* hardening cement systems.[92] However, compared to the original bone tissue, CaPs exhibit significantly lower mechanical stability due to their brittleness, limiting the use to non-load-bearing application sites. The improvement of the mechanical properties is currently part of research.[93,94]

Calcium orthophosphates are by definition composed of the elements calcium (Ca), phosphorus (P), and oxygen (O), with the orthophosphate group (PO_4^{3-}) differing in structure from the meta (PO_3^-), pyro ($P_2O_7^{4-}$) or poly $(PO_3)_n^{n-}$ group.[95] Thereby, CaPs can be chemically defined as salts consisting of a calcium (Ca^{2+}) ion on the one side and primary ($H_2PO_4^-$), secondary ($H_2PO_4^{2-}$) or tertiary (PO_4^{3-}) phosphate ions on the other side, with only the latter two naturally occurring in bones and teeth.[96]

There are various CaP phases, which differ in their chemical composition, Ca/P ratio and solubility.[97] Different calcium phosphates are listed in Table 1.

Table 1. Different CaP phases with their corresponding chemical formula, Ca/P ratio and solubility at 25 °C ordered by an increasing Ca/P ratio.[97,98]

CaP phase	Chemical formula	Ca/P ratio	Solubility mg L^{-1}
Monocalcium phosphate monohydrate (MCPM)	$Ca(H_2PO_4)_2 \cdot 2H_2O$	0.5	~18000
Monocalcium phosphate anhydrous (MCPA)	$Ca(H_2PO_4)_2$	0.5	~17000
Dicalcium phosphate dihydrate (DCPD - brushite)	$CaHPO_4 \cdot 2H_20$	1	~88
Dicalcium phosphate anhydrous (DCPA - monetite)	$CaHPO_4$	1	~48
Octacalcium phosphate (OCP)	$Ca_8(HPO_4)_2(PO_4)_4 \cdot 5H_2O$	1.33	~8.1
α-tricalcium phosphate (α-TCP)	α-$Ca_3(PO_4)_2$	1.5	~2.5
β-tricalcium phosphate (β-TCP)	β-$Ca_3(PO_4)_2$	1.5	~0.5
Calcium deficient hydroxyapatite (CDHA)	$Ca_{10-x}(HPO_4)_x(PO_4)_{6-x}OH_{2-x}$	1.5 - 1.67	~9.4
Hydroxyapatite (HA)	$Ca_{10}(PO_4)_6(OH)_2$	1.67	~0.3
Tetracalcium phosphate (TTCP)	$Ca_4(PO_4)_2O$	2.0	~0.7

The solubility of different CaPs is strongly dependent on the pH value of the environment and can differ by several orders of magnitude depending on this value. Figure 3 shows the solubility isotherms of different CaP phases. The solubility is given as the calcium concentration of the saturated solution.[32]

If the solubility curve of a CaP phase at a given pH value is lower than that of another, the former phase is more stable since it has a lower solubility. For this reason, biological apatite, which is an impure form of HA, is the most common form of CaP in the body, as other phases are transformed over time in a physiological environment.[32]

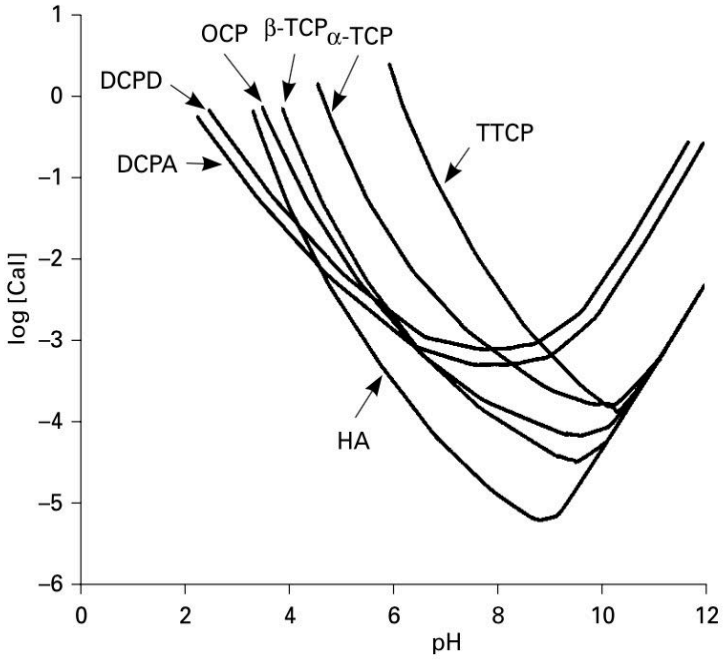

Figure 3. Solubility phase diagram of various calcium phosphates. The curves represent the solubility isotherms of hydroxyapatite (HA), dicalcium phosphate anhydrous (DCPA, monetite), dicalcium phosphate dihydrate (DCPD, brushite), octacalcium phosphate (OCP), β-tricalcium phosphate (β-TCP), α-tricalcium phosphate (α-TCP), and tetracalcium phosphate (TTCP) at 25 °C. Reproduced from reference [32] with permission, Copyright © 2001 Karger Publishers, Basel, Switzerland.

The solubility of a CaP also determines its degradability *in vivo*. If the solubility of the mineral bone component is higher than that of the CaP, the implant will degrade only very poorly or not at all. If, on the other hand, the solubility of the CaP is higher than that of the mineral component of bone, the implant is degradable.[99]

In principle, two types of CaPs can be distinguished. High temperature phases are formed by thermal treatment (e.g. sintering) at high temperatures.[100] Low-temperature CaPs form in a supersaturated solution by precipitation of a less soluble phase than the initial material. This usually occurs at low temperatures around room temperature.[99]

2.2.1 High-temperature CaPs

2.2.1.1 Tricalcium phosphates

Tricalcium phosphates (TCPs) belong to the group of high temperature CaPs. While the crystal structure of the α-phase is monoclinic, β-TCP crystallizes in the rhombohedral space group.[101] α-TCP can be formed by a solid-state reaction of stochiometric amounts of monetite ($CaHPO_4$) and calcium carbonate ($CaCO_3$) at temperatures above 1125 °C. However, after high-temperature treatment, the α-TCP must be quenched to avoid phase transformation to β-TCP.[102] The latter phase occurs at temperatures of about 900 - 1100 °C.[101] Consequently, by heating β-TCP to temperatures above 1125 °C, α-TCP can be obtained again. Due to the structural differences, the solubility of α- and β-TCP

differs, with α-TCP being significantly more soluble than β-TCP under acidic to slightly basic conditions.[99]

2.2.1.2 Hydroxyapatite

Due to its chemical composition, which is similar to the mineral component of bones and teeth, HA is widely used clinically.[103] In the high-temperature approach, HA can, for instance, be prepared by solid state reaction of various precursors such as TCP and calcium hydroxide ($Ca(OH)_2$), $CaCO_3$ and monetite or $CaCO_3$ and ammonium dihydrogen phosphate ($NH_4H_2PO_4$) at temperatures above 1000 °C. However, the phase purity depends on the sintering temperature, the molar ratio, and the chemical composition of the starting materials.[103,104]

2.2.2 Low-temperature CaPs

Calcium phosphate cements (CPCs) were developed in the mid-1980s by Brown and Chow.[105] These systems consist of one or more calcium phosphate powders and an aqueous solution. When the two phases are mixed, the raw powder dissolves, resulting in a solution-precipitation reaction. A less soluble CaP precipitates due to the supersaturation of the solution with respect to the reaction product. This leads to the growth and entanglement of crystals, providing mechanical stability of the hardened cement.[106,107]

CPCs are bioactive, osteoconductive, injectable and moldable and are therefore used clinically in the form of prefabricated granules or blocks but are also applied directly to defects as a paste due to their moldability.[108-110] CPCs can be combined with antibiotics or growth factors for local applications.[111]

Cements obtained from non-precompacted pastes (to create application-oriented circumstances) exhibit very high compressive strengths of up to 80 MPa.[112] However, cured CPCs behave like brittle ceramics and exhibit low flexural strength compared to bones and teeth.[93] Therefore, their application is currently limited to non-load bearing defects such as in the dental and craniofacial[113] or maxillofacial region[114].

Such low-temperature phases formed by a solution-precipitation reaction include CDHA, monetite, and brushite.[115,116] Due to the crystals growing during the hardening of the cement, CPC scaffolds are characterized by a much higher specific surface area than sintered monoliths. An example of this are apatite cements with a specific surface area of up to 100 m^2/g. Sintered ceramics, in contrast, only possess a specific surface area of around 1 m^2/g.[92]

2.2.2.1 Hydroxyapatite forming cements

HA forming cements are interesting for clinical applications because of their chemical composition being similar to that of the mineral bone component, combined with the high

specific surface area caused by their nanocrystallinity.[42,117] One formation route for a CDHA setting cement is the reaction of α-TCP as raw powder with water as the liquid phase (equation (1)).[97,118]

$$3\ \alpha\text{-}Ca_3(PO_4)_2 + H_2O \longrightarrow Ca_9(PO_4)_5(HPO_4)OH \quad (1)$$

α-TCP has a significantly higher solubility than CDHA. If the soluble phase has a pH above 4.2, CDHA is the least soluble phase that is consequently precipitated. (Figure 3) The setting process takes several minutes to hours, which can be a problem for clinical applications.[119] In addition to approaches such as increasing the temperature, reducing the liquid phase, using a raw powder with smaller particle sizes, or adding HA seed crystals, the addition of orthophosphate ions is a further way to reduce the setting time.[93,119-123] The latter leads to supersaturation of the liquid phase with respect to the reaction product. Disodium hydrogen phosphate (Na_2HPO_4) can be used for this purpose.[120]

CDHA CPCs are relatively slowly resorbed *in vivo* and replaced by bone tissue. Since the surrounding environment is supersaturated with respect to HA, the degradation process can take several years.[93,97] Therefore, the cements do not dissolve passively, but are only actively resorbed by osteoclast activity and a local decrease in pH, resulting in higher solubility of the CDHA phase.[93,124-126]

2.2.2.2 Brushite and monetite forming cements

Brushite and monetite are the two least soluble phases below a pH of 4.2. (Figure 3) Thus, these CaP phases belong to the group of acidic CPCs, setting in an acid-base reaction.[97] Brushite is found in the human body, where it appears in pathological calcifications, like dental calculi, urinary stones or calcifications in the vascular system.[127-130] However, brushite is also applied in the form of cement as a bone substitute material. The great advantage of cements like brushite and monetite is that they exhibit significantly higher solubility *in vivo* than apatite cements. Thus, brushite and monetite are completely resorbed within a few months[107,131] and hence are interesting candidates for bone graft substitutes.[132]

Brushite can, for instance, be crystallized by precipitation of calcium ions with hydrogen phosphate ions in slightly acidic aqueous solutions.[44,133] In literature, brushite is often prepared by mixing β-TCP (basic) with monocalcium phosphate monohydrate (MCPM, $Ca(H_2PO_4)_2 \cdot 2H_2O$, acidic) according to equation (2).[97,99,134] Instead of MCPM, monocalcium anhydrous (MCPA, $Ca(H_2PO_4)_2$) can also be used for the synthesis.[97,135] Alternatively, mixing β-TCP powder with an aqueous phosphoric acid (H_3PO_4) solution leads to the precipitation of brushite crystals (equation (3)).[136,137]

$$\beta\text{-}Ca_3(PO_4)_2 + Ca(H_2PO_4)_2 \cdot 2H_2O \longrightarrow 4\ CaHPO_4 \cdot 2H_2O \quad (2)$$

$$\beta\text{-}Ca_3(PO_4)_2 + H_3PO_4 + 6H_2O \longrightarrow 3\ CaHPO_4 \cdot 2H_2O \quad (3)$$

Due to the chemically identical composition, α-TCP can be used analogously to the β-phase (equation (4)).[97,131]

$$\alpha\text{-}Ca_3(PO_4)_2 + H_3PO_4 + 6H_2O \longrightarrow 3\ CaHPO4 \cdot 2H_2O \quad (4)$$

Dicalcium phosphate anhydrous (DCPA, monetite) is the anhydrous form of brushite, which occurs when dicalcium phosphate dihydrate (DCPD, brushite) is heated above 80 °C by dehydration[44] or modifying the precipitation conditions to favor a crystallization into monetite[131]. A detailed overview of possible synthesis routes is beyond the scope of this thesis and can be found elsewhere.[138]

Brushite crystallizes in the monoclinic crystal system. The morphology of precipitated crystals varies with different growth conditions. According to Abbona *et al.,* different crystal forms can be distinguished. Specifically, these are irregular and regular crystals, crystal twins and aggregates.[139] At the end of a crystallization process, one of these forms is usually dominant. The main factors influencing the resulting morphology are the pH value and the concentrations of precipitants. A majority of the synthetically produced brushite crystals exhibits a flat, plate-like shape.[139]

The morphology of monetite crystals also depends on the synthesis method and the starting materials used. Thus, crystals can be fine nanoparticles or plate-shaped[140,141], take the form of whiskers with a hexagonal cross section[142], have a spherical rod-like morphology[143], appear as ellipsoidal particles[144] or exhibit various other shapes[138].

An overview of the reaction mechanisms for the previously described apatitic and brushitic cement types, is shown in Figure 4. Crystals precipitated during the cement reaction to HA are either needle-shaped or plate-shaped. If the starting powder used for the cement reaction is finely ground, it has a higher specific surface area, is thus more reactive, and the degree of supersaturation within the solution is increased. This promotes the formation of crystals, which appear finer, more numerous and needle-like. If, on the other hand, coarser ground starting particles are used, platelet-shaped crystals with lower specific surface area are formed.[122,145,146] Plate-like crystals in brushite cements show an entangled and stacked formation.

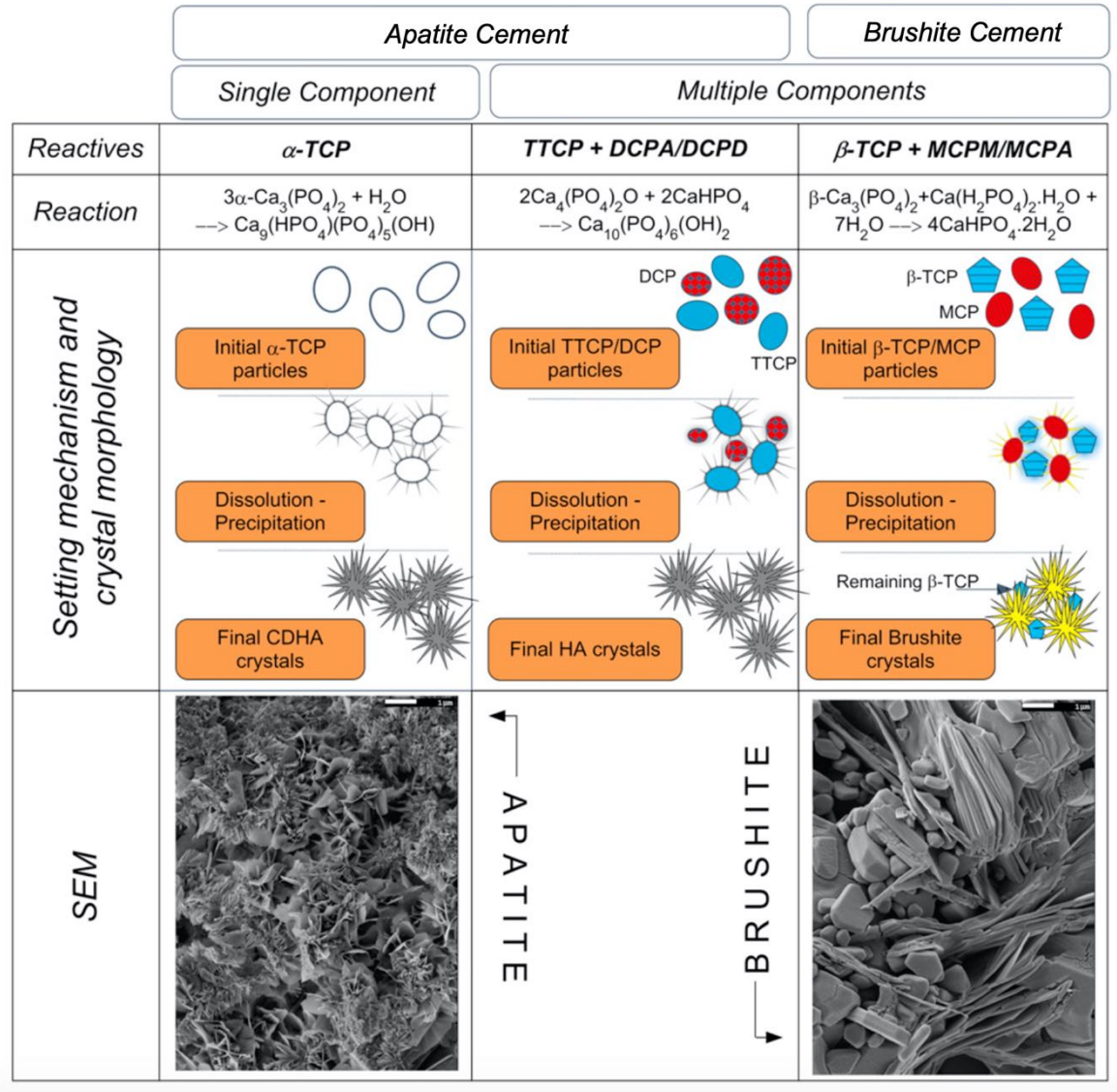

Figure 4. Overview of the apatite and brushite cement reaction. HA can be formed either by the hydrolysis of α-TCP (single component) or the reaction of TTCP with DCPA or DCPD (multiple components). Brushite can also be synthesized by using multiple components in the solid phase. The morphology of the precipitated crystals depends on the cement type. Reprinted and adapted from reference [145], Copyright (2012), with permission from Elsevier.

2.2.3 CaP based bone graft substitutes

Although autologous bone is still the clinical gold standard in bone reconstruction, a variety of synthetic bone graft materials are already commercially available. These grafts exist in the form of granules, prefabricated blocks, pellets, foams, or injectable cement pastes.[147] A selection of commercially available CaPs, which are clinically used for the regeneration of bone defects, is shown in Table 2. In addition, numerous other CaP ceramics and cements are commercially available.[92,148-150]

The pore distribution and porosity of the implant are of considerable importance for the subsequent healing success, since cell ingrowth and vascularization possibilities of the graft depend on these factors. Both the existence of macropores (>100 µm) and micropores (<10 µm) are particularly relevant to allow cell ingrowth and vascularization.[151]

In addition, pores increase the surface area of the implant, subsequently leading to a better mechanical connection between bone and graft.[152,153] A distinction is also made between interconnecting and closed pores. While interconnecting pores are connected with each other and accessible by gases or liquids, closed pores are isolated.[152,154] Therefore, to ensure blood vessel formation and cell migration throughout the implant, interconnectivity is essential.[152]

The macroporosity of a ceramic implant, which is crucial for bone tissue ingrowth, can, for instance, be influenced by using porogens. Porogens are additives that are included in the starting material in order to generate pores by removing these substances at a later stage.[152] These can be volatile or soluble substances such as salts[155,156], sugars[157], naphthalene[158-161] or hydrogen peroxide[162-164]. Alternatively, spherical particles can be added to the starting material, which are then burned out by sintering. However, this method has the drawback of only providing poor interconnectivity of the pores.[152]

Microporosity of the bioceramics provides a larger surface area that is crucial for protein adsorption, which also leads to higher solubility and ion release. If the pores are interconnected, they act as fine channels through which the osteocytes can be connected and act as mechanosensors.[152,165,166]

In CPCs, pores are formed during the setting process when crystals entangle during growth, resulting in the formation of micropores.[149,167] The microporosity of CPCs can be as high as 60% and be influenced by the choice of particle size of the raw powder or the powder-to-liquid ratio (PLR) of the slurry. The smaller the particles, the finer crystals are formed, leading to smaller pores. A reduction of the PLR leads to larger pores as well as higher porosity of the implant.[146,149] However, a balance must always be found between a high overall porosity and sufficient mechanical strength. The higher the porosity, the less mechanically stable the implant.[115]

Table 2. Commercially available synthetic CaP bone graft substitutes.

Product	Composition	Form / Structure	Clinical application	Porosity / Pore structure	Reference
Guidor easy-graft®	β-TCP granules coated with poly(lactic-*co*-glycolic acid)	microporous CaP granules	dental surgery	isotropic; microporous CaP granules with pore sizes of 1-10 µm, high porosity 70%	168,169
Vitoss®	β-TCP	foam pack, foam strip, morsels, and blocks	bony voids in intrinsically non-weightbearing structures	isotropic: up to 90% complex inter-pore channels pore sizes 1-1000 µm	20,150,168,170
Eurobone®	brushite	injectable cement paste	bony voids in intrinsically non-weightbearing structures	isotropic after setting	92,168
ChronOS® Bone void filler	β-TCP	granules, preforms/blocks	bony voids in intrinsically non-weightbearing structures	isotropic: 60% (granules), 70% (preforms) micro- (<10 µm) and macropores (100-500 µm)	20,171-173
ChronOS® inject	brushite, β-TCP	injectable brushite cement containing β-TCP granules	various bone defects	isotropic: (33.3 - 37.6%) after setting	174
Osteomatrix	HA (60%) and β-TCP (40%)	sponge strips	bony voids in intrinsically non-weightbearing structures	isotropic	171
PerOssal™	nanocrystalline HA (51.5%) and calcium sulphate (48.5%)	hemi-cylindrical pellets, (6 mm height, 6 mm diameter)	filling and reconstruction of bone defects, e.g. spinal surgery, drug carrier	capillary porosity	175,176
ApaPore™ 60	phase pure sintered HA	granules	hip replacement; implant fixation	isotropic: 60% micro (<20 µm) and macro (>50 µm) pores	177,178
Cerasorb®	β-TCP	granules, polygonal structure	alveolar reconstruction	isotropic: ~65%	179,180

Also for CPCs it is aimed to increase the macroporosity by using different additives. However, in contrast to ceramics, where biocompatibility of the porogen plays only a minor role because the substances are removed during sintering, this factor is of greater importance for cement pastes that are intended to be injected directly into the body.[181-185] Therefore, there are different approaches to increase the macroporosity of hardened CPCs.[181] One possibility is to introduce a phase into the cement which degrades faster than the CPC or is water soluble and therefore the macroporosity is developed over time or when the hardened implant is immersed in water to dissolve the crystals.[181,186] Additives such as mannitol[187], sucrose[188] or poly(lactic-*co*-glycolic acid) fibers or particles[189-191] are suitable for this purpose.[181] Glucose microparticles were also applied to enhance macroporosity.[192,193] A further approach is the foaming of the cement paste. By adding gases generated by components such as hydrogen peroxide[162] or sodium bicarbonate[186,194], macroporous constructs are created.[181] Besides this, albumen can also be used as a foaming agent.[195-197]

Although native bone is a highly ordered tissue with an anisotropic lamellar structure, commercially available products have an isotropic pore distribution. In addition to mimicking the physiological tissue structure of bone, anisotropic porosity has the advantage of facilitating cell ingrowth and allowing angiogenesis to occur more rapidly in the direction of the pores.[21] For this reason, this thesis deals with the development of anisotropic porous CaP scaffolds for the use as bone graft substitutes.

2.3 Response of the immune system to biomaterials

Upon implantation of a biomaterial, the host body will always initially react with an inflammatory response. However, if the inflammation becomes chronic, the implant is encapsulated fibrously and will no longer fulfill its function.[27,198] To avoid rejection and failure of the material it is important that the inflammatory reaction does not persist.[27]

The immune system is the defense system of the human body. It fights microorganisms and foreign bodies and therefore protects the host from invaders. It also maintains homeostasis and is involved in tissue regeneration.[199,200] Two types of immune system can be distinguished: the innate and the adaptive immune system.[201] The two parts are in constant and close crosstalk.[199] The innate immune system provides the first but non-specific response against invaders like pathogens and acts immediately upon contact.[202,203] It comprises physiological barriers like skin or mucus membranes as well as numerous proteins and cell types such as polymorphonuclear cells (granulocytes, basophils, eosinophils), mononuclear phagocyte cells (dendritic cells, monocytes, macrophages), and lymphocytes (natural killer cells, gamma delta T cells, innate lymphoid

cells).[199,201] It depends on the type of pathogen or invader, which cells and factors are ultimately involved in the response process and in which order they are activated.[204]
Unlike the innate immune system, the reaction of the adaptive immune system is highly specific.[203] It responds antigen-specifically and develops a long-term memory throughout life through contact with pathogens and foreign bodies. The adaptive immune system includes B and T lymphocytes.[202]
Implantation of a biomaterial is inevitably associated with an injury caused by the surgical procedure, with both the innate and adaptive immune system being involved in the subsequent inflammatory response.[199,205] Implantation is followed by blood-material interactions, protein adsorption, provisional matrix formation, immune cell recruitment, acute inflammation, chronic inflammation, granulation tissue development, foreign body reaction (FBR) and fibrous capsule development (Figure 5).[206,207]

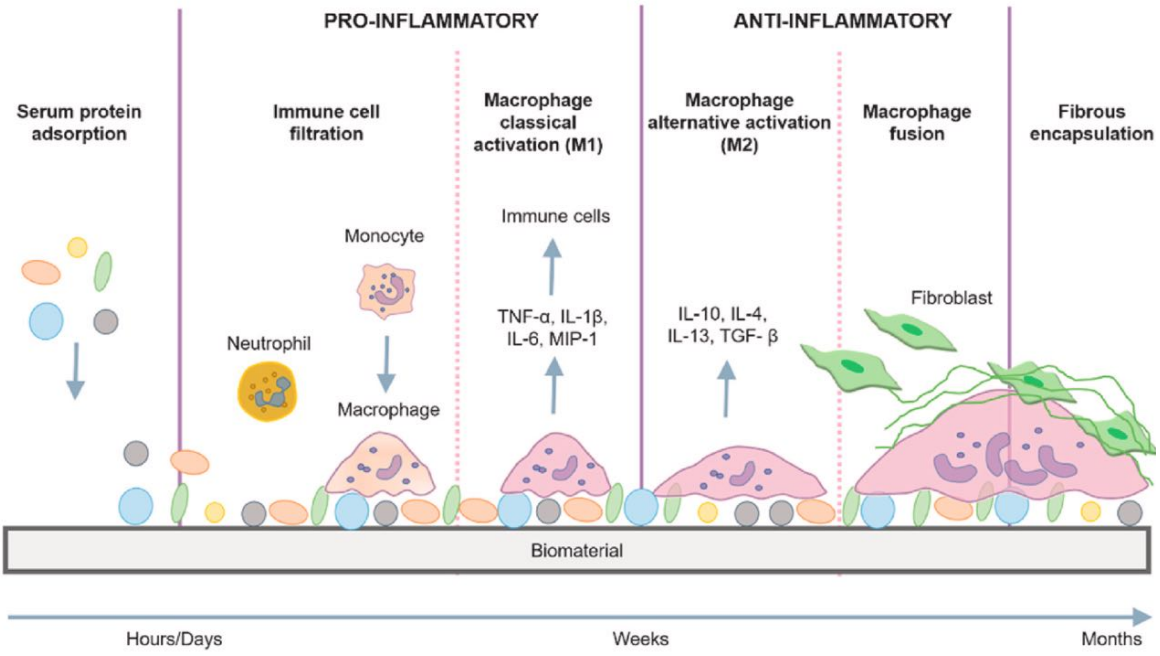

Figure 5. Foreign body immune response. Immediately after implantation of the biomaterial, proteins adsorb on the surface. In the subsequent inflammatory phase, neutrophils are among the first cells to appear at the implantation site, which in turn recruit monocytes. These initially differentiate to macrophages of the pro-inflammatory M1 phenotype, releasing pro-inflammatory cytokines to recruit further immune cells. Along with a transition of the pro-inflammatory M1 to the anti-inflammatory M2 phenotype, macrophages fuse and form foreign body giant cells. Secretion of pro-fibrotic factors attracts fibroblasts, which produce matrix collagens, ultimately resulting in fibrous encapsulation of the biomaterial. Reprinted from reference [207], Copyright (2021), with permission from Elsevier.

Acute inflammation is an always occurring and necessary response of the innate immune system to pathogens or tissue injury, as by implantation of a biomaterial (a foreign body to the immune system).[208] Properties of the biomaterial, such as size, composition, surface morphology and chemistry, determine the type and amount of the adsorbed molecules and the recruitment of additional cells in the hours to days following implantation.[200,208,209] Therefore, the material properties play a crucial role in the response of the host tissue to

implanted biomaterials.[200,210] The design of the implants thus determines whether a short-term and necessary inflammation phase occurs that leads to healing of the tissue or whether a prolonged, chronic inflammatory phase follows, resulting in the failure of the implant.[208]

Immediately after implantation, the material is exposed to blood and proteins (albumin, fibrinogen, fibronectin, vitronectin, gammaglobulins), lipids, sugars and ions adsorb on the surface.[200,210] A blood-based provisional matrix is formed by the thrombus developed at the implantation site or the interface between tissue and implant.[206] In the subsequent inflammatory phase, neutrophils appear as one of the first cell types at the implantation site through injured blood vessels and attempt to degrade the implant through phagocytosis, degranulation and the release of neutrophil extracellular traps (NETs).[27,200,206,207] Through the release of diverse immune-regulatory signals by active neutrophils and the apoptosis of these cells, further immune cells such as lymphocytes and monocytes are attracted and initiate the chronic inflammatory phase.[206]

Monocyte-derived macrophages play a crucial role in the initial inflammatory response. Their reaction to the implant during the FBR determines whether fibrous capsule formation will occur or whether the inflammatory process will subside, leading to final tissue regeneration.[200,206]

Two subtypes of macrophages can be distinguished. Macrophages of the classically activated M1 phenotype are described as pro-inflammatory, whereas alternatively activated M2-like macrophages are considered the anti-inflammatory, pro-healing type.[211] Monocytes that have entered the implant site differentiate into the M1 type. Adherent macrophages promote the migration of further inflammatory cells by releasing chemokines and cytokines.[200] Additionally, the macrophages, as phagocytotic cells, attempt to degrade the implant by secreting reactive oxygen species and degradative enzymes and internalizing the biomaterial.[207] However, if the foreign body is too large to be internalized (>50 nm), macrophages will undergo the so-called “frustrated phagocytosis”. Accompanied by a switch of the pro-inflammatory M1 phenotype into anti-inflammatory M2 macrophages, this leads to macrophage fusion and formation of foreign body giant cells (FBGC) to improve their ability to perform phagocytosis.[29,207,212-214] FBGC formation is promoted by the activation of mast cells, basophils, and T helper cells, which release interleukin (IL)-4 and IL-13. This in turn fosters macrophage fusion.[200,215,216] Due to the FBGCs adhering to the surface of the implant, a barrier can be formed between the tissue and the biomaterial, which may result in implant rejection.[200] FBGCs secrete pro-fibrotic factors. Consequently, fibroblasts are recruited, which in turn form an avascular fibrotic capsule by producing matrix collagens.[206,207,217] Excessive and uncontrolled release of pro-fibrotic factors may lead to tissue fibrosis. Collagenous fibrous encapsulation of the

biomaterial prevents integration of the host tissue into the implant, which may lead to the loss of its function and ultimately to implant failure.[207,218] However, if the immune response to implantation proceeds in a more regulated manner, the tissue is regenerated or restored by parenchymal cells in the final healing phase.[208]

2.3.1 The role of macrophages in the immune response

Macrophages play a major role in the healing process of all wounds. During healing, a transition from the pro-inflammatory M1 type to the anti-inflammatory M2 phenotype occurs. In non-healing wounds, such as diabetic ulcers, the phase of inflammation persists and macrophages remain in the pro-inflammatory status and thus in the first phase of wound healing.[28] The main function of macrophages as phagocytic cells of the innate immune system is the internalization of dead cells, pathogens, foreign bodies and debris.[219] Moreover, they secrete a wide range of pro- and anti-inflammatory cytokines depending on different external stimuli the cells are exposed to.[220]

Macrophages can develop from monocytes circulating in the blood, which have evolved from myeloid progenitor cells residing in the bone marrow. When monocytes enter the injured tissue via blood vessels, they differentiate into macrophages.[221,222] Based on their origin, these cells are referred to as monocyte-derived macrophages. They play a key role in the initiation and resolution of inflammatory processes caused by pathogens, foreign bodies or injuries by responding to influences from their environment through differentiation into the M1 or M2 phenotypes mentioned above.[222,223]

2.3.1.1 Macrophage polarization

Monocyte-derived macrophages are a heterogeneous population of cells with different markers and functions. After invading the injured or inflamed tissue, macrophages are activated as a reaction to signals released by other cells. As a result, macrophages increase the expression of cytokines, chemokines, and other molecules and adopt various phenotypes. These phenotypes are characterized by specific functional properties and gene expression patterns.[222]

In principle, two phenotypes, M1 and M2, can be distinguished.[221] This classification is a very simplified representation for distinguishing the pro- and anti-inflammatory type. *In vivo*, the actual macrophage phenotype lies on a continuum between the M1 and M2 extremes.[222,224] In particular, M2 macrophages, which are associated with pro-healing properties, can adopt a variety of different phenotypes, depending on environmental influences. However, an in-depth description of these subgroups is not in the scope of this thesis and can be found in literature.[225-229]

2.3.1.2 Classically activated M1 phenotype

M1 macrophages are described as the "classically activated" and pro-inflammatory phenotype. Differentiation is induced by pro-inflammatory signals such as interferon-γ (IFN-γ), which is secreted by other immune cells like neutrophils[208] or macrophages[230], or additionally in combination with microbial products such as lipopolysaccharide (LPS) or the cytokine tumor necrosis factor-α (TNF-α).[222,231,232] Macrophages of the M1 phenotype release pro-inflammatory cytokines like IL-1β, IL-6, IL-12, IL-23 and TNF-α.[222,233,234] In addition, the M1 type is characterized by a high level of microbicidal and tumoricidal performance.[235] The inflammatory response initially required for final tissue regeneration after implantation of a biomaterial is fostered by the presence of M1 macrophages. However, a prolonged existence of this macrophage type causes a strong FBR, chronic inflammation and fibrous encapsulation of the graft, leading to implant failure.[236]

Therefore, it is important that a transition from the pro-inflammatory M1 to the pro-healing M2 phenotype occurs over time, resulting in the resolution of the initial inflammation phase. This allows the integration of repairing cells like fibroblasts or endothelial cells, which contribute to tissue regeneration and ultimately lead to the integration of the biomaterial.[237]

2.3.1.3 Alternatively activated M2 phenotype

M2 macrophages, described as 'alternatively activated' and anti-inflammatory, can be subdivided into several subtypes, including M2a, M2b, M2c.[236]

M2a macrophages are activated by cytokines such as IL-4 or IL-13 released by basophils, mast cells, and other granulocytes.[236,238] In addition, they are hallmarked by high expression levels of the mannose receptor CD206 and the secretion of pro-fibrotic factors such as fibronectin, insulin-like growth factor, and transforming growth factor (TGF)-β.[239] Due to their properties conducive to tissue regeneration, these macrophages are also referred to as "wound-healing" macrophages.[224]

Activation of M2b macrophages occurs through stimulation by immune complexes and toll-like receptor agonists. Both M2a and M2b macrophages exert immunoregulatory effects through the release of the cytokines IL-10, IL-1ra, and IL-6.[236] However, even though M2 macrophages are generally regarded as the anti-inflammatory type, M2b macrophages produce both pro- (L-1β, IL-6, TNF-α) and anti-inflammatory (IL-10) factors.[240,241]

M2c macrophages are induced by IL-10. Through the secretion of TGF-β and IL-10, they contribute significantly to the inhibition of inflammatory immune responses and therefore have a key function in tissue regeneration.[236,241] M2c macrophages are also referred to as deactivated macrophages as their high expression level of IL-10 leads to the downregulation of pro-inflammatory cytokines, such as TNF-α, IL-6, IL-8, and IL-12.[241]

In addition, two other subtypes of M2 macrophages have been identified so far: M2d und M2f. M2d macrophages are also called tumor-associated macrophages (TAMs) and are characterized by high secretion of anti-inflammatory IL-10 and vascular endothelial growth factor and low release of pro-inflammatory IL-12, TNF-α and L-1β. Thereby, TAMs are thought to play a major role in promoting tumor angiogenesis and cancer metastasis.[242-244] The M2f macrophage type is hallmarked by the production of anti-inflammatory factors following engulfment of apoptotic cells.[245,246]

However, the balance between M1 and M2 macrophages is a major factor influencing remodeling.[247,248] Although a high ratio of M2:M1 macrophages in the environment of implants has been thought to lead to better tissue regeneration,[249] an excessive and especially prolonged presence of M2 macrophages may lead to the development of FBGCs and biomaterial encapsulation.[206,236]

2.3.1.4 Macrophage extracellular traps

Macrophages can produce extracellular traps (ETs), which are referred to as “macrophage extracellular traps” (METs), as an immune response. ETs are thought to immobilize and kill microorganisms but are also involved in disorders such as aseptic inflammation and autoimmune diseases.[250] ETs are net-like, sticky structures composed of cellular DNA and loaded with histones, antimicrobial peptides, and proteases.[251] (Figure 6)

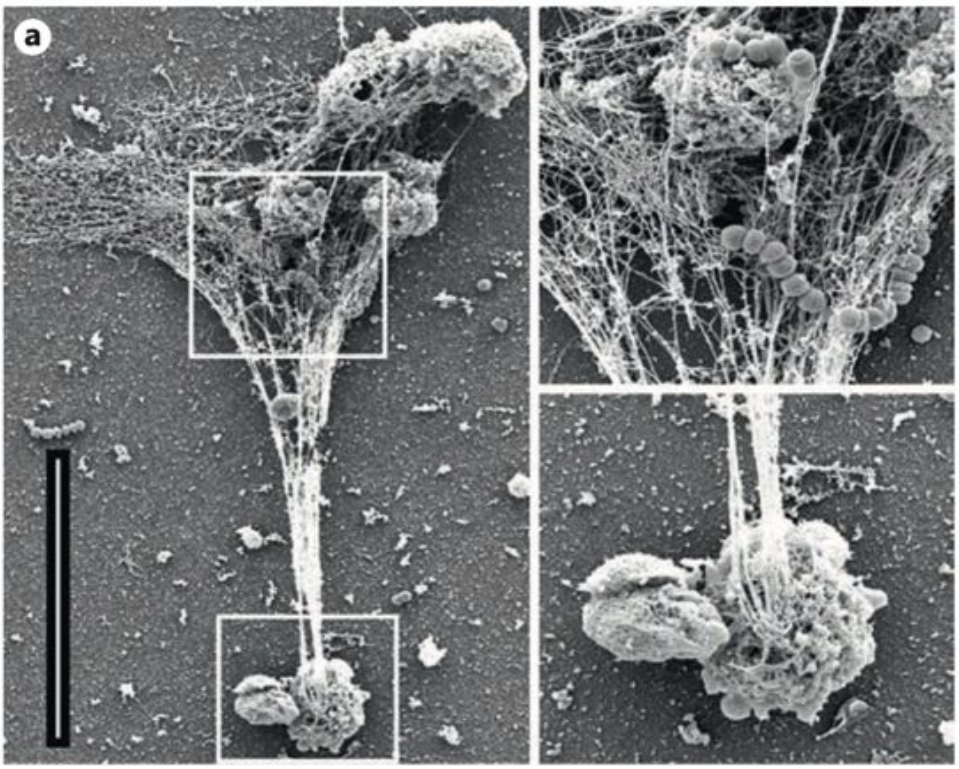

Figure 6. Macrophage extracellular traps. Macrophages release extracellular traps, sticky fibers composed of cellular DNA, to kill and immobilize microorganisms. Scale bar: 20 µm. Reproduced from reference [250] with permission, Copyright © 2017 Karger Publishers, Basel, Switzerland.

Thereby, the cell undergoes a cell death program called "ETosis," in which intracellular DNA is extruded from the cell to form sticky fibers that can capture and kill microorganisms.[250,252,253] The release of ETs by neutrophils is well known and has been extensively described in literature.[254-257] Despite the loss of nuclei induced by the ETosis process, it has even been reported that neutrophils can maintain their viability as well as their chemotactic and phagocytotic functions.[251,258] For macrophages, ET formation was first reported in 2010.[251,259] Here, the ETosis associated with the release of METs can proceed very rapidly, i.e., in less than 30 min.[260,261] A variety of triggers such as different bacterial species, parasites, bacilli, fungi and chemical stimuli can trigger the formation of METs. However, whether and how exactly the release of METs is related to a pro-inflammatory M1 macrophage phenotype remains to be conclusively elucidated and is thus subject of research.[250]

2.3.2 Influence of biomaterials on macrophage polarization

The influence of biomaterials on the formation of METs has not been reported so far and was demonstrated for the first time through the work presented in this thesis (Chapter 5). However, biomaterial properties such as the chemical composition, pore size, surface topography, mechanical properties and implant dimension are known to influence macrophage polarization.[247] The impact of these factors is multifaceted and reviewed and described in detail in literature.[236]

The effect of pore sizes in 3D scaffolds on macrophage polarization was, for example, investigated in an *in vivo* study by Sussman *et al.*.[262] For this purpose, the response of macrophages to poly-(2-hydroxyethyl methacrylate) (p-HEMA) scaffolds with uniformly sized small (34 µm) and large (160 µm) spherical pores in subcutaneous mouse tissue was assessed 21 d after implantation. Macrophages inside the 34 µm pore-sized scaffolds showed significantly higher expression of M1 markers than macrophages located outside the scaffold, for which high M2 marker expression was revealed. However, higher vascularization, reduced fibrosis, and stronger remodeling were observed in the scaffolds with smaller pores, indicating that macrophages of the M1 phenotype are not necessarily detrimental to the process of tissue regeneration.[262]

The influence of 3D-printed poly(lactic) acid (PLA) and chitosan-based scaffolds with varying surface properties on human monocyte-derived macrophages *in vitro* was studied by Almeida *et al.*.[263] In addition to the two different materials, the focus was on the influence of pore structure on polarization, comparing an orthogonal pore geometry with a diagonal one. Although the material itself had the greatest impact on macrophages, resulting in greater secretion of TNF-α in the case of chitosan and higher release of IL-6, IL-12/23, and IL-10 for PLA, pore geometry also affected the cell response. Larger pores and wider

angles resulted in an increased production of pro-inflammatory cytokines such as TNF-α and IL-12/23 in chitosan scaffolds. In addition, the diagonal pore geometry led to a higher percentage of elongated cells and weaker FBGC formation.[263]

This observation is consistent with studies on 2D structures conducted by McWhorter *et al.*.[264] They found that the shape of murine bone marrow-derived macrophages was associated with their polarization.[264] Micropatterning was applied to prepare cell culture substrates with 20 µm and 50 µm wide grooves. This allowed direct control of macrophage cell shape through topological constraints, resulting in elongated cells (Figure 7) and influencing macrophage polarization. Elongation alone, without the addition of M2 inducing cytokines, resulted in the expression of M2 characteristic markers. In addition, the release of pro-inflammatory cytokines was inhibited.[236,264]

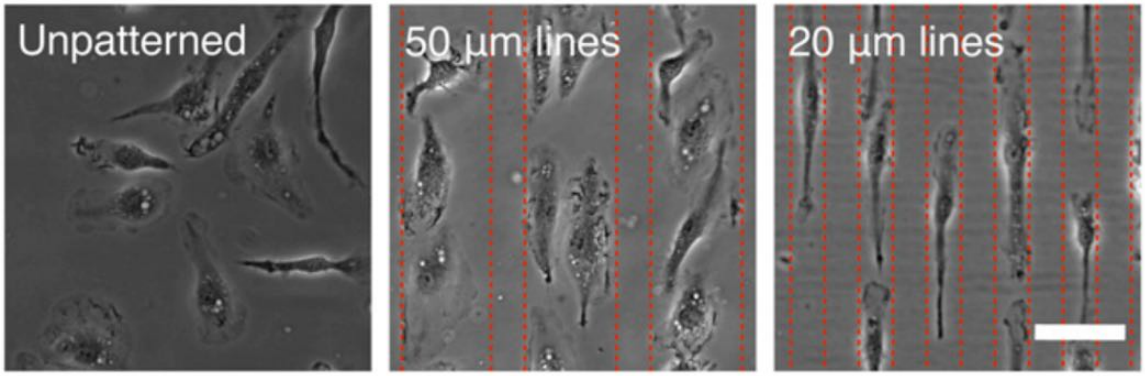

Figure 7. Elongation of murine bone-marrow macrophages. Micropatterning was used to produce substrates with 50 µm and 20 µm grooves, leading to the forced elongation of macrophages and preferential M2 polarization. Scale bar: 50 µm. Reprinted from reference [264], National Academy of Science.

Using lithographic patterning of poly(ε-caprolactone) (PCL), PLA and poly(dimethyl siloxane) (PDMS) substrates, Chen *et al.* prepared parallel gratings with a line width of 250 nm - 2 µm.[265] RAW 264.7 cells showed elongation induced by the gratings regardless of surface chemistry, with only gratings larger than 500 nm led to cell stretching. (Figure 8) In addition, a clearly reduced inflammatory response was observed *in vitro* in association with elongation occurring at larger gradings. Subcutaneous *in vivo* studies in Sprague-Dawley rats revealed that macrophages on the gratings with 2 µm line width showed weaker fusion and thus FBGC formation three weeks after implantation compared to the planar control.[265]

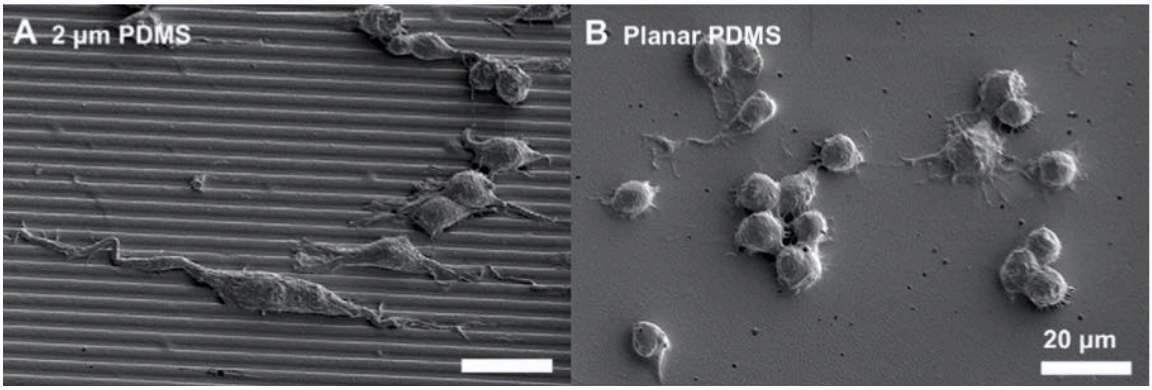

Figure 8. Macrophage shape on PDMS gratings and planar substrates. Gratings with 2 µm line width led to macrophage elongation while cells had a roundish morphology on a planar surface. Reprinted from reference [265], Copyright (2010), with permission from Elsevier.

These studies show that macrophage shape and polarization can be influenced by the choice of biomaterials with appropriate properties such as surface topography, architecture, and other physical and chemical cues. An elongated macrophage shape is predominantly associated with the anti-inflammatory phenotype.

2.3.3 Primary biological response to bone substitute materials

When a synthetic bone graft substitute is implanted, the biological response is similar to the phases of bone healing beginning after a fracture, as described in chapter 2.1.3. Directly after implantation, the bone graft comes into contact with tissue and body fluids such as blood and consequently with proteins, blood cells and immune cells. In the early phase, a thrombus develops, and the immune system is activated.[266-270] Within the inflammatory phase, which occurs approximately within the first 24 h after implantation, the TNF-α and other inflammatory mediators such as IL-1, IL-6, IL-11, IL-18 are secreted and further immune cells and MSCs are attracted. Macrophages play a particularly important role in this process, as they have a key role in the further healing process.[266,271] Depending on the reaction of the immune cells, this phase will determine the fate of the biomaterial, i.e., encapsulation and rejection of the implant or healing and remodeling into bone tissue. Thereby, the properties of the graft material such as porosity, specific surface area, surface structure and roughness and, of course, chemical composition are of significant importance.[266,272] In the bone formation phase, woven bone is formed by vascularization and mineralization of the soft callus. This is followed by the bone remodeling stage, where woven bone is remodeled into lamellar bone tissue.[266] (Figure 9)

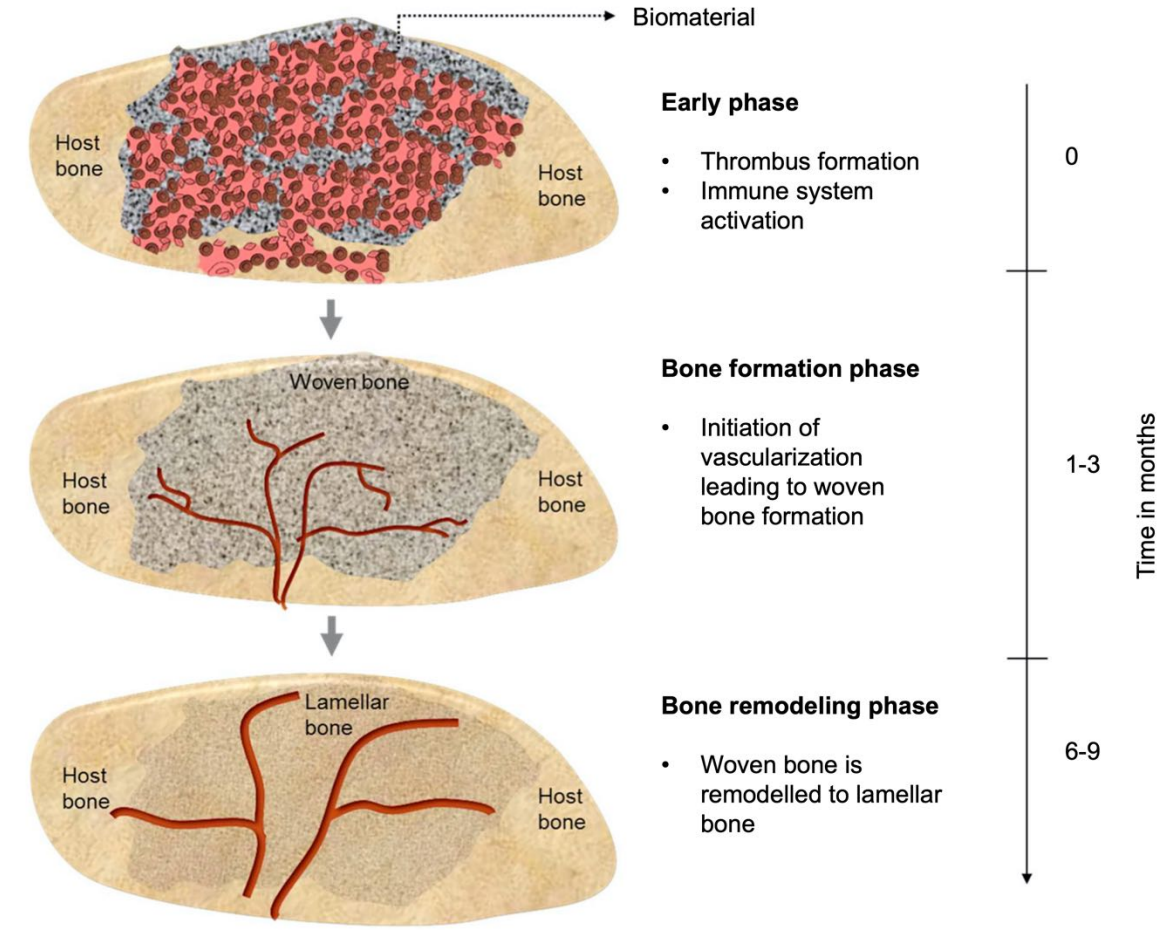

Figure 9. Primary biological response to the implantation of a bone graft. In the early phase, a hematoma which is invaded by immune cells is formed. In the bone formation phase, soft callus is mineralized, leading to the formation of hard callus which is remodeled to lamellar bone in the bone remodeling phase. Reprinted and adapted from reference [266], Copyright (2018), with permission from Elsevier.

2.4 Fundamentals of directional freezing

Unidirectional freezing is a valuable tool for the fabrication of anisotropic porous structures. In this process, a solution or slurry is frozen in the presence of an external temperature gradient, resulting in parallel growth of ice crystals as the solution solidifies. After ice crystal removal, a scaffold with highly aligned pores remains.

To understand this process in more detail, it is necessary to first understand the mechanisms underlying the freezing of water. In the further course, the physical background of unidirectional freezing will be explained.

2.4.1 Solidification of water

Understanding the solidification of water first requires knowledge of the atomic structure of a water molecule (H_2O). A water molecule is formed by two hydrogen atoms and one oxygen atom. The oxygen atom within a water molecule is sp^3-hybridized. The hydrogen atoms therefore form a tetrahedron with the two orbitals of the free electron pairs, in the middle of which the oxygen atom is located. Bonding electrons (between oxygen and

hydrogen atoms) are more strongly attracted to the oxygen atom. This results in a negative excess charge on the oxygen atom, while a positive excess charge exists on the hydrogen atom. Due to the partial charges present in the water molecule, hydrogen bonds are formed to adjacent H_2O molecules.[273]

At atmospheric pressure, water freezes into ice at 0 °C, increasing in volume by about 9%. Via the hydrogen bonds, ice crystals which crystallize in the hexagonal crystal system are formed. These are present in the so-called stable ice phase I_h. Here, one hydrogen atom is located between two oxygen atoms (Figure 10 a). Each water molecule in I_h has four nearest neighbors. Within the so-called basal plane, each molecule has three bonding partners, and one bonding partner to a parallel plane. For this reason, ice crystals have a mechanical anisotropy.[273] In addition to the hexagonal ice phase, there are nineteen other currently known phases which occur depending on the temperature and pressure.[274-277] Ice crystal growth in the stable ice phase I_h, which occurs in the form of hexagonal prisms, is shown schematically in Figure 10 b.

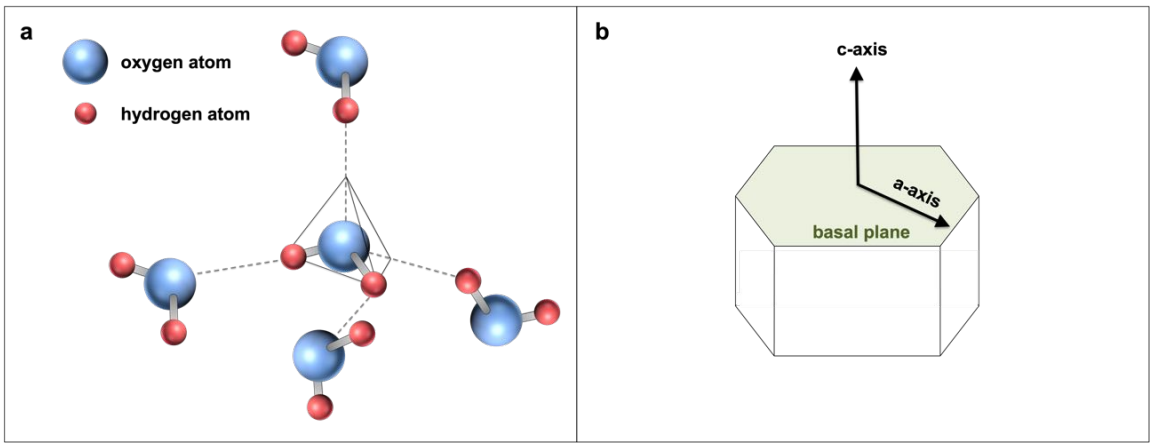

Figure 10. Ice crystal growth. a) Arrangement of water molecules in ice. b) Hexagonal ice crystal growth. The c-axis corresponds to the normal of the basal plane, while the a-axis lies perpendicular to one edge of the hexagon. Based on reference [273].

The basal plane normal is called the c-axis, while the normal lying to one of the edges of the hexagon corresponds to the a-axis.[273] In ice, the preferred direction is the c-axis, around which three-fold symmetry can be observed.[278] The growth speed in ice is strongly anisotropic.[279] Within the basal plane or c-plane, water molecules preferably attach themselves laterally to the lattice already formed. Here, only two adjacent H_2O molecules are required for a stable bond. However, in some cases, an incorporated molecule forms only one bond, but immediately forms another binding site for the next molecule. In this case, fewer hydrogen bonds must be formed to the molecules already present in the lattice than in the case for the formation of a new c-plane. For the formation of such a further plane, the first three water molecules can each form only one bond to the lattice molecules of the plane below (and not to each other). Only a fourth water molecule can form stable

bonds with the three molecules already existing in this plane.[278,279] This results in a 10^2-10^3 times higher growth rate within the basal plane than perpendicular to it in the direction of the c-axis.[280]

2.4.2 Unidirectional freezing - principle

When seawater freezes, the pure hexagonal ice crystals, which have randomly aligned horizontal c-axes, form a matrix while growing. Impurities contained in the water are forced into the spaces between this matrix.[281] This naturally occurring effect is also utilized in freeze structuring approaches. In principle, the process consists of two steps. A material in solution is frozen and then lyophilized. This results in a porous sample structure, representing a negative of the ice crystal morphology in the frozen state.[282]

In unidirectional freezing, a temperature field with a constant gradient is superimposed on the sample during the freezing process, resulting in a preferred growth direction of the ice front. By means of controlled growth rates and temperature gradients, the ice crystal structure can be specifically influenced.[283]

A detailed theoretical description of the fundamentals of solidification of metal alloys is provided by W. Kurz and D. Fisher.[284] However, the basic principles can also be applied to aqueous solutions. The dependence of crystal morphology on solidification parameters has been described by theoretical models for metal alloys and is still an important part of research.[285-290] For suspensions, the interactions between a growing planar ice front and suspended inert particles have been theoretically characterized by G. F. Bolling *et al.*.[291] However, these models cannot be transferred to any other system.

The materials used in this thesis, such as alginate, chitosan or hyaluronic acid, are biopolymers interacting with each other to different degrees according to their concentration and molecular weight. The addition of CaP powders further complexifies the situation. For this reason, the theoretical description of the dependence of the ice crystal morphology on the parameters governing the freezing process is highly complex. A detailed determination of these parameters is a challenge not to be neglected, as these factors are themselves often functions of other variables, which can change during the solidification process. An example of this is the heat capacity of water, which increases strongly when the liquid is cooled down to values below -15 °C.[292] Therefore, the setup of a theoretical mathematical model describing the ice crystal morphology as a function of several freezing parameters is beyond the scope of this thesis.

2.4.3 Unidirectional freezing for the generation of aligned pore structures

At the beginning of the solidification process in solutions, a planar ice front initially grows. Ice crystal formation occurs through the attachment of pure water molecules to the crystal lattice. The solutes are largely not incorporated into the lattice and are forced ahead of the

front. The distribution coefficient k, which is very small in this case, is described by the following equation (5):[284,293]

$$k = \frac{c_{solid}}{c_{liquid}} \quad (5)$$

Here, c_{solid} is the solute concentration on the side of the ice front that is in solid phase. The concentration of the substance in liquid phase is described as c_{liquid}.[284,293]

The particles located ahead of the ice front are transported away by diffusion and convection, for instance, and are distributed uniformly in the solution again. However, if the velocity at which this process occurs is lower than that of the ice front, an increased solute concentration ahead of the front can be observed.[284]

The concentration of the substance $c(x)$ within the solution thus depends on the position x. It exhibits the highest value c_{max} directly at the boundary to the ice front (x = 0) and decreases again to its original value c_0 with increasing distance. The higher the velocity of the ice front, the steeper the slope of the concentration curve ahead of the front.[284] The course of the concentration is shown in Figure 11 a.

The liquidus temperature $T_L(x)$ of the solution depends on the solute concentration and decreases with increasing concentration.[284] Therefore, $T_L(x)$ decreases with increasing proximity to the ice front, where the solute concentration is highest. (Figure 11 b)

The freezing point of the solution is lowered by the dissolved substances ahead of the ice front. If a liquid is below its solidification temperature in the liquid phase, this thermodynamically metastable state is called "supercooled liquid". If, additionally, the cause of supercooling is an increased concentration of the substance, the term "constitutional supercooling" coined by J.W. Rutter and B. Chalmers is used.[294]

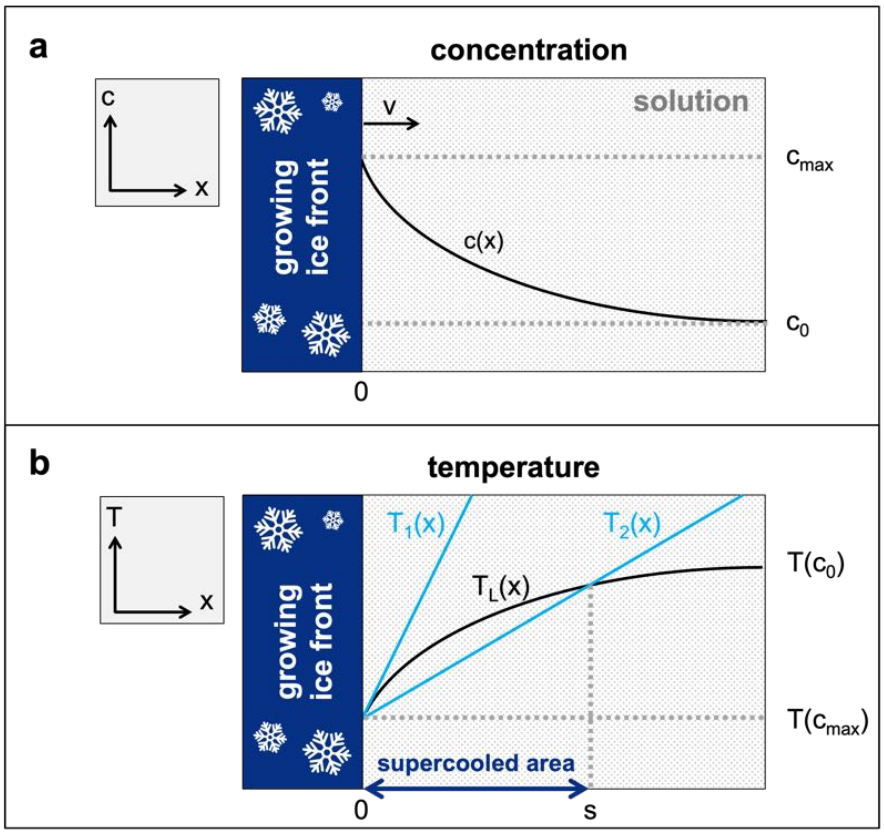

Figure 11. Growing ice front during unidirectional freezing. a) As the distance from the ice front increases, the solute concentration in the solution decreases. b) For this reason, the liquidus temperature $T_L(x)$ reduces as the proximity to the ice front is increased. $T_1(x)$ and $T_2(x)$ represent two possible imposed temperature fields. Based on references [284,295].

Figure 11 b shows the exemplary profiles of two temperature fields. In the case of the temperature field $T_1(x)$ with the gradient ∇T_1, the temperatures at all positions x of the sample are higher than the respective liquidus temperature. Therefore, no supercooled zone exists, leading to a stable and planar morphology of the ice front that is resistant to perturbations.[284,295]

In the case of the temperature field $T_2(x)$ with the corresponding internal gradient ∇T_2, there is a constitutionally supercooled region ($0 < x < s$) in which the temperature of the solution is lower than the liquidus temperature. The gradient criterion states that constitutional supercooling occurs when the magnitude of the gradient at the phase boundary ∇T is smaller than that of the gradient of the liquidus temperature ∇T_L.[284,295] The latter corresponds to the slope of the tangent to the liquidus curve at the interface. Below the liquidus temperature, a phase transformation from liquid to solid occurs in the thermodynamic equilibrium of a system. Due to the existing constitutional supercooling, the system is in a metastable state and no phase transition occurs initially. If disturbances occur at the ice front, it is energetically favorable for foreign particles to form bulges or to grow into the supercooled zone.[284,295]

The gradient of the local concentration and consequently that of the local liquidus temperature becomes steeper due to the emerging perturbations, promoting the growth of

further ones. However, the more such perturbations exist, the larger the interface between solution and ice front and the higher the energy required for the formation of this interface (interfacial energy E_i). This in turn leads to the stabilization of the planar ice front morphology. Thus, the gradient criterion alone is not sufficient to describe the formation of a non-planar ice front.[295] A theoretical consideration of the stability of the growing ice front was provided by W.W. Mullins and R. F. Sekerka.[296] In addition to the gradient criterion, another term was included that also considers the interfacial energy.[295] If this term is added to the difference of ∇T and ∇T_L at the ice front, the expression for system instability must be less than zero. If this criterion is met, the ice front breaks up and the growth of a non-planar ice front can be observed.[284]

The rate at which the solution freezes decisively determines what morphology the scaffold will ultimately exhibit. Therefore, the simple and important premise is that particles in the solution are displaced by the growing ice front since the particles would otherwise be uniformly distributed in the frozen construct. The interfacial free energies present in the system are associated with both the particle-solid, particle-liquid and solid-liquid interfaces and are therefore referred to as E_{ps}, E_{pl} and E_{sl} respectively. The following requirement must thus be fulfilled for the displacement of the particles from the front (equation (6)):[297]

$$\Delta E_0 = E_{ps} - \left(E_{pl} + E_{sl}\right) > 0 \tag{6}$$

Both repulsive (interparticle van der Waals interactions at the solid-liquid interface) and attractive (viscous drag) forces act on a particle in solution with respect to the growing front.[297] By equating these forces, the critical velocity of the ice front v_{cr}, above which entrapment of the particles and finally homogeneous distribution in the frozen solution occurs, can be described using equation (7).

$$v_{cr} = \frac{\Delta E_0 d}{3\eta r}\left(\frac{a_0}{d}\right)^n \tag{7}$$

Here, the distance between the particle and the ice front (d), the mean distance between two particles (a_0), the particle radius (r), the solution viscosity (η) and a constant for correcting the repulsive forces, which ranges from 1 to 5, are included.[283,297]

The morphology that occurs as a function of the critical speed is shown in Figure 12.

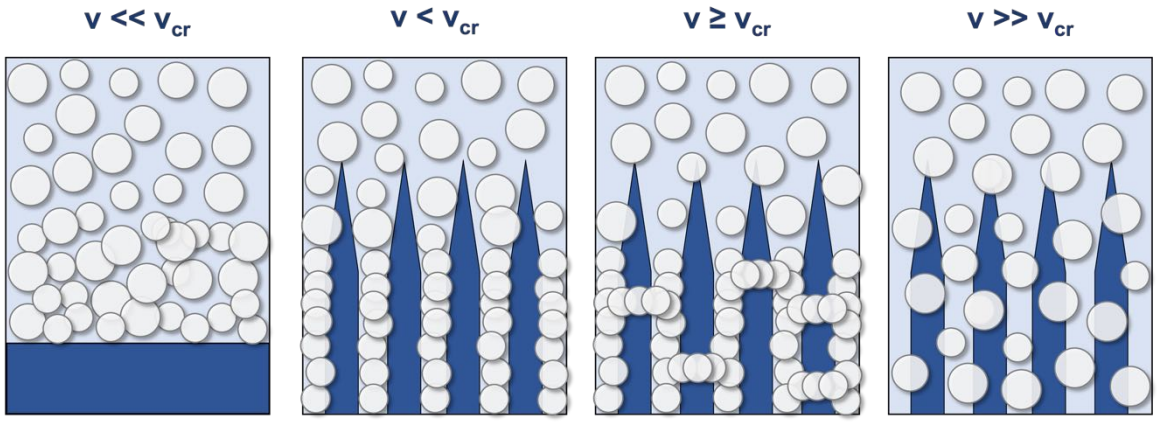

Figure 12. Ice front morphology in directional freezing. Whether the particles are rejected or entrapped by the growing ice depends strongly on the critical velocity v_{cr}. At velocities well below v_{cr} ($v << v_{cr}$), the particles are displaced from the planar front and accumulate in front of it. At higher velocities ($v < v_{cr}$), the ice front breaks up and the growing lamellar ice crystals push the surrounding particles between them. However, if the critical velocity is exceeded ($v \geq v_{cr}$), bridging between neighboring lamellae occurs due to the entrapment of particles in the ice lamellae. At very high velocities ($v >> v_{cr}$) the particles are entrapped in the ice front, leading to an isotropic pore structure. Based on reference [297].

If the velocity of the growing ice front is far below v_{cr}, the particles are forced in front of the planar front and accumulate there. The ice front breaks up at velocities that are within a reasonable range below v_{cr}, and the solutes accumulate between the lamellar growing ice crystals. If the velocity is equal to v_{cr} or slightly above, particles will be entrapped between the ice crystals, resulting in bridging between adjacent lamellae after freeze drying. However, if the velocity is significantly above v_{cr}, particles will be enclosed in the ice front.[298] Thereby, the final pore structure of the freeze-dried scaffolds under the given conditions depends on the composition of the solution, the speed of the solidification front, and thus the temperature gradient.[299,300]

Naglieri *et al.* developed a descriptive morphology map for directional freezing of silicone carbide scaffolds.[300] It shows graphically how the resulting pore morphology depends on the solid load and the cooling rate. (Figure 13) Here, three zones can be distinguished: processing conditions resulting in lamellar, dendritic or isotropic porosity due to particle entrapment. The latter is caused by the application of very high cooling rates and occurs with increasing solid load. Decreasing the cooling rate and particle concentration leads to a change in morphology from isotropic to dendritic. A lamellar porosity, on the other hand, is achieved by lower cooling rates or the reduction of the suspension concentration. Thus, the final morphology depends strongly on those parameters that determine the degree of constitutional supercooling. These include the freezing temperatures, the speed of the growing ice front and the concentration of the suspension.[300]

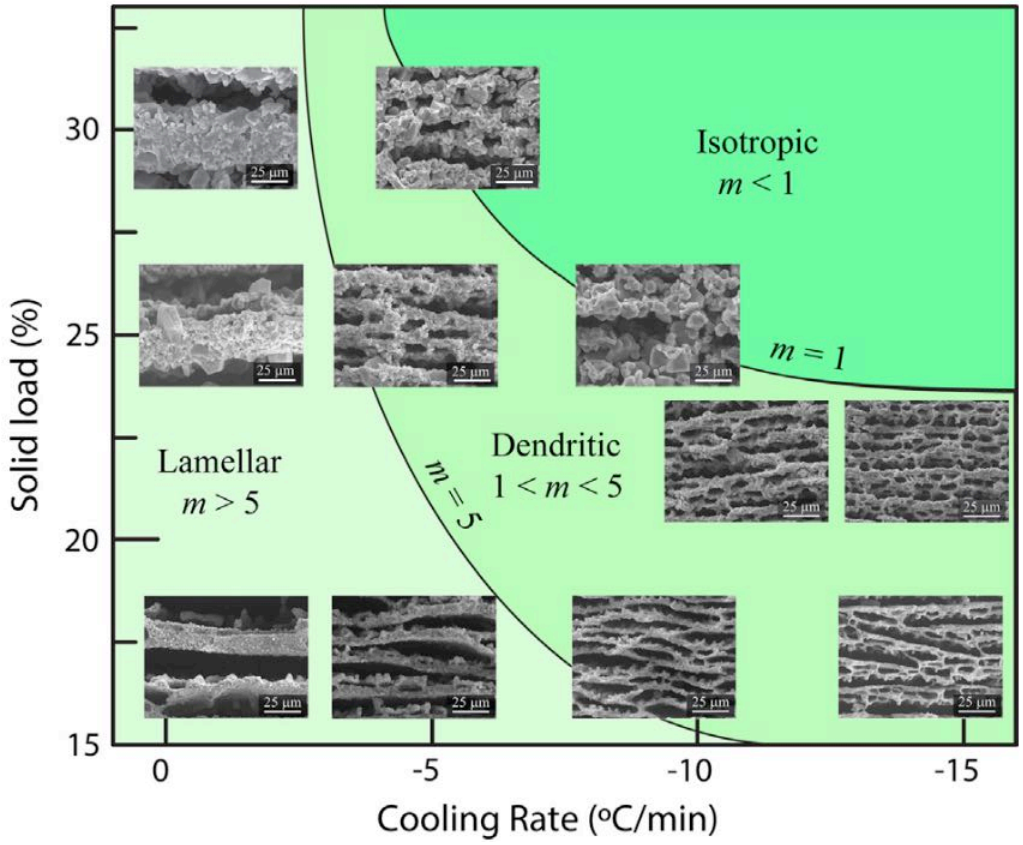

Figure 13. Morphology of directionally frozen silicon carbide scaffolds as a function of cooling rate and solid load. The morphological parameter *m* divides the map into zones of lamellar, dendritic and isotropic porosity. High solid load and high velocities result in an isotropic porosity of the scaffold. If these parameters are reduced, the pore morphology transitions to dendritic and finally to lamellar. Reprinted from reference [300], Copyright (2013), with permission from Elsevier.

2.4.4 Directional freezing for biomedical applications

A valuable overview of freeze-structuring approaches for the fabrication of anisotropic porous polymers for biomedical applications is given in the literature review, which was co-authored by the author of this thesis.[283] However, a selection of studies that have focused on the great potential of ice-templating to fabricate tissue substitutes is presented in more detail below.

Directional freezing was used to prepare anisotropic porous silk-based biomaterials containing porcine cardiac tissue-derived extracellular matrix for cardiac tissue engineering applications. Solutions were directionally frozen using a bath containing dry ice and 100% ethanol. The scaffolds were designed not only to match the structure and architecture of native cardiac tissue, but also to ensure proper cell-matrix contact and thus promoted cell infiltration. *In vivo* studies in rats showed that the scaffolds were 99% invaded by cells after four weeks and exhibited improved vascularization.[301]

Stokols *et al.* also used dry ice to fabricate anisotropic porous agarose scaffolds by directional freezing for nerve guidance applications. By supporting the ordered organization of regenerating axons after spinal cord injury, such scaffolds may significantly improve the success of regeneration and help restore the functionality of the newly formed

neural tissue. Soft and flexible scaffolds were designed to promote cell alignment and be loaded with growth-stimulating proteins for nerve growth support.[302]

In a systematic study, Pawelec *et al*. aimed to understand and influence the pore structure and architecture of scaffolds with anisotropic open porosity prepared by ice templating. Scaffolds with dimensions of at least 10 mm in each dimension, thus suitable for biomedical applications, were successfully fabricated by freezing collagen slurries. They found that the pore morphology depended sensitively on the distance to the cooling surface and the local cooling rate.[303]

The development of scaffolds suitable for bone regeneration was the aim of a study conducted by Rödel *et al*.. For this purpose, CaP (MCPA and brushite) mineralized silk fibroin scaffolds with primarily disordered porosity were prepared. To demonstrate that such scaffolds may also be prepared in the future with a highly ordered, anisotropic pore structure, silk fibroin solutions were directionally solidified, yielding scaffolds with parallel pores and diameters of 30-50 µm.[304]

Silk fibroin-chitosan scaffolds with oriented pores and predefined microfluidic channels were engineered by Mao *et al.*. The aim here was to mimic vascularized 3D organs with larger dimensions, uniform cell distribution within the construct, and sufficient nutrient supply. The aligned pores had a diameter of about 100 µm and led to a significantly better uptake of cell culture medium and a high cell viability after 5 d also inside the scaffold. The authors hypothesized that by rolling up the 2 mm high, 1.5 mm wide and 7.5 mm long scaffolds, which were previously seeded with primary cells and in the microfluidic channels with endothelial cells, thick prevascularized organs could be realized.[305]

Schoof *et al.* developed anisotropic porous collagen sponges, the application of which is of general high interest due to the natural occurrence of collagen in the human body. Scaffolds with directional porosity were prepared by directional freezing. These had a height of 10 mm, and the pore diameter could be adjusted between 20 µm and 40 µm by choosing the acetic acid concentration in the collagen suspension.[306]

All these examples clearly show that the biomedical applications of such anisotropic porous scaffolds prepared by directional freezing are manifold. The final properties of the sample depend on the initial parameters and materials used and can be adapted to the requirements of the intended application.

Chapter 3

Morphological Control of Freeze-Structured Scaffolds by Selective Temperature and Material Control in the Ice-Templating Process

Chapter 3 was published as original research article (Annika Seifert, Julia Gruber, Uwe Gbureck, Jürgen Groll, Morphological Control of Freeze-Structured Scaffolds by Selective Temperature and Material Control in the Ice-Templating Process in *Advanced Engineering Materials* **2021**, 2100860), reproduced from reference [307] as an open access article distributed under the Creative Commons Attribution 4.0 International License (CC BY 4.0), which permits unrestricted use, distribution, and reproduction in any medium.

The article is based on the work of the author of this thesis, Annika Seifert, who conducted all experiments and data evaluation and wrote the manuscript.

The author contributions to the original research article are as follows:

Publication (complete reference):

A. Seifert, J. Gruber, U. Gbureck, J. Groll, Morphological Control of Freeze-Structured Scaffolds by Selective Temperature and Material Control in the Ice-Templating Process. *Advanced Engineering Materials* **2021,** 2100860.
DOI: https://doi.org/10.1002/adem.202100860

Participated in	**Author Initials,** Responsibility decreasing from left to right				
Study Design	A.S.	J.Gru. U.G. J.Gro.			
Methods Development	A.S.		U.G. J.Gro.		
Data Collection	A.S.		J.Gru.		
Data Analysis and Interpretation	A.S.		U.G. J.Gro.		
Manuscript Writing	A.S.	.	J.Gru. J.Gro. U.G.		
Writing of Introduction	A.S.				
Writing of Materials & Methods	A.S.				
Writing of Discussion	A.S.		J.Gru.		
Writing of First Draft	A.S.				

Chapter 3

The author contributions to the figures and tables are as follows:

Publication (complete reference):

A. Seifert, J. Gruber, U. Gbureck, J. Groll, Morphological Control of Freeze-Structured Scaffolds by Selective Temperature and Material Control in the Ice-Templating Process. *Advanced Engineering Materials* **2021,** 2100860.
DOI: https://doi.org/10.1002/adem.202100860

Figure	**Author Initials,** Responsibility decreasing from left to right				
Figure 14	A.S.				
Figure 15	A.S.				
Figure 16	A.S.				
Figure 17	A.S.				
Figure 18	A.S.				
Figure 19	A.S.				
Figure 20	A.S.				
Figure 21	A.S.				
Figure 22	A.S.				

Table	**Author Initials,** Responsibility decreasing from left to right				
Table 3	A.S.				
Table 4	A.S.				
Table 5	A.S.				

The doctoral researcher confirms that she has obtained permission from both the publishers and the co-authors for legal second publication.

The doctoral researcher and the primary supervisor confirm the correctness of the above mentioned assessment.

Annika Seifert		Würzburg	
Doctoral Researcher's Name	Date	Place	Signature

Prof. Dr. Jürgen Groll		Würzburg	
Primary Supervisor's Name	Date	Place	Signature

3.1 Abstract

Herein, it is aimed to highlight the importance of the process parameter choice during directional solidification of polymer solutions, as they have a significant influence on the pore structure and orientation. Biopolymer solutions (alginate and chitosan) are directionally frozen while systematically varying parameters such as the external temperature gradient, the temperature of the overall system and the temperatures of the cooling surfaces. In addition, the effect of material properties such as molecular weight, solution concentration or viscosity on the sample morphology is investigated. By selecting appropriate temperature gradients and cooling surface temperatures, aligned pores ranging in size between (50 ± 22) µm and (144 ± 56) µm are observed in the alginate samples, whereas the pore orientation is influenced by altering the external temperature gradient. As this gradient increases, the pores are increasingly oriented perpendicular to the sample surface. This is also observed in the chitosan samples. However, if the overall system is too cold, i.e., using temperatures of the lower cooling surface down to -60 °C combined with low temperatures of the upper cooling surface, control over the pore orientation is lost. This is also found when the viscosity of chitosan solutions is above ~5 Pas near the freezing point.

3.2 Introduction

Ice-templating, also often referred to as freeze-casting or freeze-structuring, is a very straightforward, simple, low-cost and versatile process for the fabrication of highly porous scaffolds with an anisotropic pore structure. Due to the wide range of applications of scaffolds produced by ice-templating, a large number of research articles and reviews exist[283,297,298,308-314], highlighting the increasing importance of this emerging process in recent years. Scaffolds with aligned porosity are highly interesting for various fields, from supercapacitors[315-318], electrodes in batteries[319,320] or thermal insulators[3,321] to biomaterials for tissue engineering[301,303,322,323], 3D cell culture[324] or as cell containing solid-state scaffolds[325].

There are different ways of ice-templating.[297] In the conventional unidirectional freezing method, a single temperature gradient is superimposed on the sample during freezing, whereby ice crystallization begins in a disordered manner on the cooled surface, resulting in a scaffold with an anisotropic structure in vertical direction and with several domains of different orientation in the horizontal plane.[326,327] A further possibility is bidirectional freezing[327,328], where dual temperature gradients cause the ice to propagate both horizontally and vertically, resulting in a large-scale uniform scaffold structure. Besides, there are other approaches to influence the horizontal domain orientation[297], such as radial[329], magnetic[330], electrical[331] or ultrasonic freeze casting[332], all of which lead to various morphologies of the resulting scaffolds and require different complex technical equipment.[297] This demonstrates the wide range of possibilities for the resulting scaffold morphology through the choice of an appropriate freezing process.

A major advantage of unidirectional freezing is that this easy-to-use process does not require complex and costly laboratory equipment. In general, a solution, suspension, or slurry is frozen in the presence of an external temperature gradient. Solutes are forced between the growing ice lamellae. After removal of the ice crystals by freeze-drying, the scaffold represents a negative of the original ice morphology.[333] Consequently, a highly anisotropic porous sample is obtained. The morphological properties, such as vertical pore orientation or pore size of the scaffolds, play a decisive role depending on the application in which the scaffold is intended to be used. In terms of pore size, pores can be generated at different size scales, with pore diameters well above 100 µm being feasible.[25,334]

Scaffolds, which are to be used as bone substitute materials in tissue engineering applications, may serve as an example. Values of at least 100 µm up to several hundred micrometers (> 300 µm) are considered optimal pore sizes for cell ingrowth, nutrient and oxygen supply, and subsequent vascularization.[335-337] All these parameters are positively affected by the use of ice-templated scaffolds with a highly ordered anisotropic pore structure[338,339] and can therefore be adjusted by choosing the right pore properties.

In addition, orientation of the pores is of significance. Thus, by varying the temperature gradients and hence the pore orientation, a monolithic anatomically shaped meniscus was fabricated using unidirectional freeze-structuring.[25]

Whether specifically for the use as biomaterials or for any of the other various applications mentioned earlier, a fundamental knowledge of the relationship between freezing parameters and pore size and orientation is important for unidirectional freeze-structuring. Thereby, it is important to note that the choice of material and material properties has a direct influence on the resulting pores. In this study, a custom-built device (patented process[25,340]) was used to ice template alginate or chitosan solutions in the presence of an external temperature gradient, which was varied systematically. Several material parameters such as polymer concentration in the solution, molecular weight (MW), and hence viscosity were altered. The resulting pore morphology was assessed as a function of the polymer properties as well as different freezing parameters such as temperature gradient, cooling rate, and absolute temperatures of the cooling surfaces.

3.3 Experimental Section

3.3.1 Freeze-structuring device

The in-house developed freeze-structuring system that was used for the ice-templating process in this study (Figure 14 a-c) basically consisted of a copper block and a copper lid, which can be opened and closed pneumatically for injecting the solutions. The core of the freeze-structuring unit included two superimposed Peltier elements (PEs). These were connected to two laboratory power supplies ("PSP 12 010," Voltcraft, Wollerau, Switzerland), which provided the PEs with the current necessary for the selected temperatures.

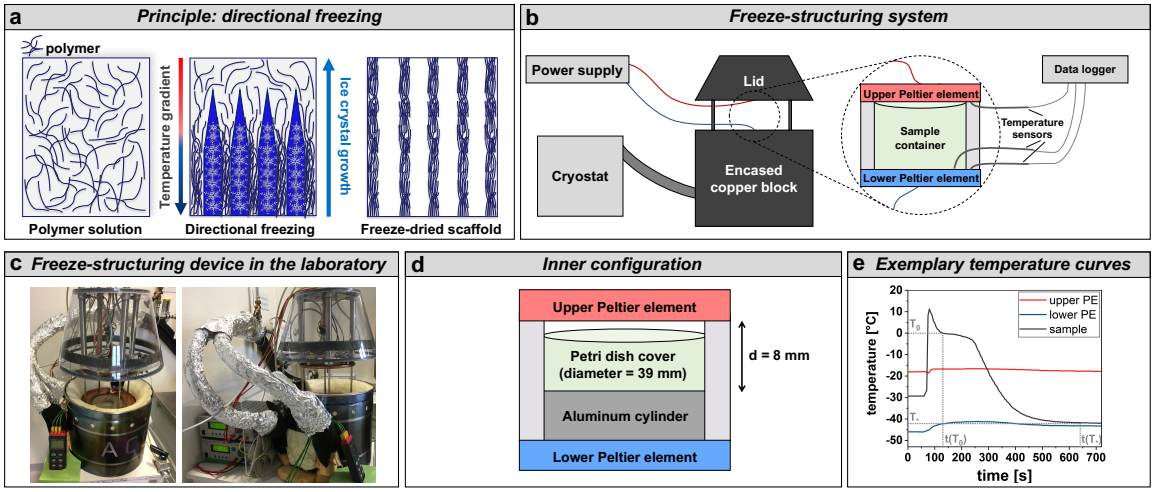

Figure 14. Directional freezing with a custom-built device. a) In directional freezing, a polymer solution is frozen in the presence of a temperature gradient. After freeze-drying, a porous scaffold with anisotropic porosity is obtained. b) The in-house developed freeze-structuring system consisted of a copper block coupled to a cryostat. The sample was located between two PEs that were tempered differently to generate an external temperature gradient. Three temperature sensors measured the PE and sample temperatures. c) Photograph of the freeze-structuring device in the laboratory. d) A petri dish cover with a diameter of 39 mm served as sample container and was placed on an aluminum cylinder. e) Exemplary measurement curves of PE and sample temperatures (upper PE (red), lower PE (blue), sample (black)) during directional freezing. The temperature of the completely frozen sample T_* as well as the temperature T_0 (0 °C) and the corresponding time points $t(T_*)$ and $t(T_0)$ are indicated in grey. Adapted from reference [307].

3 mL of the polymer solution was poured into a sample container located between the PEs and directionally frozen. Both the PEs and the sample were surrounded by a polyether ether ketone (PEEK) thermal isolation unit, which allowed for the generation of a directional external temperature gradient. This gradient was created by varying the temperature of the PEs, with the lower PE always being colder than the upper PE for all experiments. Thus, the heat flow occurred in the direction from the upper to the lower PE, which also corresponded to the direction of the external temperature gradient described by equation (8).[25]

$$\vec{\nabla}T = \frac{\partial T}{\partial \vec{x}} \cong \frac{\left|T_{upper\ PE} - T_{lower\ PE}\right|}{\vec{x}_{upper\ PE} - \vec{x}_{lower\ PE}} \qquad (8)$$

Here, $T_{upper\ PE}$ is the temperature of the upper and $T_{lower\ PE}$ of the lower PE. $\vec{x}_{upper\ PE}$ and $\vec{x}_{upper\ PE}$ represent the corresponding position vectors of the PEs. As only the gradient perpendicular to the surfaces of the PEs was considered, the temperature gradient was expressed as a scalar in the following.[25] This external temperature gradient generated by the PEs was superimposed by the latent heat released during the freezing of the solution. Consequently, a distinction must be made between the external and the internal, resulting temperature gradient. However, the internal temperature gradient is not determined within the scope of this study. Therefore, the values given in the further course of this work describe the magnitude of the external temperature gradient.

The lower PE was in thermal contact with the cylindrical copper block, which was coupled to a cryogenic environmental thermostat ("FPW 91", Julabo, Seelbach, Germany) and perfused by coolant ("Thermal HY", Julabo, Seelbach, Germany). The choice of the coolant temperature was also used to vary the temperature of the overall system and thus the limits of the temperatures that were achievable by the PEs. As the temperature of the lower PE reached a plateau at a certain threshold voltage, the temperature of the coolant flowing through the copper block determined the minimum temperature of the lower PE. This in turn was decisive for the choice of the temperature of the upper PE at a given temperature gradient (see equation (8)).

The sample container used in this work was a petri dish cover with a diameter of 39 mm and a height of 5 mm. Figure 14 d shows a schematic side view of the setup used for sample fabrication in this study. Due to a built-in heat-conducting aluminum cylinder on which the cover was placed, a PE distance of 8 mm was assumed for the calculation of the external temperature gradient. The temperature differences of the PEs required for the respective temperature gradients are shown in Table 3.

Table 3. PE temperature differences required for the different temperature gradients.

Temperature gradient [K/mm]	Temperature difference [K]
1	8
1.5	12
2	16
2.5	20
3	24
3.5	28
4	32

In this study, two different series of experiments were conducted for the directional freezing of alginate solutions. In experiments 1-4, the temperature of the upper PE remained largely constant for all temperature gradients, whereas the temperature of the lower PE changed,

while this was the opposite for experiments 5-7. The experiments were conducted at different temperature regimes, where the temperatures were determined by the coolant temperature in the freeze-structuring unit. The coolant temperatures used for each experiment are shown in Table 4.

Temperatures were measured with three sensors inside the freeze-structuring device. Two temperature sensors were in contact with the upper and lower PE, respectively, to measure the temperatures of the PEs and consequently the temperature gradient. A third temperature sensor was located in the sample and monitored the temperature profile during the freezing process. To ensure the same position of this sensor for each experiment, it was bent in such a way that the tip touched the bottom of the Petri dish. The sensors were connected to a datalogger ("K204 Datalogger," Voltcraft, Wollerau, Switzerland), which recorded the temperature curve over time. (Figure 14 b)

Table 4. Coolant temperatures used for the directional freezing of alginate solutions. The temperatures of the coolant determined the temperature of the overall system.

	Temperature upper PE	Temperature lower PE	Coolant temperature [°C]
Experiment 1	identical	variable	-47
Experiment 2	identical	variable	-33
Experiment 3	identical	variable	-30
Experiment 4	identical	variable	-25
Experiment 5	variable	identical	-47
Experiment 6	variable	identical	-40
Experiment 7	variable	identical	-33

3.3.2 Temperature curves and cooling rate

Exemplary measurement curves of the PE temperatures as well as the temperature within the sample measured by the temperature sensors are shown in Figure 14 e. At the beginning of every experiment, the selected temperatures of the upper PE (red line) and the lower PE (blue line) were set. When the system was in thermal equilibrium, the polymer solution was injected and the temperature within the sample (black line) was measured. Using these temperature curves, the cooling rate v_c, which describes the heat removal per time unit from the sample, can be calculated from equation (9):[25]

$$v_c = \frac{T_* - T_0}{t(T_*) - t(T_0)} \tag{9}$$

According to Stuckensen *et al.,* T_* corresponds to the temperature of the completely frozen sample, which was defined as the temperature that the frozen sample first keeps constant for at least 30 s. The starting point of this level is given by the time $t(T_*)$. Accordingly, $t(T_0)$ corresponds to the time at which the sample reaches the temperature T_0 = 0 °C.[25]

The temperature gradient was calculated according to equation (8) and from the arithmetic mean of the PE temperatures at times $t(T_*)$ and $t(T_0)$.
For each setting and sample type, three samples were freeze-structured. The mean values of the cooling rate and the temperature gradient were given with standard deviation.

3.3.3 Freeze-drying

After freezing, the samples were freeze-dried at -57 °C and a maximum of 1 mbar ("Alpha 1-2 LDplus", Christ, Osterode am Harz, Germany).

3.3.4 Polymer solutions

3.3.4.1 Preparation of polymer solutions

The alginate solutions had a concentration of 2% (w/w) and were prepared by dissolving sodium alginate powder ("Protanal LF 10/60FT," FMC Biopolymer, Philadelphia, USA) in ultrapure water.
The solvent for the chitosan powders was 1% (v/v) acetic acid prepared by diluting acetic acid (≥ 99.8%, Sigma-Aldrich, St. Louis, USA) in ultrapure water. A total of three different chitosan solutions was prepared. Solutions containing low-MW chitosan (Sigma-Aldrich, St. Louis, USA) were obtained by dissolving the chitosan powder at both 2% (w/w) and 4% (w/w) concentrations in 1% (v/v) acetic acid. In addition, a 2% (w/w) chitosan solution was prepared from high-MW chitosan powder (Sigma-Aldrich, St. Louis, USA).
After complete dissolution of the powders, solutions were centrifuged ("Mega Star 1.6 R," VWR, Radnor, USA) for 5 min at room temperature and 4500 rpm to remove any air bubbles present in the solution.

3.3.4.2 MW and dispersity

The MW and dispersity of the alginate were determined using an aqueous gel permeation chromatography (GPC) system (Malvern, Herrenberg, Germany) and are shown in Table 5. Here M_n is the number average, M_w the weight average, and M_z the centrifuge average.

Table 5. Molecular weights and dispersity of alginate used for the systematic investigations.

	Molecular weight [kDa]			Dispersity
	M_n	M_w	M_z	
Alginate *Protanal LF 10/60 FT*	99.9	156.9	248.6	1.572

Alginate powder was dissolved at a concentration of 1 mg L^{-1} in an aqueous solution of 8.5 g L^{-1} $NaNO_3$ and 0.2 g L^{-1} NaN_3, which was also used as eluent, for 24 h. Prior to measurement, solutions were filtered through a 0.45 µL cellulose filter. Subsequently,

100 µL of the respective solutions were measured using a GPC system containing the following components: Viscotek GPCmax, column oven (35 °C), "Viscotek VE3580" refractive index detector, "Viscotek SEC-MALS 20", two "A6000M" Viscotek A-columns (length = 300 mm, width = 8 mm, porous polymethyl methacrylate, particle size: 13 µm). After calibration with polyethylene glycol standards, data was evaluated with the MALS calibration.
The MW of the low-MW chitosan was reported by the manufacturer to be 50-190 kDa, while that of the high-MW chitosan was specified as 310-375 kDa.

3.3.4.3 Determination of viscosity as a function of temperature

The temperature-dependent viscosity of the polymer solutions used for freeze-structuring was determined using a rheometer (“MCR702,” Anton Paar, Graz, Austria) at a parallel plate geometry with a diameter of 25 mm and a plate distance of 0.5 mm. Solutions were cooled from 25 °C to 0 °C at a cooling rate of 4 K min^{-1} during the measurement. Three measurements were taken for each solution type and the arithmetic mean value of viscosity was plotted with the standard deviation as a function of temperature.

3.3.5 Sample characterization

3.3.5.1 Imaging

Prior to imaging of the sample surface or cross section, scaffolds were cut using a razor blade. Sample sections were first examined using the “SteREO Discovery.V20" stereomicroscope (Zeiss, Jena, Germany) and the associated “ZEN2012 pro” software. Samples were then fixed with the cement “Leit C Conductive Carbon Cement” (PLANO GmbH, Wetzlar, Germany) on scanning electron microscopy (SEM) specimen holders (Agar Scientific, Stansted, UK). A high vacuum coater (“EM ACE600,” Leica, Wetzlar, Germany) was used to apply a 6 nm thick platinum layer with a current of 35 mA to avoid electrical charging of the samples during imaging using a scanning electron microscope (“Crossbeam 340" Zeiss, Jena, Germany).

3.3.5.2 Pore size determination

The pore diameters were measured manually using the software “ImageJ.“ For this purpose, a representative SEM image of the cross section was taken at 50 x magnification for each sample. The broadest area of each individual pore visible on the image was then measured. The arithmetic mean of the measured values with standard deviation was defined as the pore diameter.

3.4 Results

3.4.1 Alginate

3.4.1.1 a-factor and cooling rate

One objective of the systematic investigations in this study was to reveal the influence of the absolute PE temperatures used for the respective temperature gradients on the cooling rates as well as on the resulting sample morphology of alginate samples.

The cooling rate during freezing is an important parameter in directional freezing, as it affects the resulting pore size and scaffold morphology.[341,342] However, the magnitude of the external temperature gradient, which influences pore orientation, also plays an important role. As a temperature gradient is defined only by the temperature difference and the distance of the PEs, there is a multitude of possible PE temperatures to be able to set the same temperature gradient. Here, it is only of crucial importance that the temperature difference calculated based on equation (8) is maintained. Therefore, alginate solutions with a concentration of 2% (w/w) were used to systematically investigate how the choice of PE temperatures affects the course of the cooling rate as a function of the external temperature gradient.

For this, two different series of experiments were conducted. In series of experiments 1, the temperature of the upper PE remained almost the same for all temperature gradients, whereas the temperature of the lower PE gradually decreased for larger temperature gradients. Deviations at low temperature gradients were due to technical reasons. The experiments were conducted for different temperature ranges. The overall system was coldest for experiment 1 and warmest for experiment 4. (Figure 15 a and Table 4)

Temperatures in series of experiments 2 were chosen inversely. The temperature of the lower PE remained the same for all temperature gradients, whereas that of the upper PE gradually increased for higher temperature gradients. (Figure 15 d) Different temperature ranges were also selected in these experiment series. The overall system was coldest in experiment 5 and warmest in experiment 7.

In this study, a factor that includes the average temperature of the PEs and is therefore referred to as the average (a-)factor, was developed (equation (10)). By including the PE average temperature, the total temperature of the system is considered. In addition, the absolute temperature of the lower cooling surface, which is in direct contact with the sample, is taken into account. The freezing process and consequently the nucleation of ice crystals start at the lower surface. With the help of this a-factor, it is possible to predict the course of cooling rates as a function of the external temperature gradient at given PE temperatures.

$$a = \frac{T_{upper\ PE} + T_{lower\ PE}}{2} \cdot T_{lower\ PE} \qquad (10)$$

The development of this a-factor offers the advantage that, for given parameters, the magnitude and course of the cooling rates, and thus to some extent the morphology of the samples, such as pore orientation and size, can be predicted. Figure 15 b and e show the a-factor as a function of the temperature gradient. For experiment series 1, it became clear that the a-factor increased with increasing temperature gradient and was generally higher for colder overall systems. The curve for experiment 1 was the highest, whereas the courses of the experiments with warmer overall systems were below it in the corresponding order. (Figure 15 b) For the series of experiment 2, the a-factor decreased with increasing temperature gradients. Again, the temperature range of the system had an effect on the magnitude of the a-factor. (Figure 15 e)

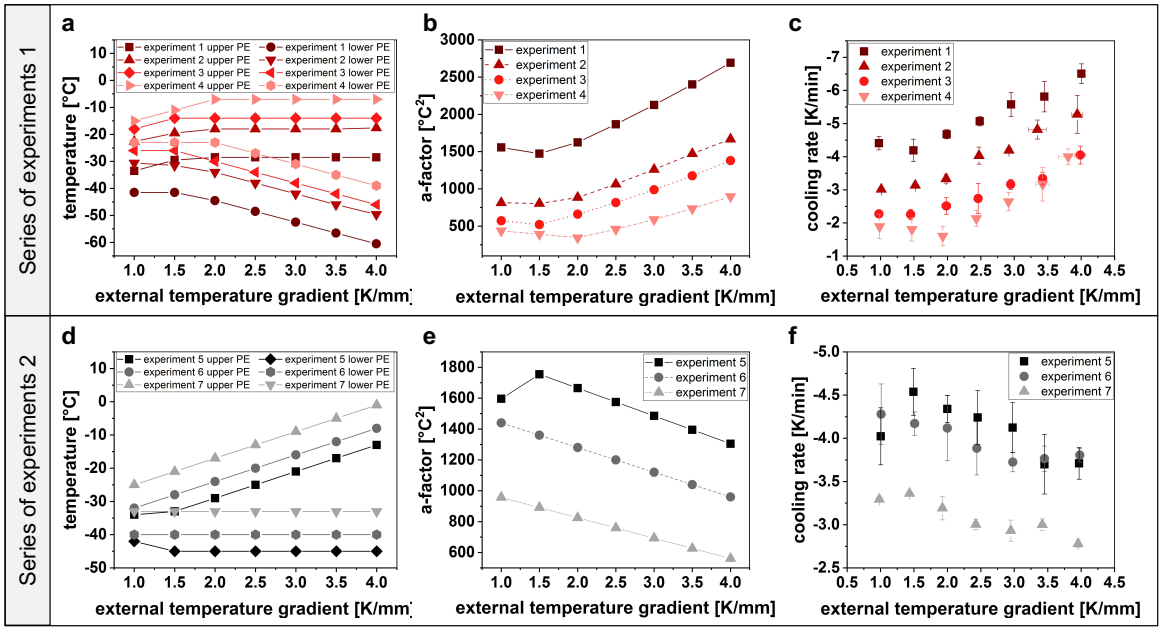

Figure 15. Cooling rate and a-factor of directionally frozen alginate samples. a) The temperatures of the upper PE were largely the same for the series of experiments 1, whereas the temperatures of the lower PE were gradually lowered for higher temperature gradients. b) The calculated course of the a-factor as a function of the external temperature gradient was confirmed by the c) experimental determination of the cooling rates. d) In series of experiments 2, the temperature of the lower PE was nearly constant for all temperature gradients, whereas that of the upper PE was gradually increased for higher gradients. e) The cooling rates theoretically predicted by the a-factor decreased with increasing temperature gradient, f) which was also observed experimentally. Adapted from reference [307].

The courses of the cooling rates predicted by the a-factor could be confirmed experimentally for both experimental series. (Figure 15 c, f) The colder the overall system, the higher the cooling rates observed.

3.4.1.2 SEM and pore size distribution

The impact of the various freezing parameters such as temperature gradients, cooling rates, and overall system temperatures and their effect on pore orientation and size is of significant interest.

SEM imaging of the samples was used to assess the pore orientation and size. In the following, the term “pore size” always refers to the pore diameter measured in the SEM cross section images of the samples. The lamellar pore structure that is characteristic for the directionally frozen samples was revealed by combining SEM imaging of the surfaces of four exemplary samples from experiment 2 (Figure 16) with imaging of sample cross sections. (Figure 17) Highly porous samples with anisotropic continuous pores were observed independently of the temperature gradient and the PE temperatures during the freezing process.

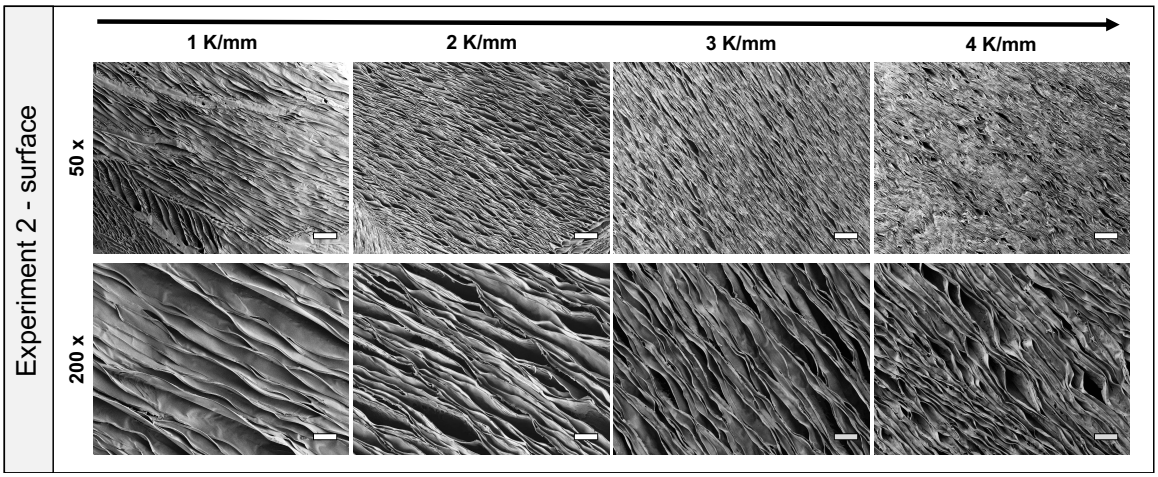

Figure 16. SEM surface images of alginate samples. Images of an exemplary sample series from experiment 2 show a lamellar pore structure. The top row shows one sample surface per temperature gradient at 50 x magnification, whereas the sample surfaces at 200 x magnification are presented in the bottom row. Scale bars are 200 µm in the top row and 50 µm in the bottom row.

Figure 17 a shows the samples associated with experiments 1-4, in which the upper PE had nearly the same temperature for all temperature gradients, whereas the temperature of the lower PE was gradually lowered for higher gradients. For experiment 1, where the overall system was the coldest and the highest cooling rates appeared, no distinct dependence of the pore orientation on the external temperature gradient was found. Examination of the corresponding images suggested that the structuring process was kinetically controlled using too low temperatures and that, in some cases, several domains of different orientations were formed in close proximity to each other. This was also found when examining larger sample sections using stereomicroscopy. (Figure 19 a)

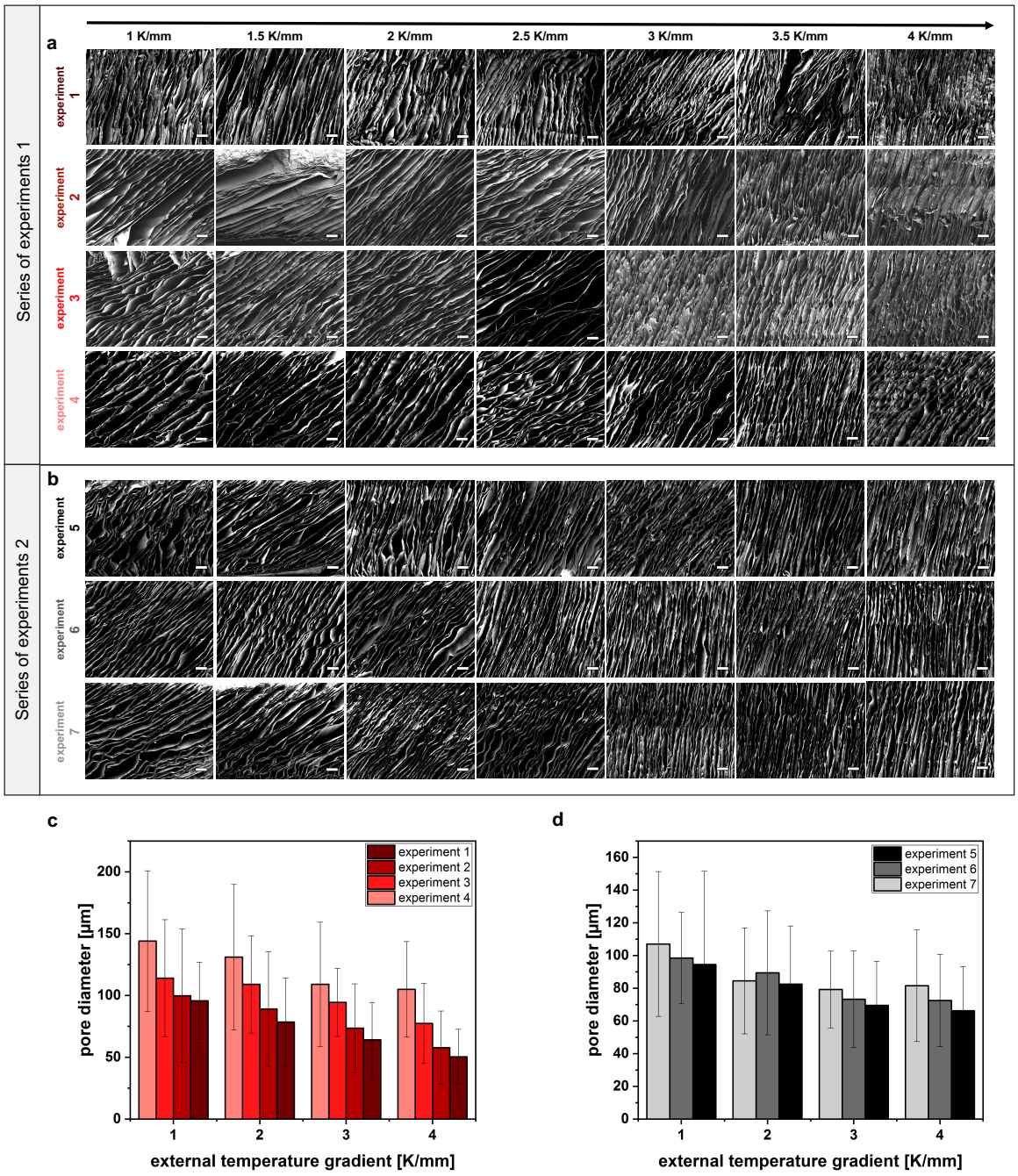

Figure 17. Pore orientation and diameter of directionally frozen alginate samples. a) SEM cross-section images of samples from experiment series 1. No clear dependence of the pore orientation on the external temperature gradient was observed for the samples of experiment 1. In experiments 2-4, the pores were increasingly oriented perpendicular to the surface as the temperature gradient increased. b) This trend was also observed for the samples of experiment series 2. c) The pore diameter of the samples from experiment series 1 decreased with increasing temperature gradient. Smaller pores were observed for colder systems. d) Similar was found for the samples of experiment series 2. Scale bars in a) and b) are 200 µm.

However, for experiments 2-4, it became evident in both the SEM and stereomicroscope images (Figure 17 a and Figure 19 a) that the freezing process was well controlled. Pores were increasingly oriented perpendicular to the surface with increasing external temperature gradient (Figure 16 and Figure 17 a) and exhibited a uniform morphology.

The measurement of the pore sizes revealed for experiments 1-4 that the pore size was to a certain degree adjustable by the choice of suitable parameters. (Figure 17 c) In general, a higher temperature gradient and higher cooling rates resulted in smaller pore sizes. (Figure 17, Figure 18 a-d) Compared with experiment 1 with the highest cooling rates (Figure 18 a), pore diameters were shifted towards higher values when lower cooling rates were used (experiment 4, Figure 18 d). In this way, pore sizes between (50 ± 22) µm (temperature gradient 4 K mm^{-1}, experiment 1) and (144 ± 56) µm (temperature gradient 1 K mm^{-1}, experiment 4) could be obtained only by varying the freezing parameters. If the pore orientation is also taken into account, that is, only one gradient is considered, pore size differences of about 40 µm could be obtained in the various experiments.

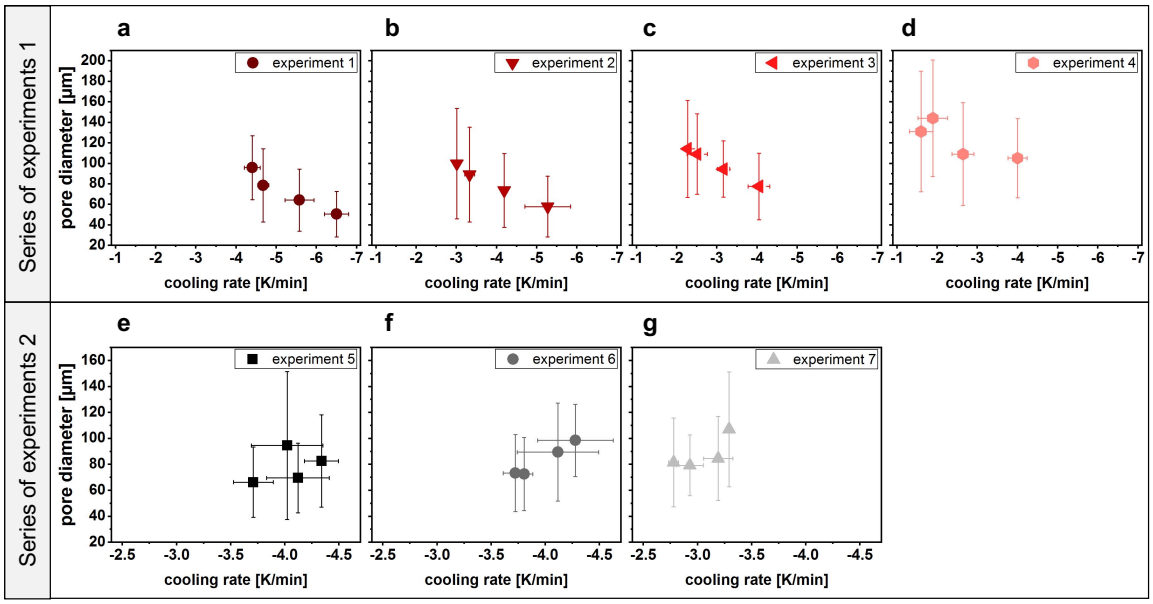

Figure 18. Pore diameter of alginate samples as a function of cooling rate. For experiment series 1, the pore diameter decreased with increasing cooling rates: a) experiment 1, b) experiment 2, c) experiment 3, d) experiment 4). This trend was also found for experiment series 2: e) experiment 5, f) experiment 6, g) experiment 7). Adapted from reference [307].

Figure 17 b shows the SEM images of the samples from experiments 5 to 7. Again, the tendency for the pores to be increasingly oriented perpendicular to the surface with increasing temperature gradient became evident. This was also visible in stereomicroscopic observation of larger sample sections, where nearly all scaffolds showed a uniform structuring. (Figure 19 b) Consideration of the different temperature regimes showed that lower cooling rates tended to cause larger pores than higher cooling rates. (Figure 17 d, Figure 18 e-g)

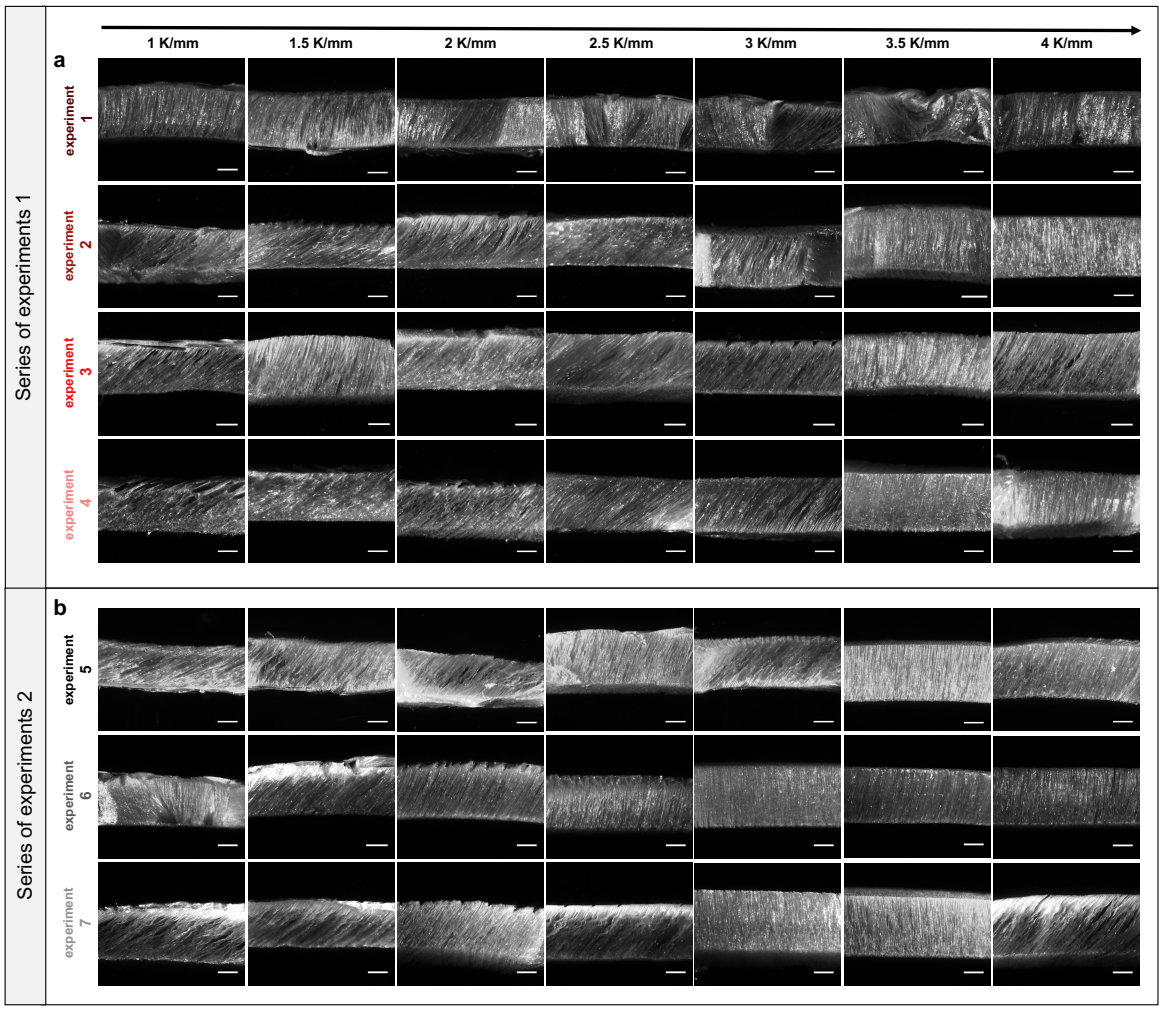

Figure 19. Stereomicroscopic cross-section images of ice-templated alginate samples. a) Examining larger areas of the samples of experiments series 1, no dependence of the pore orientation on the temperature gradient was found for experiment 1. Increasing the temperature gradient caused the pores to be increasingly oriented perpendicular to the surface in experiments 2-4. b) This trend was also found for the series of experiments 2. Scale bars in a) and b) are 1 mm.

Comparing the two series of experiments, it can be concluded that the pore orientation does not depend on the temperatures of the PEs, but on the magnitude of the temperature gradient. The PE temperatures determine the resulting cooling rates, which in turn are responsible for the pore size. However, if the overall system is too cold (see experiment 1), control over the pore orientation is lost.

3.4.2 Chitosan

3.4.2.1 Viscosities

In addition to the systematic investigations with alginate solutions, experiments with a further biopolymer, chitosan, were conducted. Here, the focus was on the influence of various properties of the solution, such as concentration, MW of the polymer, and, as a result, viscosity, on the freeze-structuring process. For this purpose, two chitosan solutions of different concentrations (2% (w/w) and 4% (w/w)) of a low-MW chitosan were compared. Furthermore, the influence of MW on freeze-structuring was investigated using a 2% (w/w)

solution of a high-MW chitosan. The effect of concentration and MW on viscosity during cooling of the solutions from room temperature to 0 °C is shown in Figure 20.

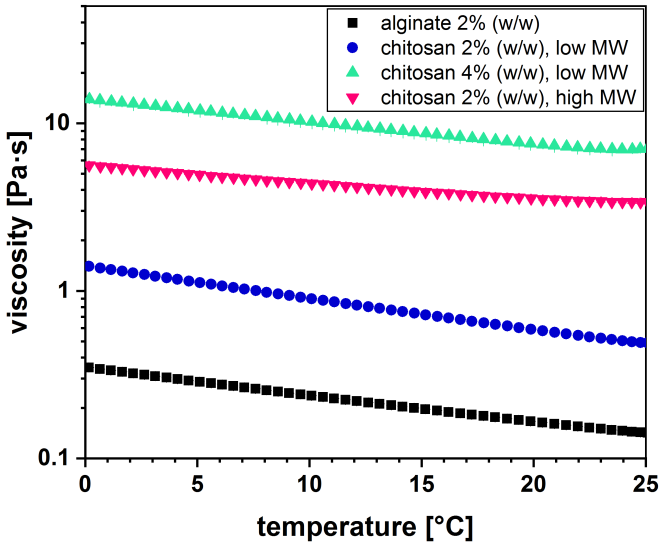

Figure 20. Viscosities of the polymer solutions used for directional freezing as a function of temperature. Viscosities of the alginate 2% (w/w), chitosan low-MW 2% (w/w), chitosan high-MW 2% (w/w) and chitosan low-MW 4% (w/w) solution are shown in black, blue, pink and green, respectively.

The 4% (w/w) solution of the low-MW chitosan had the highest viscosity of the solutions compared. Depending on the temperature, this was between (7.11 ± 0.07) Pas at 25 °C and (14.91 ± 0.08) Pas near 0 °C. Lower values of (3.39 ± 0.06) Pas at 25 °C to (5.61 ± 0.04) Pas close to the freezing point were measured for the still highly viscous 2% (w/w) solution of the high-MW chitosan. By contrast, the 2% (w/w) solution of the low-MW chitosan was considerably less viscous with a viscosity of (0.490 ± 0.003) Pas to (1.401 ± 0.003) Pas, depending on the temperature.

For comparison, the viscosity of the alginate solution used for the systematic investigations described previously is shown in black. From (0.142 ± 0.001) Pas to (0.348 ± 0.002) Pas, it is clearly below the viscosities found for the chitosan solutions.

3.4.2.2 a-factor and cooling rate

According to the freeze-structuring of alginate solutions, both process parameters external temperature gradient and PE temperatures were varied.

Two different temperature ranges were selected. In the case of PE temperatures 1 (Figure 21 a), the temperature of the upper PE remained nearly the same, while that of the lower PE was gradually reduced for increasing gradients. The choice of temperatures was analogous to those used from experiment 2 in the freeze-structuring of the alginate solutions (Figure 15 a). The course of the cooling rate predicted by the a-factor (inset in Figure 21 a) increased with increasing temperature gradients, as the overall system became colder with higher gradients. This could be confirmed experimentally for all

concentrations and MWs. No significant difference was found between the different MWs (Figure 21 b) or the different concentrations (Figure 21 c).

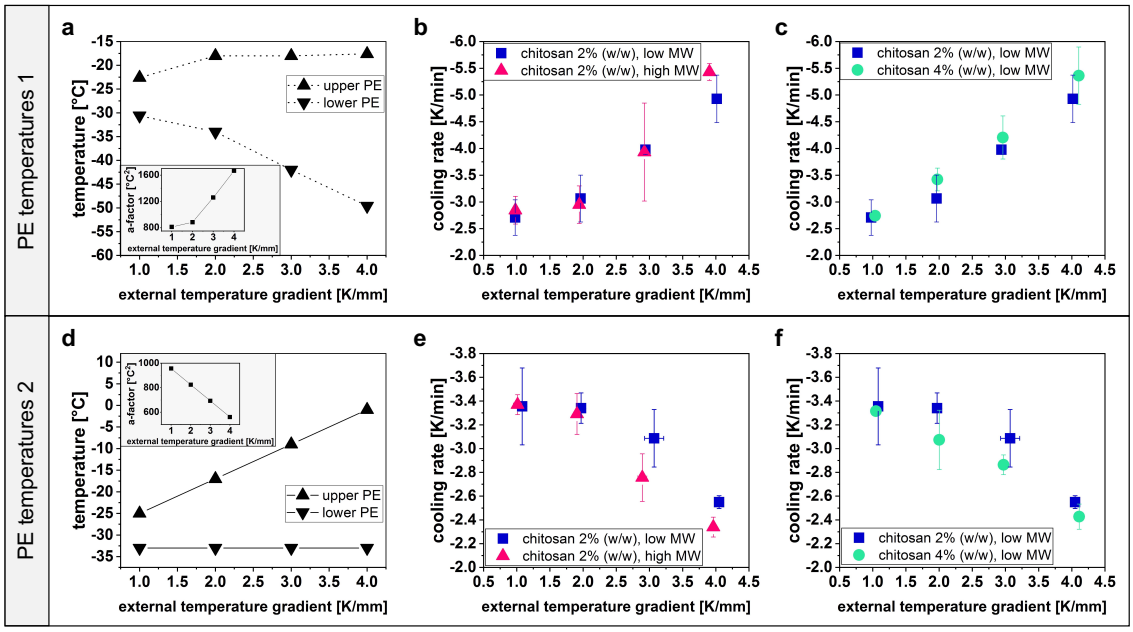

Figure 21. Cooling rate and a-factor of freeze-structured chitosan samples. a) For PE temperatures 1, the temperature of the upper PE remained largely constant, while that of the lower PE was decreased for increasing temperature gradients. According to the theoretical prediction by the a-factor (inset), the cooling rate increased with increasing temperature gradient. This was also observed experimentally for both b) different molecular weights (low MW (blue), high MW (pink)) and c) solution concentrations (2% (w/w) (blue), 4% (w/w) (green)). d) For PE temperatures 2, the temperature of the lower PE remained largely constant, while that of the upper PE was increased for higher gradients. The cooling rate predicted by the a-factor (inset) decreased with increasing gradient, which was also found experimentally for both e) different molecular weights and f) solution concentrations. Adapted from reference [307].

Similar results were obtained in the case of PE temperatures 2. Here, the overall system became warmer with increasing temperature gradient, as the temperature of the lower PE remained constant, whereas that of the upper PE was gradually increased for higher gradients (temperatures analogous to alginate experiments, experiment 7, Figure 15 d). Based on the a-factor, it was therefore expected that the cooling rate would decrease with increasing gradients (inset in Figure 21 d), which was confirmed experimentally. However, again no clear difference in the magnitude of the cooling rates as a function of MW (Figure 21 e) or concentration (Figure 21 f) appeared.

3.4.2.3 SEM and pore size distribution

An anisotropically aligned porous structure was found for all samples when observed by SEM. (Figure 22)

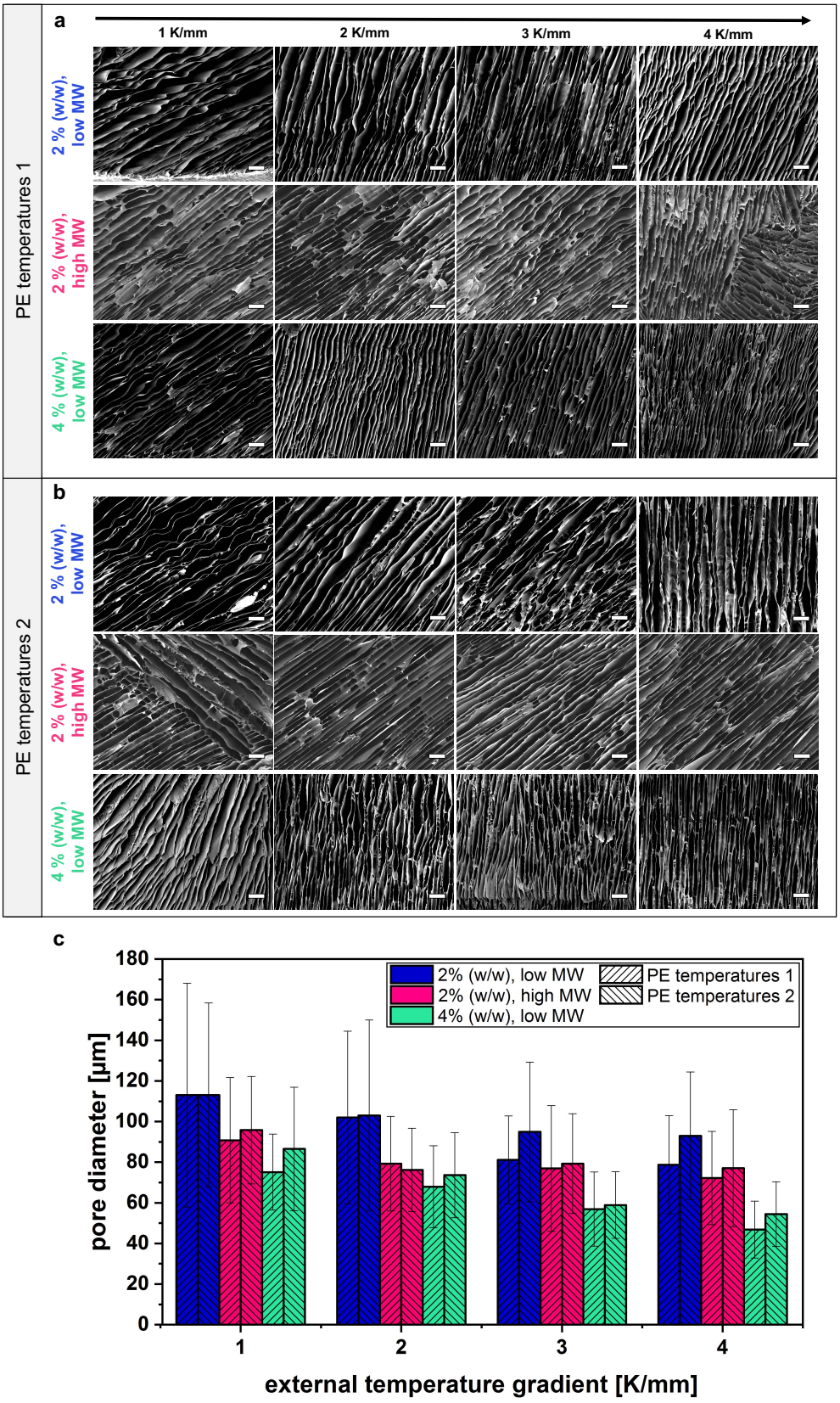

Figure 22. Pore orientation and diameter of directionally frozen chitosan samples. SEM cross-section images. a) At PE temperatures 1, an increasingly perpendicular orientation of the pores to the surface was observed with higher temperature gradients for the 2% (w/w), low-MW (blue) chitosan samples. For the 2% (w/w), high-MW (pink) and 4% (w/w), low-MW samples (green), no dependence of the pore orientation on the gradient was evident. b) A similar behavior was observed for the samples prepared at PE temperatures 2. c) With increasing temperature gradient, smaller pore diameters were observed. The largest pores were found for the 2% (w/w), low-MW chitosan samples, whereas freeze-structuring of 4% (w/w), low-MW solution led to the smallest pores. Scale bars in a) and b) are 200 µm.

For the samples obtained in the experiments with PE temperatures 1, it was found that a too high viscosity prevented a controlled pore orientation. (Figure 22 a) Thus, for the samples prepared through structuring of a low-MW chitosan solution with a concentration of 2% (w/w), an increasingly perpendicular orientation to the surface with an increasing temperature gradient was identified. This was consistent with the observations of the systematic investigations on alginate. (Figure 17) However, when the concentration of the solution was doubled to 4% (w/w), no clear trend in the pore direction was evident. The pores, except for the smallest temperature gradient, were all oriented nearly perpendicular to the surface. Similar results were obtained for the high-MW 2% (w/w) samples. No clear dependence of pore orientation on the external temperature gradient was found, the pores were all oriented obliquely to the surface. In addition, it was observed for some samples that the pore orientation frequently changed inside the sample and domains with different orientations appeared.

A similar observation was made for samples freeze-structured at PE temperatures 2. (Figure 22 a) A tendency for pores oriented more perpendicular to the surface with increasing temperature gradient could only be confirmed for the low-MW 2% (w/w) samples. For scaffolds from the higher-concentrated low-MW 4% (w/w) solution, the pores were oriented perpendicular to the surface, especially for the higher gradients. 2% (w/w) samples from a high-MW solution exhibited pores oriented at an angle to the sample surface regardless of the external gradient. It was also noticeable here that an orientation change of the pores within the sample was found in some scaffolds.

Although a highly ordered, anisotropic pore structure could be observed for all samples (Figure 22 a, b), a pore orientation controllable by the temperature gradient could thus only be ensured for both temperature ranges for the low-MW 2% (w/w) samples. This control was lost with higher viscosities. Another interesting observation was the occasional occurrence of different domains within the high-MW 2% (w/w) samples.

Measurement of the pore diameters showed that pores of the low-MW 2% (w/w) samples tended to be the largest, followed by the 2% (w/w) high-MW scaffolds. (Figure 22 c) The samples prepared from the 4% (w/w) solutions tended to have the smallest pores. In general, the trend toward smaller pores with increasing external temperature gradient was also evident here for all sample types. Comparing the scaffolds prepared at the two different temperature ranges of the PEs, there was no significant difference between the pore sizes.

3.5 Discussion

In this study, the importance of the freezing parameter choice in directional freezing was highlighted, as this has a major impact on the process. It was shown that it is not sufficient to specify only the external temperature gradient used during the freezing process. Rather, factors such as the temperature of the overall system, the absolute temperatures of the cooling surfaces, and material properties such as the solution concentration, the MW, and consequently the viscosity must also be defined as these parameters have a significant influence on the process itself and the resulting scaffold morphology. Among other things, this study revealed that a too cold overall system during the freezing process, that is, temperatures of the lower cooling surface down to -60 °C combined with low temperatures of the upper cooling surface, led to a loss of control over pore orientation. This was also observed when using solutions with high viscosities above ~5 Pas near the freezing point. It is known that the orientation of the aligned, anisotropic pores formed during directional freezing can be influenced by the choice of the external temperature gradient.[25] As the temperature gradient is determined only by the distance of the cooling surfaces as well as their temperature difference, the same temperature gradient can be set by numerous different possible temperatures. However, to the best of our knowledge, a systematic investigation of the influence of the cooling surface temperatures on the resulting scaffold morphology is still lacking. To fill this gap, solutions of the biopolymers alginate and chitosan were directionally frozen in this study. For alginate, the influence of different temperature regimes on the resulting pore structure within the samples was investigated, whereas for the ice-templating of chitosan solutions, the focus was on the impact of different solution properties, such as concentration and MW and consequently the viscosity.

When comparing the results of the present study with those of other groups, it is important to note that there are a variety of options for freeze-structuring setups, complicating a direct comparison. For example, Yin *et al.* used a radial freeze-structuring apparatus to texture 3.5% (w/v) chitosan dissolved in 1.5% acetic acid for use as a ureteral stent.[343] The solution viscosity was not measured but given by the material supplier as 150-350 mPas for 1% (w/w) chitosan in 1% acetic acid at 20 °C. For structuring, the solution was placed in appropriate molds and frozen at -80 °C in a freezer. Neither the cooling rates nor the temperatures of the cooling surfaces were determined. However, the resulting morphology showed a multiplicity of domains[343], which is consistent with our observations at low temperatures. The results presented in our study show that a more uniform pore structure can be achieved by selecting appropriate freezing parameters, such as the temperature of the overall system. For example, by choosing not too low PE temperatures, the number of domains can be reduced. (Figure 17 and Figure 19)

In unidirectional freeze casting, ice crystals begin to nucleate in a disordered manner once the solution is injected on the cooled surface, which results in the observed different domains of varying orientations.[326,327] This effect is even more pronounced at lower surface temperatures, accelerating ice crystal nucleation and leading to a more heterogenous pore orientation as also observed in the present study. Solution viscosity also played a crucial role in the process, as texturing became more difficult, or pore alignment control was even lost at higher viscosities (Figure 22). This is consistent with a study from Florczyk *et al*., who investigated the influence of viscosities of chitosan-alginate solutions frozen in a freezer at -20 °C. It was found that a lower viscosity resulted in a more uniform pore structure.[344]

A study conducted by Francis *et al.* dealt with the directional freezing of a chitosan-alginate solution (1.5% (w/w)) using a PTFE mold placed on a cold finger being in contact with liquid nitrogen.[345] Here, the temperature of the cooled copper surface was decreased with a cooling rate of 1 °C min^{-1} until a temperature of -150 °C was reached. An external temperature gradient or the solution viscosity were not reported in the study. Regarding the MW, a range of 50-190 kDa and 270-325 kDa was given for chitosan and alginate, respectively.[345] Therefore, the MW of alginate was higher than that used in our study, while that of chitosan was similar to the low-MW weight chitosan. The freeze-dried scaffolds exhibited pore sizes of about 69 µm.[345] This was thus roughly in the size range of the pores observed in our study, which were found in alginate scaffolds frozen under an temperature gradient of 3 K mm^{-1} (experiments 1 and 2) and 3 K mm^{-1} or 4 K mm^{-1} (experiments 5 and 6), respectively. (Figure 17 c,d) Here, the cooling rates lay between about -3.7 K min^{-1} and -5.6 K min^{-1}. In the present study, it was shown that the pore size can be adjusted by the temperature of the overall system as well as the solution properties. This allows the scaffold morphology to be specifically influenced and adapted to the intended application. The influence of the applied cooling rates during directional freezing on the sample morphology, especially on the pore diameter, was investigated by Nematollahi *et al*. using freeze-structuring of silk-chitosan solutions.[346] Here, medium-MW chitosan, which was not specified further, was dissolved in 2% (w/v) acetic acid, mixed with silk solution in a ratio of 1:3 and directionally frozen using a PTFE mold on a copper cylinder connected to a liquid nitrogen bath. Freezing was conducted using the three different cooling rates 0.5 °C min^{-1}, 1 °C min^{-1} and 2 °C min^{-1}. A decrease in pore diameter with increasing freezing rate was revealed.[346] This was also observed in the results presented in this study. (Figure 17, Figure 18) A decreasing pore diameter with increasing freezing rates was also found by Christiansen *et al*.,[347] who used a freezing system similar to the device utilized in the present study.[347]

Pore orientation was assessed by Yin *et al*., who used a 3.5% chitosan solution in 1.5% (v/v) acetic acid inserted between two molds and then frozen at -80 °C to prepare tubular scaffolds with aligned porosity. Pores showed an orientation oblique to the freezing surfaces as well as multiple domains with different pore orientations,[348] which is consistent with the findings in the present study, especially at low temperatures. (Figure 17 and Figure 19) Again, the absolute temperatures of the freezing surfaces, the temperature gradient, the cooling rates or the solution viscosity were not determined.

Considering all these comparisons, the importance of specifying the parameters used during directional solidification becomes apparent. The overall system, such as temperatures, temperature gradient, and freezing rates, but also solution properties such as viscosity must always be taken into account, as these factors can limit the process.

3.6 Conclusion

The aim of this study was to demonstrate that various parameters used in directional freezing have a significant influence on the resulting sample morphology and pore structure. Apart from the external temperature gradient, also the temperatures of the cooling surfaces, the cooling rate, as well as material properties such as the concentration, the MW (when using polymers), and the viscosity of the solution determine pore size and orientation after solidification. Here, inappropriate parameter settings may cause a loss of control over pore alignment during freezing, for example, when the temperature of the lower cooling surface goes below a limit of -60 °C or solution viscosity exceeds ~5 Pas near the freezing point. Beyond these limitations, ice templating of alginate revealed that pore alignment could be controlled by the choice of the external temperature gradient, with a higher gradient leading to pores oriented increasingly perpendicular to the surface. The temperature of the overall system both influenced cooling rates and affected the pore diameters, leading to smaller pores at higher cooling rates. Although a custom-developed device was used for the systematic investigations presented in this study, the findings should also be applicable to other devices that offer the same frame conditions for unidirectional freeze-structuring.

Chapter 4

Phase Conversion of Ice-Templated α-Tricalcium Phosphate Scaffolds into Low-Temperature Calcium Phosphates with Anisotropic Open Porosity

Chapter 4 was published as original research article (Annika Seifert, Jürgen Groll, Jan Weichhold, Anne V. Boehm, Frank A. Müller, Uwe Gbureck, Phase Conversion of Ice-Templated α-Tricalcium Phosphate Scaffolds into Low-temperature Calcium Phosphates with Anisotropic Open Porosity in *Advanced Engineering Materials* **2021**, 23(5), 2001417), reproduced from reference [349] as an open access article distributed under the Creative Commons Attribution-NonCommercial 4.0 International License (CC BY-NY 4.0), which permits unrestricted use, distribution, and reproduction in any non-commercial medium.

The article is based on the work of the author of this thesis Annika Seifert, who conducted all experiments and data evaluation and wrote the manuscript.

The author contributions to the original research article are as follows:

Publication (complete reference):

A. Seifert, J. Groll, J. Weichhold, A. V. Boehm, F. A. Müller, U. Gbureck, Phase Conversion of Ice-Templated α-Tricalcium Phosphate Scaffolds into Low-Temperature Calcium Phosphates with Anisotropic Open Porosity. *Advanced Engineering Materials* **2021**, 23(5), 2001417.
DOI: https://doi.org/10.1002/adem.202001417.

Participated in	**Author Initials,** Responsibility decreasing from left to right				
Study Design	A.S.	U.G.	J.Gro. F.A.M.		
Methods Development	A.S.	U.G..	J.Gro. F.A.M		
Data Collection	A.S.		J.W.		
Data Analysis and Interpretation	A.S.		J.W. A.V.B.		
Manuscript Writing	A.S.	.	J.W. J.Gro. U.G. F.A.M.		
Writing of Introduction	A.S.				
Writing of Materials & Methods	A.S.		J.W.		
Writing of Discussion	A.S.				
Writing of First Draft	A.S.				

Chapter 4

The author contributions to the figures and tables are as follows:

Publication (complete reference):

A. Seifert, J. Groll, J. Weichhold, A. V. Boehm, F. A. Müller, U. Gbureck, Phase Conversion of Ice-Templated α-Tricalcium Phosphate Scaffolds into Low-Temperature Calcium Phosphates with Anisotropic Open Porosity. *Advanced Engineering Materials* **2021**, 23(5), 2001417.
DOI: https://doi.org/10.1002/adem.202001417.

Figure	**Author Initials,** Responsibility decreasing from left to right				
Figure 23	A.S.				
Figure 24	A.S.				
Figure 25	A.S.				
Figure 26	A.S.				
Figure 27	A.S.				
Figure 28	A.S.				
Figure 29	A.S.				
Figure 30	A.S.				
Figure 31	A.S.				

Table	**Author Initials,** Responsibility decreasing from left to right				
Table 6	J.W.	A.S.			

The doctoral researcher confirms that she has obtained permission from both the publishers and the co-authors for legal second publication.

The doctoral researcher and the primary supervisor confirm the correctness of the above mentioned assessment.

Annika Seifert		Würzburg	
Doctoral Researcher's Name	Date	Place	Signature

Prof. Dr. Jürgen Groll		Würzburg	
Primary Supervisor's Name	Date	Place	Signature

4.1 Abstract

The current study aims to extend the material platform for anisotropically structured calcium phosphates to low-temperature phases such as calcium deficient hydroxyapatite (CDHA) or the secondary phosphates monetite and brushite. This is achieved by the phase-conversion of highly porous α-tricalcium phosphate (α-TCP) scaffolds fabricated by ice-templating into the aforementioned phases by hydrothermal treatment or incubation in phosphoric acid. Prior to these steps, α-TCP scaffolds are either sintered for 8 h at 1400 °C or remain in their original state. Both non-sintered and sintered α-TCP specimens are converted into CDHA by hydrothermal treatment, while a transformation into monetite and brushite is achieved by incubation in phosphoric acid. Hydrothermal treatment for 72 h at 175 °C increases the porosity in non-sintered samples slightly from 85% to 88% and from 75% to 88% in the sintered ones. An increase of the specific surface area from (1.102 ± 0.005) to (9.17 ± 0.01) $m^2 g^{-1}$ and from (0.190 ± 0.004) to (2.809 ± 0.002) $m^2 g^{-1}$ due to the phase conversion is visible for both the non-sintered and the sintered samples, respectively. Compressive strength of the non-sintered samples increases significantly from (0.76 ± 0.11) to (5.29 ± 0.94) MPa due to incubation in phosphoric acid.

4.2 Introduction

While bone is a hierarchically structured tissue with an anisotropic orientation of the building blocks on different length scales[37,350,351], most bone replacement materials based on calcium phosphate ceramics only feature an isotropic distribution of their pore network. These interconnecting pores are intended to enable cell infiltration, interaction with adjacent tissues and vascularization, which is indispensable for the successful implantation.[85] The formation and ingrowth of newly formed bone into the implant is enhanced by the use of highly porous scaffolds. The pore size considered ideal depends on the clinical application but should be at least 100 µm.[336,352] However, only a few bone graft substitute examples are known in which hierarchical and ordered pore designs are used. These unidirectional structures cause a more rapid cell ingrowth[338], improved nutrient supply, and vascularization capabilities in the preferred pore direction.[339] Such scaffolds can, for instance, be fabricated with the aid of additive manufacturing techniques such as 3D powder printing or dispense plotting.[109,353-360] However, these methods are only suitable for the fabrication of pores in the order of more than a few hundred microns. A promising approach to achieve an ordered lamellar structure with precisely adjustable pore sizes below 100 µm and a specifically modified pore orientation is directional freezing.[25] Here, a ceramic slurry is frozen in the presence of an external temperature gradient. The growing ice lamellae expel all components of the slurry and accumulate them between the ice crystals. By removing the ice crystals through freeze-drying, a porous scaffold with highly aligned pores is created, which represents a negative of the ice crystal structure.[282] This process is currently limited to high-temperature calcium phosphates (CaPs) such as hydroxyapatite[31] (HA) or tricalcium phosphate (TCP)[30]. However, these microcrystalline high-temperature CaPs only dissolve poorly at physiological pH and have a lower absorption rate *in vivo* than low-temperature CaPs, such as calcium deficient hydroxyapatite (CDHA, $Ca_9(PO_4)_5(HPO_4)OH$), brushite ($CaHPO_4 \cdot 2H_2O$) or monetite ($CaHPO_4$).[99,361] CDHA, for example, is nanocrystalline with a high specific surface area, which, in turn, is supposed to improve the biological performance of the implant.[99] Although brushite and monetite are usually microcrystalline, their higher solubility when compared with secondary calcium phosphates leads to faster resorption and bone regeneration *in vivo*.[131]

The current study aims to expand the material platform for ice-templated and highly porous calcium phosphate ceramics to the low-temperature phases CDHA, brushite, and monetite. This was achieved by structuring α-TCP into highly porous scaffolds, which were subsequently converted by hydrothermal treatment[362] or by incubation in phosphoric acid.[363] Hydrothermal treatment initiates a cement reaction of α-TCP and water, which, according to equation (11), results in CDHA as the end product:[118]

$$3\ \alpha\text{-}Ca_3(PO_4)_2 + H_2O \longrightarrow Ca_9(PO_4)_5(HPO_4)OH \quad (11)$$

Incubation in phosphoric acid converts α-TCP to monetite or brushite using equation (12) and (13), respectively.

$$\alpha\text{-}Ca_3(PO_4)_2 + H_3PO_4 \longrightarrow 3\ CaHPO_4 \quad (12)$$

$$\alpha\text{-}Ca_3(PO_4)_2 + H_3PO_4 + 6H_2O \longrightarrow 3\ CaHPO_4 \cdot 2H_2O \quad (13)$$

Here, different processing parameters such as duration and temperature of the hydrothermal treatments were systematically varied and their influence on sample morphology, phase composition, and mechanical properties of the resulting scaffolds was investigated. The latter are thought to have a high clinical potential due to the higher solubility of the obtained calcium phosphate phases, which will, in turn, accelerate bone regeneration.

4.3 Experimental Section

4.3.1 Slurry preparation

Calcium phosphate scaffolds with aligned pore orientation were fabricated by directional freezing and subsequent freeze-drying of slurries. The slurries consisted of α-TCP powder, which was mixed with a 2% (w/w) alginate solution.

α-TCP powder was synthesized in-house by mixing calcium hydrogen phosphate ($CaHPO_4$, J. T. Baker, Fisher Scientific GmbH, Schwerte, Germany) and calcium carbonate ($CaCO_3$, Merck, Darmstadt, Germany) powder in a molar ratio of 2:1 for 1 h. Subsequently, the mixture was sintered for 5 h at 1400 °C. The sinter cake was then mortared, and the powder was sieved to sizes <350 µm. Afterward, grinding was conducted in a planetary ball mill (PM400, Retsch, Haan, Germany) for 4 h at 200 rpm.

The alginate presolution (2% (w/w)) was prepared by dissolving sodium alginate powder ("Protanal LF 10/60FT", FMC Biopolymer, Philadelphia, USA) in ultrapure water under continuous stirring for 1 h. To remove existing air bubbles, the solution was centrifuged ("Mega Star 1.6R", VWR, Radnor, USA) for 5 min at 20 °C and 4500 rpm. Subsequently, the α-TCP powder and the alginate solution were mixed in a powder-to-liquid ratio of 1 g mL^{-1} on a glass plate using a spatula.

4.3.2 Directional freezing

Ice-templating of the slurries took place in a custom-built device (for detailed description see the study by Stuckensen *et al.*[25]). The core of this unit is a copper block through which coolant flows. On its top there are two Peltier elements (PEs) one above the other. With the help of the cooled copper block, both the heat generated by the PEs and the heat released during the freezing process can be effectively dissipated. The PEs were tempered differently, which resulted in the generation of an external temperature gradient. After the system was in thermal equilibrium, the slurry was transferred to a mold located between the two PEs for structuring.

To examine the morphology by SEM, the porosity by mercury porosimetry, the specific surface area by nitrogen adsorption, and the phase composition by XRD measurements, samples were fabricated in a mold with a diameter of 39 mm and a height of 5 mm. For mechanical compression tests, the cylinders had a diameter and height of 1 cm.

4.3.3 Freeze-drying and sintering

After freeze-structuring, the specimens were lyophilized at -57 °C and a maximum of 1 mbar for 24 h using a freeze-dryer ("Alpha 1-2 LDplus," Christ, Osterode am Harz, Germany). Subsequently, two-thirds of all specimens were sintered for 8 h at 1400 °C with

a heating rate of 5 °C min^{-1} and a cooling rate of 10 °C min^{-1} (“TC 5050,” Arnold Schröder, Flörsheim am Main, Germany).

4.3.4 Further specimen treatment

For a phase conversion into nanocrystalline HA, specimens were hydrothermally treated for 3 h, 5 h, and 8 h, respectively, in a pressure vessel (“Pressure Cooker BPR 700 BSS,” Sage, Düsseldorf, Germany) at 80 kPa gauge pressure and 117 °C. To avoid dissolution, non-sintered samples were put on a grid, placed above the level of demineralized water, while sintered samples had to be treated in 2.5% (w/w) Na_2HPO_4 solution for phase conversion. For technical reasons, the maximum incubation time at 117 °C was 8 h. For longer treatment durations of 12 h, 24 h, 48 h, and 72 h, a higher temperature and pressure of 175 °C and 800 kPa, a hydrothermal reactor (“4560 MiniReactor 600 mL,” Parr Instruments, Moline, USA) was used. Here, both scaffold types were placed on a custom-made aluminum frame above the water level (demineralized water) during the treatment. Afterward, the samples were dried for 24 h at 60 °C.

To convert α-TCP into the low-temperature calcium phosphates monetite and brushite, non-sintered and sintered samples were subjected to acidic treatment. For this purpose, they were immersed twice for 30 s in 10% phosphoric acid solution (orthophosphoric acid, Merck, Darmstadt, Germany) and then dried at room temperature.

4.3.5 Sample Characterization

X-ray diffractometry (XRD) measurements were performed using a Bragg–Brentano diffractometer (“D8 Advance DaVinci design,” Bruker AXS, Karlsruhe, Germany). For this purpose, one specimen per sample type was ground to fine powder, measured using Cu-$K_{\alpha,1}$ line with an acceleration voltage of 40 kV, an emission current of 40 mA, a wavelength of λ = 1.5406 Å, a 2θ range of 10° - 60°, a step size of 0.02°, and an integration time of 1 s.

The present phases were qualitatively determined using the PDF2 Database and an evaluation tool (“Diffrac.EVA,” Bruker AXS, Karlsruhe, Germany). Rietveld refinement of the corresponding crystal structures of α-TCP (ICDD# 290359), β-TCP (ICDD# 90169), CDHA (ICSD# 26204), brushite (ICSD# 16132), and monetite (ICSD# 31046) was used (“Diffrac.TOPAS,” Bruker AXS, Karlsruhe, Germany) to determine both the quantitative content and crystallite size of the aforementioned phases.

To investigate morphological changes caused by hydrothermal and acidic treatment, scanning electron microscopy (SEM) images of the samples were used. For this purpose, one sample per specimen type was broken and fixed with a carbon cement glue (“Leit C Conductive Carbon Cement,” PLANO GmbH, Wetzlar, Germany) on SEM specimen

holders (Agar Scientific, Stansted, UK) in such a manner that the fractured surfaces could be examined. A high-vacuum coater (“EM ACE600”, Leica, Wetzlar, Germany) was used at a current of 35 mA to apply a 6 nm-thick platinum layer to avoid electrical charging of the samples during SEM examination. A field-emission scanning electron microscope (“Crossbeam 340,” Zeiss, Jena, Germany) with an acceleration voltage of 2 - 5 kV was used for image acquisition.

For the quantitative determination of the length of the crystals resulting from the phase transformation by hydrothermal treatment, crystals were measured using an open source image processing software (“ImageJ”, Version 2.0.0). This involved 25 measurements for each sample type. The mean value indicates the respective crystal length, while the error corresponds to the standard deviation.

The pore size distribution, relative pore volume, and porosity of the samples were determined by mercury porosimetry (“Pascal 140” and “Pascal 440,” Porotec GmbH, Hofheim, Germany). One exemplary sample was measured for each specimen type.

To determine the specific Brunauer-Emmett-Teller (BET) surface area, a volumetric adsorption analyzer (“ASAP 2020” and “ASAP2010,” Micromeritics, Norcross, USA) was applied to measure the nitrogen adsorption isotherm at 77 K. Prior to analysis, the samples were degassed at 150 °C for at least 2 h. For each analysis, a mass of about 1.5 - 2 g was used. The isotherms were evaluated in the relative pressure range below 0.3 with respect to the specific BET surface area using the software “microactive” by the instruments’ supplier.

The mechanical properties of the specimens were evaluated by compression strength measurements using a universal testing machine (“Z010,” ZwickRoell, Ulm, Germany) equipped with a 10 kN load cell. Sample cylinders were loaded with a force parallel to their longitudinal axis at a test speed of 1 mm min^{-1} until complete failure occurred. With this failure force F and the surface area A of the cylinder, the compressive strength σ was calculated using equation (14):

$$\sigma = \frac{F}{A} \tag{14}$$

For each sample type five measurements were performed. The mean value indicates the compressive strength, while the error corresponds to the standard deviation.

4.3.6 Statistical Methods

Statistical analysis was performed using the software “SigmaPlot” (Version 12.5). First, normal distribution of the raw data was proved using the Kolmogorov test. This was followed by applying a one-way ANOVA with post hoc Tukey test. Significant differences are indicated with *($p<0.05$) and **($p<0.001$).

4.4 Results

4.4.1 Phase composition

The phase transformation of α-TCP induced by the different post-treatments was analyzed by XRD measurements. (Figure 23) During the hydrothermal treatment at 117 °C it was observed for both sample types, i.e., non-sintered and sintered, that a partial phase transformation from α-TCP to β-TCP, CDHA, and, in addition, monetite in the non-sintered samples occurred. (Figure 23 a, b and Figure 24) While monetite appeared as a transition phase, a complete phase transformation to CDHA was found in both cases after hydrothermal treatment for at least 48 h. (Figure 23 c, d and Figure 24)

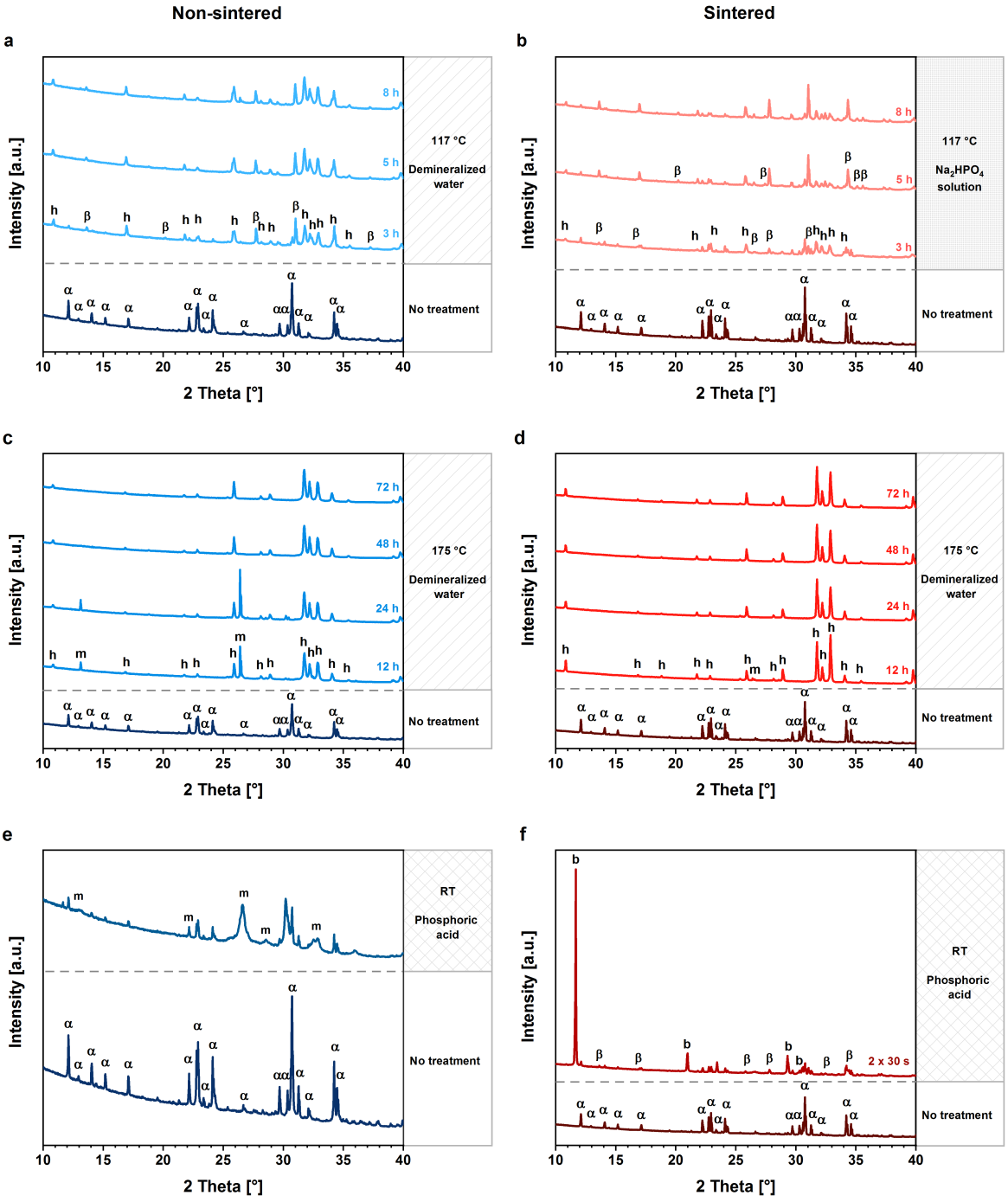

Figure 23. XRD patterns of non-sintered and sintered specimens. In the left column, XRD measurements of the non-sintered samples are shown in shades of blue, while those of the sintered samples are shown in red in the right column. The XRD spectra in the different rows are sorted by treatment, i.e., hydrothermal treatment at a,b) 117 °C (upper row), c.d) 175 °C (middle row) and e.f) incubation in phosphoric acid solution (lower row). The intensity maxima for (α) α-TCP, (β) β-TCP, (h) CDHA, (m) monetite, and (b) brushite are indicated.

Treatment in phosphoric acid solution led to a partial recrystallization of α-TCP into monetite for the non-sintered samples and into β-TCP and highly crystalline brushite for the sintered ones. (Figure 23 e, f and Figure 24)

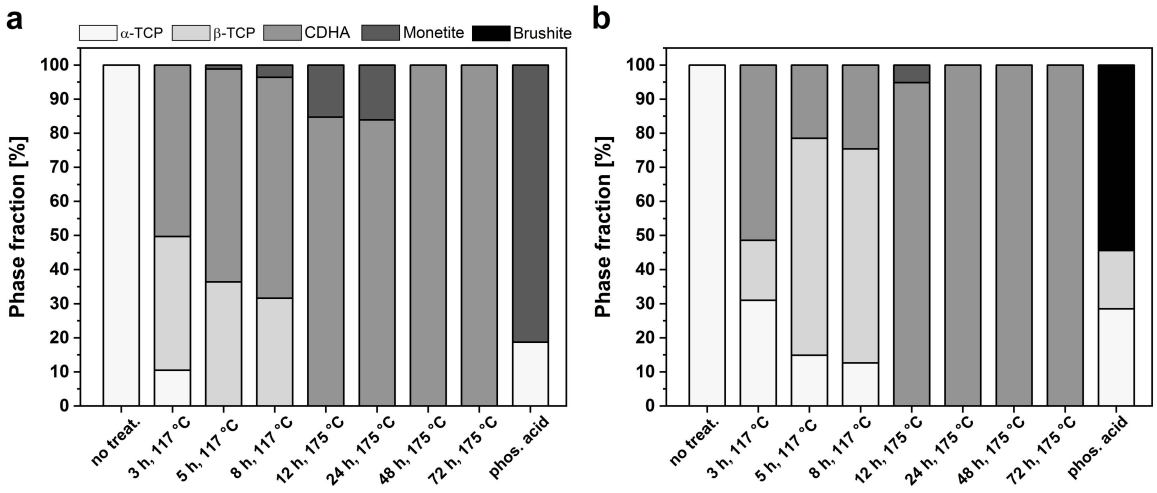

Figure 24. Changes in phase composition due to different treatment types. a) Non-sintered samples: with increasing incubation time and temperature of the hydrothermal treatment, α-TCP converted completely to CDHA after 48 h via the intermediate phases β-TCP and monetite. Incubation in phosphoric acid solution caused a partial conversion to monetite. b) Sintered samples: with increasing incubation time and temperature of the hydrothermal treatment, α-TCP converted completely to CDHA after 24 h via the intermediate phases β-TCP and monetite. Incubation in phosphoric acid solution caused a partial conversion to β-TCP and brushite.

Furthermore, the crystallite size was determined, as shown in Table 6 (n.c.=not calculable; either the crystallite size was too low <10 nm or too high >1000 nm).

It can be seen that the crystallite sizes increase with the sintering process. During sintering, the small precipitated crystals fuse into a larger crystallite due to solid diffusion.

Table 6. Crystallite size in dependence of different treatments.

Treatment		**Crystallite size [nm]**				
		α-TCP	**β-TCP**	**CDHA**	**Monetite**	**Brushite**
No treatment	non-sintered	359	-	-	-	-
	sintered	n.c.	-	-	-	-
8 h, 117 °C	non-sintered	-	249	88	249	-
	sintered	n.c.	541	135		-
72 h, 175 °C	non-sintered	-	-	119	-	-
	sintered	-	-	319	-	
2 x 30 s, phosphoric acid solution	non-sintered	n.c.	-	-	40	-
	sintered	n.c.	n.c.	-		n.c.

4.4.2 Morphological changes

Structural changes that occurred during the hydrothermal or acidic treatment of the non-sintered α-TCP samples were visualized by SEM. (Figure 25)

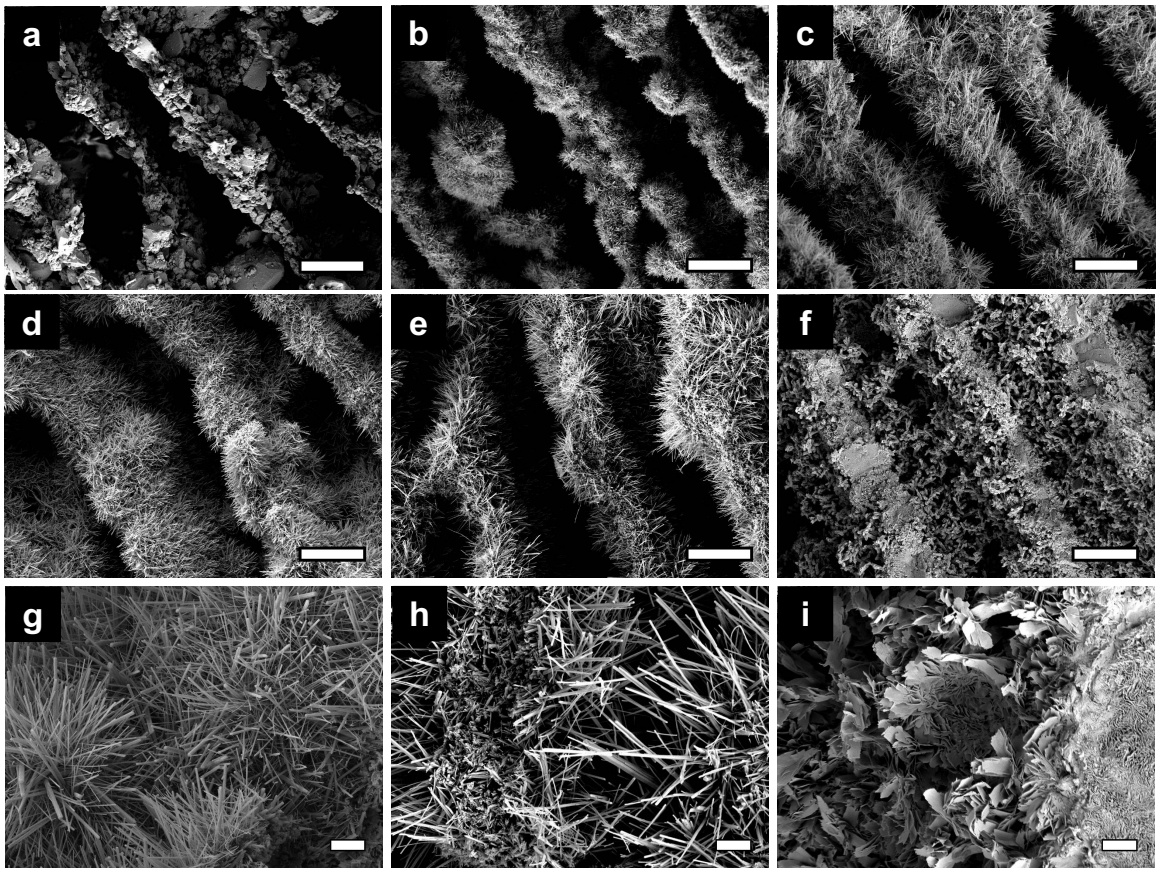

Figure 25. Influence of hydrothermal and acidic treatment on the morphology of non-sintered specimens. a) Highly ordered pores in a freeze-structured sample after freeze-drying. α-TCP crystals could be observed on the lamellae. b, c) Due to hydrothermal treatment at 117 °C for 3 h and 8 h, respectively, fine CDHA whiskers grew on the lamellae. The structure was similar d) after incubation for 12 h at 175 °C and e) 72 h at 175 °C. f) After incubation in phosphoric acid solution, platelet-shaped monetite crystals grew into the pores. g) Magnification of a selected lamella after 8 h at 117 °C. Fine CDHA needles were arranged in tufts. h) This was also visible after 72 h at 175 °C. i) Magnification of crystals resulting from incubation in phosphoric acid solution. Scale bars are 15 µm in the two top rows (a-f) and 2 µm in the lower row (g-i).

After the freeze-drying of the specimens, it became apparent that the pores were arranged parallel to each other in a highly ordered manner. The lamellae between the pores consisted of α-TCP crystals and alginate. (Figure 25 a) Due to the hydrothermal treatment at 117 °C for 3 h, the morphology of the lamellae changed. Here, fine CDHA needles or whiskers appeared, which originated in the lamellae and partially protruded into the pores. (Figure 25 b) These needle-like structures were also visible after 8 h of hydrothermal treatment. (Figure 25 c) A closer look at one selected lamella showed that the CDHA whiskers were arranged in tufts and distributed over the entire lamella. (Figure 25 g) This structure did not change significantly by hydrothermal treatment at higher temperatures and longer durations. (Figure 25 d, e) The only notable difference was that the needles seemed to become slightly thicker. (Figure 25 h)

An apparently different morphology could be observed after incubation in phosphoric acid. Small platelet-shaped monetite crystals emerged from the lamellae, grew into the pores, and filled them nearly completely in a still porous manner. (Figure 25 f, i)

The remaining samples were sintered after freeze-drying and subjected to hydrothermal or acidic treatment afterward. After the sintering process, without any treatment step, the aligned pore structure was preserved. The lamella surfaces were smooth without individual crystals being visible. (Figure 26 a)

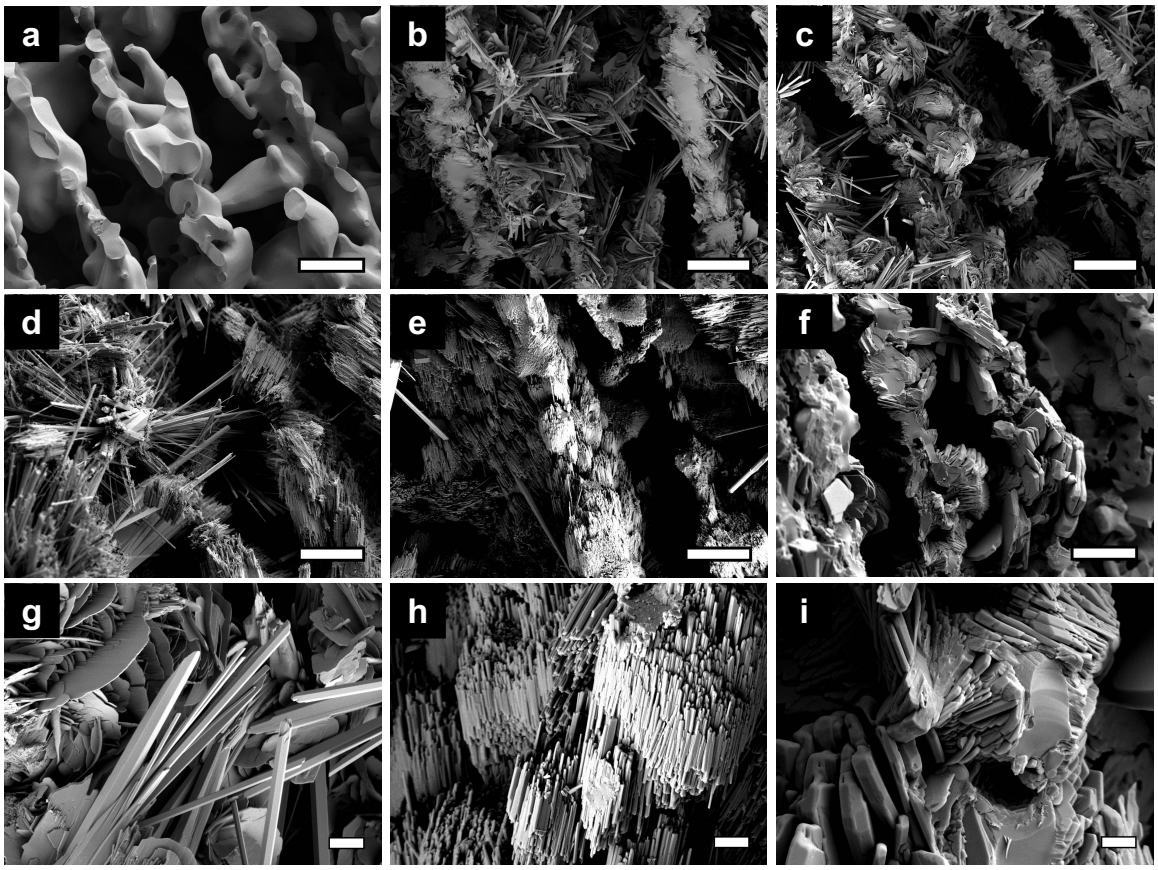

Figure 26. Influence of hydrothermal and acidic treatment on the morphology of sintered specimens. a) Highly ordered pores in a freeze-structured sample after sintering with a smooth lamella surface. b, c) Due to hydrothermal treatment at 117 °C for 3 h and 8 h, respectively, platelet-shaped and needle-like CDHA crystals, which protruded into the pores, appeared. During incubation for d) 12 h at 175 °C and e) 72 h at 175 °C, bundles of CDHA crystals were formed. f) Due to incubation in phosphoric acid solution, small brushite crystals developed. g) Magnification of a selected lamella after 8 h at 117 °C. CDHA crystals were flat and long. h) Magnification of CDHA needle bundles, which were formed after 72 h at 175 °C. i) Magnification of brushite crystals resulting from incubation in phosphoric acid solution, which also tended to be arranged in bundles. Scale bars are 15 µm in the two top rows (a-f) and 2 µm in the lower row (g-i).

After the treatment at 117 °C for 3 h, the plain surface changed. Both platelet-shaped and needle- or rod-like CDHA crystals, which protruded into the pores, were visible. (Figure 26 b) This structure also occurred after 8 h. (Figure 26 c, g) A more detailed examination of the structure showed that the CDHA needles were thicker, flatter, and longer than in the non-sintered scaffolds. Due to the hydrothermal treatment at 175 °C, the platelet-shaped crystals disappeared. (Figure 26 d) In addition, the needles became shorter and were increasingly located on the lamellae. It could also be shown that,

especially with long treatment times, CDHA needles became shorter, arranged parallel to each other, and formed bundles. The size of these bundles was in the order of several micrometers. (Figure 26 e, h) However, crystal length was examined in a separate investigation, as shown in Figure 27.

Due to the incubation in phosphoric acid, a distinct structural change occurred. While the pores were still aligned, a complete transformation of the smooth lamellar structure was observed. Small brushite crystals appeared, which did not protrude into the pores, but were localized on the lamellae. (Figure 26 f) These crystals also tended to be arranged in bundles. (Figure 26 i)

A comparison of the CDHA needles of non-sintered and sintered samples obtained by incubation at 117 °C for 8 h (Figure 25 g and Figure 26 g) shows that the needles of non-sintered samples were thinner and shorter than those of the sintered ones. These were flatter, broader, and sturdier.

A quantitative evaluation of the length of crystals growing into the pores after hydrothermal treatment at 175 °C (both sample types were treated in demineralized water vapor at this temperature) is shown in Figure 27 a. Needles in the non-sintered specimens were between nine and eleven times shorter than those in the sintered ones. A reduction in crystal length in the non-sintered samples was found after 24 h, while it increased again after 48 h and 72 h. In the sintered samples, a significant ($p<0.001$) increase was observed only after 72 h of hydrothermal treatment.

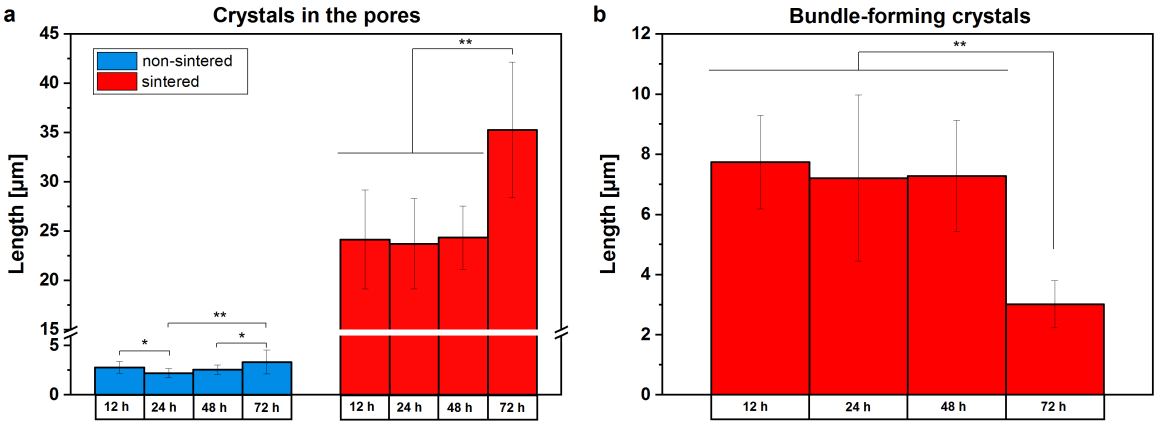

Figure 27. Effect of incubation time on CDHA crystal length due to hydrothermal treatment at 175 °C. a) Length of CDHA crystals growing into the pores. Needle-like crystals of the non-sintered samples were shorter than those of sintered ones. The length increased for sintered samples with increasing incubation time. The crystal lengths of non-sintered samples are shown in blue, those of sintered samples in red. b) Influence of incubation time on the length of bundle-forming crystals in the sintered samples. These became shorter with increasing incubation time. (mean ± SD, n = 25, *$p<0.05$, **$p<0.001$)

Figure 27 b shows the length of CDHA crystals within the bundles formed in the sintered samples during incubation at 175 °C. These became significantly ($p<0.001$) shorter after 72 h incubation time and decreased by a factor of approximately 2.5.

4.4.3 Pore size distribution and porosity

Pore size distribution, relative pore volume, and porosity were measured by mercury porosimetry. Although the widely used characterization method of microcomputed tomography (µ-CT) offers several advantages, such as nondestructive measurement and detection of both closed and open pores, the main benefit of mercury intrusion is the detection of accessible pores down to a size of 0.0036 µm (according to the manufacturer's information, see Experimental Section). Compared to µ-CT with a detection limit of 1 µm[364], this resolution is thus significantly higher.

The effects of hydrothermal and acidic treatment on pore size distribution, specific volume, and porosity are shown in Figure 28. For the purpose of better clarity, only the pore size distributions without treatment, after 8 h at 117 °C, after 72 h at 175 °C, and after incubation in phosphoric acid were presented in an exemplary manner.

Considering the non-sintered samples, a nearly monomodal narrow pore size distribution with a maximum of 23 µm was revealed without treatment. (Figure 28 a) Due to hydrothermal treatment at 117 °C, this distribution widened especially to smaller pore sizes and also the maximum shifted slightly in this direction to 9 µm. (Figure 28 c) After 72 h at 175 °C, this maximum was increased again and shifted to a size of 16 µm. (Figure 28 e) A trimodal pore size distribution could be observed after the treatment in phosphoric acid solution. (Figure 28 g) Total porosity decreased from 85% to 82% after the treatment for 8 h at 117 °C and increased again to a value of 88% due to the treatment for 72 h at 175 °C. The porosity decreased to a value of 79% by incubation in phosphoric acid solution. (Figure 28 a, c, e, g)

The overall porosity of sintered samples was lower than that of the non-sintered ones. However, a similar trend could be observed. Here, the porosity increased from 75% to 77% and 88% due to the treatment for 8 h at 117 °C and 72 h at 175 °C, respectively, and dropped to 59% due to acidic treatment. (Figure 28 b, d, f, h) The pore size distribution showed a monomodal distribution for both untreated and hydrothermally treated samples. Here, the maximum ranged between 23 µm and 11 µm. After incubation in phosphoric acid solution, the distribution spread again to smaller pores. The maximum was reduced to one-third, i.e., 3 µm (Figure 28 h)

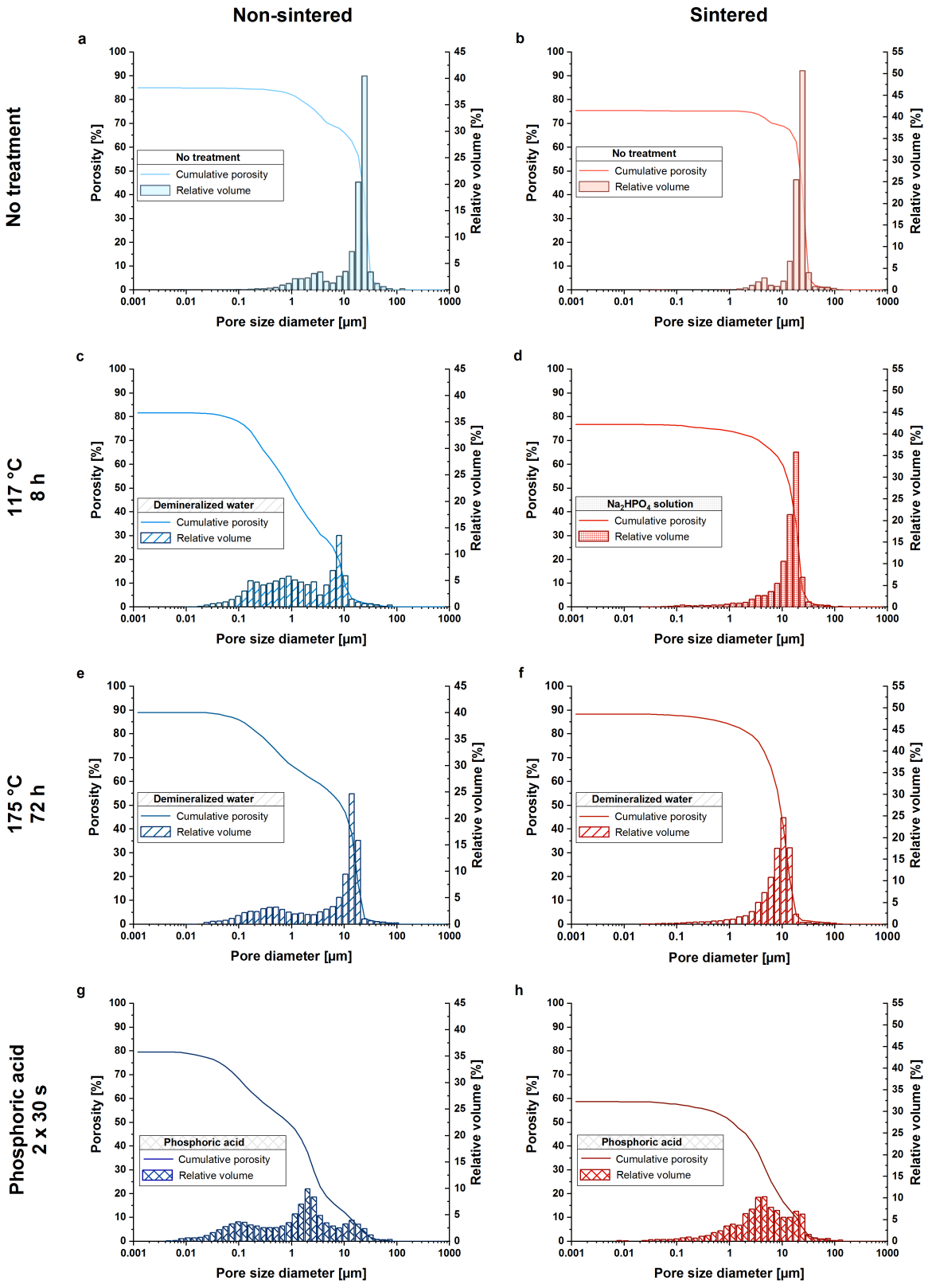

Figure 28. Pore size distribution, relative volume, and porosity of non-sintered and sintered samples before and after different treatments. In the left column, measurements of the non-sintered samples are shown in shades of blue, while those of the sintered samples are shown in red in the right column. The rows indicate the treatment type. From top to bottom: a,b) no treatment, c,d) hydrothermal treatment for 8 h at 117 °C, e,f) hydrothermal treatment for 72 h at 175 °C, and g,h) incubation in phosphoric acid solution. Both the non-sintered and sintered samples showed a monomodal pore size distribution with a maximum at 23 µm for both sample types without treatment. The different treatments shifted this maximum to lower values. Porosity ranged from 79% (incubation in phosphoric acid solution (g)) to 88% (hydrothermal treatment for 72 h at 175 °C) for the non-sintered samples and from 59% (incubation in phosphoric acid solution (h)) to 88% (hydrothermal treatment for 72 h at 175 °C) for the sintered samples.

4.4.4 Specific surface area

The specific BET surface area is shown in Figure 29. An increase in the specific surface area from (1.102 ± 0.005) m^2 g^{-1} to (9.17 ± 0.01) m^2 g^{-1} and from (0.190 ± 0.004) m^2 g^{-1} to (2.809 ± 0.002) m^2 g^{-1} due to hydrothermal treatment for 5 h at 117 °C is visible for both the non-sintered and the sintered samples, respectively.

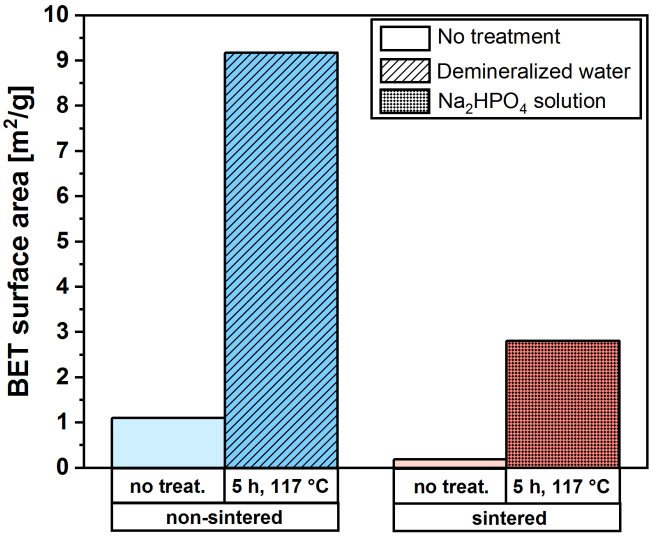

Figure 29. Specific BET surface area. The lighter blue bar corresponds to a non-sintered sample without treatment, darker blue to a non-sintered sample treated for 5 h at 117 °C. The respective equivalents for sintered samples are shown in shades of red.

4.4.5 Mechanical properties

The influence of hydrothermal and acidic treatment on the mechanical properties was investigated by compressive strength tests. (Figure 30)

While the compressive strength of non-sintered samples did not change considerably after 3 h and 5 h of hydrothermal treatment at 117 °C and was slightly below 1 MPa, it increased significantly ($p<0.001$) to (1.60 ± 0.11) MPa after 8 h. After hydrothermal treatment at 175 °C, the compressive strength dropped again to (0.51 ± 0.31) MPa after 72 h but remained at a similar level for all treatment durations. Due to incubation in phosphoric acid solution, a significant increase to (5.29 ± 0.94) MPa was observed. (Figure 30 a)

This value is comparable to the compressive strength of sintered samples. (Figure 30 b) During the treatment of these samples at 117 °C in disodium hydrogen phosphate (Na_2HPO_4) solution, the values remained approximately constant. After hydrothermal treatment at 175 °C, compressive strength decreased significantly ($p<0.001$) to values around 2 MPa, whereby the incubation time had no influence on the compressive strength. Also, due to incubation in phosphoric acid solution, the compressive strength remained within this range.

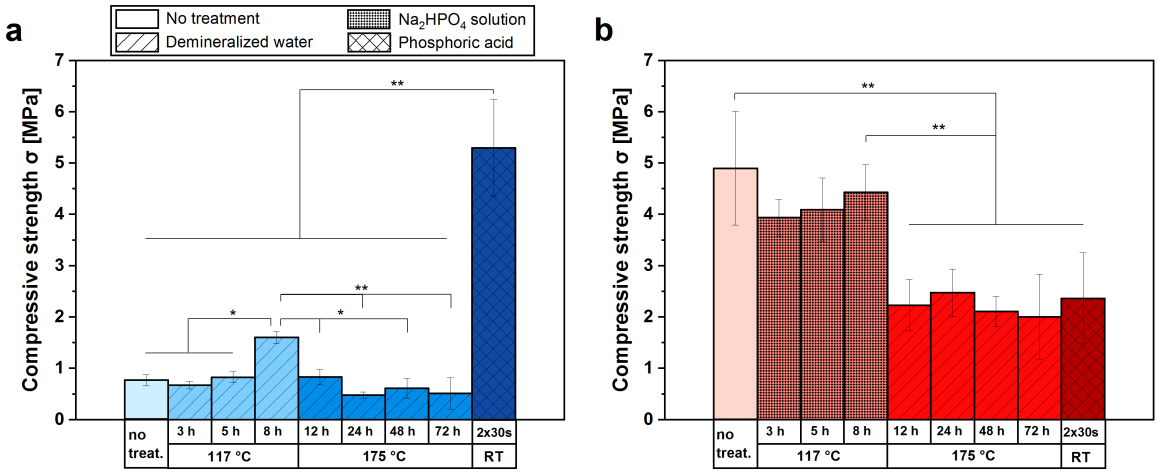

Figure 30. Influence of hydrothermal and acidic treatment on the compressive strength. a) Non-sintered samples: compressive strength without treatment is shown in light blue; strengths after hydrothermal treatment at 117 °C and 175 °C and after incubation in phosphoric acid are represented in darker shades of blue. b) Sintered samples: compressive strength without treatment is shown in light red; strengths after hydrothermal treatment at 117 °C and 175 °C and after incubation in phosphoric acid are represented in darker shades of red. (mean ± SD, n = 5, *p<0.05, **p<0.001)

4.5 Discussion

The aim of this study was to extend the material field for freeze-structured and highly porous calcium phosphate ceramics with anisotropic pores from high-temperature ceramics to the low-temperature phases CDHA, brushite, and monetite. The principle of directional solidification has been known for a very long time and is widely used as it is one of the most important steps in the metal casting process.[299] In addition to such high-temperature applications, the use of low-temperature processes, i.e., the controlled freezing of aqueous solutions, is also widespread. Therefore, freeze-structuring of a variety of materials is being investigated for applications in various other areas, ranging from research on novel battery applications[1], thermal energy storage[365] and cryopreservation of cells[366] to the fabrication of hierarchically structured biomaterials[298]. Advantages of a directional pore structure for biomaterials include enhanced cell migration[338] and facilitation of vascularization[339]. In addition, a much higher loading capacity can be observed along the z-axis, i.e., in the freezing direction, compared with the direction perpendicular to pore orientation.[327] The directional pores can also be adjusted in their properties, for example, their diameter or orientation, by selecting suitable freezing parameters, such as the magnitude of the external temperature gradient.[25] An important biomaterial application of such freeze-structured scaffolds is bone replacement, where (apart from the gold-standard autologous bone transplantation) usually porous calcium phosphate ceramics with isotropic pore orientation[367,368] are used to fill a defect. More recently, freeze-structured ceramic scaffolds consisting of sintered hydroxyapatite[31,369-372] or β-TCP[30] have been presented as a novel approach for bone tissue engineering. However, such high-temperature phases have slow resorption kinetics and would therefore only lead to a long-term defect regeneration. Here, an improvement in terms of regeneration speed could be achieved by using either nanocrystalline HA or secondary calcium phosphates such as brushite or monetite. As these phases are only stable at low temperature, the fabrication process has to be adequately designed to achieve sufficient mechanical stability while avoiding a final sintering regime. In the current study, this was achieved by ice-templating of α-TCP slurries with a subsequent phase transformation into various low-temperature CaPs, by taking advantage of the different stabilities of calcium phosphates depending on the pH value.[32]

Therefore, incubation in acidic phosphate solution was chosen for the conversion of reactive α-TCP[373] into brushite and monetite, while α-TCP scaffolds were hydrothermally treated in water vapor at nearly pH neutral conditions for a conversion into CDHA. By using this reactive system, it was possible to produce both non-sintered and sintered scaffolds after freeze-structuring, which were subsequently converted into the aforementioned low-temperature phases without affecting the highly ordered, directional pore structure. This is

shown by the SEM images for both the non-sintered (Figure 25) and the sintered samples (Figure 26). The idea of first fabricating the scaffold in its final structure and shape and then converting it into a low-temperature calcium phosphate by a cement reaction was already realized by Galea *et al*..[362,363] However, these samples did not exhibit ordered porosity.

In non-sintered samples, hydrothermal treatment resulted in the transformation of α-TCP crystals into tuft-like, fine CDHA needles without affecting the overall scaffold porosity. This is demonstrated by considering the phase composition determined by the corresponding XRD measurements (Figure 23), in which the CDHA content ranged between 50% and 100% (Figure 24). This is consistent with previous studies which showed that the cement reaction caused by hydrothermal treatment led to the precipitation of CDHA in the form of fine needles.[374] After hydrothermal treatment of sintered samples, HA needles were also found, but these were considerably thicker than the fine needles in non-sintered samples, leading to an increase in porosity from 75% to 88% after 72 h at 175 °C (Figure 28). This is even higher than the porosity achieved by particle leaching from CDHA cements, which reached porosities of up to 81% and open macropores of 400 - 500 µm in size.[375] Such formation of rod-shaped hydroxyapatite crystals under hydrothermal treatment, especially in the presence of vapor[376] or in Na_2HPO_4 solution[377], has previously been observed in other studies and confirms our observations. However, it was remarkable that at a treatment temperature of 175 °C, bundles of HA needles were formed in the sintered samples, which was also found in sintered α-TCP-blocks[362], whereas this phenomenon could not be observed in non-sintered samples.

Nanocrystalline hydroxyapatite is structurally very similar to the inorganic component in bone.[36,45,378] Due to its nanocrystallinity, it has a much higher specific surface area, which leads to an increased kinetic solubility.[136] Our results show that the specific surface area of the non-sintered samples was increased eightfold by the conversion of α-TCP into CDHA, caused by the formation of fine whiskers. Similar findings were observed for the sintered samples, where the specific surface area was even increased by a factor of 15 due to the growth of rod- and platelet-shaped CDHA crystals (Figure 29).

Another low temperature approach for the preparation of CDHA nanocomposites was described by Kniep *et al*.[379-383], whose group investigated the process of biomineralization on the model system gelatin-fluorapatite. Here, gelatin was mineralized using a double diffusion technique. Solutions containing calcium and phosphate ions were located in two different reservoirs and migrated into a gelatin gel, which was located in between. This led to the formation of gelatin-apatite nanocomposites. Drawbacks of this process include the sensitive dependence on the materials used and the limited material spectrum. This issue is not present in our samples because the reactive α-TCP system can be converted into

the selected material by a cement reaction through suitable post-treatment steps. Here, the previously mentioned advantages of an aligned pore structure were combined with the benefits of using the low-temperature calcium phosphates CDHA, brushite, and monetite. Incubation of ice-templated samples in phosphoric acid solution resulted in a conversion to the secondary phosphates such as monetite and brushite. Both minerals are often used as materials in bone replacement applications due to their high resorption rate under physiological conditions, which makes them highly interesting for medical treatments[131,384-386]. Immersion of the non-sintered samples in phosphoric acid solution resulted in a phase transformation to monetite with a platelet-shaped, microcrystalline crystal structure growing into the pores. In contrast, the sintered samples transformed into brushite crystals, which tended to form bundles. Brushite usually crystallizes in different morphologies depending on the growth conditions. Abbona *et al.* reported that often several crystal types were found at the same time, but depending on the concentration, at low pH and 25 °C, flat tabular crystals were more frequently observed.[139] These can also be seen in the SEM images of the brushite samples from our study (Figure 26 f, i).

For conventionally prepared, non-structured brushite cements with a powder-to-liquid ratio of 1 g mL^{-1}, Sheik *et al*. reported a porosity of 65% and a bimodal pore size distribution with modal values of 4 µm and 9 µm. If these cements were converted into monetite by autoclaving or dry heating, porosities of 60% and pore sizes of about 5-8 µm and 3-8 µm, respectively, could be achieved.[387] When comparing these values with the parameters determined by us, it is noticeable that the brushite samples had a slightly lower porosity of 59%, which was due to the crystal ingrowth into the pores. The pore sizes were in a similar range, whereby also pores much larger than 10 µm were observed in our samples. For monetite cements, clearly higher porosities (almost 80%) were achieved by freeze-structuring, with the advantage of aligned pores in the entire sample. (Figure 28) Another study that investigated brushite cements with a powder-to-liquid ratio of 2 g mL^{-1} reported a total porosity of around 70% after the storage of the specimens in PBS for 24 h. After conversion to monetite through autoclaving, the porosity measured nearly 72%.[388]

All scaffolds presented in this study were highly porous, especially after conversion to CDHA by hydrothermal treatment for 72 h at 175 °C, where a porosity of 88% could be achieved. (Figure 28) Such high porosities are beneficial in terms of the ingrowth of newly formed bone.[352] As the minimum pore size for bone graft substitutes is regarded as 100 µm[336], pore diameters of the scaffolds presented in this study are below this value. Nevertheless, larger pores could be realized with only minor effort, e.g., by adjusting the freezing parameters[25] or using a lower powder-to-liquid ratio: the more water available in the slurry, the more ice is formed during the freezing process, resulting in larger pores after lyophilization.

In addition to properties such as architecture, structure, and phase composition of a scaffold, the mechanical properties of a bone replacement material are of crucial importance. Even if the scaffold is to be used in non-load bearing areas, it must be stable enough to allow handling during surgery, which should be given at a strength of a few MPa. A comparison of the porosity-dependent compressive strengths determined in our study with previously found values[375,387,388] is shown in Figure 31.

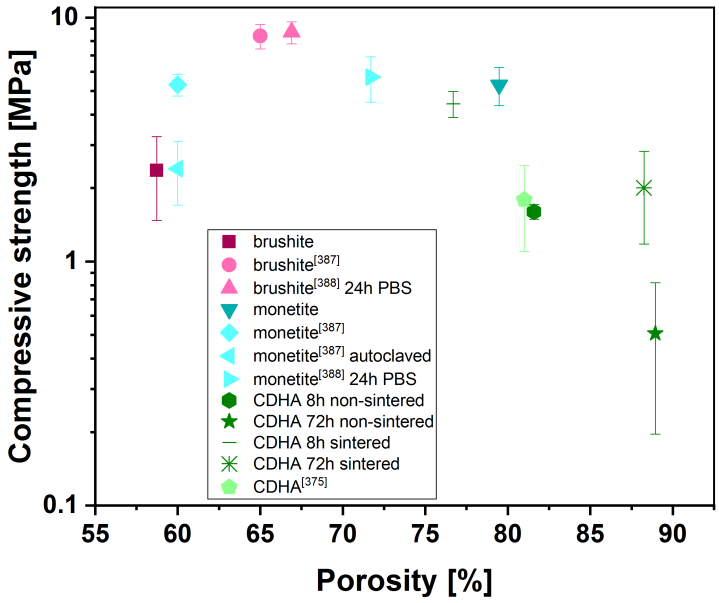

Figure 31. Compressive strength as a function of porosity and comparison with literature values. Compressive strengths determined in the present study for brushite, monetite and CDHA are shown in dark red, dark turquoise and dark green, respectively. The values described in the literature[375, 387, 388] are shown in the corresponding colors in lighter tones. The references in the figure have been adjusted from reference [349] to the order of references in this thesis.

Despite the lower porosity, the strength of our brushite specimens was below the values found in literature.[387,388] In contrast, the monetite samples presented in our study exhibited a higher porosity of almost 80% and a higher or comparable compressive strength. In addition, the CDHA samples showed comparable or improved properties compared with results reported in previous studies.[375]

It can be concluded that despite the high porosity, which was around 90% for certain specimens in the presented study (Figure 28), the compressive strength of all samples was between about 1 MPa and 5 MPa. Compared to human cortical bone, which has a compressive strength of about 130-210 MPa[389-391], this is low, but the values fit in the range of trabecular bone, which is between 0.1 MPa and 16 MPa[390]. Thus, it was demonstrated that all samples had sufficient stability to be used in non-load bearing areas and to be handled during surgery.

4.6 Conclusion

This study aimed to establish a generic system in which ice-templated α-TCP scaffolds with a highly ordered micropore structure were converted into the low temperature calcium phosphates CDHA, monetite and brushite, respectively, under the preservation of the aligned pore structure. This was achieved by hydrothermal and acidic treatments of both non-sintered and sintered scaffolds at comparable strength. Thus, the sintering step could be omitted to save time and energy during the fabrication process.

Chapter 5

Calcium Phosphate Based Biomaterials Trigger Human Macrophages to Release Extracellular Traps

Chapter 5 is written in the form of an original research article that had not been published at the time of thesis submission.

Shortly after the thesis submission, the article was published with slight modifications: Annika Seifert, Tina Tylek, Carina Blum, Naomi Hemmelmann, Bettina Böttcher, Uwe Gbureck, Jürgen Groll, Calcium Phosphate-Based Biomaterials Trigger Human Macrophages to Release Extracellular Traps. *Biomaterials* **2022**, 285, 121521. The article is published in this thesis retaining the rights of Elsevier.

To improve readability, figures from the supplementary information have been integrated into the main article in this thesis.

The article is based on the work of the author of this thesis, Annika Seifert, who conducted most of the experiments and data evaluation and wrote the manuscript.

The author contributions to the research article are as follows:

Publication (complete reference):

A. Seifert, T. Tylek, C. Blum, N. Hemmelmann, B. Böttcher, U. Gbureck, J. Groll, Calcium Phosphate Based Biomaterials Trigger Human Macrophages to Release Extracellular Traps. *Submitted.*

Participated in	**Author Initials,** Responsibility decreasing from left to right				
Study Design	A.S. T.T.	C.B.	U.G. J.Gro.		
Methods Development	A.S.	T.T. C.B.	U.G. J.Gro.	B.B.	
Data Collection	A.S.	T.T.	C.B.	N.H.	
Data Analysis and Interpretation	A.S.	T.T. C.B.		N.H. B.B.	
Manuscript Writing	A.S.	T.T.	U.G. J.Gro.		
Writing of Introduction	A.S.	T.T.			
Writing of Materials & Methods	A.S.		T.T.	N.H.	
Writing of Discussion	A.S.	T.T.			
Writing of First Draft	A.S.		T.T.		

Chapter 5

The author contributions to the figures and tables article are as follows:

Publication (complete reference):

A. Seifert, T. Tylek, C. Blum, N. Hemmelmann, B. Böttcher, U. Gbureck, J. Groll, Calcium Phosphate Based Biomaterials Trigger Human Macrophages to Release Extracellular Traps. *Submitted.*

Figure	**Author Initials,** Responsibility decreasing from left to right				
Figure 32	A.S.	T.T.			
Figure 33	A.S.				
Figure 34	A.S.				
Figure 35	A.S.		N.H.		
Figure 36	A.S.		N.H.		
Figure 37	A.S.	T.T.			
Figure 38	A.S.	T.T.			
Figure 39	A.S.				
Figure 40	A.S.				
Figure 41	A.S.				
Figure 42	A.S.				
Figure 43	A.S.				
Figure 44	A.S.				
Figure 45	A.S.				
Figure 46	A.S. C.B.				
Figure 47	A.S. C.B.				
Figure 48	A.S.				
Figure 49	A.S.				
Figure 50	T.T.				
Figure 51	T.T.				

Table	**Author Initials,** Responsibility decreasing from left to right				
Table 7	T.T.				

The doctoral researcher confirms that she has obtained permission from both the publishers and the co-authors for legal second publication.

The doctoral researcher and the primary supervisor confirm the correctness of the above mentioned assessment.

Annika Seifert		Würzburg	
Doctoral Researcher's Name	Date	Place	Signature

Prof. Dr. Jürgen Groll		Würzburg	
Primary Supervisor's Name	Date	Place	Signature

5.1 Abstract

As central part of the innate immune response, immune cells fight against invaders through various mechanisms, such as the release of extracellular traps (ETs). While this mechanism is mainly known for neutrophils in biomaterial contact, the release of macrophage extracellular traps (METs) in response to biomaterials has not yet been reported. An important application area for biomaterials is bone, where healing of defects of a critical size requires the implantation of grafts, which are often composed of calcium phosphates (CaPs). In this study, the response of human monocytes/macrophages *in vitro* to two different CaPs (α-tricalcium phosphate (α-TCP) and calcium deficient hydroxyapatite (CDHA)) as well as different pore structures was investigated. Scaffolds with anisotropic porosity were prepared by directional freezing, while samples with isotropic pore structure served as reference. It was revealed that ETs are released by human monocytes/macrophages in direct or indirect contact with CaP scaffolds. This was caused by mineral nanoparticles formed during incubation of α-TCP samples in culture medium supplemented with human platelet lysate, with an anisotropic pore structure attenuating MET formation. METs were significantly less pronounced or absent in association with CDHA samples. It was furthermore demonstrated that MET formation was accompanied by an increase in pro-inflammatory cytokines. Thus, this study provided the first evidence that macrophages are capable of releasing ETs in response to biomaterials.

5.2 Introduction

The host innate immune response provides the first line of defense against foreign bodies, like pathogens or implanted biomaterials. Immune cells like neutrophils, monocytes, and macrophages are key players of these processes and actively fight against invaders with several mechanisms like phagocytosis or releasing cytokines and chemokines to attract further immune cells.[392] Another mechanism is the release of extracellular traps (ETs), first reported for neutrophils in 2004.[393] ETs are sticky, web-like structures composed of double stranded DNA (dsDNA), histones, antimicrobial peptides, and proteases, and ejected to capture microbes.[394,395] However, recently it was reported that neutrophils release ETs also in the contact with biomaterials. Here, the stiffness of materials[396], the hydrophobicity[397], or mineral particles[398] induced the formation of ETs. While the release of ETs from macrophages was reported towards microorganisms[399], MET formation towards biomaterials was not observed yet.

The response to implanted biomaterials is majorly orchestrated by monocyte-derived macrophages. As highly plastic cells, their phenotype, either pro-inflammatory (M1), anti-inflammatory/pro-healing (M2), or a mixed phenotype depending on external stimuli, essentially decides if the biomaterial will be integrated or encapsulated and separated from the host tissue.[400] Therefore, improving biomaterial design for preventing an excessive inflammatory reaction and shifting the macrophage phenotype towards the M2 direction is an essential goal of biomaterial research for regenerative medicine.

The advancement of bone replacement materials in terms of the triggered immune response and wound healing capacity is crucial, as every year several million patients suffer a bone defect of a critical size, for instance due to accidents or the removal of bone tumors.[401-404] Such bone defects require the support of a substitute material to heal, leading to an extremely high demand for bone substitutes worldwide.[405]

The gold standard for the replacement of original bone tissue still is autologous bone, which has the major advantage to be osteoinductive, osteoconductive and - most importantly - leads only with a low probability to an immunological rejection.[406] However, this approach has significant disadvantages, such as donor site morbidity, the need for an additional surgery, possible wound healing problems, and limited quantity and size.[19] Thus, research is focusing on the development of synthetic bone substitute materials. Since the main inorganic component of human bone is calcium phosphate (CaP), the use of CaP bone grafts in the form of blocks, granules or injectable cements, is of great interest.[101,149]

In addition to the chemical composition and the origin of the bone graft, properties such as scaffold porosity are also of importance. Although human bone is a hierarchically arranged tissue with a highly ordered structure, most bone graft substitutes exhibit an

isotropic pore structure. Advantages of an aligned, anisotropic pore structure are, for example, enhanced nutrient transport, facilitated cell ingrowth into the scaffold, and improved vascularization possibilities.[338,339] Scaffolds with such open and anisotropic porosity can be fabricated by unidirectional freezing. Here, a slurry is frozen under superposition of an external temperature gradient, resulting in the growth of aligned and lamellar ice crystals. The components of the slurry are displaced and collected between the ice crystals. After freeze-drying, the structure of the scaffold represents a negative template of the ice crystal morphology.[282,283] By choosing appropriate parameters, such as the CaP powder concentration within the slurry, the magnitude of the temperature gradient and the cooling rate, the pore size and orientation can be influenced.[307] Until recently, only ice-templating of high temperature CaPs such as tricalcium phosphate (TCP) or sintered hydroxyapatite (HA) was reported in literature.[30,31] However, these high-temperature phases only exhibit poor solubility at physiological conditions. In contrast, low-temperature CaPs such as calcium deficient nanocrystalline hydroxyapatite (CDHA) are absorbed at a higher rate *in vivo*.[99] Recently, it was shown that ice-templated scaffolds, which consisted of the high-temperature CaP α-TCP, could be converted to CDHA by a cement reaction while retaining the aligned pore structure.[349] This combined the advantages of a highly ordered pore structure with the use of a low-temperature CaP phase.

In the presented study, we investigated the effects of anisotropically structured α-TCP and CDHA as well as their unstructured reference on human monocyte-derived macrophages. Here, we could demonstrate that mineral nanoparticles were released, especially from α-TCP samples, leading to macrophages' formation of ETs. By this, we provide the first evidence that macrophages are capable of releasing ETs as a reaction towards biomaterials, accompanied by an increase in pro-inflammatory cytokines.

5.3 Materials and methods

5.3.1 Scaffold preparation

5.3.1.1 *Slurry preparation*

A slurry consisting of α-TCP powder and hyaluronic acid solution (2% (w/w)) was ice-templated to prepare the scaffolds.

α-TCP powder was synthesized in-house by mixing calcium hydrogen phosphate ($CaHPO_4$, J. T. Baker, Fisher Scientific GmbH, Schwerte, Germany) with calcium carbonate ($CaCO_3$, Merck, Darmstadt, Germany) powder in a molar ratio of 2:1 for 1 h. The mixture was then sintered for 5 h at 1400 °C, followed by mortaring the sinter cake, sieving the powder to sizes <350 µm and grounding it in a planetary ball mill ("PM400", Retsch, Haan, Germany) for 4 h at 200 rpm.[349]

Hyaluronic acid solution (2% (w/w)) was prepared by dissolving hyaluronic acid sodium salt powder (low molecular weight, 80-100 kDa, Carbosynth, Berkshire, UK) in ultrapure water. The solution was then centrifuged for 5 min at 20 °C and 4500 rpm to remove air bubbles in the solution ("Mega Star 1.6R", VWR, Radnor, USA).

α-TCP powder and hyaluronic acid solution were mixed at a powder-to-liquid ratio of 1 g mL^{-1}. The slurry was always freshly prepared before freeze-structuring the samples.

5.3.1.2 Ice-templating

Unidirectional freezing took place in a custom-build device (for detailed information see the study by Stuckensen *et al*.[25]). The core of the device consists of two Peltier elements (PE) arranged one above the other, which were tempered differently to create an external temperature gradient. The sample molds were placed on an aluminum cylinder between the PEs, so that the distance could be specified as 8 mm. The temperature of the lower PE was set to -33 °C, while the temperature of the upper PE was -1 °C. Hence, the external temperature gradient measured 4 °C mm^{-1}. When the system was at thermal equilibrium, 0.2 mL of the α-TCP slurry was injected into silicone molds, each 1 cm in diameter and 3 mm height. Three samples were prepared per run. After successful ice-templating, samples were lyophilized at -57 °C and a maximum of 1 mbar using a freeze dryer ("Alpha 1-2 LDplus", Christ, Osterode am Harz, Germany).

5.3.1.3 Post-treatment of the scaffolds

For the biological experiments, two different freeze-structured sample types and two reference sample types (sintered α-TCP and CDHA, respectively) were compared. The ice-templated samples included sintered α-TCP scaffolds and sintered α-TCP scaffolds

that were converted to CDHA by hydrothermal treatment in disodium hydrogen phosphate (Na_2HPO_4) solution after the sintering process.

To prepare sintered α-TCP scaffolds, samples were sintered after freeze-drying for 8 h at 1400 °C with a heating rate of 5 °C min^{-1} and a cooling rate of 10 °C min^{-1} ("TC 5050", Arnold Schröder, Flörsheim am Main, Germany).[349]

Conversion of the sintered α-TCP samples to CDHA was performed by hydrothermal treatment in 2.5% (w/w) Na_2HPO_4 solution. For this purpose, the samples were placed in a pressure vessel ("Pressure Cooker BPR 700 BSS", Sage, Düsseldorf, Germany) in a glass petri dish above the water level (demineralized water). Hydrothermal treatment was performed for 2 h at 117 °C and 80 kPa gauge pressure, followed by sample drying for 24 h at 37 °C.

α-TCP reference samples were prepared as described as follows: First, a slurry consisting of hyaluronic acid solution and α-TCP powder with a powder-to-liquid ratio of 1 g mL^{-1} was prepared as described previously. 0.2 mL of the slurry were poured in the silicone molds (diameter = 1 cm, height = 3 mm) that were also used for freeze-structuring and allowed to harden for 24 h at 37 °C and 100%rh in a water bath. Subsequently, the discs were dried for 24 h at 37 °C and sintered for 8 h at 1400 °C with a heating rate of 5 °C min^{-1} and a cooling rate of 10 °C min^{-1}.

To prepare the CDHA reference samples, sintered α-TCP discs were hydrothermally treated in 2.5% (w/w) Na_2HPO_4 solution as described above and then dried for 24 h at 37 °C.

5.3.2 Scaffold characterization

5.3.2.1 Phase composition

The phase composition of the samples was determined by X-ray diffractometry (XRD) measurements using a Bragg-Brentano diffractometer ("D8 Advance DaVinci design", Bruker AXS, Karlsruhe, Germany). For this purpose, specimens were fixed with plasticine on sample holders. The surface of one sample per sample type was scanned using the Cu-$K_{\alpha,1}$ line at a wavelength of 1.5406 Å, in a 2θ range from 10° to 60°, a step size of 0.2° and an integration time of 1 s at an accelerating voltage of 40 kV and an emission current of 40 mA.[349]

5.3.2.2 Porosity and pore size distribution

Porosity, pore size distribution and relative pore volume of the ice-templated samples were measured by mercury porosimetry ("Pascal 140" und "Pascal 440", Porotec GmbH, Hofheim, Germany). One exemplary scaffold was analyzed for each sample type.[349]

5.3.2.3 Sample imaging

Sample imaging was performed using a scanning electron microscope (SEM, "Crossbeam 340", Zeiss, Jena, Germany) at an accelerating voltage of 2 - 5 kV. Both the sample surface and, for the ice-templated scaffolds, also the cross section were examined. Prior to imaging, scaffolds were fixed on SEM specimen holders (Agar Scientific, Stansted, United Kingdom) with a carbon cement glue ("Leit C Conductive Carbon Cement", PLANO GmbH, Wetzlar, Germany) and then coated with a 6 nm thick conductive platinum layer at a current of 35 mA using a high-vacuum coater ("EM ACE600", Leica, Wetzlar, Germany).[349]

5.3.3 Preparing scaffolds for *in vitro* experiments - washing and sterilization

To prevent major uptake of divalent cations such as calcium (Ca^{2+}) and magnesium (Mg^{2+}) and release of phosphate ions by the scaffolds during incubation in the macrophage culture medium, samples were washed for 5 d in phosphate buffered saline (PBS buffer) containing Ca^{2+} (0.9 mmol L^{-1} $CaCl_2$, Merck, Darmstadt, Germany) and Mg^{2+} (0.5 mmol L^{-1} $MgCl_2 6{\cdot}H_2O$, Merck, Darmstadt, Germany) ions prior to cell seeding. For each sample, 2 mL of washing medium were used. The PBS buffer was changed daily. After the washing, scaffolds were dried at 37 °C for 24 h and sterilized by γ-irradiation for the *in vitro* experiments.

5.3.4 Ion absorption and release measurements

Initial ion (Ca^{2+}, Mg^{2+} and P) absorption or release induced by incubation of samples in macrophage culture medium (RPMI-1640, GlutaMAX™, Thermo Fischer Scientific, Waltham, USA) supplemented with 10% (v/v) human platelet lysate (hPL, PL Bioscience, Aachen, Germany)[407] was determined by inductively-coupled-plasma mass-spectroscopy (ICP-MS) measurements ("iCAP RQ ICP-MS", ThermoFisher Scientific, Waltham, USA). For this purpose, three scaffolds of each sample type were cultured in macrophage culture medium supplemented with 10% (v/v) hPL at 37 °C and 5% CO_2 for 9 h. In addition, three samples each of pure macrophage culture medium and macrophage culture medium with 10% (v/v) hPL were included. The medium was changed every hour and collected for ICP-MS measurements. Prior to measurement, media were diluted 40-fold in 0.65% nitric acid (HNO_3) solution. Ion concentrations were calculated using standard solutions (Merck KGaA, Darmstadt, Germany) of known Ca^{2+}, Mg^{2+} and P content.

5.3.5 Transmission electron microscopy imaging

Transmission electron microscopy (TEM) imaging was used to visualize mineral nanoparticles formed during sample incubation in cell culture medium supplemented with 10% (v/v) hPL. Therefore, samples were incubated in culture medium containing hPL

for 1 d. Macrophage culture medium containing 10% (v/v) hPL and pure culture medium served as references.

Prior to imaging, carbon coated electron microscopy (EM)-grids were cleaned via glow discharge for 2.5 min using a plasma cleaner ("PDC-002", Harrick Plasma, Ithaca, USA) at medium intensity. 8 µL of sample volume was then applied to the grid and left to incubate for 2 min, followed by washing the grids three times with 8 µL ultrapure water. After drying, the grids were analyzed using TEM ("Tecnai Spirit" with an Eagle CCD-camera, FEI, Hillboro, USA). Image recording was done with Serial EM[408] under low dose conditions at 120 kV, a magnification of 42000 and with an electron dose of 30 e^{-} $Å^{-2}$.

5.4 Biological Methods

5.4.1 Cell culture

With the approval of the local ethics committee of the University of Würzburg to perform all experiments, human monocytes were isolated from buffy coats purchased from the Bavarian Red Cross (Blood Donor Service, German Red Cross, Wiesentheid, Germany). All blood donors were informed and gave written consent. If not indicated otherwise, each experiment was performed in triplicates and for three independent, healthy donors.

First, peripheral blood mononuclear cells were separated using density gradient centrifugation with Pancoll (Denisity: 1077 g L^{-1}; Pan-Biotech, Aidenbach, Germany). Monocytes were then isolated by negative selection (Pan Monocyte Isolation Kit, Miltenyi Biotec, Gladbach, Germany).[409]

5.4.1.1 Direct cell culture

The scaffolds were placed in tissue culture-treated 48-well plates (Nunc, Thermo Fisher Scientific, Waltham, USA), seeded with 0.6 x 10^6 monocytes each in 100 µL macrophage culture medium supplemented with 10% (v/v) hPL, as well as 1% (v/v) Penicillin-Streptomycin (Pen-Strep; 5000 U mL^{-1}, Thermo Fisher Scientific, Waltham, USA), and incubated for 30 min in a humidified atmosphere at 37 °C and 5% CO_2 to allow cell adhesion. Thereafter, samples were each incubated in 1 mL of the previously described culture medium containing hPL and Pen-Strep for up to 7 d.

5.4.1.2 Indirect cell culture in conditioned medium

For indirect cell culture experiments, scaffolds were incubated for 24 h in the macrophage medium supplemented with 10% (v/v) hPL and 1% (v/v) Pen-Strep in a humidified atmosphere at 37 °C and 5% CO_2, and the medium was collected afterwards. Hereafter, 0.6 x 10^6 monocytes each in 100 µl macrophage culture medium were seeded on glass coverslips (d = 12mm, Hartenstein, Wuerzburg, Germany) placed in tissue culture-treated

24-well plates and cultured for 1 d in the conditioned medium in a humidified atmosphere at 37 °C and 5% CO_2.

5.4.2 Imaging

5.4.2.1 Live/Dead staining

Macrophage viability was determined after 1 d and 7 d using live/dead staining. Scaffolds were incubated in macrophage medium (without additives) containing 2 µM calcein acetoxymethyl ester (Calcein A/M) and 1 µM ethidium homodimer-1 (LIVE/DEAD Viability/Cytotoxicity Kit for mammalian cells, Thermo Fisher Scientific, Waltham, USA) for 30 min in a humidified atmosphere at 37 °C and 5% CO_2 with exclusion of light. For staining of the cross section, samples were fractured before incubation in the staining solution. Cells were visualized after 1 d with a fluorescence microscope (Axioobserver, Carl Zeiss, Jena, Germany) and after 7 d using confocal fluorescence scanning microscopy ("LEICA TCS SP8", Leica, Wetzlar, Germany).

5.4.2.2 Actin staining

To assess cell morphology, cells were fixed with 4% formalin solution for 10 min and washed in PBS buffer for 3 x 5 min. After permeabilization with 0.1% Triton X-100, washing in PBS buffer for 3 x 5 min and blocking with 1% BSA for 30 min, actin filaments were stained with phalloidin 555 (Abcam, Cambridge, UK) and nuclei with Hoechst 33342 (Merck, Darmstadt, Germany). Cells were visualized after 1 d with a fluorescence microscope and after 7 d using confocal fluorescence scanning microscopy.

5.4.2.3 Scanning electron microscopy

Prior to imaging by SEM after 1 d and 7 d of cultivation, cells were fixed on the scaffolds for 1.5 h with 6% glutaraldehyde (Merck, Darmstadt, Germany) on ice. Subsequently, samples were washed twice in PBS buffer for 30 min on ice, followed by dehydration for 2 x 30 min each in 70%, 90%, and 100% (v/v) ethanol. After incubation for 2 x 30 min in hexamethyldisilazane (Merck, Darmstadt, Germany) and drying at room temperature in air, the scaffolds were fixed on SEM specimen holders and coated with a 6 nm thick platinum layer.

To cut a viewing window into the fibrous layer formed by the METs, a Capella gallium focused ion beam (FIB, "Crossbeam 340", Zeiss, Jena, Germany) was used, setting the acceleration voltage for the gallium ions to 30 kV and using a current of 700 pA.

5.4.2.4 Extracellular DNA staining

Extracellular DNA was stained with the nucleic acid dye Sytox Green (5 mM in DMSO, Thermo Fisher Scientific, Waltham, USA), while nuclei were stained with Hoechst 33342. Images were taken using confocal fluorescence microscopy.

5.4.3 Molecular Methods

5.4.3.1 DNA and RNA isolation

After 1 d or 7 d, the scaffolds were transferred in 1 mL Trizol Reagent (Invitrogen, ThermoFisher Scientific, Waltham, USA) with two steel beads (0.5 mm diameter) and homogenized for 2 min in a bead mill at 50 Hz (TissueLyser, Qiagen, Hilden, Germany). After subsequent centrifugation for 5 min at 1200 rpm, the supernatant was transferred to a fresh tube, mixed with 0.2 mL chloroform (Merck, Darmstadt, Germany), and centrifuged for 15 min at 12000 g and 4 °C, resulting in phase separation. The aqueous phase containing RNA was collected for RNA isolation via PureLink™ RNA Mini Kit as stated in the manufacturer`s protocol (Thermo Fisher Scientfic, Waltham, USA). RNA was transcribed into cDNA using the High-Capacity cDNA Reverse Transcription Kit (Thermo Fisher Scientfic, Waltham, USA) according to the user guide provided by the manufacturer. DNA was isolated from the interphase/organic layer according to the manufacturer‘s protocol (Trizol Reagent, ThermoFisher Scientific, Waltham, USA). RNA and DNA quantity and quality was measured using a plate reader (Tecan, Männerdorf, Switzerland)
The gene expression levels of macrophages were analyzed via quantitative real-time PCR (qPCR) (StepOnePlus; Thermo Fisher Scientific) with Sybr Select Mastermix (Thermo Fisher Scientific) as described previously.[407,409] The specific primers used are listed in Table 7. RPS27A served as house-keeping gene for normalization.[409] As a reference sample, 1 d cultured macrophages on reference α-TCP were used.

Table 7. Primer sequences.

Name	Sequence 5’ à 3’	Annealing temperature [°C]	Fragment size [bp]
RPS27A*		61	141
Forward	5’-TCGTGGTGGTGCTAAGAAAA-3’		
Reverse	5’-TCTCGACGAAGGCGACTAAT-3’		
IL-8		61	113
Forward	5’-CATACTCCAAACCTTTCCACCC-3’		
Reverse	5’-CTCTGCACCCAGTTTTCCTTG-3’		
IL-1β		61	120
Forward	5’-GACCTGAGCACCTTCTTTCCC-3’		
Reverse	5’-GCACATAAGCCTCGTTATCCC-3’		
CD206		61	156
Forward	5’-TCCAAACGCCTTCATTTGCC-3’		
Reverse	5’-GCTTTTCGTGCCTCTTGCC-3’		
IL-10		61	130
Forward	5' CTTTAAGGGTTACCTGGGTTGC '3		
Reverse	5' TCACATGCGCCTTGACT '3		

* Housekeeping gene

5.4.3.2 ELISA - cytokine quantification

Cytokine release of monocytes/macrophages was tested via Single Analyte Elisarray Kits (Qiagen, Hilden, Germany) after 1 d and 7 d of cultivation. The production of IL-1β, IL-6, IL-8, IL-10, and TNF-α was analyzed in supernatants according to the manufacturer's protocol. The absorbance was measured on a plate reader (Tecan, Männedorf, Switzerland) at 450 nm and corrected by the absorbance at the reference wavelength of 570 nm. The release was normalized to the corresponding determined DNA amount.[409] (Figure 32)

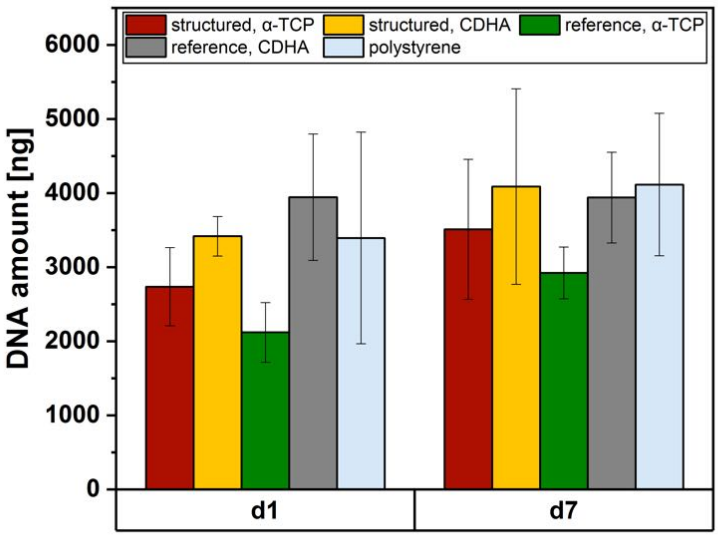

Figure 32. DNA amount after 1 d and 7 d of cultivation on all sample types and polystyrene.

5.4.4 Ion quantification in macrophage culture medium during cultivation

Ion concentrations (Ca^{2+}, Mg^{2+} and P) in the macrophage culture medium were quantified by ICP-MS measurements as described previously and analyzed after 1 d and 7 d. For measurements without cells, three samples per group were incubated in 1 mL of macrophage culture medium supplemented with 10% (v/v) hPL and 1% (v/v) Pen-Strep in a humidified atmosphere at 37 °C and 5% CO_2.

5.4.5 Statistics

The software “Sigmaplot” (Version 12.5) was used to pairwise compare ion concentrations in the medium at different time points and in the absence or presence of cells using t-test analysis.

Further determination of the statistical significance was performed by the two-way analysis of variance (ANOVA) using the Statistica 13 software (Statsoft, Hamburg, Germany). Results were considered to be significantly different at a p-value below 0.05. Data were tested for normality and homogeneity of variance.[409]

5.5 Results

5.5.1 Phase composition

The phase transformation of α-TCP induced by the hydrothermal treatment of the samples was analyzed by XRD measurements. If the samples, i.e., both the structured and the reference samples, were not treated further after sintering, they consisted entirely of the originally used α-TCP phase. (Figure 33 a, b) For all sample types, also intensity maxima which appeared due to the plasticine on which the samples were fixed during the measurement, were observed in the XRD spectra. (Figure 33 a and Figure 34 a) Due to hydrothermal treatment in Na_2HPO_4 solution, the main phase of the scaffolds was CDHA, while about 25% α-TCP was still present in the freeze-structured samples and 37% in the reference discs, respectively (Figure 33 b). In the following, ice-templated specimens will be referred to as “structured, α-TCP” or “structured, CDHA”, based on their respective main phases that occur. The references are analogously denoted by “reference, α-TCP” and “reference, CDHA”.
Washing the samples for five days in preparation for the macrophage culture experiments did not further transform or alter the phase composition of the samples. (Figure 34 a, b)

5.5.2 Sample morphology

5.5.2.1 SEM

The aligned pore structure of the freeze-structured samples as well as the various morphologies of all sample types were revealed by SEM imaging of the sample surfaces and cross sections. (Figure 33 c) Lamellae in the structured, α-TCP samples exhibited a smooth surface which was caused by the sintering process. (Figure 33 c.1) Due to the hydrothermal treatment and the resulting phase transformation, fine CDHA plates and needles protruding into the pores were found in the structured, CDHA samples. (Figure 33 c.2) Due to the lamellar structure that is characteristic for the ice-templated samples, the morphology of the sample surface resembled that of the cross section. (Figure 33 c.5, c.6)

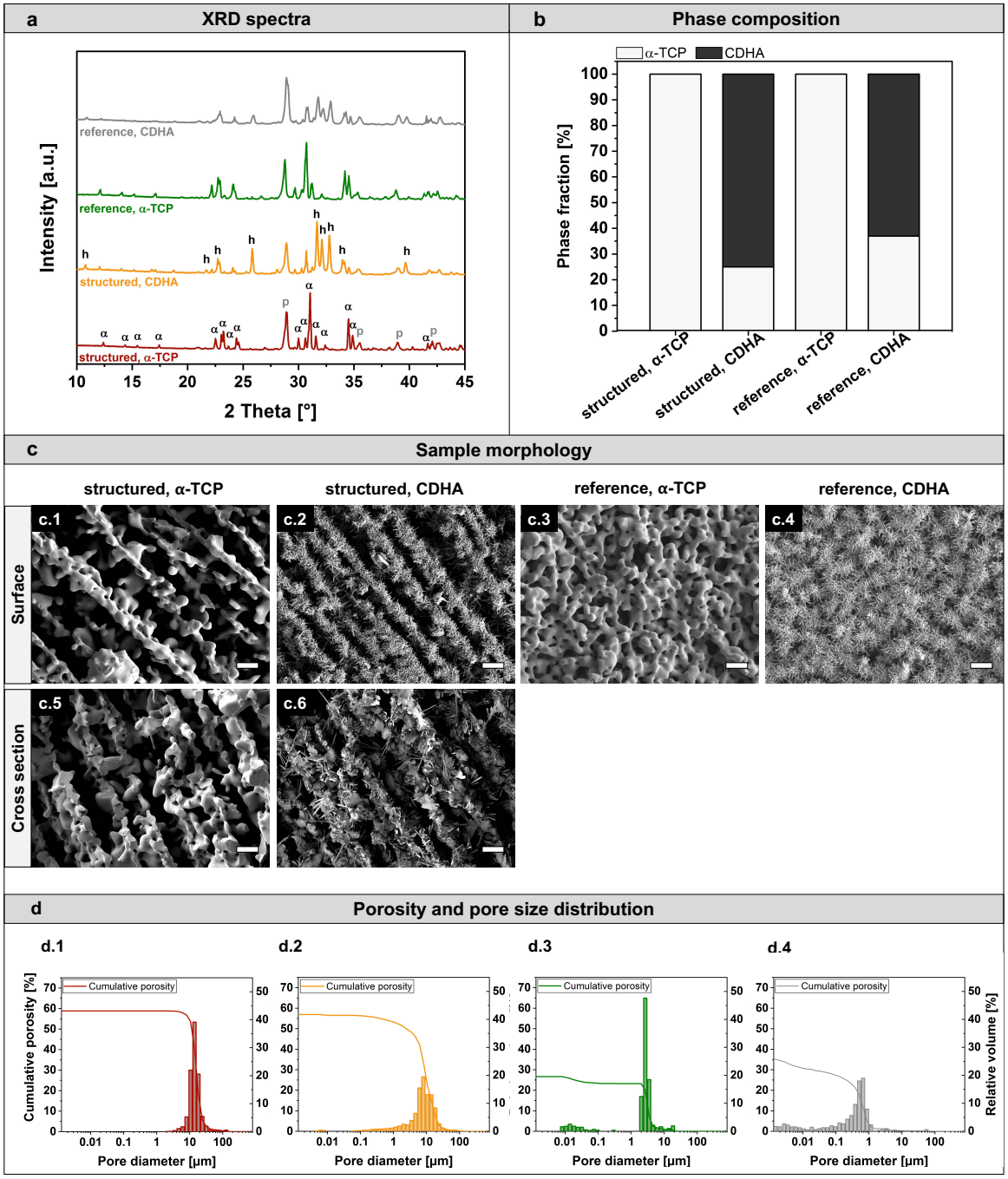

Figure 33. Phase composition, morphology, porosity and pore size distribution of samples used for the *in vitro* experiments. a) XRD spectra of all sample types. Spectra of the structured, α-TCP samples and structured, CDHA samples are shown in red and orange, while those of the reference, α-TCP and reference, CDHA discs are presented in green and gray, respectively. Intensity maxima for α-TCP (α), CDHA (h), and plasticine (p), on which the samples were fixed during the measurement, are indicated. b) Phase composition. Hydrothermal treatment led to a phase transformation of α-TCP to CDHA. c) SEM imaging. Ice-templating led to the formation of anisotropic, aligned pores, which were separated by lamellae. c.1) Surface of structured, α-TCP samples: sintering resulted in a smooth lamellar structure. c.2) Surface of structured, CDHA samples: due to the hydrothermal treatment and the resulting phase conversion, fine CDHA plates and needles protruded into the pores. c.3) Surface of reference, α-TCP samples: since the discs were prepared without any ice-templating step, an isotropic pore structure was observed. The surface showed a smooth morphology. c.4) Surface of reference, CDHA samples: CDHA needles appeared on the surface of the discs. Due to the lamellar pore structure, the SEM images of the cross section resembled those of the surface of structured, α-TCP (c.5) and structured, CDHA (c.6) samples. Scale bars are 20 µm. d) Porosity and pore size distribution. d.1) Measurements of the pore size distribution showed a monomodal, narrow pore size distribution with a maximum of 14 µm for the structured, α-TCP samples. d.2) Due to the needles and plates formed during the phase conversion, the pore size distribution of structured, CDHA scaffolds was widened, and the maximum shifted to 8 µm. Wider pore size distributions as well as considerably smaller pores in the nanometer range were measured for both the reference, α-TCP (d.3) and the reference, CDHA (d.4) samples.

Since the flat reference discs were prepared without using any ice-templating process, only their surfaces were examined. Here, a smooth surface of the reference, α-TCP samples was observed (Figure 33 c.3). After phase transformation, the reference, CDHA samples showed a spiky appearing surface, since CDHA appeared in the form of fine needles (Figure 33 c.4). Again, no changes in morphology were detected after washing the samples in PBS buffer for five days prior to cell culture experiments. (Figure 34 c)

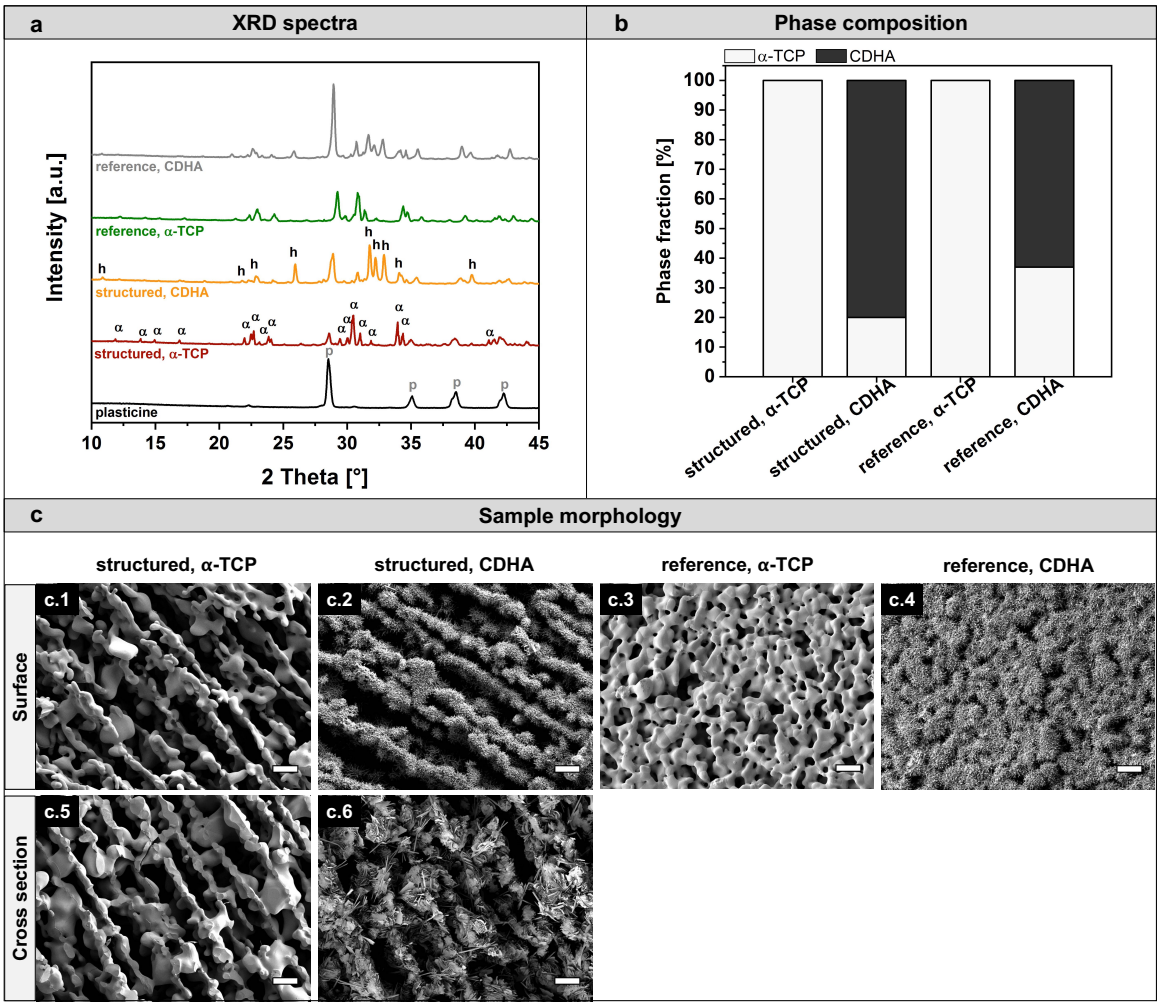

Figure 34. Phase composition and sample morphology after washing the samples for 5 d in calcium and magnesium containing PBS buffer. a) Spectra of the structured, α-TCP samples and structured, CDHA samples are shown in red and orange, while those of the reference, α-TCP and reference, CDHA discs are presented in green and gray, respectively. The spectrum measured for plasticine, which was used for sample fixation during the measurements, is shown in black. Intensity maxima for α-TCP (α), CDHA (h), and plasticine (p) are indicated. b) Phase composition of all sample types. Hydrothermal treatment in Na_2HPO_4 solution led to a phase transformation of α-TCP to CDHA. c) SEM imaging of all sample types. c.1) Surface of structured, α-TCP samples. The smooth lamellar structure caused by the sintering process was not affected by the washing step. Also, the surfaces of the structured, CDHA (c.2), reference, α-TCP (c.3), and reference, CDHA (c.4) samples did not change due to washing. The same applies to the cross sections of the structured, α-TCP (c.5) and structured, CDHA (c.6) samples. Scale bars are 20 µm.

5.5.2.2 Porosity and pore size distribution

The influence of hydrothermal treatment on pore size distribution, relative volume and sample porosity was investigated using mercury porosimetry (Figure 33 d). For the ice-templated samples, a monomodal pore size distribution with a maximum of about 14 µm

for the structured, α-TCP samples (Figure 33 d.1) and 8 µm for the structured, CDHA samples (Figure 33 d.2) was revealed. The pore size distribution was relatively narrow in the structured, α-TCP samples due to the smooth lamella surfaces. Due to thin CDHA needles and plates appearing in the structured, CDHA specimens, smaller pores were formed, resulting in a broadening of the pore size distribution spectrum towards lower values. Both ice-templated sample types were highly porous, with a porosity of nearly 59% (structured, α-TCP) and 57% (structured, CDHA), respectively.

Broader pore size distributions were measured for both the α-TCP and CDHA reference samples. (Figure 33 d.3, d.4) In particular, small pore sizes in the nanometer range were detected. Due to the CDHA needles formed throughout the sample, smaller pores were found in the reference, CDHA samples compared to the reference, α-TCP samples. Moreover, the distribution maximum was observed at lower pore sizes than for the structured samples. The overall porosity of about 27% for the reference, α-TCP and 35% for the reference, CDHA discs was distinctly lower than for the structured samples.

5.5.3 Ion release and absorption of samples incubated in cell culture medium

Since CaP scaffolds are known to cause ionic changes in cell culture medium during incubation[410], concentrations of calcium, magnesium, and phosphorous in the medium during the first 9 h of incubation were measured. The cumulative ion absorption or release occurring with respect to ion concentrations present in pure cell culture medium with 10% (v/v) hPL is depicted in Figure 35 a.

Magnesium ions were absorbed by all sample types within the first 9 h, with the structured, CDHA samples showing the highest uptake, followed by the structured, α-TCP samples. The reference plates showed the lowest absorption rate. (Figure 35 a.1)

A different behavior was observed for calcium ions (Figure 35 a.2). Here, a marked ion release into the culture medium was found for the structured, α-TCP samples. Structured, CDHA as well as reference, α-TCP samples showed only a low calcium release, while slight ion absorption was detected for the reference, CDHA samples.

Phosphorous release into the medium was higher for the ice-templated samples than for the reference discs. (Figure 35 a.3)

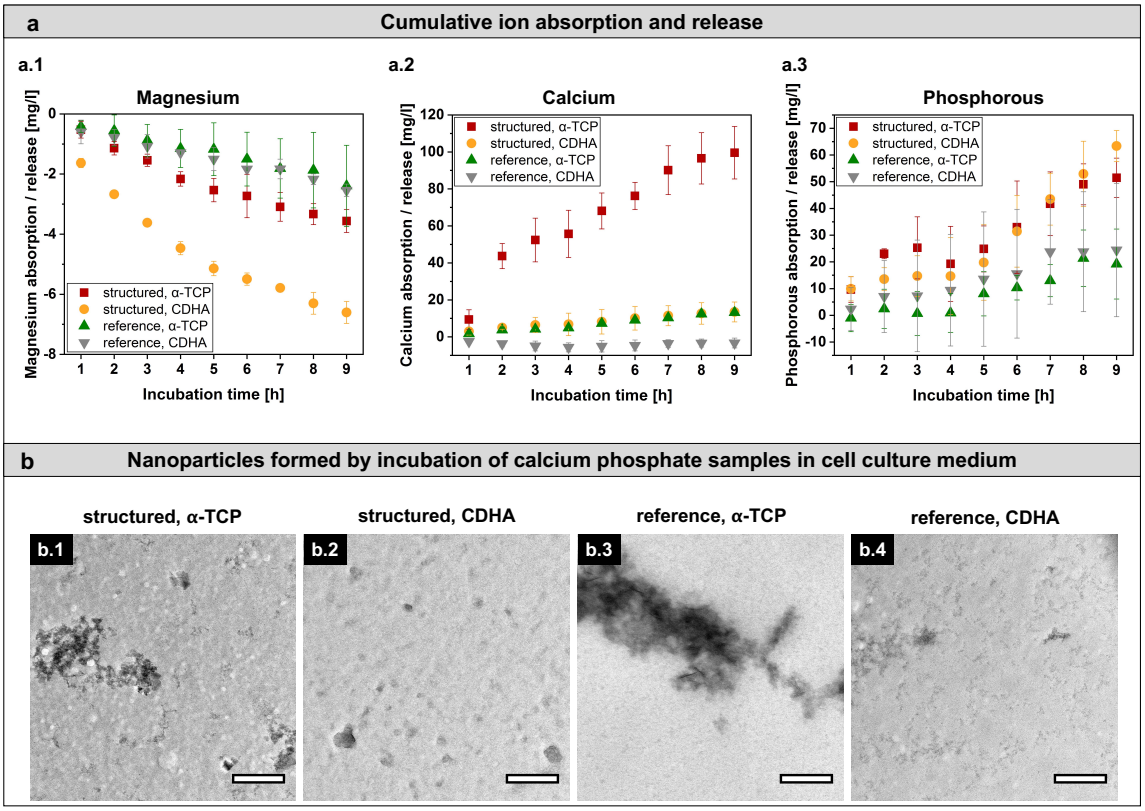

Figure 35. ICP-MS measurements of conditioned macrophage culture medium and TEM imaging of nanoparticles found in conditioned culture medium. a) Cumulative magnesium (a.1), calcium (a.2) and phosphorous (a.3) absorption and release of samples incubated in cell culture medium containing 10% (v/v) hPL. b) TEM imaging of culture medium supplemented with 10% (v/v) hPL, in which structured, α-TCP (b.1), structured, CDHA (b.2), reference, α-TCP (b.3) and reference, CDHA (b.4) samples were incubated for 24 h. Particles larger than 100 nm were detected in the medium of structured, α-TCP (b.1) and reference, α-TCP (b.3) samples. Scale bars are 200 nm.

5.5.4 Nanoparticle formation in conditioned cell culture medium supplemented with 10% (v/v) hPL

Mineral nanoparticles are formed in serum containing cell culture medium. This formation is accelerated by the addition of calcium and phosphate ions, which also influence particle size and morphology.[411,412]

As shown by the ICP-MS measurements (Figure 35 a), samples used for macrophage culture experiments released calcium and phosphate ions when incubated in culture medium supplemented with hPL. The presence of nanoparticles in the cell culture medium in which the samples were incubated for 24 h was confirmed by TEM imaging. (Figure 35 b) Nanoparticles with sizes of more than 100 nm were detected in conditioned medium of both the structured, α-TCP (Figure 35 b.1) and reference, α-TCP (Figure 35 b.3) samples. In contrast, no or only small particles were found in the media of the CDHA samples. (Figure 35 b.2, b.4) In culture medium containing 10% (v/v) hPL and pure cell culture medium (Figure 36), used for comparison, no nanoparticles were found.

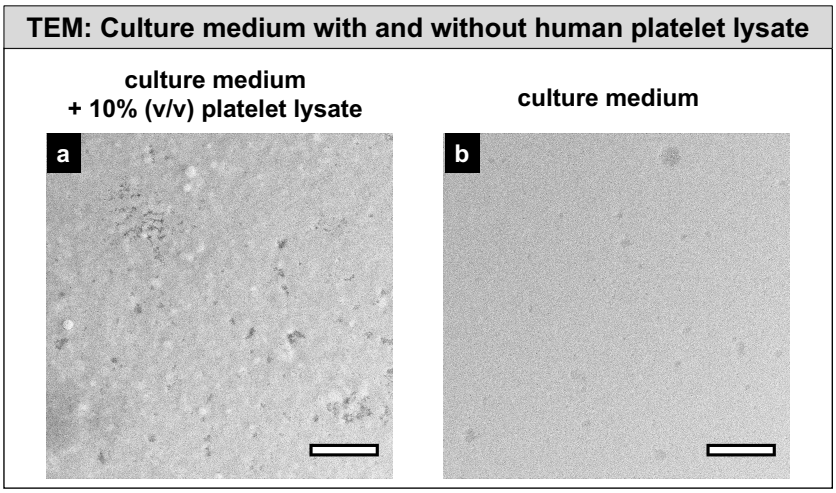

Figure 36. TEM imaging of culture medium containing 10% (v/v) hPL and pure culture medium. No mineral particles were found in either a) lysate-containing medium or b) pure culture medium. Scale bars are 200 nm.

5.5.5 Scaffold influence on macrophage morphology

5.5.5.1 Macrophage viability and morphology

Human monocyte/macrophage viability was examined after 1 d and 7 d using live/dead staining. (Figure 37 a and Figure 38 a) Cells showed high viability on all scaffolds both on the surfaces and in the cross sections. Viable cells could be detected inside the structured, α-TCP scaffolds, more than 100 µm from the sample surface, suggesting sufficient media exchange and nutrient supply during cultivation. This was also observed for the structured, CDHA samples, although macrophages were not detectable as far inside the sample.

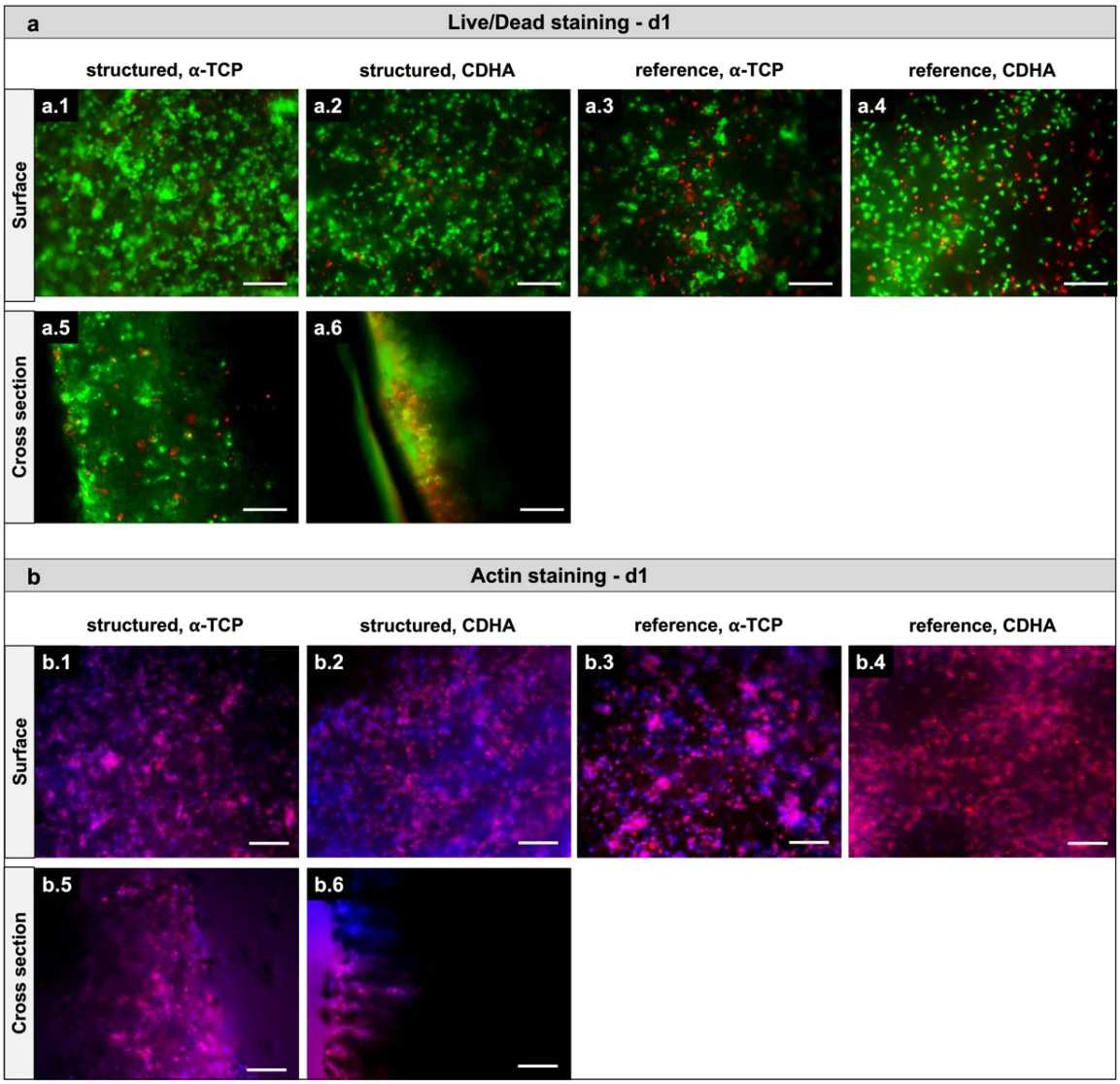

Figure 37. Viability and morphology of macrophages seeded on structured and reference samples after 1 d of cultivation. a) Live/Dead staining showed high cell viability (alive cells are stained in green, dead cells in red) on both structured, α-TCP (a.1) and structured, CDHA (a.2) scaffolds as well as on reference, α-TCP (a.3) and reference, CDHA (a.4) discs. The cross section of the structured, α-TCP (a.5) samples showed viable macrophages deeper in the sample than in the structured, CDHA (a.6) scaffolds. b) Assessment of cell morphology by actin staining (actin filaments are stained in red (phalloidin), nuclei in blue (Hoechst)) revealed that macrophages on the structured, α-TCP (b.1) and the reference, α-TCP (b.3) samples exhibited a roundish and agglomerated shape. This was not found on the structured, CDHA (b.2) or reference, CDHA (b.4) samples. Again, cells were detected in the cross sections (b.5, b.6) of both sample types. Scale bars are 100 µm.

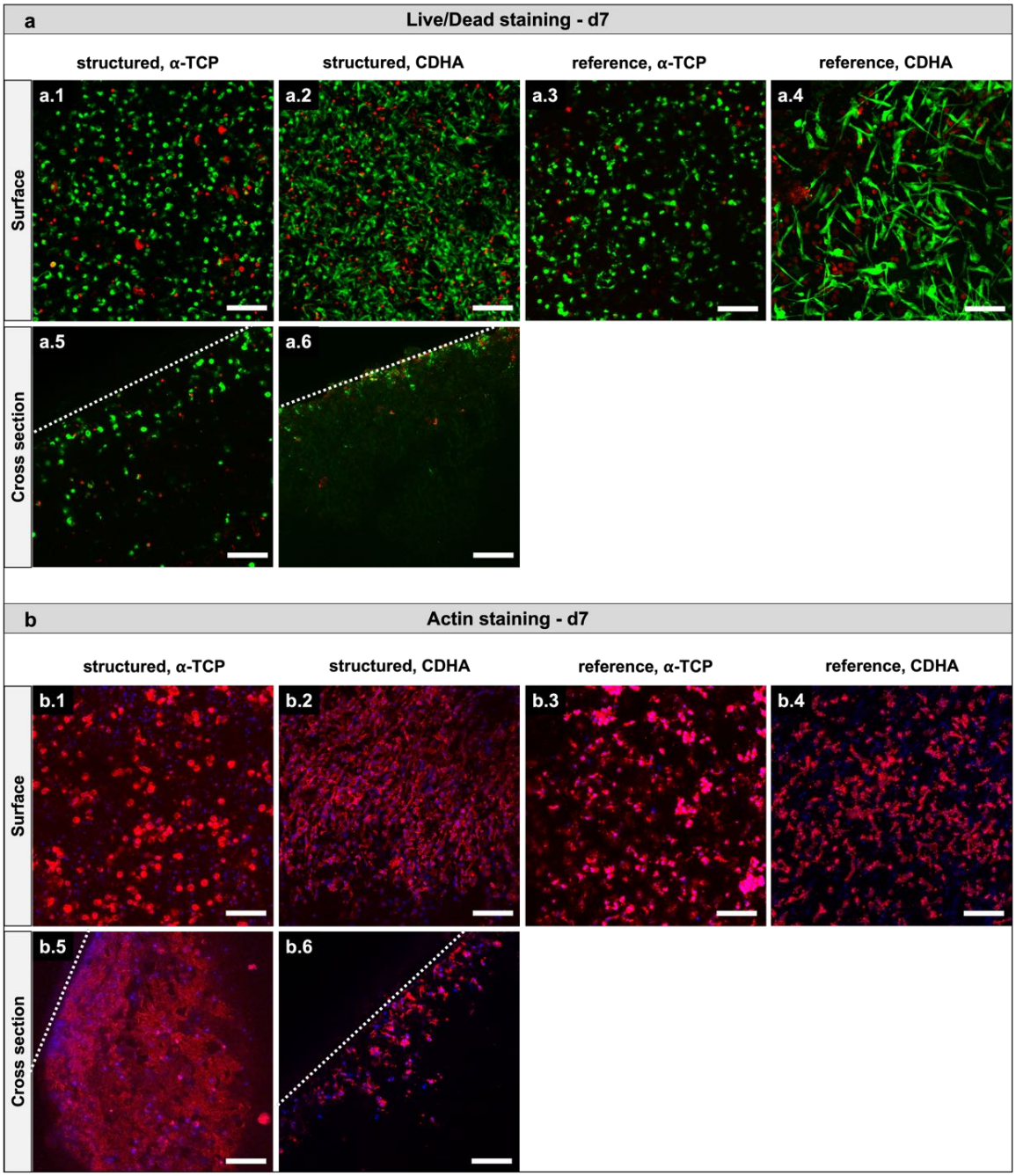

Figure 38. Viability and morphology of macrophages seeded on structured and reference samples after 7 d of cultivation. a) Live/Dead staining showed high cell viability (alive cells are stained in green, dead cells in red) on both (a.1) structured, α-TCP and (a.2) structured, CDHA scaffolds as well as on (a.3) reference, α-TCP and (a.4) reference, CDHA discs. The cross section of the structured, α-TCP (a.5) samples showed viable macrophages deeper in the sample than in the structured, CDHA (a.6) scaffolds. b) Assessment of cell morphology by actin staining (actin filaments are stained in red (phalloidin), nuclei in blue (Hoechst)) revealed that macrophages on the structured, α-TCP (b.1) samples exhibited a roundish shape, whereas they appeared to align elongated towards the lamellar structure on the surface of the structured, CDHA (b.2) samples. Again, cells were detected in the (b.5, b.6) cross section of both sample types. Roundish cell agglomerates were found on the reference, α-TCP (b.3) samples, while macrophages on the reference, CDHA (b.4) samples had an elongated shape. Scale bars are 100 µm.

To assess cell morphology, actin staining and SEM imaging were performed after 1 d and 7 d of cultivation.

Actin staining (Figure 37 b and Figure 38 b) revealed that the cells on the α-TCP samples appeared roundish. Elongated macrophages, however, were clearly visible on the surface of both the structured, CDHA samples and the reference, CDHA samples. Examination of the sample cross section also showed that cells were present inside both structured sample types.

As already observed in the actin staining, SEM imaging of the sample cross section revealed macrophages inside the structured samples. However, after 7 d, only a few macrophages were found in the structured, α-TCP scaffolds. (Figure 39)

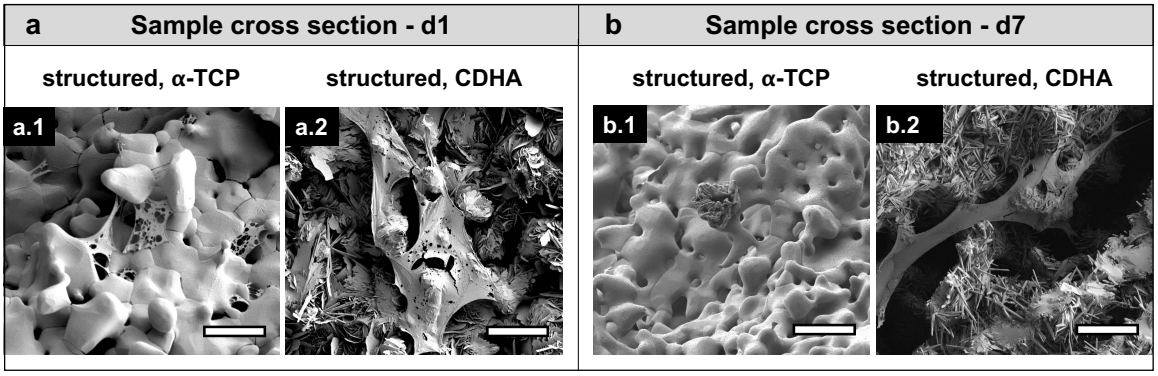

Figure 39. SEM imaging of the sample cross section after 1 d and 7 d of cultivation. a) After 1 d, macrophages inside the structured, α-TCP (a.1) and structured, CDHA (a.2) scaffolds were observed. b) Only few macrophages were found inside the structured, α-TCP scaffolds (b.1), while cells stretching over well more than 20 µm were observed in the structured, CDHA (b.2) samples after 7 d. Scale bars are 20 µm.

In SEM surface imaging, net-like structures and carpets, identified as monocyte/macrophage extracellular traps (METs), which were formed on both α-TCP sample types after 1 d (Figure 40 a) and still present after 7 d (Figure 41), were observed. While on the reference, CDHA samples no METs were found, smaller areas covered with METs were visible on the structured, CDHA samples after 1 d. However, after 7 d, they could no longer be detected.

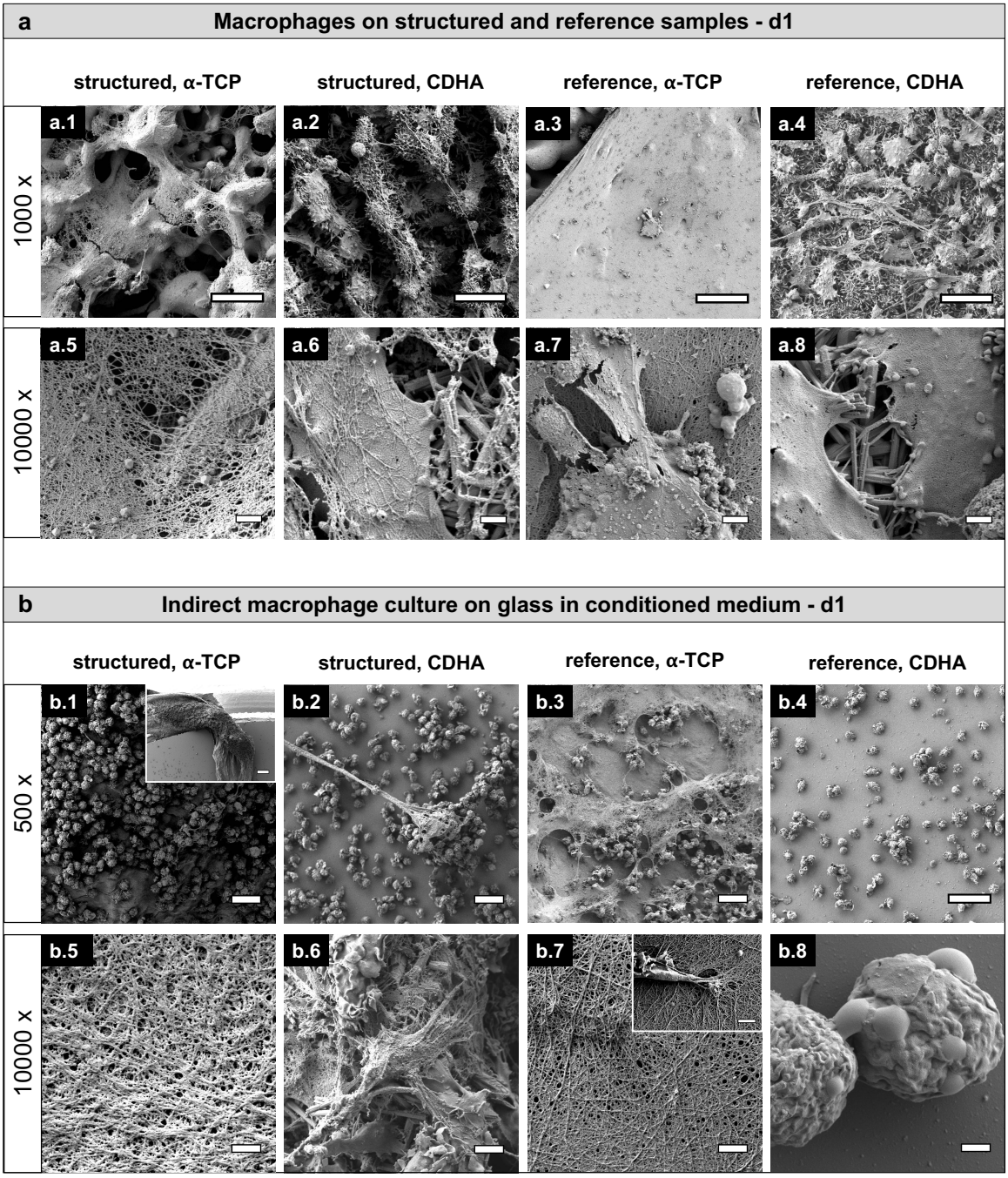

Figure 40. SEM imaging of macrophages in direct and indirect culture after 1 d. a) Macrophages on structured and reference samples. METs were found on the surface of the α-TCP samples. The MET carpet was less pronounced on the structured, α-TCP (a.1, a.5) samples than on the reference, α-TCP samples (a.3, a.7). Smaller areas with METs were also observed on the surface of the structured, CDHA samples (a.2, a.6). On the reference, CDHA samples (a.4, a.8), no METs were found. The top and lower row show surface images at 1000 x (a-1-a.4) and 10000 x (a.5-a.8) magnification, respectively. Scale bars are 20 µm (1000 x magnification) and 1 µm (10000 x magnification). b) Indirect macrophage culture on glass in conditioned medium for 1 d. Macrophages formed METs when cultured in conditioned medium of α-TCP samples (b.1, b.3, b.5, b.7). This was not found for the CDHA samples (b.2, b.4, b.6, b.8). The top and lower row show images at 500 x (b.1-b.4) and 10000 x (b.5-b.8) magnification, respectively. Scale bars are 20 µm (500 x magnification) and 1 µm (10000 x magnification). Inset in b.1 (50 x magnification), scale bar: 200 µm; inset in b.7 (15000 x magnification), scale bar: 1 µm.

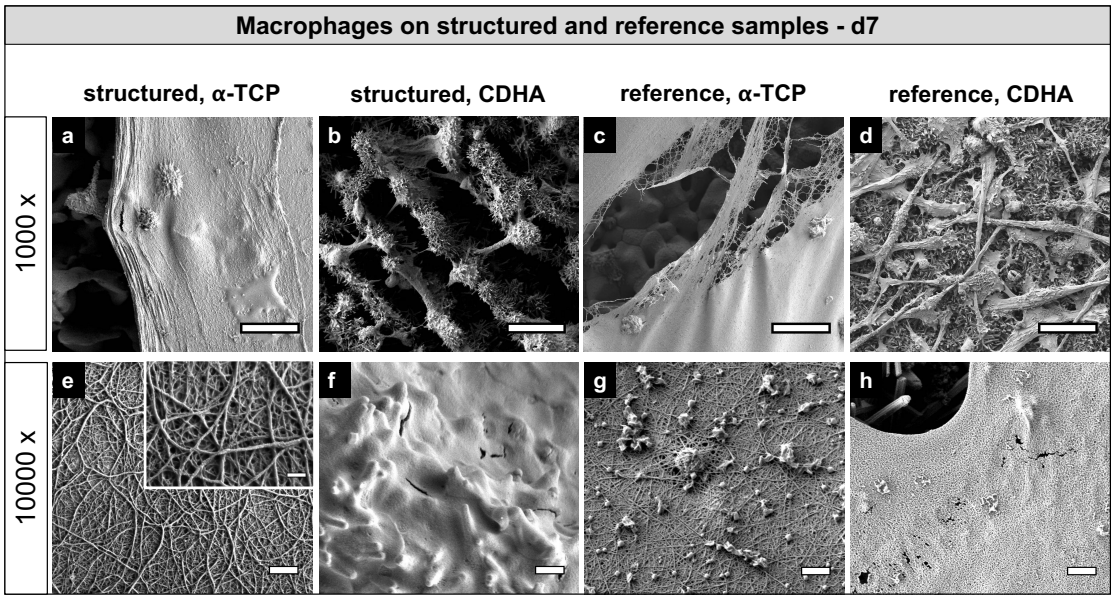

Figure 41. Macrophages on structured and reference samples after 7 d. Morphologically, macrophages resembled those imaged after 1 d of cultivation. A distinct MET formation was observed on the surface of α-TCP scaffolds (a,c,e,g). No METs were found on both the structured, CDHA samples (b, f) and the reference, CDHA samples (d,h). Scale bars are 20 µm in the upper row (1000 x magnification) and 1 µm in the lower row (10000 x magnification). Inset in (e) (50000 x magnification), scale bar: 100 nm.

Magnification of the carpets on α-TCP samples showed that METs were formed from disordered fibers that were only a few nanometers thick, typical for DNA, released by macrophages. The carpet was more pronounced on the reference, α-TCP discs than on the structured samples, covering large areas of the surface of the structured, α-TCP samples and the entire surface of the reference, α-TCP discs. (Figure 40 a, Figure 41 and Figure 42)

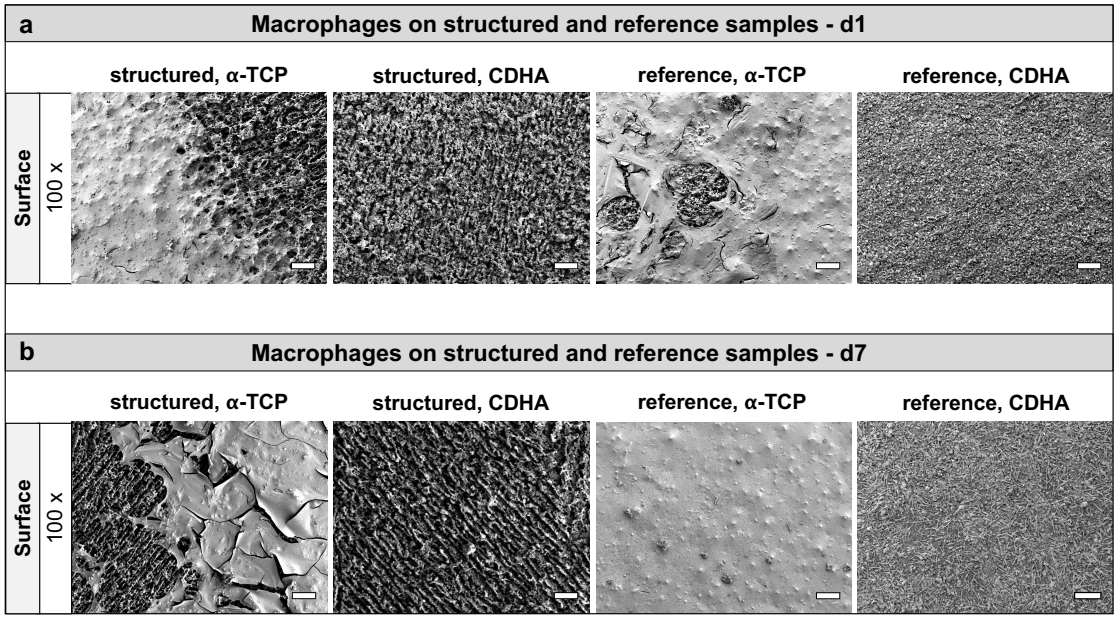

Figure 42. SEM imaging after 1 d and 7 d of direct macrophage culture on the samples at 100 x magnification. a) Already after 1 d, a pronounced formation of METs was observed on α-TCP samples, whereas the carpet on the structured, α-TCP samples did not cover the complete sample surface as it was the case for the reference, α-TCP samples. No carpet was found on the CDHA samples. b) The same was observed after 7 d of macrophage cultivation. Scale bars are 100 µm.

These pronounced METs were not only found on the surfaces of the reference, α-TCP samples, but also spread to the side surfaces of the discs until after 7 d these were also completely covered. (Figure 43)

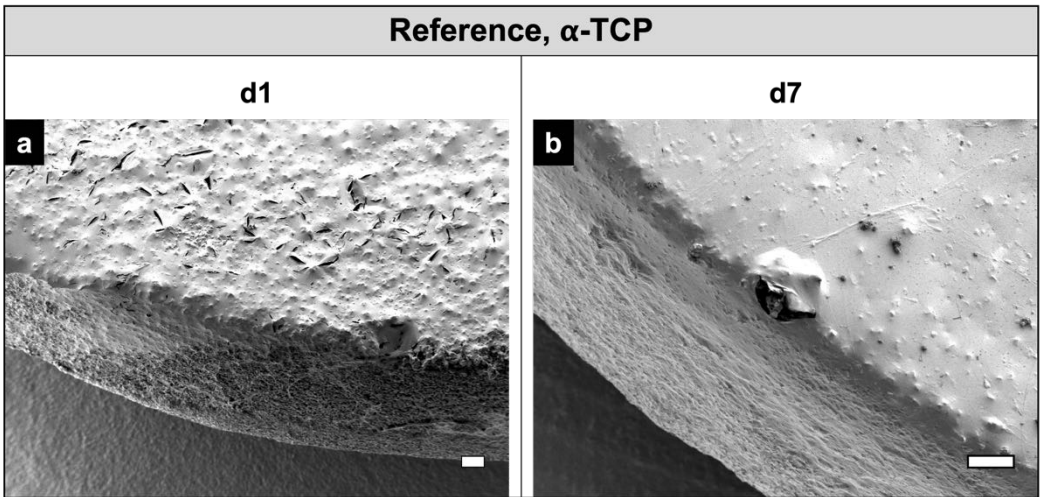

Figure 43. METs on reference, α-TCP discs. a) After 1 d, METs had spread from the surface to the side surfaces. b) These were completely covered after 7 d. Scale bars are 100µm

To further investigate the properties, in particular the thickness, of the MET-carpet, a hole was cut in a carpet that had developed after 1d of direct culture on a reference, α-TCP sample using a focused ion beam (FIB). SEM images revealed that the layer formed by the fibers was about 150 nm thick and that macrophages were located directly beneath it. (Figure 44)

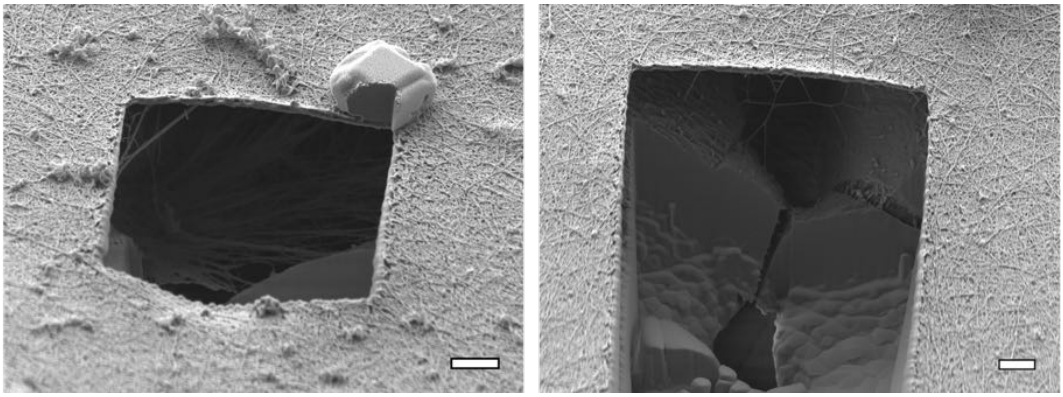

Figure 44. Thickness of a MET-carpet on a reference, α-TCP sample after 1 d. The layer formed by the fibers was only about 150 nm thick, while the cells releasing those fibers were directly underneath it. Scale bars are 1 µm.

To obtain information on the cause of the MET formation and whether this occurred only in direct cell culture, monocytes were cultured without direct sample contact on glass plates in conditioned medium of CaP samples for 1 d. In this way, the influence of nanoparticles formed in conditioned cell culture medium supplemented with 10% (v/v) hPL (Figure 35 b) on MET formation was investigated. SEM images confirmed that monocytes/macrophages cultured in α-TCP conditioned medium formed a MET-carpet on

the glass plates after only 1 d. (Figure 40 b) In contrast, no MET formation was observed on the glass plates on which monocytes/macrophages were cultured in conditioned medium from structured, CDHA samples. Occasionally, METs appeared when, due to the experimental procedure, cement fragments were present on the glass plates. (Figure 40 b.2, b.6) The morphology of the other macrophages resembled that of cells cultured in conditioned medium from reference, CDHA samples, or non-conditioned medium containing hPL. (Figure 45) Thus, the presence of nanoparticles in the cell culture medium triggered the formation of METs.

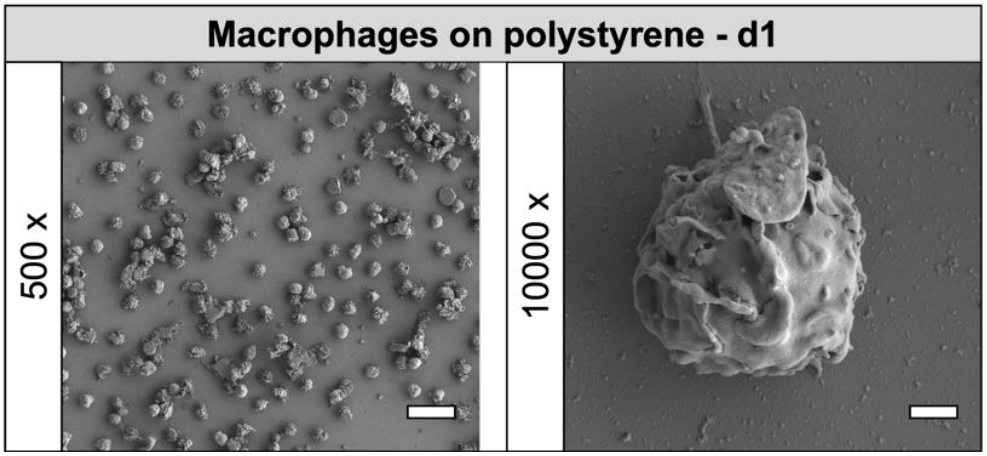

Figure 45. SEM imaging of macrophages cultured in macrophage culture medium containing 10% (v/v) hPL. Scale bars are 20 µm (500 x magnification) and 1 µm (10000 x magnification).

The occurrence of METs was furthermore confirmed by extracellular DNA staining with the nucleic acid dye Sytox Green, while nuclei were stained with Hoechst. Already after 1 d, METs were identified on the α-TCP samples as well as on glass plates during indirect culture. (Figure 46)

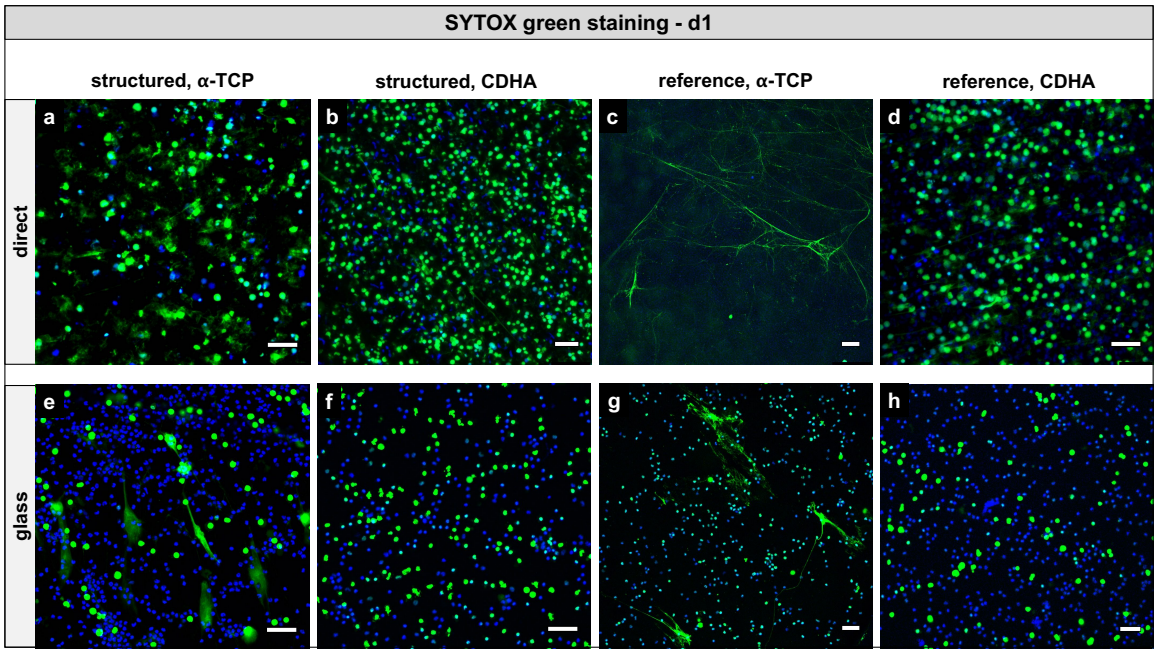

Figure 46. SYTOX green staining of extracellular DNA after 1 d. Nuclei were stained in blue (Hoechst). Macrophages were cultured in direct sample contact (a-d) and on glass plates in conditioned macrophage culture medium (e-h). MET formation was observed for the α-TCP samples in both direct sample contact (a,c) and in indirect culture (e g). Slight MET formation was also observed on the structured, CDHA (b) samples, while no METs were found on the surfaces of reference, CDHA (d) samples or in conditioned medium of structured, CDHA (f) and reference, CDHA (h) samples. Scale bars are 50 µm.

Images after 7 d revealed that METs were formed on both the structured, α-TCP and reference, α-TCP samples, with the formation of METs being most pronounced on the latter ones and reaching across the entire sample. (Figure 47) However, MET carpets detached easily during preparation and subsequent imaging, making it challenging to visualize METs in some cases. (Figure 47 a) To a much lesser extent than on the α-TCP samples, MET formation also occurred on the structured, CDHA scaffolds. No extracellular DNA could be stained on the reference, CDHA samples, indicating the non-existence of METs, in consistency with the SEM images.

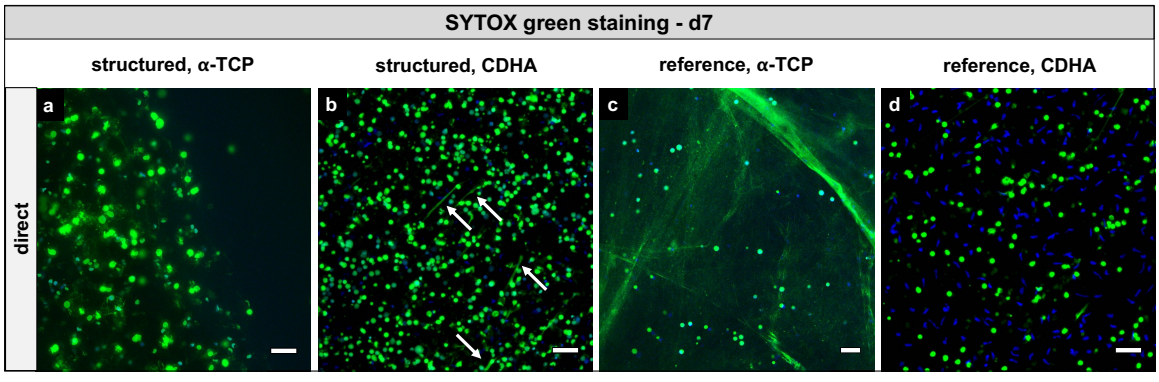

Figure 47. SYTOX green staining of extracellular DNA after 7 d. Nuclei were stained in blue (Hoechst). Cell carpets adhered poorly to the sample surface, resulting in difficulties in visualizing METs on the surface of structured, α-TCP samples (a). Pronounced MET formation was observed on the reference, α-TCP samples (c), while slight MET formation occurred on the structured, CDHA scaffolds (b, white arrows). No METs were found on the reference, CDHA samples (d). Scale bars are 50 µm.

5.5.5.2 With vs. without human platelet lysate

Since mineral nanoparticles were formed in the cell culture medium only in the presence of serum, the influence of the addition of hPL (and thus nanoparticle development) on MET formation was investigated in two exemplary experiments. For this, macrophages were cultured in conditioned medium on glass plates with and without the addition of hPL.

In the "with human platelet lysate" experiment, a reference, α-TCP sample was first incubated for 1 d in medium without hPL. The next day, human monocytes were seeded on a glass plate and cultured in the conditioned reference, α-TCP medium and 10% (v/v) hPL was freshly added. Therefore, the ions released into the medium during sample incubation allowed nanoparticles to be subsequently formed. Monocytes were then cultured for 1 d. MET formation was observed (Figure 48), although the carpet was not as pronounced as in the samples in which the lysate had already been added for 1 d during sample incubation. (Figure 40 b.3, b.7)

For the "without serum" sample, monocytes were seeded on glass and macrophage culture medium supplemented with 10% (v/v) hPL was added to allow cell adhesion. The next day, this medium was removed and replaced with conditioned reference, α-TCP medium without hPL (the sample was incubated in the medium for 24 h), so that no nanoparticles were formed and the formation of METs was not expected to be triggered. This was confirmed by SEM imaging. (Figure 48)

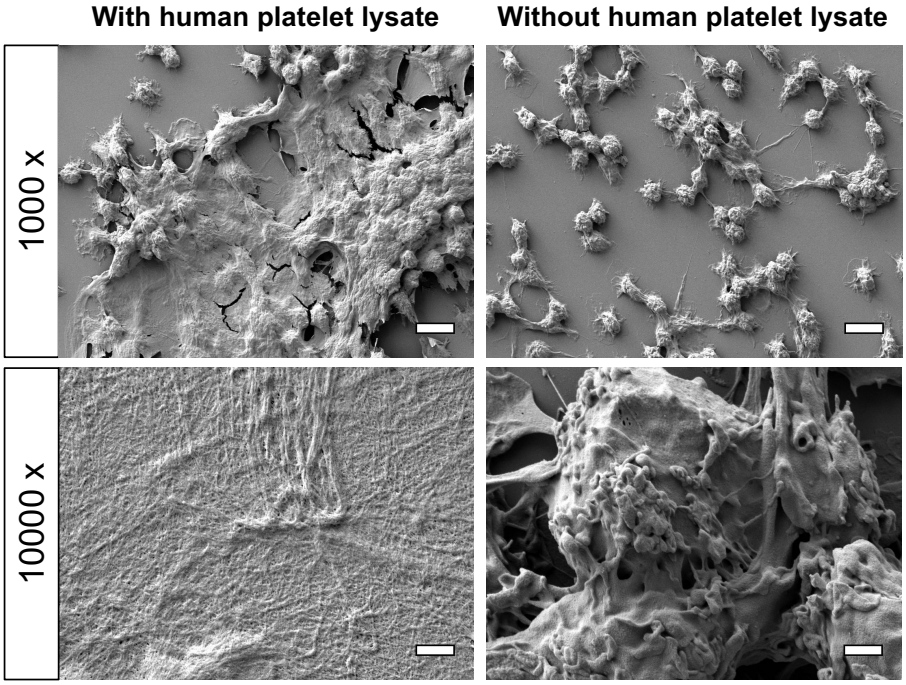

Figure 48. Effect of hPL in conditioned culture medium on the formation of METs. Macrophages were cultured on glass plates. To prepare the conditioned culture medium, reference, α-TCP samples were incubated for 1 d in medium with or without hPL. If hPL was added to the macrophage culture medium during sample incubation, the formation of METs was triggered (left column). In contrast, no METs were formed if the conditioned medium was not supplemented with hPL (right column). Scale bars are 10 µm in the upper and 1 µm in the lower row.

5.5.6 Mg^{2+}, Ca^{2+}, PO_4^{3-} concentrations in cell culture medium during cultivation

To determine ion concentrations in the macrophage culture medium during the cultivation period, ICP-MS measurements were performed (Figure 49). Since it is known that ceramic or cement samples interact with the cell culture medium, i.e., absorb Mg^{2+}, Ca^{2+} or PO_4^{3-} ions from or release them into the medium[410], samples with and without macrophage seeding were compared. From this, conclusions on the influence of macrophages on ion concentration changes in the culture medium could be drawn.

Interestingly, macrophages on the structured, α-TCP samples caused a significant decrease in Mg^{2+} and Ca^{2+} concentrations in the medium already after 1 d and even more pronounced after 7 d (Figure 49 a, b). Here, only a very small amount of magnesium was left in the medium (Figure 49 a) and also the phosphorus content was significantly reduced (Figure 49 c). However, this was not observed in the reference, α-TCP samples, on which, as on the structured, α-TCP scaffolds, METs were released by the macrophages. Here, only a significant decrease in magnesium concentration was measured after 1 d of cultivation.

For the structured, CDHA samples, seeding with macrophages had no significant effect on the ion concentration in the medium. A different effect was seen for the reference, CDHA samples. The magnesium concentration increased significantly due to the presence of macrophages both after 1 d and after 7 d, while a significant calcium decrease was measured.

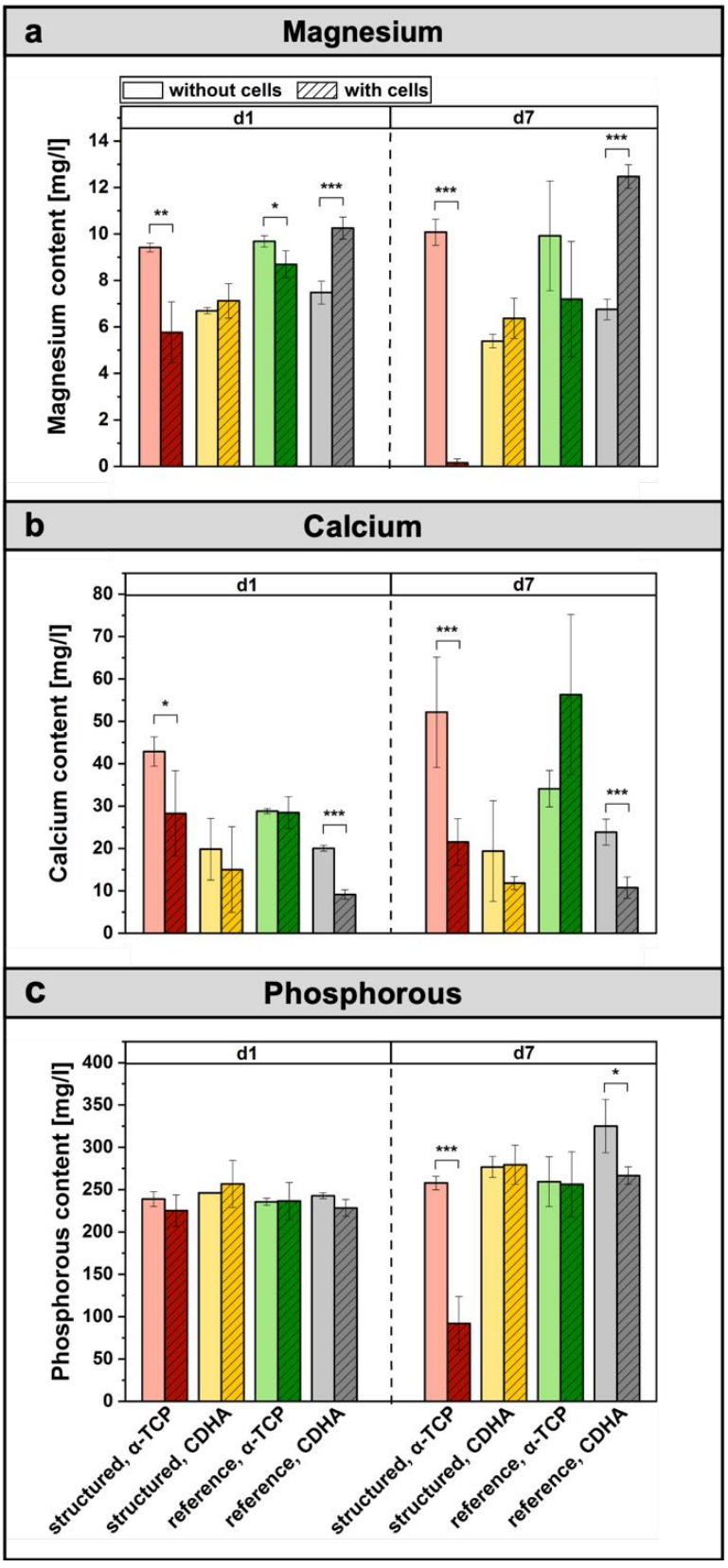

Figure 49. Comparison of ion concentration (Mg^{2+}, Ca^{2+}, PO_4^{3-}) in macrophage culture medium in the absence and presence of macrophages. The (a) magnesium, (b) calcium and (c) phosphorous concentrations after 1 d and 7 d are shown. The structured, α-TCP group is shown in red, the structured, CDHA group in orange, the reference, α-TCP group in green, and the reference, CDHA group in grey. Diagonal lines indicate the presence of macrophages. (mean ± SD, samples without cells: n=3, samples with macrophages: n=3, N=2). *p<0.05, **p<0.01, ***p≤0.001.

5.5.7 CDHA samples reduce pro-inflammatory cytokine expression in human monocytes/macrophages

As macrophage ETs are known to be released as a response to microbes, and the recognition of these usually results in the release of inflammatory cytokines, we were interested if such an inflammatory response was also part of the reaction to mineral particles. Therefore, gene expression (Figure 50) and cytokine release analysis (Figure 51) were performed.

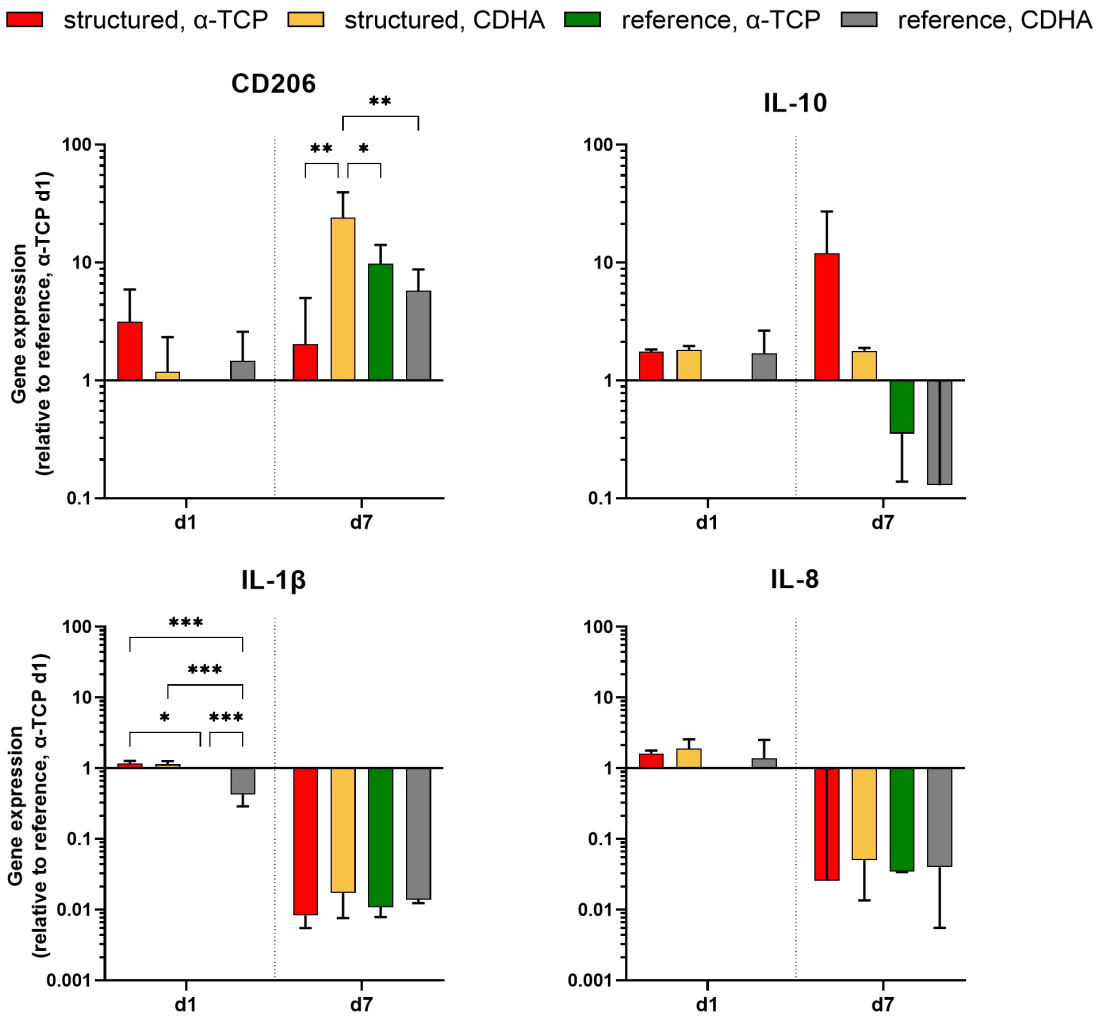

Figure 50. Gene expression profile of spontaneously differentiated macrophages on reference, α-TCP and reference, CDHA as well as the respective structured samples on day 1 and 7. Gene expression was analyzed via qPCR. Spontaneous differentiation was observed on all tested scaffolds. Gene expression of the M1 markers, IL-1β and IL-8, as well as of the M2 markers, CD206, and IL-10, was examined. (Mean ± SD, n = 3). *p < 0.05; **p < 0.01, ***p < 0.001.

The gene expression analysis revealed a relatively similar expression pattern for all groups on day 1, but with significantly lower IL-1β expression on the reference, CDHA group compared to all others. However, after 7 d, both pro-inflammatory markers IL-1β and IL-8 were downregulated in all samples. Instead, the M2 markers were expressed differently with CD206 highest upregulated by macrophages cultivated on structured CDHA and

increased, but insignificant, IL-10 expression by structured, α-TCP. Interestingly, IL-10 was also higher upregulated on structured, CDHA compared to the respective reference. In contrast to the gene expression, monocytes on day 1 on the α-TCP samples compared to CDHA samples released significantly higher amounts of pro-inflammatory cytokines, IL-1β, TNF-α, IL-8 and IL-6. (Figure 51) Furthermore, while the secretion decreased after seven days, macrophages on α-TCP samples released still more pro-inflammatory cytokines than on CDHA samples, especially on the structured ones.

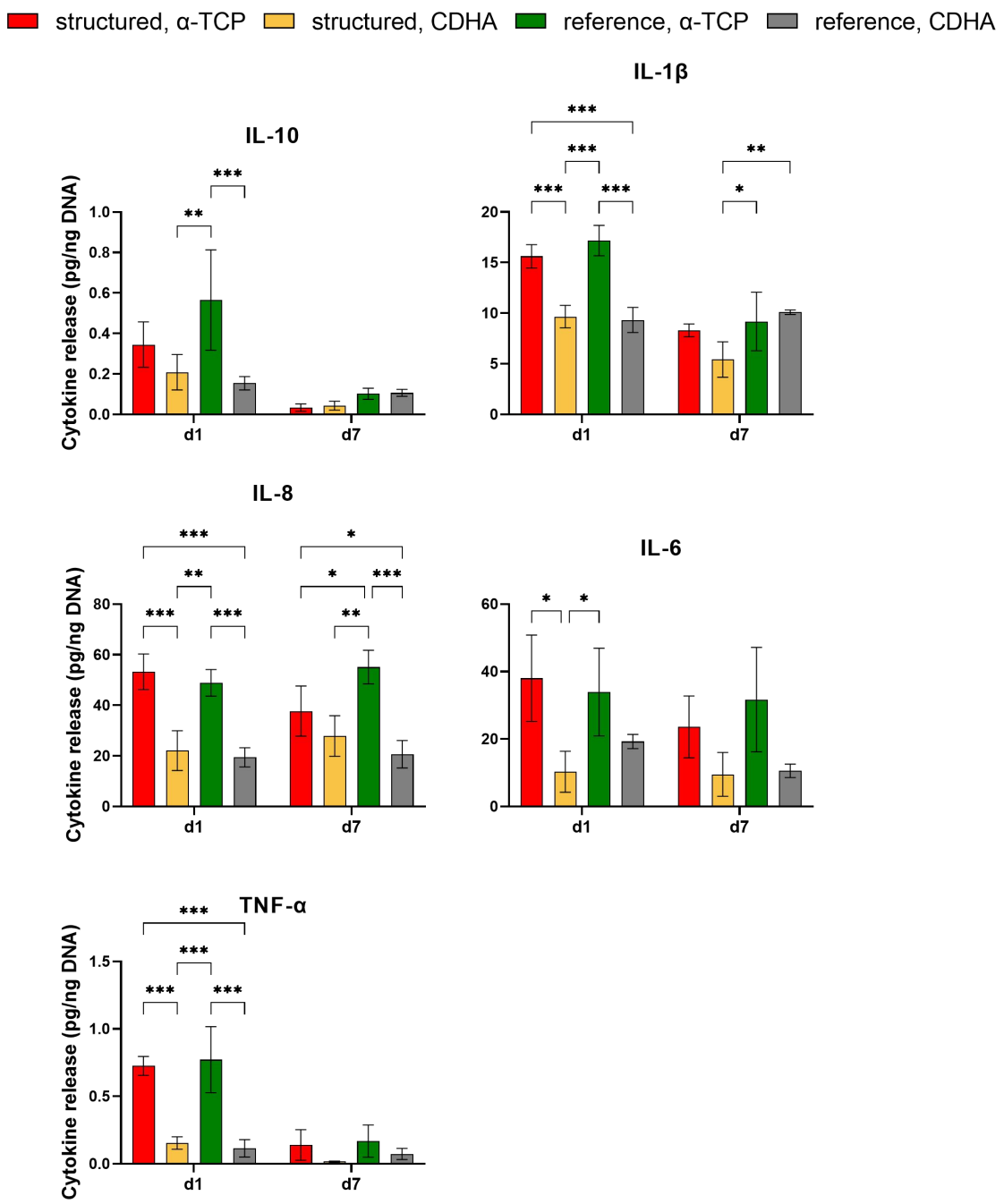

Figure 51. Cytokine release of spontaneously differentiated monocyte-derived macrophages. The cytokine release of IL-10, IL-1β, IL-8, IL-6 and TNF-α was measured using supernatants of monocytes/macrophages cultivated on reference, α-TCP and reference, CDHA as well as the respective structured samples on day 1 and 7. The amounts of released cytokines were normalized to the DNA content of the corresponding sample. (mean ± SD, n = 3). *p <0.05; **p < 0.01, ***p < 0.001.

5.6 Discussion

The present study demonstrated that ETs were released by human monocytes/macrophages *in vitro* in direct or indirect contact with CaP scaffolds. The influence of the high-temperature CaP phase α-TCP and the low temperature phase CDHA as well as two different pore structures were compared. While MET formation occurred in a pronounced manner on samples composed of α-TCP, METs occurred only to a limited extent on samples consisting of CDHA.

METs were only visible in SEM images (Figure 40 and Figure 41) but not in the live/dead or actin stainings (Figure 37 and Figure 38). We assume that this was caused by the poor adhesion to the sample surface, which in turn led to carpet detachment during sample preparation or imaging. However, not only the direct sample and material contact was responsible for the formation of METs, as they were also observed in indirect culture in α-TCP conditioned culture medium. (Figure 40 b)

Macrophages are known to form METs as an immune response to immobilize bacteria and microorganisms, possessing similar properties to ETs released by neutrophils. In response to microorganisms, macrophages undergo a cell death program called "METosis" that can occur within the first few hours and during which fibers composed of cellular DNA are released.[250,260] So far, the formation of METs has not been observed as a response to any materials. However, nanometer-sized fibers and ET-like structures were present in our study after 1 d of contact with the materials. (Figure 40 a) Extracellular DNA release could be confirmed using SYTOX green staining. (Figure 46 and Figure 47)

For neutrophils, Peng *et al.* reported that mineral nanoparticles that were phagocytosed by the cells induced the formation of extracellular traps.[398] These mineral particles are formed by the addition of serum to cell culture medium as calcium and phosphate ions bind to proteins and undergo an amorphous-to-crystalline transformation over time.[411] If ions such as calcium and phosphate are additionally added to the medium, the formation of nanoparticles is strongly accelerated, with the particle size being dependent on the ion and serum concentration.[412] Accordingly, by incubating the CaP samples in cell culture medium enriched with hPL, calcium and phosphate ions were released into the medium (Figure 35 a), thus accelerating nanoparticle formation. The release of calcium into the cell culture medium was particularly pronounced for the structured, α-TCP samples. The increased surface area of the anisotropically structured samples generally enhanced the effect of ion uptake or release. Calcium ions were released into the medium for all sample types where MET formation was observed, whereas this was not the case for the reference, CDHA samples. Crystalline nanoparticles in conditioned medium of α-TCP samples were identified using TEM imaging. (Figure 35 b)

In the absence of serum in the medium, however, calcium and phosphate ions cannot bind to proteins, leading to no mineral particle formation.[411] When α-TCP samples were incubated in the presence of hPL in the medium so that mineral nanoparticles were formed, macrophages released METs during cultivation in this medium. (Figure 40 b and Figure 48) At physiological conditions, α-TCP has higher solubility than CDHA,[413] facilitating ion release through α-TCP samples and favoring mineral particle formation. However, MET release was less pronounced when hPL was added after incubation of the samples in the culture medium and immediately before the cultivation of monocytes in this medium. (Figure 48) This was most likely caused by less time for the nanoparticles to form. If no serum and consequently no mineral nanoparticles were present in the conditioned medium, no METs were observed. (Figure 48)

Platelets are part of the wound healing response. When it comes to an injury and when biomaterials are implanted into the body, platelets start to aggregate and degranulate, leading to the release of a huge amount of growth factors and cytokines.[414] By this, platelets interact with other immune cells, like monocytes and macrophages.[415] Therefore, by using platelet lysate in our study as human serum substitute, we are close to mimicking *in vivo* situations. Thus, we assume that MET formation would also be part of the host body's response to mineral particles released by TCP scaffolds. One explanation for this yet unexplored phenomenon could be that no study has been performed with primary human (monocyte-derived) macrophages so far. Moreover, our study observed a loose adherence of the carpet-like METs onto the samples in stainings which could be easily overseen during *ex vivo* analysis.

The increased release of pro-inflammatory cytokines usually accompanies ETs released by macrophages in response to microorganisms.[416] In our study, we detected a similar response. Macrophages cultivated in direct contact with samples that lead to an increased formation of METs (α-TCP) also showed a significantly higher release of the pro-inflammatory cytokines IL-1β, TNF-α, IL-6 and IL-8 compared to CDHA samples. (Figure 51) This is contrary to a study of Sadowska *et al.*, showing that β-TCP samples were less pro-inflammatory than CDHA samples. However, this study was performed with murine RAW264.7 cells and no METs were detected.[417] In addition, β-TCP exhibits lower solubility than α-TCP under physiological conditions.[413] It is therefore possible that the inhibited ion release resulted in no or only small amounts of mineral particles that could have caused MET formation. The mechanism of whether METs stimulate or are an additional part of the pro-inflammatory response is not yet explored. However, it could already be shown that ETs released by neutrophils activate inflammatory pathways in macrophages.[418] A similar pathway could be activated when macrophages release ETs by themselves.

Our tested samples not only stimulated MET formation and pro-inflammatory cytokine release but also changes in macrophage morphology. While macrophages on TCP samples adopted a more roundish morphology, macrophages on CDHA samples were elongated. This elongation of macrophages can lead to phenotype changes towards the M2 type as it was previously shown both in our studies[409,419,420] and those of others[264], in particular, by aligned, anisotropic structures.

We observed similar effects in this study, macrophages released significantly less pro-inflammatory cytokines on CDHA samples and upregulated the M2 marker CD206 on structured CDHA. Thus, together with the decreased release of IL-1β and TNF-α on structured CDHA compared to the reference, the anisotropic structure benefits macrophage polarization towards an anti-inflammatory type, possibly by pronounced elongation inside the scaffold.

5.7 Conclusion

This study shows the ability of human monocyte-derived macrophages to release extracellular traps (METs) in response to biomaterials for bone replacement. Furthermore, by TEM analysis, we demonstrated that this response is driven by mineral nanoparticles forming by phosphate and calcium ions binding with human platelet lysate. Specifically, cell culture on α-TCP resulted in pronounced particle formation leading to increased release of METs, which was accompanied by increased release of pro-inflammatory cytokines compared to calcium-deficient hydroxyapatite (CDHA). In addition, CDHA, particularly the anisotropically structured samples, promoted polarization towards the M2 type by upregulating the M2 marker CD206 and decreasing the release of M1 cytokines correlated with cell elongation. Thus, in this study, we not only demonstrate a novel response mechanism of macrophages to bone replacement biomaterials, but we also highlight that anisotropically structured CDHA holds promise as a biomaterial for bone replacement applications, leading to a less pro-inflammatory response compared to standard TCP ceramics.

Chapter 6

Concluding discussion and further perspectives

6.1 Concluding discussion

In the present doctoral thesis, directional freezing was applied to prepare anisotropic porous scaffolds with a highly ordered pore structure for biomedical applications. For this purpose, a directional freezing device previously developed at the Department for Functional Materials in Medicine and Dentistry was used to fabricate scaffolds with anisotropic open porosity. The core of the system consists of two PEs arranged one above the other. By varying the PE temperatures, a temperature gradient is generated which is crucial for the process of directional freezing. The advantage of the process used in this thesis is that the temperature gradients can be varied selectively through defined control of the PE temperatures. Thus, process parameters such as the cooling rate can be adjusted. This allows the resulting pore structure within the scaffold to be specifically influenced and adapted to the requirements of a particular application.[307] In addition, the process can in principle be realized using a low-complexity setup and is robust with respect to the application of different material systems. This distinguishes it from other structuring methods such as 3D printing[22,23] or ionotropic gelation[21].

The present dissertation can be divided in three main parts. (Figure 52) The basis of the thesis was to gain a deeper understanding of the directional freezing process described above. (**Part 1**) For this, process parameters such as the cooling rate, temperature gradient and temperatures of the PEs as well as material properties such as the molecular weight, solution concentration and viscosity were systematically varied during the directional freezing step. The resulting scaffold morphology was analyzed as a function of parameter alteration and limitations of the process were identified.[307] Although the mentioned parameters have a significant impact on the directional freezing process and thus also on the sample porosity, a systematic investigation of the influence of cooling surface temperatures in connection with the cooling rates and solution properties has been lacking so far. This gap was filled by the results presented in chapter 3. Here, aqueous solutions of the biopolymers alginate and chitosan were frozen, with the focus for alginate being on the influence of different temperature regimes and gradients on pore orientation and diameter. The studies on chitosan mainly focused on the impact of material properties such as molecular weight, concentration, and viscosity on scaffold morphology. In principle, it was found that higher cooling rates led to smaller pore diameters and that the pore orientation became increasingly perpendicular to the surface as the external temperature gradient increased. In addition, an average (a-)factor was developed that includes the PE temperatures in order to predict the course of the cooling rate as a function of the external temperature gradient. This in turn allows conclusions to be drawn about the resulting pore morphology.[307] With the help of these systematic investigations, it was

possible to lay an essential foundation for further studies, in which knowledge of the aforementioned influences on the resulting scaffold morphology as well as the limitations of the process are of important significance. This is not only of great interest for biomedical applications, where directional freezing is investigated for fields like cardiac tissue engineering[301], nerve[302] or bone regeneration[304]. In addition, aligned pore structures are also highly attractive for use as solid-state lithium batteries[1] or thermal insulators[3]. Limitations of the process were revealed when the temperatures of the lower PE were too low, i.e., down to -60 °C combined with low temperatures of the upper PE. This resulted in disordered crystallization at the beginning of the freezing process, leading to multiple domains with different orientations and consequently a loss of control over pore orientation. Another limitation was found for high viscosities above ~5 Pas, which also resulted in uncontrollable pore orientation.[307]

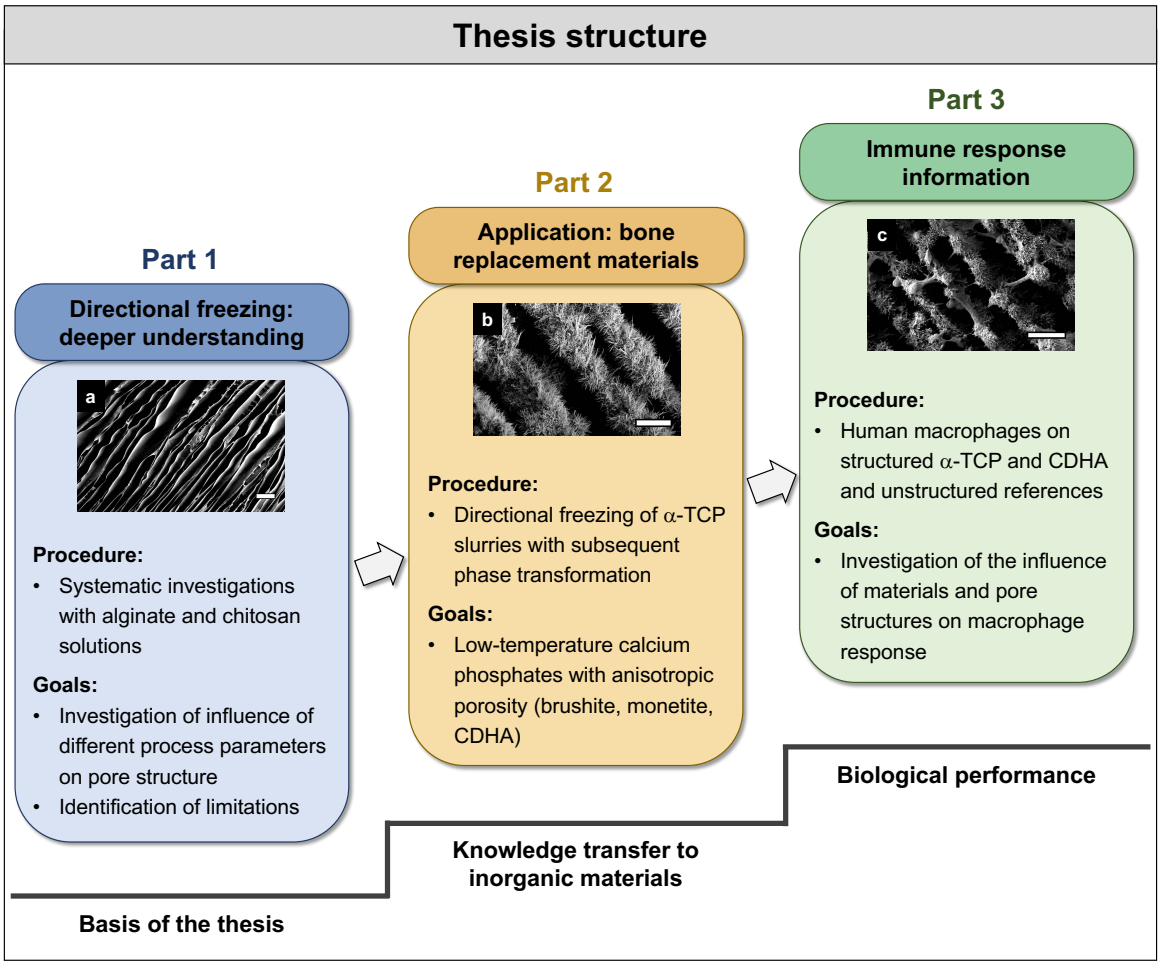

Figure 52. Structure of the present doctoral thesis. In the first part of the thesis, a deeper understanding of the freeze-structuring process was obtained by systematic investigations on alginate and chitosan solutions. In the second part, the knowledge gained was used to prepare CaP scaffolds with anisotropic open porosity for bone replacement applications. The influence of such scaffolds on human monocyte-derived macrophages was investigated in the last part. Scale bars are a) 200 µm, b) 15 µm and c) 20 µm.

Based on these results, the knowledge acquired was applied to create a platform for low-temperature CaP scaffolds with anisotropic porosity for the use as bone graft substitutes in the second part of this thesis. (**Part 2**) Although bone has a highly hierarchical and ordered structure, most bone graft substitutes exhibit isotropic porosity. However, it is known that an anisotropic pore structure facilitates cell ingrowth into the implant as well as nutrient supply and blood vessel ingrowth.[21,339] Previous approaches for bone replacement grafts presented in literature have focused only on anisotropic porous scaffolds prepared by directional freezing of high-temperature CaPs such as β-TCP[30] or HA[31]. These phases exhibit lower solubility and resorbability *in vivo* than low-temperature CaPs.[99,131] Therefore, in the second part of this thesis, scaffolds consisting of the high-temperature CaP α-TCP and alginate as support structure were directionally frozen. Inspired by two studies by Galea *et al*.[362,363], non-sintered or sintered scaffolds were converted into low-temperature CaPs by hydrothermal treatment or immersion in phosphoric acid.[349] By hydrothermal treatment, without a previous sintering step, α-TCP scaffolds were transformed into CDHA, while immersion in phosphoric acid led to phase transformation into monetite. For sintered samples, these post-treatments led to a conversion to CDHA and brushite, respectively. In all cases, the aligned pore structure was preserved.[349] Thus, a material platform of different low-temperature CaPs with anisotropic open porosity was successfully established in this thesis. This is highly interesting for clinical applications as the directional pore structure can be combined with low-temperature CaPs as implant material. Starting from sintered or non-sintered scaffolds, the desired CaP phase for a specific clinical application can be obtained by choosing the appropriate post-treatment.

In the last section of the thesis (**Part 3**), information on the initial immune response after implantation of previously developed and selected CaP scaffolds was obtained. Therefore, the reaction of human monocyte-derived macrophages on anisotropically structured α-TCP and CDHA as well as their unstructured references were evaluated. In the initial defense against a foreign body like an implant, immune cells such as macrophages play a crucial role. Invaders are actively fought with various mechanisms such as the release of cytokines and chemokines, as this enables further immune cells to be attracted.[392] Macrophages are known to release ETs, sticky and net-like fibers composed of intracellular DNA, to immobilize and kill microorganisms.[250] While it has been previously found that neutrophils also produce ETs in response to a biomaterial[396-398], this was first shown for macrophages in this thesis. Mineral nanoparticles, which were particularly formed by incubation of α-TCP samples in serum-containing macrophage culture medium, led to the formation of METs. This was associated with an increase in pro-inflammatory cytokines.

6.2 Further perspectives

Based on the results presented in this thesis, numerous further research questions arise, the answers to which are highly interesting for future projects.

Therefore, it would be of great value to repeat systematic studies, such as those presented in **Chapter 3** for biopolymers, with synthetic polymers like polyvinyl alcohol (PVA). PVA is already approved by the U.S. Food and Drug Administration (FDA) as a food additive, is widely used for pharmaceutical applications[421], and is therefore very attractive for research on tissue substitutes. In addition, it is known to inhibit the formation of ice crystals, making it a promising candidate for use as a cryoprotectant.[422] Cryoprotectants are essential if biological materials are to be cryopreserved. The use of these protective agents can prevent damage that occurs to the material, especially during the critical defrosting process. During thawing, larger crystals form from smaller ones due to so-called Ostwald ripening[423], which may lead to cell rupture and finally cell death.[424] However, the commonly used cryoprotectants dimethyl sulfoxide (DMSO) or glycerol require relatively high concentration (5-20 wt%) and exhibit undesirable properties such as toxicity to cells and the host.[422,425,426] For follow-up studies, it would therefore be highly interesting to perform experiments on the directional freezing of PVA-containing constructs. After a feasibility study, which shows that solutions with PVA can principally be freeze-structured, it would be particularly important to vary different molecular weights, since the ability for ice crystal inhibition depends on this factor.[427] In addition, different temperatures as well as cooling and thawing rates should be varied as these also have sensitive influences on the success of cryopreservation.[428] It is also important to ensure that the scaffold retains its anisotropic porosity after thawing, which could be achieved by crosslinking polymers. Subsequently, it would be possible to combine cryopreservation of cells with directional cell freezing, as it was already shown for endothelial cells[429], red blood cells[430] or adherent mammalian cells[366], to obtain cell-loaded constructs for use as tissue substitutes after thawing.

Follow-up experiments should also include the specific modification of the pore morphology within a monolithic scaffold. Thus, ice crystal growth and crystallization at the beginning of the freezing process could be influenced by modifying or patterning the surface on which the freezing process starts. This may be achieved by applying lithographic methods to establish hydrophilic and hydrophobic zones[431] or topographic changes[432]. Through the latter, for instance, defined microfluidic channels could be introduced into the scaffolds.[305]

Further experiments based on **Chapter 4** could focus on the introduction of precisely designed macropores into the anisotropic porous scaffolds. For this, a sacrificial template could be produced, for example, by 3D printing, which is then combined with the slurry during freeze-structuring and burned out in the following sintering step. In addition, it would

be advantageous if the diameter of the aligned pores could be manipulated in a wider range. This should easily be achievable by using different powder-to-liquid ratios of the slurries, since a higher liquid content leads to more ice formation during freezing, resulting in larger pores after freeze-drying. Primary cells may then be seeded on the scaffold, while endothelial cells could be introduced into the macropores.[305] In this way, vascularized scaffolds could be generated after appropriate cultivation in a bioreactor. A potential material candidate would be sintered β-TCP, as it is already in clinical use (Table 2), although high-temperature CaPs have poorer solubility *in vivo* than low-temperature CaPs.[131]

Therefore, it would be important to extend the material platform developed for CaPs to other cement types, especially magnesium phosphate cements. Newberyite ($MgHPO_4 \cdot 3H_2O$) forming magnesium phosphate cements can be prepared through the mixture of magnesium oxide (MgO) with an aqueous phosphoric acid (H_3PO_4) solution, while struvite ($MgNH_4PO_4 \cdot 6H_2O$) forming cements can be produced by using ammonium dihydrogen phosphate ($NH_4H_2PO_4$) solution instead of phosphoric acid.[433,434] Therefore, magnesium oxide could be added to the slurry during freeze-structuring instead of calcium phosphate powder as presented in **Chapter 4**, and the subsequent cement reaction could be realized by incubation in H_3PO_4 or $NH_4H_2PO_4$ solution. This would combine the advantages of the anisotropic aligned pore structure with the even higher degradability and resorption rate of magnesium phosphate cements like struvite than calcium phosphate cements *in vivo*.[435]

Follow-up experiments based on **Chapter 5** should investigate the response of human monocyte-derived macrophages to β-TCP, since α- and β-TCP are chemically identical and differ only in their crystal structure and solubility.[99,101] Considering that β-TCP is used clinically (Table 2) and does not induce pronounced inflammatory processes but leads to healing[436], it would be valuable to examine whether human monocyte-derived macrophages also release ETs *in vitro* when in contact with such scaffolds.

Since β-TCP exhibits lower solubility than α-TCP[99], it is likely that the formation of mineral particles in serum-containing cell culture medium is delayed or does not proceed at all. Therefore, the occurrence as well as the size of potential particles should be investigated with further TEM measurements and the effects on macrophages should be observed. Finally, *in vivo* experiments are certainly needed to further analyze the strong release of METs observed in **Chapter 5** in association with α-TCP as well as the lower expression on CHDA scaffolds. Hereby, it should be assessed whether this phenomenon possibly only occurs *in vitro* due to the ion concentration changes in the medium caused by incubation of the CaP scaffolds.[410]

Furthermore, scaffolds could be implanted not only in bone but also in soft tissue, for example subcutaneously or in muscle tissue. This could be employed to investigate whether angiogenesis caused by the anisotropic pore structure can be observed and whether the implant may even show osteoinductive properties.

Chapter 7

Summary / Zusammenfassung

7.1 Summary

A multitude of human tissues, such as bones, tendons, or muscles, are characterized by a hierarchical and highly ordered structure. In many cases, the loss of these tissues due to accidents or diseases, for instance, requires reconstruction using biocompatible replacement materials. In addition to the chemical composition, the architecture of the biomaterial plays an important role in tissue regeneration and ultimately in the healing success of the implant. Also in the field of bone replacement, the pore structure of the material has a crucial influence. In addition to structurally mimicking native tissue, the use of materials with anisotropic porosity would have the advantage of facilitating the ingrowth of cells and newly formed blood vessels as well as the transport of nutrients.

In the present doctoral thesis, anisotropic porous scaffolds with a highly ordered pore structure were fabricated using unidirectional freezing. Therefore, a device developed in previous works was used to generate a defined temperature gradient for directional solidification. The core of the system consists of two superimposed Peltier elements (PEs), between which the sample solution is located. By varying the PE temperatures, the ice crystal growth and ultimately the pore structure within the biomaterial can be selectively influenced and adapted to the requirements of a particular application.

The **aim of this thesis** was to gain a deeper understanding of the freeze-structuring process and to apply the knowledge gained to the development of anisotropically structured bone substitute materials. For this, systematic investigations were carried out on biopolymer solutions (alginate and chitosan) in **Chapter 3**. It was shown that, in addition to the external temperature gradient, the temperatures of the PEs, the cooling rate, and material properties such as the molecular weight, concentration, and viscosity of the solution influence the pore structure. The temperature of the overall system affected both the cooling rates and the pore diameters, with higher cooling rates resulting in smaller pores. Furthermore, the pore orientation could be controlled by the external temperature gradient, with pores oriented increasingly perpendicular to the sample surface as the gradient increased. However, certain parameter constellations, such as a temperature of the lower cooling surface below -60 °C combined with a low temperature of the upper PE, or high viscosities (above ~5 Pas near 0 °C), led to a loss of control over pore orientation.

On the basis of **Chapter 4**, the previously existing material platform for anisotropically structured calcium phosphates could be extended to low-temperature phases such as calcium deficient hydroxyapatite (CDHA) or the secondary phosphates monetite and brushite. For this, sintered or non-sintered α-tricalcium phosphate (α-TCP) with anisotropic pore structure was converted into the aforementioned phases by hydrothermal treatment or incubation in phosphoric acid. Hydrothermal treatment resulted in phase conversion to

CDHA for both non-sintered and sintered α-TCP samples, whereas incubation in phosphoric acid led to the transformation into monetite and brushite. Moreover, hydrothermal treatment for 72 h at 175 °C slightly increased the porosity from 85% to 88% for the non-sintered samples, while an increase from 75% to 88% was observed for the sintered ones. The phase conversion into CDHA was accompanied by an increase in specific surface area due to the formation of fine crystal needles and platelets. Regarding the mechanical properties, it was particularly remarkable that the compressive strength of the non-sintered samples significantly increased from (0.76 ± 0.11) to (5.29 ± 0.94) MPa due to the phase transformation into monetite.

In **Chapter 5**, the influence of anisotropically structured α-TCP and CDHA scaffolds as well as their unstructured references on human monocytes/macrophages was investigated. After the implantation of a biomaterial, the inevitably triggered initial immune response plays a key role in the success of a graft, with immune cells such as neutrophils or macrophages being of particular importance. Macrophages can produce extracellular traps (ETs) to immobilize and kill microorganisms. While previous work has demonstrated that neutrophils can produce ETs in response to biomaterials, this mechanism was first shown for macrophages in this thesis. ET release was driven by mineral nanoparticles, which were formed due to the binding of phosphate and calcium ions to human platelet lysate. In particular, incubation of α-TCP samples in lysate containing cell culture medium resulted in pronounced particle formation and enhanced release of ETs. This was accompanied by an increased release of proinflammatory cytokines compared with CDHA. In follow-up experiments to this thesis, systematic studies such as those presented in **Chapter 3** for biopolymers could, for example, be repeated with synthetic polymers such as polyvinyl alcohol (PVA). PVA is a promising candidate for use as a cryoprotectant, the application of which is essential for the cryopreservation of biological materials. Furthermore, *in vivo* experiments would be required to analyze the pronounced release of ETs by macrophages in response to structured α-TCP scaffolds as well as the lower expression on CDHA scaffolds more deeply.

7.2 Zusammenfassung

Eine Vielzahl menschlicher Gewebe, wie beispielsweise Knochen, Sehnen oder Muskeln, ist durch eine hierarchische und zum Teil hochgradig geordnete Struktur gekennzeichnet. Der beispielsweise durch Unfälle oder Krankheiten bedingte Verlust dieser Gewebe erfordert in vielen Fällen eine Rekonstruktion mit biokompatiblen Ersatzmaterialien. Neben der chemischen Zusammensetzung spielt deren Architektur eine wichtige Rolle für die Geweberegeneration und schließlich den Heilungserfolg des Implantats. Auch im Bereich des Knochenersatzes hat die Porenstruktur des Materials hierauf einen zentralen Einfluss, wobei der Einsatz von Materialien mit anisotroper Porosität neben der strukturellen Nachahmung des Gewebes den Vorteil hätte, dass das Einwachsen von Zellen und neu gebildeten Blutgefäßen sowie der Nährstofftransport erleichtert würden.

In der vorliegenden Doktorarbeit wurden anisotrop poröse Scaffolds mit einer hochgradig geordneten Porenstruktur mit Hilfe der Gefrierstrukturierung hergestellt. Hierfür wurde eine in früheren Arbeiten entwickelte Anlage verwendet, um einen definierten Temperaturgradienten in der Probe zur gerichteten Erstarrung zu erzeugen. Der Kern des Systems besteht aus zwei übereinander angeordneten Peltier-Elemente (PEs), zwischen denen sich die Probenlösung befindet. Durch die Variation der PE-Temperaturen kann das Eiskristallwachstum und schließlich die Porenstruktur innerhalb des Biomaterials gezielt beeinflusst und an die Anforderungen einer gewünschten Anwendung angepasst werden.

Das **Ziel dieser Arbeit** war, ein tieferes Verständnis des Gefrierstrukturierungsprozesses zu erlangen und die gewonnenen Erkenntnisse auf die Entwicklung anisotrop poröser Knochenersatzmaterialien zu übertragen. Hierfür wurden in **Kapitel 3** zunächst systematische Untersuchungen an Biopolymerlösungen (Alginat und Chitosan) durchgeführt. Dabei konnte gezeigt werden, dass neben dem äußeren Temperaturgradienten auch die Temperaturen der PEs, die Kühlrate sowie Materialeigenschaften wie das Molekulargewicht, die Konzentration und die Viskosität der Lösung die Porenstruktur beeinflussen. Die Temperatur des Gesamtsystems bestimmte sowohl die Kühlrate als auch die Porendurchmesser, so dass höhere Kühlraten zu kleineren Poren führten. Die Porenorientierung konnte hingegen durch den externen Temperaturgradienten beeinflusst werden, wobei die Poren mit steigendem Gradienten zunehmend senkrecht zur Probenoberfläche orientiert ausgerichtet waren. Bestimmte Parameterkonstellationen, wie beispielsweise eine Temperatur der unteren Kühlfläche unterhalb von -60 °C kombiniert mit einer geringen Temperatur des oberen PE sowie eine hohe Viskosität (über ~5 Pas nahe 0 °C) der Vorlösung führten allerdings dazu, dass die Porenausrichtung nicht mehr kontrollierbar war.

Auf Basis von **Kapitel 4** konnte die bis dato für anisotrop strukturierte Calciumphosphate existierende Materialplattform auf Niedrigtemperaturphasen wie calciumarmen Hydroxylapatit (CDHA) oder die sekundären Phosphate Monetit und Bruschit erweitert werden. Hierfür wurde gesintertes oder ungesintertes α-Tricalciumphosphat (α-TCP) mit anisotroper Porenstruktur durch hydrothermale Behandlung oder Inkubation in Phosphorsäure in die oben genannten Phasen umgewandelt. Durch die hydrothermale Behandlung konnte sowohl bei ungesinterten als auch bei gesinterten α-TCP-Proben eine Phasenumwandlung in CDHA erzielt werden. Die Inkubation in Phosphorsäure führte zu einer Umwandlung in Monetit und Bruschit. Durch die hydrothermale Behandlung für 72 h bei 175 °C erhöhte sich die Porosität der ungesinterten Proben geringfügig von 85 % auf 88 %, während bei den gesinterten Proben ein Anstieg von 75 % auf 88 % zu beobachten war. Darüber hinaus ging eine Phasenumwandlung in CDHA durch die Bildung von feinen Kristallnadeln und -plättchen mit einer Vergrößerung der spezifischen Oberfläche einher. Hinsichtlich der mechanischen Eigenschaften war besonders bemerkenswert, dass die Druckfestigkeit der ungesinterten Proben durch die Phasenumwandlung in Monetit signifikant von (0.76 ± 0.11) auf (5.29 ± 0.94) MPa erhöht wurde.

In **Kapitel 5** wurde der Einfluss von anisotrop porösen α-TCP und CDHA Scaffolds sowie unstrukturierten und aus den gleichen Calciumphosphatphasen bestehenden Referenzproben auf humane Monozyten/Makrophagen untersucht. Nach der Implantation eines Biomaterials spielt die unweigerlich ausgelöste erste Immunreaktion eine Schlüsselrolle für den Erfolg eines Transplantats, wobei Immunzellen wie Neutrophile oder Makrophagen eine entscheidende Rolle spielen. Makrophagen können zur Immobilisierung und zum Abtöten von Mikroorganismen extrazelluläre Fasern (ETs) produzieren. Während in früheren Arbeiten nachgewiesen werden konnte, dass Neutrophile als Reaktion auf Biomaterialien ETs produzieren können, wurde dieser Mechanismus für Makrophagen erstmals in der vorliegenden Doktorarbeit gezeigt. Die ET-Freisetzung wurde von mineralischen Nanopartikeln ausgelöst, welche durch die Bindung von Phosphat- und Calciumionen an menschliches Thrombozytenlysat gebildet wurden. Insbesondere die Inkubation von α-TCP Proben in lysathaltigem Zellkulturmedium führte zu einer ausgeprägten Partikelformierung und schließlich zu einer verstärkten Bildung von ETs. Dies ging mit einer erhöhten Freisetzung von pro-inflammatorischen Zytokinen im Vergleich zu CDHA einher.

An diese Arbeit anschließende Experimente könnten beispielsweise die Wiederholung von systematischen Studien, wie sie in **Kapitel 3** für Biopolymere vorgestellt wurden, mit synthetischen Polymeren wie Polyvinylalkohol (PVA) umfassen. PVA ist ein für den Einsatz als Kryoprotektor vielversprechendes Material, dessen Verwendung für die

Kryokonservierung von biologischen Materialien zwingend notwendig ist. Darüber hinaus wäre die Durchführung von *in vivo* Experimenten erforderlich, um die starke Freisetzung von ETs durch Makrophagen als Reaktion auf strukturierte α-TCP Scaffolds sowie die geringere Expression auf CDHA Scaffolds eingehender zu analysieren.

References

1 Shen, H.; Yi, E. Y.; Amores, M.; Cheng, L.; Tamura, N.; Parkinson, D. Y.; Chen, G. Y.; Chen, K.; Doeff, M., Oriented porous LLZO 3D structures obtained by freeze casting for battery applications. *Journal of Materials Chemistry A* **2019**, 7(36), 20861-20870.

2 Liu, X.; Taiwo, O. O.; Yin, C.; Ouyang, M.; Chowdhury, R.; Wang, B.; Wang, H.; Wu, B.; Brandon, N. P.; Wang, Q.; Cooper, S. J., Aligned Ionogel Electrolytes for High-Temperature Supercapacitors. *Advanced Science* **2019**, 6(5), 1801337.

3 Apostolopoulou-Kalkavoura, V.; Hu, S. Q.; Lavoine, N.; Garg, M.; Linares, M.; Munier, P.; Zozoulenko, I.; Shiomi, J.; Bergstrom, L., Humidity-Dependent Thermal Boundary Conductance Controls Heat Transport of Super-Insulating Nanofibrillar Foams. *Matter* **2021**, 4(1), 276-289.

4 Zhu, M.; Song, J.; Li, T.; Gong, A.; Wang, Y.; Dai, J.; Yao, Y.; Luo, W.; Henderson, D.; Hu, L., Highly Anisotropic, Highly Transparent Wood Composites. *Advanced Materials* **2016**, 28(26), 5181-5187.

5 Barthelat, F.; Tang, H.; Zavattieri, P. D.; Li, C. M.; Espinosa, H. D., On the mechanics of mother-of-pearl: A key feature in the material hierarchical structure. *Journal of the Mechanics and Physics of Solids* **2007**, 55(2), 306-337.

6 Wenk, H. R.; Yu, R.; Cardenes, V.; Lopez-Sanchez, M. A.; Sintubin, M., Fabric and anisotropy of slates: From classical studies to new results. *Journal of Structural Geology* **2020**, 138, 104066.

7 Kues, U.; Navarro-Gonzalez, M., How do Agaricomycetes shape their fruiting bodies? 1. Morphological aspects of development. *Fungal Biology Reviews* **2015**, 29(2), 63-97.

8 Newell, N.; Little, J. P.; Christou, A.; Adams, M. A.; Adam, C. J.; Masouros, S. D., Biomechanics of the human intervertebral disc: A review of testing techniques and results. *Journal of the Mechanical Behavior of Biomedical Materials* **2017**, 69, 420-434.

9 Fox, A. J. S.; Bedi, A.; Rodeo, S. A., The basic science of articular cartilage: structure, composition, and function. *Sports Health* **2009**, 1(6), 461-468.

10 Chevrier, A.; Nelea, M.; Hurtig, M. B.; Hoemann, C. D.; Buschmann, M. D., Meniscus structure in human, sheep, and rabbit for animal models of meniscus repair. *Journal of Orthopaedic Research* **2009**, 27(9), 1197-1203.

11 Torrent-Guasp, F.; Kocica, M. J.; Corno, A. F.; Komeda, M.; Carreras-Costa, F.; Flotats, A.; Cosin-Aguillar, J.; Wen, H., Towards new understanding of the heart structure and function. *European Journal of Cardio-Thoracic Surgery* **2005**, 27(2), 191-201.

12 Frontera, W. R.; Ochala, J., Skeletal Muscle: A Brief Review of Structure and Function. *Calcified Tissue International* **2015**, 96(3), 183-195.

13 Xu, M.; Liu, J.; Sun, J.; Xu, X.; Hu, Y.; Liu, B., Optical Microscopy and Electron Microscopy for the Morphological Evaluation of Tendons: A Mini Review. *Orthopaedic Surgery* **2020**, 12(2), 366-371.

14 Wegst, U. G. K.; Bai, H.; Saiz, E.; Tomsia, A. P.; Ritchie, R. O., Bioinspired structural materials. *Nature Materials* **2015**, 14(1), 23-36.

15 Reznikov, N.; Shahar, R.; Weiner, S., Three-dimensional structure of human lamellar bone: the presence of two different materials and new insights into the hierarchical organization. *Bone* **2014**, 59, 93-104.

16 Atala, A., Tissue engineering and regenerative medicine: concepts for clinical application. *Rejuvenation Research* **2004**, 7(1), 15-31.

17 Langer, R.; Vacanti, J. P., Tissue engineering. *Science* **1993**, 260(5110), 920-926.

References

18 Yang, Y. G.; Sykes, M., Xenotransplantation: current status and a perspective on the future. *Nature Reviews Immunology* **2007**, 7(7), 519-531.

19 Chiarello, E.; Cadossi, M.; Tedesco, G.; Capra, P.; Calamelli, C.; Shehu, A.; Giannini, S., Autograft, allograft and bone substitutes in reconstructive orthopedic surgery. *Aging Clinical and Experimental Research* **2013**, 25, 101-103.

20 Bow, A.; Anderson, D. E.; Dhar, M., Commercially available bone graft substitutes: the impact of origin and processing on graft functionality. *Drug Metabolism Reviews* **2019**, 51(4), 533-544.

21 Bernhardt, A.; Despang, F.; Lode, A.; Demmler, A.; Hanke, T.; Gelinsky, M., Proliferation and osteogenic differentiation of human bone marrow stromal cells on alginate-gelatine-hydroxyapatite scaffolds with anisotropic pore structure. *Journal of Tissue Engineering and Regenerative Medicine* **2009**, 3(1), 54-62.

22 Pei, N.; Hao, Z.; Wang, S.; Pan, B.; Fang, A.; Kang, J.; Li, D.; He, J.; Wang, L., 3D Printing of Layered Gradient Pore Structure of Brain-like Tissue. *International Journal of Bioprinting* **2021**, 7(3), 71-85.

23 Mandal, S.; Meininger, S.; Gbureck, U.; Basu, B., 3D powder printed tetracalcium phosphate scaffold with phytic acid binder: fabrication, microstructure and in situ X-Ray tomography analysis of compressive failure. *Journal of Materials Science: Materials in Medicine* **2018**, 29(3), 29.

24 Li, F. P.; Li, J. S.; Xu, G. S.; Liu, G. J.; Kou, H. C.; Zhou, L., Fabrication, pore structure and compressive behavior of anisotropic porous titanium for human trabecular bone implant applications. *Journal of the Mechanical Behavior of Biomedical Materials* **2015**, 46, 104-114.

25 Stuckensen, K.; Schwab, A.; Knauer, M.; Muinos-Lopez, E.; Ehlicke, F.; Reboredo, J.; Granero-Molto, F.; Gbureck, U.; Prosper, F.; Walles, H.; Groll, J., Tissue Mimicry in Morphology and Composition Promotes Hierarchical Matrix Remodeling of Invading Stem Cells in Osteochondral and Meniscus Scaffolds. *Advanced Materials* **2018**, 30(28), 1706754.

26 Stuckensen, K.; Lamo-Espinosa, J. M.; Muinos-Lopez, E.; Ripalda-Cemborain, P.; Lopez-Martinez, T.; Iglesias, E.; Abizanda, G.; Andreu, I.; Flandes-Iparraguirre, M.; Pons-Villanueva, J.; Elizalde, R.; Nickel, J.; Ewald, A.; Gbureck, U.; Prosper, F.; Groll, J.; Granero-Molto, F., Anisotropic Cryostructured Collagen Scaffolds for Efficient Delivery of RhBMP-2 and Enhanced Bone Regeneration. *Materials* **2019**, 12(19), 3105.

27 Zhou, G.; Groth, T., Host Responses to Biomaterials and Anti-Inflammatory Design-a Brief Review. *Macromolecular Bioscience* **2018**, 18(8), 1800112.

28 Krzyszczyk, P.; Schloss, R.; Palmer, A.; Berthiaume, F., The Role of Macrophages in Acute and Chronic Wound Healing and Interventions to Promote Pro-wound Healing Phenotypes. *Frontiers in Physiology* **2018**, 9, 419.

29 Porcheray, F.; Viaud, S.; Rimaniol, A. C.; Leone, C.; Samah, B.; Dereuddre-Bosquet, N.; Dormont, D.; Gras, G., Macrophage activation switching: an asset for the resolution of inflammation. *Clinical and Experimental Immunology* **2005**, 142(3), 481-489.

30 Flauder, S.; Gbureck, U.; Muller, F. A., Structure and mechanical properties of beta-TCP scaffolds prepared by ice-templating with preset ice front velocities. *Acta Biomaterialia* **2014**, 10(12), 5148-5155.

31 Deville, S.; Saiz, E.; Tomsia, A. P., Freeze casting of hydroxyapatite scaffolds for bone tissue engineering. *Biomaterials* **2006**, 27(32), 5480-5489.

32 Chow, L. C., Calcium phosphate cements. *Monographs in Oral Science* **2001**, 18, 148-163.

33 Seifert, A. Korrelation von Verfahrensparametern und resultierender Morphologie bei der gerichteten Erstarrung von Eiskristallen in Hydrogelen, Julius-Maximilians-Universität Würzburg, **2017**.

34 Doblare, M.; Garcia, J. M.; Gomez, M. J., Modelling bone tissue fracture and healing: a review. *Engineering Fracture Mechanics* **2004**, 71(13-14), 1809-1840.

35 Aumüller, G.; Aust, G.; Conrad, A.; Engele, J.; Kirch, J.; Maio, G.; Mayerhofer, A.; Mense, S.; Reißig, D., Duale Reihe Anatomie. 4., aktualisierte Auflage, Thieme **2017**, 75-76.

36 Weiner, S.; Wagner, H. D., The material bone: Structure mechanical function relations. *Annual Review of Materials Science* **1998**, 28, 271-298.

37 Olszta, M. J.; Cheng, X. G.; Jee, S. S.; Kumar, R.; Kim, Y. Y.; Kaufman, M. J.; Douglas, E. P.; Gower, L. B., Bone structure and formation: A new perspective. *Materials Science & Engineering: R: Reports* **2007**, 58(3-5), 77-116.

38 Liu, Y.; Luo, D.; Wang, T., Hierarchical Structures of Bone and Bioinspired Bone Tissue Engineering. *Small* **2016**, 12(34), 4611-4632.

39 Lowenstam, H. A.; Weiner, S., On biomineralization. Oxford University Press **1989**.

40 Keene, D. R.; Sakai, L. Y.; Burgeson, R. E., Human Bone Contains Type-III Collagen, Type-VI Collagen, and Fibrillin - Type-III Collagen Is Present on Specific Fibers That May Mediate Attachment of Tendons, Ligaments, and Periosteum to Calcified Bone Cortex. *Journal of Histochemistry & Cytochemistry* **1991**, 39(1), 59-69.

41 de Carmejane, O.; Morris, M. D.; Davis, M. K.; Stixrude, L.; Tecklenburg, M.; Rajachar, R. M.; Kohn, D. H., Bone chemical structure response to mechanical stress studied by high pressure Raman spectroscopy. *Calcified Tissue International* **2005**, 76(3), 207-213.

42 Reznikov, N.; Shahar, R.; Weiner, S., Bone hierarchical structure in three dimensions. *Acta Biomaterialia* **2014**, 10(9), 3815-3826.

43 Zimmermann, E. A.; Ritchie, R. O., Bone as a Structural Material. *Advanced Healthcare Materials* **2015**, 4(9), 1287-1304.

44 Dorozhkin, S. V.; Epple, M., Biological and medical significance of calcium phosphates. *Angewandte Chemie International Edition* **2002**, 41(17), 3130-3146.

45 Rho, J. Y.; Kuhn-Spearing, L.; Zioupos, P., Mechanical properties and the hierarchical structure of bone. *Medical Engineering & Physics* **1998**, 20(2), 92-102.

46 Reznikov, N.; Chase, H.; Brumfeld, V.; Shahar, R.; Weiner, S., The 3D structure of the collagen fibril network in human trabecular bone: relation to trabecular organization. *Bone* **2015**, 71, 189-195.

47 Sikavitsas, V. I.; Temenoff, J. S.; Mikos, A. G., Biomaterials and bone mechanotransduction. *Biomaterials* **2001**, 22(19), 2581-2593.

48 Liu, M.; Lv, Y., Reconstructing Bone with Natural Bone Graft: A Review of In Vivo Studies in Bone Defect Animal Model. *Nanomaterials* **2018**, 8(12), 999.

49 Lüllmann-Rauch, R.; Asan, E., Taschenlehrbuch Histologie. . 6., überarbeitete Auflage, Thieme **2019**, 182-210.

50 Alexander, P. G.; Gottardi, R.; Lin, H.; Lozito, T. P.; Tuan, R. S., Three-dimensional osteogenic and chondrogenic systems to model osteochondral physiology and degenerative joint diseases. *Experimental Biology and Medicine* **2014**, 239(9), 1080-1095.

51 Ott, S. M., Cortical or Trabecular Bone: What's the Difference? *American Journal of Nephrology* **2018**, 47(6), 373-375.

52 Chappard, D.; Basle, M. F.; Legrand, E.; Audran, M., Trabecular bone microarchitecture: a review. *Morphologie* **2008**, 92(299), 162-170.

53 Hadjidakis, D. J.; Androulakis, I. I., Bone remodeling. *Annals of the New York Academy of Sciences* **2006**, 1092, 385-396.

54 Qing, H.; Bonewald, L. F., Osteocyte remodeling of the perilacunar and pericanalicular matrix. *International Journal of Oral Science* **2009**, 1(2), 59-65.

55 Tietze, S.; Hofmann, A.; Wolk, S.; Reeps, C., Grundlagen der zellulären Mechanotransduktion. *Gefässchirurgie* **2020**, 25(4), 244-248.

56 Ash, P.; Loutit, J. F.; Townsend, K. M., Osteoclasts derived from haematopoietic stem cells. *Nature* **1980**, 283(5748), 669-670.

References

57 Gregory, C. A.; Prockop, D. J.; Spees, J. L., Non-hematopoietic bone marrow stem cells: molecular control of expansion and differentiation. *Experimental Cell Research* **2005**, 306(2), 330-335.

58 Driessens, F. C.; Planell, J. A.; Boltong, M. G.; Khairoun, I.; Ginebra, M. P., Osteotransductive bone cements. *Proceedings of the Institution of Mechanical Engineers, Part H* **1998**, 212(6), 427-435.

59 Lacombe, J.; Karsenty, G.; Ferron, M., Regulation of lysosome biogenesis and functions in osteoclasts. *Cell Cycle* **2013**, 12(17), 2744-2752.

60 Robling, A. G.; Castillo, A. B.; Turner, C. H., Biomechanical and molecular regulation of bone remodeling. *Annual Review of Biomedical Engineering* **2006**, 8, 455-498.

61 Parfitt, A. M., Quantum concept of bone remodeling and turnover: implications for the pathogenesis of osteoporosis. *Calcified Tissue International* **1979**, 28(1), 1-5.

62 Caplan, A. I., Bone development and repair. *Bioessays* **1987**, 6(4), 171-175.

63 Mahamid, J.; Sharir, A.; Gur, D.; Zelzer, E.; Addadi, L.; Weiner, S., Bone mineralization proceeds through intracellular calcium phosphate loaded vesicles: A cryo-electron microscopy study. *Journal of Structural Biology* **2011**, 174(3), 527-535.

64 Posner, A. S.; Betts, F.; Blumenthal, N. C., Properties of Nucleating Systems. *Metabolic Bone Disease & Related Research* **1978**, 1(2), 179-183.

65 Boivin, G.; Meunier, P. J., Changes in bone remodeling rate influence the degree of mineralization of bone. *Connective Tissue Research* **2002**, 43(2-3), 535-537.

66 Schindeler, A.; McDonald, M. M.; Bokko, P.; Little, D. G., Bone remodeling during fracture repair: The cellular picture. *Seminars in Cell & Developmental Biology* **2008**, 19(5), 459-466.

67 Loi, F.; Cordova, L. A.; Pajarinen, J.; Lin, T. H.; Yao, Z. Y.; Goodman, S. B., Inflammation, fracture and bone repair. *Bone* **2016**, 86, 119-130.

68 Jagodzinski, M.; Krettek, C., Effect of mechanical stability on fracture healing - an update. *Injury-International Journal of the Care of the Injured* **2007**, 38, S3-S10.

69 Claes, L.; Recknagel, S.; Ignatius, A., Fracture healing under healthy and inflammatory conditions. *Nature Reviews Rheumatology* **2012**, 8(3), 133-143.

70 Giannoudis, P. V.; Einhorn, T. A.; Marsh, D., Fracture healing: the diamond concept. *Injury-International Journal of the Care of the Injured* **2007**, 38 Suppl 4, S3-S6.

71 Perren, S. M., Physical and Biological Aspects of Fracture-Healing with Special Reference to Internal-Fixation. *Clinical Orthopaedics and Related Research* **1979**, (138), 175-196.

72 McKibbin, B., The biology of fracture healing in long bones. *The Journal of Bone and Joint Surgery. British volume* **1978**, 60-B(2), 150-162.

73 Hak, D. J.; Toker, S.; Yi, C.; Toreson, J., The influence of fracture fixation biomechanics on fracture healing. *Orthopedics* **2010**, 33(10), 752-755.

74 Marsell, R.; Einhorn, T. A., The biology of fracture healing. *Injury-International Journal of the Care of the Injured* **2011**, 42(6), 551-555.

75 Baht, G. S.; Vi, L.; Alman, B. A., The Role of the Immune Cells in Fracture Healing. *Current Osteoporosis Reports* **2018**, 16(2), 138-145.

76 Kolar, P.; Schmidt-Bleek, K.; Schell, H.; Gaber, T.; Toben, D.; Schmidmaier, G.; Perka, C.; Buttgereit, F.; Duda, G. N., The early fracture hematoma and its potential role in fracture healing. *Tissue Engineering. Part B, Reviews* **2010**, 16(4), 427-434.

77 Ozaki, A.; Tsunoda, M.; Kinoshita, S.; Saura, R., Role of fracture hematoma and periosteum during fracture healing in rats: interaction of fracture hematoma and the periosteum in the initial step of the healing process. *Journal of Orthopaedic Science* **2000**, 5(1), 64-70.

78 Einhorn, T. A., The cell and molecular biology of fracture healing. *Clinic Orthopaedics and Related Research* **1998**, (355 Suppl), S7-21.

79 Jiang, X. X.; Zhang, Y.; Liu, B.; Zhang, S. X.; Wu, Y.; Yu, X. D.; Mao, N., Human mesenchymal stem cells inhibit differentiation and function of monocyte-derived dendritic cells. *Blood* **2005**, 105(10), 4120-4126.

80 Nemeth, K.; Keane-Myers, A.; Brown, J. M.; Metcalfe, D. D.; Gorham, J. D.; Bundoc, V. G.; Hodges, M. G.; Jelinek, I.; Madala, S.; Karpati, S.; Mezey, E., Bone marrow stromal cells use TGF-beta to suppress allergic responses in a mouse model of ragweed-induced asthma. *Proceedings of the National Academy of Sciences of the United States of America* **2010**, 107(17), 5652-5657.

81 Nemeth, K.; Leelahavanichkul, A.; Yuen, P. S. T.; Mayer, B.; Parmelee, A.; Doi, K.; Robey, P. G.; Leelahavanichkul, K.; Koller, B. H.; Brown, J. M.; Hu, X. Z.; Jelinek, I.; Star, R. A.; Mezey, E., Bone marrow stromal cells attenuate sepsis via prostaglandin E-2-dependent reprogramming of host macrophages to increase their interleukin-10 production *Nature Medicine* **2009**, 15(4), 42-49.

82 Rafei, M.; Campeau, P. A.; Aguilar-Mahecha, A.; Buchanan, M.; Williams, P.; Birman, E.; Yuan, S.; Young, Y. K.; Boivin, M. N.; Forner, K.; Basik, M.; Galipeau, J., Mesenchymal Stromal Cells Ameliorate Experimental Autoimmune Encephalomyelitis by Inhibiting CD4 Th17 T Cells in a CC Chemokine Lisgand 2-Dependent Manner. *Journal of Immunology* **2009**, 182(10), 5994-6002.

83 DelaRosa, O.; Lombardo, E.; Beraza, A.; Mancheno-Corvo, P.; Ramirez, C.; Menta, R.; Rico, L.; Camarillo, E.; Garcia, L.; Abad, J. L.; Trigueros, C.; Delgado, M.; Buscher, D., Requirement of IFN-gamma-Mediated Indoleamine 2,3-Dioxygenase Expression in the Modulation of Lymphocyte Proliferation by Human Adipose-Derived Stem Cells. *Tissue Engineering Part A* **2009**, 15(10), 2795-2806.

84 Saikia, K. C.; Bhattacharya, T. D.; Bhuyan, S. K.; Talukdar, D. J.; Saikia, S. P.; Jitesh, P., Calcium phosphate ceramics as bone graft substitutes in filling bone tumor defects. *Indian Journal of Orthopaedics* **2008**, 42(2), 169-172.

85 Kolk, A.; Handschel, J.; Drescher, W.; Rothamel, D.; Kloss, F.; Blessmann, M.; Heiland, M.; Wolff, K. D.; Smeets, R., Current trends and future perspectives of bone substitute materials - from space holders to innovative biomaterials. *Journal of Cranio-Maxillofacial Surgery* **2012**, 40(8), 706-718.

86 Kao, S. T.; Scott, D. D., A review of bone substitutes. *Oral and Maxillofacial Surgery Clinics of North America* **2007**, 19(4), 513-521.

87 Gupta, A.; Kukkar, N.; Sharif, K.; Main, B. J.; Albers, C. E.; El-Amin III, S. F., Bone graft substitutes for spine fusion: A brief review. *World Journal of Orthopaedics* **2015**, 6(6), 449-456.

88 Fernyhough, J. C.; Schimandle, J. J.; Weigel, M. C.; Edwards, C. C.; Levine, A. M., Chronic donor site pain complicating bone graft harvesting from the posterior iliac crest for spinal fusion. *Spine* **1992**, 17(12), 1474-1480.

89 Silber, J. S.; Anderson, D. G.; Daffner, S. D.; Brislin, B. T.; Leland, J. M.; Hilibrand, A. S.; Vaccaro, A. R.; Albert, T. J., Donor site morbidity after anterior iliac crest bone harvest for single-level anterior cervical discectomy and fusion. *Spine* **2003**, 28(2), 134-139.

90 Mertsching, H.; Walles, T.; Hofmann, M.; Schanz, J.; Knapp, W. H., Engineering of a vascularized scaffold for artificial tissue and organ generation. *Biomaterials* **2005**, 26(33), 6610-6617.

91 Moore, W. R.; Graves, S. E.; Bain, G. I., Synthetic bone graft substitutes. *Anz Journal of Surgery* **2001**, 71(6), 354-361.

92 Bohner, M.; Gbureck, U.; Barralet, J. E., Technological issues for the development of more efficient calcium phosphate bone cements: A critical assessment. *Biomaterials* **2005**, 26(33), 6423-6429.

93 Geffers, M.; Groll, J.; Gbureck, U., Reinforcement Strategies for Load-Bearing Calcium Phosphate Biocements. *Materials* **2015**, 8(5), 2700-2717.

94 Dorozhkin, S. V., Calcium orthophosphate-based biocomposites and hybrid biomaterials. *Journal of Materials Science* **2009**, 44(9), 2343-2387.

References

95 Wang, L. J.; Nancollas, G. H., Calcium Orthophosphates: Crystallization and Dissolution. *Chemical Reviews* **2008**, 108(11), 4628-4669.

96 Kucko, N. W.; Herber, R. P.; Leeuwenburgh, S. C. G.; Jansen, J. A. in *Principles of Regenerative Medicine* (ed Academic Press) 591-611 (2019).

97 Dorozhkin, S. V., Calcium orthophosphate cements for biomedical application. *Journal of Materials Science* **2008**, 43(9), 3028-3057.

98 Dorozhkin, S. V., Calcium Orthophosphates in Nature, Biology and Medicine. *Materials* **2009**, 2(2), 399-498.

99 Bohner, M., Calcium orthophosphates in medicine: from ceramics to calcium phosphate cements. *Injury-International Journal of the Care of the Injured* **2000**, 31, S37-S47.

100 Champion, E., Sintering of calcium phosphate bioceramics. *Acta Biomaterialia* **2013**, 9(4), 5855-5875.

101 Jeong, J.; Kim, J. H.; Shim, J. H.; Hwang, N. S.; Heo, C. Y., Bioactive calcium phosphate materials and applications in bone regeneration. *Biomaterials Research* **2019**, 23, 4.

102 Cicek, G.; Aksoy, E. A.; Durucan, C.; Hasirci, N., Alpha-tricalcium phosphate (alpha-TCP): solid state synthesis from different calcium precursors and the hydraulic reactivity. *Journal of Materials Science: Materials in Medicine* **2011**, 22(4), 809-817.

103 Pu'ad, N. A. S.; Haq, R. H. A.; Noh, H. M.; Abdullah, H. Z.; Idris, M. I.; Lee, T. C., Synthesis method of hydroxyapatite: A review. *Materials Today: Proceedings* **2020**, 29, 233-239.

104 Rao, R. R.; Roopa, H. N.; Kannan, T. S., Solid state synthesis and thermal stability of HAP and HAP - beta-TCP composite ceramic powders. *Journal of Matererials Science: Materials in Medicine* **1997**, 8(8), 511-518.

105 Brown, W. E.; Chow, L. C. Dental restorative cement pastes. US Patent No. 4518430, **1985**.

106 Rokidi, S.; Combes, C.; Koutsoukos, P. G., The Calcium Phosphate-Calcium Carbonate System: Growth of Octacalcium Phosphate on Calcium Carbonates. *Crystal Growth & Design* **2011**, 11(5), 1683-1688.

107 Luo, J.; Engqvist, H.; Persson, C., A ready-to-use acidic, brushite-forming calcium phosphate cement. *Acta Biomaterialia* **2018**, 81, 304-314.

108 Xu, H. H. K.; Wang, P.; Wang, L.; Bao, C. Y.; Chen, Q. M.; Weir, M. D.; Chow, L. C.; Zhao, L.; Zhou, X. D.; Reynolds, M. A., Calcium phosphate cements for bone engineering and their biological properties. *Bone Research* **2017**, 5, 17056.

109 Seitz, H.; Deisinger, U.; Leukers, B.; Detsch, R.; Ziegler, G., Different Calcium Phosphate Granules for 3-D Printing of Bone Tissue Engineering Scaffolds. *Advanced Engineering Materials* **2009**, 11(5), B41-B46.

110 Vorndran, E.; Geffers, M.; Ewald, A.; Lemm, M.; Nies, B.; Gbureck, U., Ready-to-use injectable calcium phosphate bone cement paste as drug carrier. *Acta Biomaterialia* **2013**, 9(12), 9558-9567.

111 Ambard, A. J.; Mueninghoff, L., Calcium phosphate cement: review of mechanical and biological properties. *Journal if Prosthodontics* **2006**, 15(5), 321-328.

112 Gbureck, U.; Spatz, K.; Thull, R.; Barralet, J. E., Rheological enhancement of mechanically activated alpha-tricalcium phosphate cements. *Journal of Biomedical Materials Research. Part B, Applied Biomaterials* **2005**, 73(1), 1-6.

113 Chen, W. C.; Thein-Han, W.; Weir, M. D.; Chen, Q. M.; Xu, H. H. K., Prevascularization of biofunctional calcium phosphate cement for dental and craniofacial repairs. *Dental Materials* **2014**, 30(5), 535-544.

114 Klammert, U.; Gbureck, U.; Vorndran, E.; Rodiger, J.; Meyer-Marcotty, P.; Kubler, A. C., 3D powder printed calcium phosphate implants for reconstruction of cranial and maxillofacial defects. *Journal of Cranio-Maxillofacial Surgery* **2010**, 38(8), 565-570.

115 Dorozhkin, S. V., Self-setting calcium orthophosphate formulations. *Journal of Functional Biomaterials* **2013**, 4(4), 209-311.

116 Song, Y.; Feng, Z.; Wang, T., In situ study on the curing process of calcium phosphate bone cement. *Journal of Materials Science: Materials in Medicine* **2007**, 18(6), 1185-1193.

117 Kasten, P.; Luginbuhl, R.; van Griensven, M.; Barkhausen, T.; Krettek, C.; Bohner, M.; Bosch, U., Comparison of human bone marrow stromal cells seeded on calcium-deficient hydroxyapatite, beta-tricalcium phosphate and demineralized bone matrix. *Biomaterials* **2003**, 24(15), 2593-2603.

118 Monma, H.; Kanazawa, T., The hydration of alpha-tricalcium phosphate. *Journal of the Ceramic Society of Japan* **2000**, 108(8), S75-S80.

119 Driessens, F. C. M.; Boltong, M. G.; Bermudez, O.; Planell, J. A., Formulation and Setting Times of Some Calcium Orthophosphate Cements - a Pilot-Study. *Journal of Materials Science-Materials in Medicine* **1993**, 4(5), 503-508.

120 Cardoso, H. A. I.; Motisuke, M.; Zavaglia, A. C., The influence of three additives on the setting reaction kinetics and mechanical strength evolution of [alpha]-tricalcium phosphate cements. . *Key Engineering Materials* **2011**, 493-494, 397-402.

121 Bohner, M.; Malsy, A. K.; Camire, C. L.; Gbureck, U., Combining particle size distribution and isothermal calorimetry data to determine the reaction kinetics of alpha-tricalcium phosphate-water mixtures. *Acta Biomaterialia* **2006**, 2(3), 343-348.

122 Ginebra, M. P.; Driessens, F. C. M.; Planell, J. A., Effect of the particle size on the micro and nanostructural features of a calcium phosphate cement: a kinectic analysis. *Biomaterials* **2004**, 25(17), 3453-3462.

123 Ginebra, M. P.; Fernandez, E.; Driessens, F. C. M.; Boltong, M. G.; Muntasell, J.; Font, J.; Planell, J. A., The effects of temperature on the behaviour of an apatitic calcium phosphate cement. *Journal of Materials Science-Materials in Medicine* **1995**, 6(12), 857-860.

124 Grossardt, C.; Ewald, A.; Grover, L. M.; Barralet, J. E.; Gbureck, U., Passive and Active In Vitro Resorption of Calcium and Magnesium Phosphate Cements by Osteoclastic Cells. *Tissue Engineering Part A* **2010**, 16(12), 3687-3695.

125 Detsch, R.; Mayr, H.; Ziegler, G., Formation of osteoclast-like cells on HA and TCP ceramics. *Acta Biomaterialia* **2008**, 4(1), 139-148.

126 Wenisch, S.; Stahl, J. P.; Horas, U.; Heiss, C.; Kilian, O.; Trinkaus, K.; Hild, A.; Schnettler, R., In vivo mechanisms of hydroxyapatite ceramic degradation by osteoclasts: Fine structural microscopy. *Journal of Biomedical Materials Research Part A* **2003**, 67a(3), 713-718.

127 Boanini, E.; Silingardi, F.; Gazzano, M.; Bigi, A., Synthesis and Hydrolysis of Brushite (DCPD): The Role of Ionic Substitution. *Crystal Growth & Design* **2021**, 21(3), 1689-1697.

128 LeGeros, R. Z., Formation and transformation of calcium phosphates: relevance to vascular calcification. *Zeitschrift für Kardiologie* **2001**, 90, 116-124.

129 Gourgas, O.; Khan, K.; Schwertani, A.; Cerruti, M., Differences in mineral composition and morphology between men and women in aortic valve calcification. *Acta Biomaterialia* **2020**, 106, 342-350.

130 Dorozhkin, S. V., Calcium orthophosphates (CaPO4): occurrence and properties. *Progress in Biomaterials* **2016**, 5, 9-70.

131 Tamimi, F.; Sheikh, Z.; Barralet, J., Dicalcium phosphate cements: Brushite and monetite. *Acta Biomaterialia* **2012**, 8(2), 474-487.

132 Engstrand, T.; Kihlstrom, L.; Neovius, E.; Skogh, A. C. D.; Lundgren, T. K.; Jacobsson, H.; Bohlin, J.; Aberg, J.; Engqvist, H., Development of a bioactive implant for repair and potential healing of cranial defects. *Journal of Neurosurgery* **2014**, 120(1), 273-277.

133 Oliveira, C.; Georgieva, P.; Rocha, F.; Ferreira, A.; de Azevedo, S. F., Dynamical model of brushite precipitation. *Journal of Crystal Growth* **2007**, 305(1), 201-210.

134 Nasrollahi, N.; Dehkordi, A. N.; Jamshidizad, A.; Chehelgerdi, M., Preparation of brushite cements with improved properties by adding graphene oxide. *International Journal of Nanomedicine* **2019**, 14, 3785-3797.

References

135 Tamimi, F.; Torres, J.; Lopez-Cabarcos, E.; Bassett, D. C.; Habibovic, P.; Luceron, E.; Barralet, J. E., Minimally invasive maxillofacial vertical bone augmentation using brushite based cements. *Biomaterials* **2009**, 30(2), 208-216.

136 Barralet, J. E.; Lilley, K. J.; Grover, L. M.; Farrar, D. F.; Ansell, C.; Gbureck, U., Cements from nanocrystalline hydroxyapatite. *Journal of Materials Science-Materials in Medicine* **2004**, 15(4), 407-411.

137 Bohner, M.; vanLanduyt, P.; Merkle, H. P.; Lemaitre, J., Composition effects on the pH of a hydraulic calcium phosphate cement. *Journal of Materials Science-Materials in Medicine* **1997**, 8(11), 675-681.

138 Zhou, H.; Yang, L.; Gbureck, U.; Bhaduri, S. B.; Sikder, P., Monetite, an important calcium phosphate compound-Its synthesis, properties and applications in orthopedics. *Acta Biomaterialia* **2021**, 127, 41-55.

139 Abbona, F.; Christensson, F.; Angela, M. F.; Madsen, H. E. L., Crystal Habit and Growth-Conditions of Brushite, CaHPO4 · 2H2O *Journal of Crystal Growth* **1993**, 131(3-4), 331-346.

140 Sheikh, Z.; Drager, J.; Zhang, Y. L.; Abdallah, M. N.; Tamimi, F.; Barralet, J., Controlling Bone Graft Substitute Microstructure to Improve Bone Augmentation. *Advanced Healthcare Materials* **2016**, 5(13), 1646-1655.

141 Suchanek, K.; Bartkowiak, A.; Perzanowski, M.; Marszalek, M., From monetite plate to hydroxyapatite nanofibers by monoethanolamine assisted hydrothermal approach. *Scientific Reports* **2018**, 8, 15408.

142 Jinawath, S.; Pongkao, D.; Suchanek, W.; Yoshimura, M., Hydrothermal synthesis of monetite and hydroxyapatite from monocalcium phosphate monohydrate. *International Journal of Inorganic Materials* **2001**, 3(7), 997-1001.

143 Karimi, M.; Ramsheh, M. R.; Ahmadi, S. M.; Madani, M. R., One-step and low-temperature synthesis of monetite nanoparticles in an all-in-one system (reactant, solvent, and template) based on calcium chloride-choline chloride deep eutectic medium. *Ceramics International* **2017**, 43(2), 2046-2050.

144 Tas, A. C., Monetite (CaHPO4) Synthesis in Ethanol at Room Temperature. *Journal of the American Ceramic Society* **2009**, 92(12), 2907-2912.

145 Ginebra, M. P.; Canal, C.; Espanol, M.; Pastorino, D.; Montufar, E. B., Calcium phosphate cements as drug delivery materials. *Advanced Drug Delivery Reviews* **2012**, 64(12), 1090-1110.

146 Espanol, M.; Perez, R. A.; Montufar, E. B.; Marichal, C.; Sacco, A.; Ginebra, M. P., Intrinsic porosity of calcium phosphate cements and its significance for drug delivery and tissue engineering applications. *Acta Biomaterialia* **2009**, 5(7), 2752-2762.

147 Habraken, W.; Habibovic, P.; Epple, M.; Bohner, M., Calcium phosphates in biomedical applications: materials for the future? *Materials Today* **2016**, 19(2), 69-87.

148 Bohner, M., Design of Ceramic-Based Cements and Putties for Bone Graft Substitution. *European Cells & Materials* **2010**, 20, 1-12.

149 Lodoso-Torrecilla, I.; van den Beucken, J.; Jansen, J. A., Calcium phosphate cements: Optimization toward biodegradability. *Acta Biomaterialia* **2021**, 119, 1-12.

150 Hing, K. A., Bioceramic bone graft substitutes: Influence of porosity and chemistry. *International Journal of Applied Ceramic Technology* **2005**, 2(3), 184-199.

151 Leteve, M.; Passuti, N., Current concepts in bone graft substitutes. *New Journal of Glass and Ceramics* **2018**, 8, 39-54.

152 Dorozhkin, S. V., Calcium Orthophosphate-Based Bioceramics. *Materials* **2013**, 6(9), 3840-3942.

153 Tancred, D. C.; McCormack, B. A. O.; Carr, A. J., A synthetic bone implant macroscopically identical to cancellous bone. *Biomaterials* **1998**, 19(24), 2303-2311.

154 Miao, X. G.; Sun, D., Graded/Gradient Porous Biomaterials. *Materials* **2010**, 3(1), 26-47.

155 Pal, K.; Pal, S., Development of porous hydroxyapatite scaffolds. *Materials and Manufacturing Processes* **2006**, 21(3), 325-328.

156 Tas, A. C., Preparation of porous apatite granules from calcium phosphate cement. *Journal of Materials Science-Materials in Medicine* **2008**, 19(5), 2231-2239.

157 Maeda, H.; Kasuga, T.; Nogami, M.; Kagami, H.; Hata, K.; Ueda, M., Preparation of bonelike apatite composite sponge. *Bioceramics 16* **2004**, 254-2, 497-500.

158 Li, S. H.; de Wijn, J. R.; Layrolle, P.; de Groot, K., Novel method to manufacture porous hydroxyapatite by dual-phase mixing. *Journal of the American Ceramic Society* **2003**, 86(1), 65-72.

159 De Oliveira, J. F.; De Aguiar, P. F.; Rossi, A. M.; Soares, G. A., Effect of process parameters on the characteristics of porous calcium phosphate ceramics for bone tissue scaffolds. *Artificial Organs* **2003**, 27(5), 406-411.

160 Swain, S. K.; Bhattacharyya, S., Preparation of high strength macroporous hydroxyapatite scaffold. *Materials Science & Engineering C-Materials for Biological Applications* **2013**, 33(1), 67-71.

161 Pecqueux, F.; Tancret, F.; Payraudeau, N.; Bouler, J. M., Influence of microporosity and macroporosity on the mechanical properties of biphasic calcium phosphate bioceramics: Modelling and experiment. *Journal of the European Ceramic Society* **2010**, 30(4), 819-829.

162 Almirall, A.; Larrecq, G.; Delgado, J. A.; Martinez, S.; Planell, J. A.; Ginebra, M. P., Fabrication of low temperature macroporous hydroxyapatite scaffolds by foaming and hydrolysis of an alpha-TCP paste. *Biomaterials* **2004**, 25(17), 3671-3680.

163 Huang, X.; Miao, X. G., Novel porous hydroxyapatite prepared by combining H2O2 foaming with PU sponge and modified with PLGA and bioactive glass. *Journal of Biomaterials Applications* **2007**, 21(4), 351-374.

164 Li, B.; Chen, X. N.; Guo, B.; Wang, X. L.; Fan, H. S.; Zhang, X. D., Fabrication and cellular biocompatibility of porous carbonated biphasic calcium phosphate ceramics with a nanostructure. *Acta Biomaterialia* **2009**, 5(1), 134-143.

165 Wang, Z.; Sakakibara, T.; Sudo, A.; Kasai, Y., Porosity of beta-tricalcium phosphate affects the results of lumbar posterolateral fusion. *Journal of Spinal Disorders and Techniques* **2013**, 26(2), E40-E45.

166 Levengood, S. K. L.; Polak, S. J.; Wheeler, M. B.; Maki, A. J.; Clark, S. G.; Jamison, R. D.; Johnson, A. J. W., Multiscale osteointegration as a new paradigm for the design of calcium phosphate scaffolds for bone regeneration. *Biomaterials* **2010**, 31(13), 3552-3563.

167 Rey, C.; Combes, C.; Drouet, C.; Grossin, D.; Bertrand, G.; Soulié, J., 1.11 Bioactive Calcium Phosphate Compounds: Physical Chemistry. *Comprehensive Biomaterials II* **2017**, 1, 244-290.

168 Sheikh, Z.; Hamdan, N.; Ikeda, Y.; Grynpas, M.; Ganss, B.; Glogauer, M., Natural graft tissues and synthetic biomaterials for periodontal and alveolar bone reconstructive applications: a review. *Biomaterials Research* **2017**, 21, 9.

169 Guidor. GUIDOR easy-graft, https://www.guidor.com/global/easy-graft.html. (26.11.2021).

170 Stryker. Vitoss Synthetic Bone Graft, https://www.stryker.com/us/en/spine/products/vitoss.html. (26.11.2021).

171 Lobb, D. C.; DeGeorge, B. R., Jr.; Chhabra, A. B., Bone Graft Substitutes: Current Concepts and Future Expectations. *The Journal of Hand Surgery* **2019**, 44(6), 497-505.

172 Kanter, A. S.; Gandhoke, G. S.; Welch, W. C.; Arnold, P. M.; Cheng, J. S.; Okonkwo, D. O., A prospective, multi-center clinical and radiographic outcomes evaluation of ChronOS strip for lumbar spine fusion. *Journal of Clinical Neuroscience* **2016**, 25, 36-40.

173 Synthes, D. chronOS Bone Void Filler, http://synthes.vo.llnwd.net/o16/LLNWMB8/US%20Mobile/Synthes%20North%20America/Product%20Support%20Materials/Brochures/DSUSMOC05140059_chronOS_BVF_Brochure.pdf. (15.10.2021).

References

174 Luo, J.; Ajaxon, I.; Ginebra, M. P.; Engqvist, H.; Persson, C., Compressive, diametral tensile and biaxial flexural strength of cutting-edge calcium phosphate cements. *Journal of Mechanical Behavior of Biomedical Materials* **2016**, 60, 617-627.

175 van Vugt, T. A.; Geurts, J.; Arts, J. J., Clinical Application of Antimicrobial Bone Graft Substitute in Osteomyelitis Treatment: A Systematic Review of Different Bone Graft Substitutes Available in Clinical Treatment of Osteomyelitis. *BioMed Research International* **2016**, 2016, 6984656.

176 von Stechow, D.; Rauschmann, M. A., Effectiveness of Combination Use of Antibiotic-Loaded PerOssal (R) with Spinal Surgery in Patients with Spondylodiscitis. *European Surgical Research* **2009**, 43(3), 298-305.

177 McNamara, I.; Deshpande, S.; Porteous, M., Impaction grafting of the acetabulum with a mixture of frozen, ground irradiated bone graft and porous synthetic bone substitute (Apapore 60). *Journal of Bone and Joint Surgery-British Volume* **2010**, 92b(5), 617-623.

178 Coathup, M.; Smith, N.; Kingsley, C.; Buckland, T.; Dattani, R.; Ascroft, G. P.; Blunn, G., Impaction grafting with a bone-graft substitute in a sheep model of revision hip replacement. *The Journal of Bone and Joint Surgery. British volume* **2008**, 90(2), 246-253.

179 Horch, H. H.; Sader, R.; Pautke, C.; Neff, A.; Deppe, H.; Kolk, A., Synthetic, pure-phase beta-tricalcium phosphate ceramic granules (Cerasorb) for bone regeneration in the reconstructive surgery of the jaws. *Inteernational Journal of Oral and Maxillofacial Surgery* **2006**, 35(8), 708-713.

180 Palm, F., CERASORB® - A new synthetic pure-phase ß-TCP ceramic material in oral and maxillofacial surgery. *Implantologie Journal* **2006**, 4, 6-12.

181 Ginebra, M. P.; Delgado, J. A.; Harr, I.; Almirall, A.; Del Valle, S.; Planell, J. A., Factors affecting the structure and properties of an injectable self-setting calcium phosphate foam. *Journal of Biomedical Materials Research Part A* **2007**, 80(2), 351-361.

182 Chu, T. M.; Orton, D. G.; Hollister, S. J.; Feinberg, S. E.; Halloran, J. W., Mechanical and in vivo performance of hydroxyapatite implants with controlled architectures. *Biomaterials* **2002**, 23(5), 1283-1293.

183 Sepulveda, P.; Jones, J. R.; Hench, L. L., Bioactive sol-gel foams for tissue repair. *Journal of Biomedical Materials Research* **2002**, 59(2), 340-348.

184 Jones, J. R.; Hench, L. L., Factors affecting the structure and properties of bioactive foam scaffolds for tissue engineering. *Journal of Biomedical Materials Research. Part B, Applied Biomaterials* **2004**, 68(1), 36-44.

185 Navarro, M.; del Valle, S.; Martinez, S.; Zeppetelli, S.; Ambrosio, L.; Planell, J. A.; Ginebra, M. P., New macroporous calcium phosphate glass ceramic for guided bone regeneration. *Biomaterials* **2004**, 25(18), 4233-4241.

186 del Real, R. P.; Wolke, J. G.; Vallet-Regi, M.; Jansen, J. A., A new method to produce macropores in calcium phosphate cements. *Biomaterials* **2002**, 23(17), 3673-3680.

187 Xu, H. H.; Quinn, J. B.; Takagi, S.; Chow, L. C.; Eichmiller, F. C., Strong and macroporous calcium phosphate cement: Effects of porosity and fiber reinforcement on mechanical properties. *Journal of Biomedical Materials Research* **2001**, 57(3), 457-466.

188 Takagi, S.; Chow, L. C., Formation of macropores in calcium phosphate cement implants. *Journal of Materials Science: Materials in Medicine* **2001**, 12(2), 135-139.

189 Ruhe, P. Q.; Hedberg, E. L.; Padron, N. T.; Spauwen, P. H.; Jansen, J. A.; Mikos, A. G., Biocompatibility and degradation of poly(DL-lactic-co-glycolic acid)/calcium phosphate cement composites. *Journal of Biomedical Materials Research Part A* **2005**, 74(4), 533-544.

190 Lodoso-Torrecilla, I.; van Gestel, N. A. P.; Diaz-Gomez, L.; Grosfeld, E. C.; Laperre, K.; Wolke, J. G. C.; Smith, B. T.; Arts, J. J.; Mikos, A. G.; Jansen, J. A.; Hofmann, S.; van den Beucken, J., Multimodal pore formation in calcium phosphate cements. *Journal of Biomedical Materials Research Part A* **2018**, 106(2), 500-509.

191 Xu, H. H.; Quinn, J. B., Calcium phosphate cement containing resorbable fibers for short-term reinforcement and macroporosity. *Biomaterials* **2002**, 23(1), 193-202.

192 Smith, B. T.; Santoro, M.; Grosfeld, E. C.; Shah, S. R.; van den Beucken, J. J. J. P.; Jansen, J. A.; Mikos, A. G., Incorporation of fast dissolving glucose porogens into an injectable calcium phosphate cement for bone tissue engineering. *Acta Biomaterialia* **2017**, 50, 68-77.

193 Grosfeld, E. C.; Smith, B. T.; Santoro, M.; Lodoso-Torrecilla, I.; Jansen, J. A.; Ulrich, D. J. O.; Melchiorri, A. J.; Scott, D. W.; Mikos, A. G.; van den Beucken, J. J. J. P., Fast dissolving glucose porogens for early calcium phosphate cement degradation and bone regeneration. *Biomedical Materials* **2020**, 15(2).

194 Georgescu, G.; Lacout, J. L.; Freche, M., A new porous osteointegrative bone cement material. *Bioceramics 16* **2004**, 254-2, 201-204.

195 Engel, E.; Asin, L.; Delgado, J. A.; Aparicio, C.; Planell, J. A.; Ginebra, M. P., Cell behaviour of calcium phosphate bone cement modified with a protein-based foaming agent. *Bioceramics 17* **2005**, 284-286, 117-120.

196 del Valle, S.; Mino, N.; Munoz, F.; Gonzalez, A.; Planell, J. A.; Ginebra, M. P., In vivo evaluation of an injectable Macroporous Calcium Phosphate Cement. *Journal of Materials Science-Materials in Medicine* **2007**, 18(2), 353-361.

197 Almirall, A.; Delgado, J. A.; Ginebra, M. P.; Planell, J. A., Effect of albumen as protein-based foaming agent in a calcium phosphate bone cement. *Key Engineering Materials* **2004**, 254-252, 253-256.

198 Anderson, J. M., Biological responses to materials. *Annual Review of Materials Research* **2001**, 31, 81-110.

199 Chung, L.; Maestas, D. R.; Housseau, F.; Elisseeff, J. H., Key players in the immune response to biomaterial scaffolds for regenerative medicine. *Advanced Drug Delivery Reviews* **2017**, 114, 184-192.

200 Mariani, E.; Lisignoli, G.; Borzi, R. M.; Pulsatelli, L., Biomaterials: Foreign Bodies or Tuners for the Immune Response? *International Journal of Molecular Sciences* **2019**, 20(3).

201 Castelo-Branco, C.; Soveral, I., The immune system and aging: a review. *Gynecological Endocrinology* **2014**, 30(1), 16-22.

202 Kumar, H.; Kawai, T.; Akira, S., Pathogen recognition by the innate immune system. *Interantional Reviews of Immunology* **2011**, 30(1), 16-34.

203 Iwasaki, A.; Medzhitov, R., Regulation of Adaptive Immunity by the Innate Immune System. *Science* **2010**, 327(5963), 291-295.

204 Eming, S. A.; Martin, P.; Tomic-Canic, M., Wound repair and regeneration: mechanisms, signaling, and translation. *Science Translational Medicine* **2014**, 6(265), 265sr266.

205 Franz, S.; Rammelt, S.; Scharnweber, D.; Simon, J. C., Immune responses to implants - a review of the implications for the design of immunomodulatory biomaterials. *Biomaterials* **2011**, 32(28), 6692-6709.

206 Anderson, J. M.; Rodriguez, A.; Chang, D. T., Foreign body reaction to biomaterials. *Seminars in Immunology* **2008**, 20(2), 86-100.

207 Kämmerling, L.; Fisher, L. E.; Antmen, E.; Simsek, G. M.; Rostam, H. M.; Vranda, N. E.; Ghaemmaghami, A. M., Mitigating the foreign body response through 'immune-instructive' biomaterials. *Journal of Immunology and Regenerative Medicine* **2021**, 12, 100040.

208 Selders, G. S.; Fetz, A. E.; Radic, M. Z.; Bowlin, G. L., An overview of the role of neutrophils in innate immunity, inflammation and host-biomaterial integration. *Regenerative Biomaterials* **2017**, 4(1), 55-68.

209 Milleret, V.; Buzzi, S.; Gehrig, P.; Ziogas, A.; Grossmann, J.; Schilcher, K.; Zinkernagel, A. S.; Zucker, A.; Ehrbar, M., Protein adsorption steers blood contact activation on engineered cobalt chromium alloy oxide layers. *Acta Biomaterialia* **2015**, 24, 343-351.

References

210 Wilson, C. J.; Clegg, R. E.; Leavesley, D. I.; Pearcy, M. J., Mediation of biomaterial-cell interactions by adsorbed proteins: a review. *Tissue Engineering Part A* **2005**, 11(1-2), 1-18.

211 Alvarez, M. M.; Liu, J. C.; Trujillo-de Santiago, G.; Cha, B. H.; Vishwakarma, A.; Ghaemmaghami, A. M.; Khademhosseini, A., Delivery strategies to control inflammatory response: Modulating M1-M2 polarization in tissue engineering applications. *Journal of Controlled Release* **2016**, 240, 349-363.

212 Christo, S. N.; Diener, K. R.; Bachhuka, A.; Vasilev, K.; Hayball, J. D., Innate Immunity and Biomaterials at the Nexus: Friends or Foes. *BioMed Research International* **2015**, 2015, 342304.

213 Gordon, S., Phagocytosis: An Immunobiologic Process. *Immunity* **2016**, 44(3), 463-475.

214 Wu, J.; Zhang, L.; Shi, J.; He, R.; Yang, W.; Habtezion, A.; Niu, N.; Lu, P.; Xue, J., Macrophage phenotypic switch orchestrates the inflammation and repair/regeneration following acute pancreatitis injury. *EBioMedicine* **2020**, 58, 102920.

215 Burd, P. R.; Thompson, W. C.; Max, E. E.; Mills, F. C., Activated mast cells produce interleukin 13. *Journal of Experimental Medicine* **1995**, 181(4), 1373-1380.

216 Venkayya, R.; Lam, M.; Willkom, M.; Grunig, G.; Corry, D. B.; Erle, D. J., The Th2 lymphocyte products IL-4 and IL-13 rapidly induce airway hyperresponsiveness through direct effects on resident airway cells. *American Journal of Respiratory Cell and Molecular Biology* **2002**, 26(2), 202-208.

217 Bridges, A. W.; Whitmire, R. E.; Singh, N.; Templeman, K. L.; Babensee, J. E.; Lyon, L. A.; Garcia, A. J., Chronic inflammatory responses to microgel-based implant coatings. *Journal of Biomedical Materials Research Part A* **2010**, 94(1), 252-258.

218 Grainger, D. W., All charged up about implanted biomaterials. *Nature Biotechnology* **2013**, 31(6), 507-509.

219 Murray, P. J.; Wynn, T. A., Protective and pathogenic functions of macrophage subsets. *Nature Reviews Immunology* **2011**, 11(11), 723-737.

220 Arango Duque, G.; Descoteaux, A., Macrophage cytokines: involvement in immunity and infectious diseases. *Frontiers in Immunology* **2014**, 5, 491.

221 Geissmann, F.; Manz, M. G.; Jung, S.; Sieweke, M. H.; Merad, M.; Ley, K., Development of monocytes, macrophages, and dendritic cells. *Science* **2010**, 327(5966), 656-661.

222 Brown, B. N.; Ratner, B. D.; Goodman, S. B.; Amar, S.; Badylak, S. F., Macrophage polarization: an opportunity for improved outcomes in biomaterials and regenerative medicine. *Biomaterials* **2012**, 33(15), 3792-3802.

223 Watanabe, S.; Alexander, M.; Misharin, A. V.; Budinger, G. R. S., The role of macrophages in the resolution of inflammation. *Journal of Clinical Investigation* **2019**, 129(7), 2619-2628.

224 Mosser, D. M.; Edwards, J. P., Exploring the full spectrum of macrophage activation. *Nature Reviews Immunology* **2008**, 8(12), 958-969.

225 Munoz, J.; Akhavan, N. S.; Mullins, A. P.; Arjmandi, B. H., Macrophage Polarization and Osteoporosis: A Review. *Nutrients* **2020**, 12(10), 2999.

226 Saradna, A.; Do, D. C.; Kumar, S.; Fu, Q. L.; Gao, P., Macrophage polarization and allergic asthma. *Translational Research* **2018**, 191, 1-14.

227 Ferrante, C. J.; Leibovich, S. J., Regulation of Macrophage Polarization and Wound Healing. *Advances in Wound Care* **2012**, 1(1), 10-16.

228 Wang, Y.; Fan, Y.; Liu, H., Macrophage Polarization in Response to Biomaterials for Vascularization. *Annals of Biomedical Engineering* **2021**, 49(9), 1992-2005.

229 Mantovani, A.; Sica, A.; Sozzani, S.; Allavena, P.; Vecchi, A.; Locati, M., The chemokine system in diverse forms of macrophage activation and polarization. *Trends in Immunology* **2004**, 25(12), 677-686.

230 Hu, X.; Ivashkiv, L. B., Cross-regulation of signaling pathways by interferon-gamma: implications for immune responses and autoimmune diseases. *Immunity* **2009**, 31(4), 539-550.

231 Martinez, F. O.; Gordon, S.; Locati, M.; Mantovani, A., Transcriptional profiling of the human monocyte-to-macrophage differentiation and polarization: new molecules and patterns of gene expression. *Journal of Immunology* **2006**, 177(10), 7303-7311.

232 Wu, X.; Xu, W.; Feng, X.; He, Y.; Liu, X.; Gao, Y.; Yang, S.; Shao, Z.; Yang, C.; Ye, Z., TNF-a mediated inflammatory macrophage polarization contributes to the pathogenesis of steroid-induced osteonecrosis in mice. *International Journal of Immunopathology and Pharmacology* **2015**, 28(3), 351-361.

233 Martinez, F. O.; Gordon, S., The M1 and M2 paradigm of macrophage activation: time for reassessment. *F1000Prime Reports* **2014**, 6, 13.

234 Verreck, F. A. W.; de Boer, T.; Langenberg, D. M. L.; Hoeve, M. A.; Kramer, M.; Vaisberg, E.; Kastelein, R.; Kolk, A.; de Waal-Malefyt, R.; Ottenhoff, T. H. M., Human IL-23-producing type 1 macrophages promote but IL-10-producing type 2, macrophages subvert, immunity to (myco)bacteria. *Proceedings of the National Academy of Sciences of the United States of America* **2004**, 101(13), 4560-4565.

235 Wang, N.; Liang, H. W.; Zen, K., Molecular mechanisms that influence the macrophage M1-M2 polarization balance. *Frontiers in Immunology* **2014**, 5.

236 Sridharan, R.; Cameron, A. R.; Kelly, D. J.; Kearney, C. J.; O'Brien, F. J., Biomaterial based modulation of macrophage polarization: a review and suggested design principles. *Materials Today* **2015**, 18(6), 313-325.

237 Boni, B. O. O.; Lamboni, L.; Souho, T.; Gauthier, M.; Yang, G., Immunomodulation and cellular response to biomaterials: the overriding role of neutrophils in healing. *Materials Horizons* **2019**, 6(6), 1122-1137.

238 Janeway, C. A.; Medzhitov, R., Innate immune recognition. *Annual Review of Immunology* **2002**, 20, 197-216.

239 Colin, S.; Chinetti-Gbaguidi, G.; Staels, B., Macrophage phenotypes in atherosclerosis. *Immunological Reviews* **2014**, 262(1), 153-166.

240 Anderson, C. F.; Mosser, D. M., A novel phenotype for an activated macrophage: the type 2 activated macrophage. *Journal of Leukocyte Biology* **2002**, 72(1), 101-106.

241 Martinez, F. O.; Sica, A.; Mantovani, A.; Locati, M., Macrophage activation and polarization. *Frontiers in Bioscience* **2008**, 13(2), 453-461.

242 Wang, L. X.; Zhang, S. X.; Wu, H. J.; Rong, X. L.; Guo, J., M2b macrophage polarization and its roles in diseases. *Journal of Leukocyte Biology* **2019**, 106(2), 345-358.

243 Arora, S.; Dev, K.; Agarwal, B.; Das, P.; Syed, M. A., Macrophages: Their role, activation and polarization in pulmonary diseases. *Immunobiology* **2018**, 223(4-5), 383-396.

244 Guo, C.; Buranych, A.; Sarkar, D.; Fisher, P. B.; Wang, X. Y., The role of tumor-associated macrophages in tumor vascularization. *Vascular Cell* **2013**, 5, 20.

245 Schlundt, C.; Fischer, H.; Bucher, C. H.; Rendenbach, C.; Duda, G. N.; Schmidt-Bleek, K., The multifaceted roles of macrophages in bone regeneration: A story of polarization, activation and time. *Acta Biomaterialia* **2021**, 133, 46-57.

246 Martin, C. J.; Peters, K. N.; Behar, S. M., Macrophages clean up: efferocytosis and microbial control. *Current Opinion Microbiology* **2014**, 17, 17-23.

247 Boersema, G. S.; Grotenhuis, N.; Bayon, Y.; Lange, J. F.; Bastiaansen-Jenniskens, Y. M., The Effect of Biomaterials Used for Tissue Regeneration Purposes on Polarization of Macrophages. *BioResearch Open Access* **2016**, 5(1), 6-14.

248 Brown, B. N.; Badylak, S. F., Expanded applications, shifting paradigms and an improved understanding of host-biomaterial interactions. *Acta Biomaterialia* **2013**, 9(2), 4948-4955.

249 Brown, B. N.; Londono, R.; Tottey, S.; Zhang, L.; Kukla, K. A.; Wolf, M. T.; Daly, K. A.; Reing, J. E.; Badylak, S. F., Macrophage phenotype as a predictor of constructive

remodeling following the implantation of biologically derived surgical mesh materials. *Acta Biomaterialia* **2012**, 8(3), 978-987.

250 Doster, R. S.; Rogers, L. M.; Gaddy, J. A.; Aronoff, D. M., Macrophage Extracellular Traps: A Scoping Review. *Journal of Innate Immunity* **2018**, 10(1), 3-13.

251 Boe, D. M.; Curtis, B. J.; Chen, M. M.; Ippolito, J. A.; Kovacs, E. J., Extracellular traps and macrophages: new roles for the versatile phagocyte. *Journal of Leukocyte Biology* **2015**, 97(6), 1023-1035.

252 Fuchs, T. A.; Abed, U.; Goosmann, C.; Hurwitz, R.; Schulze, I.; Wahn, V.; Weinrauch, Y.; Brinkmann, V.; Zychlinsky, A., Novel cell death program leads to neutrophil extracellular traps. *Journal of Cell Biology* **2007**, 176(2), 231-241.

253 Wartha, F.; Henriques-Normark, B., ETosis: a novel cell death pathway. *Science Signaling* **2008**, 1(21), pe25.

254 Mutua, V.; Gershwin, L. J., A Review of Neutrophil Extracellular Traps (NETs) in Disease: Potential Anti-NETs Therapeutics. *Clinical Reviews in Allergy and Immunology* **2021**, 61(2), 194-211.

255 Li, R. H. L.; Tablin, F., A Comparative Review of Neutrophil Extracellular Traps in Sepsis. *Frontiers in Veterinary Science* **2018**, 5, 291.

256 Sorensen, O. E.; Borregaard, N., Neutrophil extracellular traps - the dark side of neutrophils. *Journal of Clinical Investigation* **2016**, 126(5), 1612-1620.

257 Apel, F.; Zychlinsky, A.; Kenny, E. F., The role of neutrophil extracellular traps in rheumatic diseases. *Nature Reviews Rheumatology* **2018**, 14(8), 467-475.

258 Yipp, B. G.; Petri, B.; Salina, D.; Jenne, C. N.; Scott, B. N.; Zbytnuik, L. D.; Pittman, K.; Asaduzzaman, M.; Wu, K.; Meijndert, H. C.; Malawista, S. E.; de Boisfleury Chevance, A.; Zhang, K.; Conly, J.; Kubes, P., Infection-induced NETosis is a dynamic process involving neutrophil multitasking in vivo. *Nature Medicine* **2012**, 18(9), 1386-1393.

259 Chow, O. A.; von Kockritz-Blickwede, M.; Bright, A. T.; Hensler, M. E.; Zinkernagel, A. S.; Cogen, A. L.; Gallo, R. L.; Monestier, M.; Wang, Y.; Glass, C. K.; Nizet, V., Statins enhance formation of phagocyte extracellular traps. *Cell Host & Microbe* **2010**, 8(5), 445-454.

260 Halder, L. D.; Abdelfatah, M. A.; Jo, E. A.; Jacobsen, I. D.; Westermann, M.; Beyersdorf, N.; Lorkowski, S.; Zipfel, P. F.; Skerka, C., Factor H Binds to Extracellular DNA Traps Released from Human Blood Monocytes in Response to Candida albicans. *Frontiers in Immunology* **2016**, 7, 671.

261 Munoz-Caro, T.; Silva, L. M.; Ritter, C.; Taubert, A.; Hermosilla, C., Besnoitia besnoiti tachyzoites induce monocyte extracellular trap formation. *Parasitology Research* **2014**, 113(11), 4189-4197.

262 Sussman, E. M.; Halpin, M. C.; Muster, J.; Moon, R. T.; Ratner, B. D., Porous implants modulate healing and induce shifts in local macrophage polarization in the foreign body reaction. *Annals of Biomedical Engineering* **2013**, 42(7), 1508-1516.

263 Almeida, C. R.; Serra, T.; Oliveira, M. I.; Planell, J. A.; Barbosa, M. A.; Navarro, M., Impact of 3-D printed PLA- and chitosan-based scaffolds on human monocyte/macrophage responses: unraveling the effect of 3-D structures on inflammation. *Acta Biomaterialia* **2014**, 10(2), 613-622.

264 McWhorter, F. Y.; Wang, T.; Nguyen, P.; Chung, T.; Liu, W. F., Modulation of macrophage phenotype by cell shape. *Proceedings of the National Academy of Sciences of the United States of America* **2013**, 110(43), 17253-17258.

265 Chen, S.; Jones, J. A.; Xu, Y.; Low, H. Y.; Anderson, J. M.; Leong, K. W., Characterization of topographical effects on macrophage behavior in a foreign body response model. *Biomaterials* **2010**, 31(13), 3479-3491.

266 Kohli, N.; Ho, S.; Brown, S. J.; Sawadkar, P.; Sharma, V.; Snow, M.; Garcia-Gareta, E., Bone remodelling in vitro: Where are we headed? -A review on the current understanding of physiological bone remodelling and inflammation and the strategies for testing biomaterials in vitro. *Bone* **2018**, 110, 38-46.

267 Nuss, K. M.; von Rechenberg, B., Biocompatibility issues with modern implants in bone - a review for clinical orthopedics. *The Open Orthopaedics Journal* **2008**, 2, 66-78.

268 Muschler, G. F.; Nakamoto, C.; Griffith, L. G., Engineering principles of clinical cell-based tissue engineering. *The Journal of Bone and Joint Surgery* **2004**, 86(7), 1541-1558.

269 Chen, Z. T.; Klein, T.; Murray, R. Z.; Crawford, R.; Chang, J.; Wu, C. T.; Xiao, Y., Osteoimmunomodulation for the development of advanced bone biomaterials. *Materials Today* **2016**, 19(6), 304-321.

270 Woodruff, M. A.; Lange, C.; Reichert, J.; Berner, A.; Chen, F. L.; Fratzl, P.; Schantz, J. T.; Hutmacher, D. W., Bone tissue engineering: from bench to bedside. *Materials Today* **2012**, 15(10), 430-435.

271 Al-Maawi, S.; Orlowska, A.; Sader, R.; James Kirkpatrick, C.; Ghanaati, S., In vivo cellular reactions to different biomaterials-Physiological and pathological aspects and their consequences. *Seminars in Immunology* **2017**, 29, 49-61.

272 Lampin, M.; Warocquier-Clérout, R.; Legris, C.; Degrange, M.; SigotLuizard, M. F., Correlation between substratum roughness and wettability, cell adhesion, and cell migration. *Journal of Biomedical Materials Research* **1997**, 36(1), 99-108.

273 Fellin, W., Einführung in Eis-, Schnee- und Lawinenmechanik. Springer Vieweg **2013**.

274 Hansen, T. C., The everlasting hunt for new ice phases. *Nature Communications* **2021**, 12(1), 3161.

275 Bartels-Rausch, T.; Bergeron, V.; Cartwright, J. H. E.; Escribano, R.; Finney, J. L.; Grothe, H.; Gutierrez, P. J.; Haapala, J.; Kuhs, W. F.; Pettersson, J. B. C.; Price, S. D.; Sainz-Diaz, C. I.; Stokes, D. J.; Strazzulla, G.; Thomson, E. S.; Trinks, H.; Uras-Aytemiz, N., Ice structures, patterns, and processes: A view across the icefields. *Reviews of Modern Physics* **2012**, 84(2), 885-944.

276 Salzmann, C. G.; Radaelli, P. G.; Slater, B.; Finney, J. L., The polymorphism of ice: five unresolved questions. *Physical Chemistry Chemical Physics* **2011**, 13(41), 18468-18480.

277 Huang, Y. Y.; Zhu, C. Q.; Wang, L.; Cao, X. X.; Su, Y.; Jiang, X.; Meng, S.; Zhao, J. J.; Zeng, X. C., A new phase diagram of water under negative pressure: The rise of the lowest-density clathrate s-III. *Science Advances* **2016**, 2(2), e1501010.

278 Meschede, D.; Gerthsen, C., Gerthsen Physik. Vol. 25, Springer Spektrum **2015**.

279 Nada, H.; Furukawa, Y., Anisotropy in growth kinetics at interfaces between proton-disordered hexagonal ice and water: A molecular dynamics study using the six-site model of H2O. *Journal of Crystal Growth* **2005**, 283(1-2), 242-256.

280 Hobbs, P. V., Ice physics. Clarendon Press **1974**.

281 Worster, M. G.; Wettlaufer, J. S., Natural convection, solute trapping, and channel formation during solidification of saltwater. *Journal of Physical Chemistry B* **1997**, 101(32), 6132-6136.

282 Deville, S.; Saiz, E.; Nalla, R. K.; Tomsia, A. P., Freezing as a path to build complex composites. *Science* **2006**, 311(5760), 515-518.

283 Joukhdar, H.; Seifert, A.; Jungst, T.; Groll, J.; Lord, M. S.; Rnjak-Kovacina, J., Ice Templating Soft Matter: Fundamental Principles and Fabrication Approaches to Tailor Pore Structure and Morphology and Their Biomedical Applications. *Advanced Materials* **2021**, 33(34), e2100091.

284 Kurz, W.; Fisher, D. J., Fundamentals of solidification. Vol. 3, Trans Tech Publications **1992**.

285 Trivedi, R., Theory of Dendritic Growth during the Directional Solidification of Binary-Alloys. *Journal of Crystal Growth* **1980**, 49(2), 219-232.

286 Coriell, S. R.; Mcfadden, G. B.; Sekerka, R. F., Cellular Growth during Directional Solidification. *Annual Review of Materials Science* **1985**, 15, 119-145.

References

287 Hu, X. W.; Li, S. M.; Chen, W. J.; Gao, S. F.; Liu, L.; Fu, H. Z., Primary dendrite arm spacing during unidirectional solidification of Pb-Bi peritectic alloys. *Journal of Alloys and Compounds* **2009**, 484(1-2), 631-636.

288 Fan, J. L.; Li, X.; Su, Y. Q.; Guo, J. J.; Fu, H. Z., Dependency of microhardness on solidification processing parameters and microstructure characteristics in the directionally solidified Ti-46Al-0.5W-0.5Si alloy. *Journal of Alloys and Compounds* **2010**, 504(1), 60-64.

289 Eshraghi, M.; Felicelli, S. D.; Jelinek, B., Three dimensional simulation of solutal dendrite growth using lattice Boltzmann and cellular automaton methods. *Journal of Crystal Growth* **2012**, 354(1), 129-134.

290 Wang, Z. J.; Li, J. J.; Wang, J. C.; Zhou, Y. H., Phase field modeling the selection mechanism of primary dendritic spacing in directional solidification. *Acta Materialia* **2012**, 60(5), 1957-1964.

291 Bolling, G. F.; Cissé, J., A Theory for Interaction of Particles with a Solidifying Front. *Journal of Crystal Growth* **1971**, 10(1), 56-66.

292 Angell, C. A.; Oguni, M.; Sichina, W. J., Heat-Capacity of Water at Extremes of Supercooling and Superheating. *Journal of Physical Chemistry* **1982**, 86(6), 998-1002.

293 Leung, W. K. S.; Carmichael, G. R., Solute Redistribution during Normal Freezing. *Water Air and Soil Pollution* **1984**, 21(1-4), 141-150.

294 Rutter, J. W.; Chalmers, B., A Prismatic Substructure Formed during Solidification of Metals. *Canadian Journal of Physics* **1953**, 31(1), 15-39.

295 Schoof, H. Verfahren zur Herstellung gefriergetrockneter Kollagenschwämme mit definierter Porenstruktur, Rheinisch-Westfälische Technische Hochschule Aachen, **2000**.

296 Mullins, W. W.; Sekerka, R. F., Stability of Planar Interface during Solidification of Dilute Binary Alloy. *Journal of Applied Physics* **1964**, 35(2), 444-451.

297 Shao, G.; Hanaor, D. A. H.; Shen, X.; Gurlo, A., Freeze Casting: From Low-Dimensional Building Blocks to Aligned Porous Structures-A Review of Novel Materials, Methods, and Applications. *Advanced Materials* **2020**, 32(17), e1907176.

298 Wegst, U. G. K.; Schecter, M.; Donius, A. E.; Hunger, P. M., Biomaterials by freeze casting. *Philosophical Transactions of the Royal Society A. Mathematical, Physical and Engineering Sciences* **2010**, 368(1917), 2099-2121.

299 Stefanescu, D. M.; Ruxanda, R. in *ASM Handbook Volume 9 - Metallography and Microstructures* Vol. 9 (ed George F. Vander Voort) Ch. Fundamentals of Solidification, 71-92 (ASM International, 2004).

300 Naglieri, V.; Bale, H. A.; Gludovatz, B.; Tomsia, A. P.; Ritchie, R. O., On the development of ice-templated silicon carbide scaffolds for nature-inspired structural materials. *Acta Materialia* **2013**, 61(18), 6948-6957.

301 Stoppel, W. L.; Hu, D.; Domian, I. J.; Kaplan, D. L.; Black, L. D., 3rd, Anisotropic silk biomaterials containing cardiac extracellular matrix for cardiac tissue engineering. *Biomedical Materials* **2015**, 10(3), 034105.

302 Stokols, S.; Tuszynski, M. H., The fabrication and characterization of linearly oriented nerve guidance scaffolds for spinal cord injury. *Biomaterials* **2004**, 25(27), 5839-5846.

303 Pawelec, K. M.; Husmann, A.; Best, S. M.; Cameron, R. E., Understanding anisotropy and architecture in ice-templated biopolymer scaffolds. *Materials Science and Engineering: C* **2014**, 37, 141-147.

304 Rödel, M.; Baumann, K.; Groll, J.; Gbureck, U., Simultaneous structuring and mineralization of silk fibroin scaffolds. *Journal of Tissue Engineering* **2018**, 9.

305 Mao, M.; He, J.; Liu, Y.; Li, X.; Li, D., Ice-template-induced silk fibroin-chitosan scaffolds with predefined microfluidic channels and fully porous structures. *Acta Biomaterialia* **2012**, 8(6), 2175-2184.

306 Schoof, H.; Apel, J.; Heschel, I.; Rau, G., Control of pore structure and size in freeze-dried collagen sponges. *Journal of Biomedical Materials Research* **2001**, 58(4), 352-357.

307 Seifert, A.; Gruber, J.; Gbureck, U.; Groll, J., Morphological Control of Freeze-Structured Scaffolds by Selective Temperature and Material Control in the Ice-Templating Process. *Advanced Engineering Materials* **2021**, 2100860.

308 Deville, S., Freeze-casting of porous ceramics: A review of current achievements and issues. *Advanced Engineering Materials* **2008**, 10(3), 155-169.

309 Deville, S., Freeze-Casting of Porous Biomaterials: Structure, Properties and Opportunities. *Materials* **2010**, 3(3), 1913-1927.

310 Deville, S., The lure of ice-templating: Recent trends and opportunities for porous materials. *Scripta Materialia* **2018**, 147, 119-124.

311 Li, W. L.; Lu, K.; Walz, J. Y., Freeze casting of porous materials: review of critical factors in microstructure evolution. *International Materials Reviews* **2012**, 57(1), 37-60.

312 Qin, K. K.; Parisi, C.; Fernandes, F. M., Recent advances in ice templating: from biomimetic composites to cell culture scaffolds and tissue engineering. *Journal of Materials Chemistry B* **2021**, 9(4), 889-907.

313 Scotti, K. L.; Dunand, D. C., Freeze casting - A review of processing, microstructure and properties via the open data repository, FreezeCasting.net. *Progress in Materials Science* **2018**, 94, 243-305.

314 Liu, R. P.; Xu, T. T.; Wang, C. A., A review of fabrication strategies and applications of porous ceramics prepared by freeze-casting method. *Ceramics International* **2016**, 42(2), 2907-2925.

315 Bai, Y.; Liu, R.; Wang, Y. M.; Xiao, H. H.; Liu, Y.; Yuan, G. H., High Ion Transport within a Freeze-Casted Gel Film for High-Rate Integrated Flexible Supercapacitors. *Acs Applied Materials & Interfaces* **2019**, 11(46), 43294-43302.

316 Wang, Q. R.; Wang, X. Y.; Wan, F.; Chen, K. N.; Niu, Z. Q.; Chen, J., An All-Freeze-Casting Strategy to Design Typographical Supercapacitors with Integrated Architectures. *Small* **2018**, 14(23), 1800280.

317 Sahoo, P. K.; Kumar, N.; Thiyagarajan, S.; Thakur, D.; Panda, H. S., Freeze-Casting of Multifunctional Cellular 3D-Graphene/Ag Nanocomposites: Synergistically Affect Supercapacitor, Catalytic, and Antibacterial Properties. *Acs Sustainable Chemistry & Engineering* **2018**, 6(6), 7475-7487.

318 Ni, Y.; Qi, J. Q.; Zhou, B. T.; Zhu, L.; Ren, Y. J.; Zhang, D., Controllable synthesis of multilayered porous carbon by ice templating with graphene addition for supercapacitors. *Journal of Materials Science* **2021**, 56(12), 7533-7546.

319 Stolze, C.; Janoschka, T.; Flauder, S.; Muller, F. A.; Hager, M. D.; Schubert, U. S., Investigation of Ice-Templated Porous Electrodes for Application in Organic Batteries. *Acs Applied Materials & Interfaces* **2016**, 8(36), 23614-23623.

320 Huang, C.; Grant, P. S., Coral-like directional porosity lithium ion battery cathodes by ice templating. *Journal of Materials Chemistry A* **2018**, 6(30), 14689-14699.

321 Munier, P.; Apostolopoulou-Kalkavoura, V.; Persson, M.; Bergstrom, L., Strong silica-nanocellulose anisotropic composite foams combine low thermal conductivity and low moisture uptake. *Cellulose* **2020**, 27(18), 10825-10836.

322 Rezaei, H.; Shahrezaee, M.; Monfared, M. J.; Ghorbani, F.; Zamanian, A.; Sahebalzamani, M., Mussel-inspired polydopamine induced the osteoinductivity to ice-templating PLGA-gelatin matrix for bone tissue engineering application. *Biotechnology and Applied Biochemistry* **2021**, 68(1), 185-196.

323 Nystrom, G.; Fong, W. K.; Mezzenga, R., Ice-Templated and Cross-Linked Amyloid Fibril Aerogel Scaffolds for Cell Growth. *Biomacromolecules* **2017**, 18(9), 2858-2865.

324 Rieu, C.; Parisi, C.; Mosser, G.; Haye, B.; Coradin, T.; Fernandes, F. M.; Trichet, L., Topotactic Fibrillogenesis of Freeze-Cast Microridged Collagen Scaffolds for 3D Cell Culture. *Acs Applied Materials & Interfaces* **2019**, 11(16), 14672-14683.

References

325 Christoph, S.; Kwiatoszynski, J.; Coradin, T.; Fernandes, F. M., Cellularized Cellular Solids via Freeze-Casting. *Macromolecular Bioscience* **2016**, 16(2), 182-187.

326 Bouville, F.; Portuguez, E.; Chang, Y. F.; Messing, G. L.; Stevenson, A. J.; Maire, E.; Courtois, L.; Deville, S., Templated Grain Growth in Macroporous Materials. *Journal of the American Ceramic Society* **2014**, 97(6), 1736-1742.

327 Bai, H.; Chen, Y.; Delattre, B.; Tomsia, A. P.; Ritchie, R. O., Bioinspired large-scale aligned porous materials assembled with dual temperature gradients. *Science Advances* **2015**, 1(11), e1500849.

328 Bai, H.; Walsh, F.; Gludovatz, B.; Delattre, B.; Huang, C. L.; Chen, Y.; Tomsia, A. P.; Ritchie, R. O., Bioinspired Hydroxyapatite/Poly(methyl methacrylate) Composite with a Nacre-Mimetic Architecture by a Bidirectional Freezing Method. *Advanced Materials* **2016**, 28(1), 50-56.

329 Xu, W. Z.; Xing, Y.; Liu, J.; Wu, H. P.; Cuo, Y.; Li, D. W.; Guo, D. Y.; Li, C. R.; Liu, A. P.; Bai, H., Efficient Water Transport and Solar Steam Generation via Radially, Hierarchically Structured Aerogels. *Acs Nano* **2019**, 13(7), 7930-7938.

330 Nelson, I.; Ogden, T. A.; Al Khateeb, S.; Graser, J.; Sparks, T. D.; Abbott, J. J.; Naleway, S. E., Freeze-Casting of Surface-Magnetized Iron(II,III) Oxide Particles in a Uniform Static Magnetic Field Generated by a Helmholtz Coil. *Advanced Engineering Materials* **2019**, 21(3), 1801092.

331 Tang, Y. F.; Qiu, S.; Miao, Q.; Wu, C., Fabrication of lamellar porous alumina with axisymmetric structure by directional solidification with applied electric and magnetic fields. *Journal of the European Ceramic Society* **2016**, 36(5), 1233-1240.

332 Ogden, T. A.; Prisbrey, M.; Nelson, I.; Raeymaekers, B.; Naleway, S. E., Ultrasound freeze casting: Fabricating bioinspired porous scaffolds through combining freeze casting and ultrasound directed self-assembly. *Materials & Design* **2019**, 164.

333 Gutierrez, M. C.; Ferrer, M. L.; del Monte, F., Ice-templated materials: Sophisticated structures exhibiting enhanced functionalities obtained after unidirectional freezing and ice-segregation-induced self-assembly. *Chemistry of Materials* **2008**, 20(3), 634-648.

334 Zhang, H. F.; Long, J.; Cooper, A. I., Aligned porous materials by directional freezing of solutions in liquid CO2. *Journal of the American Chemical Society* **2005**, 127(39), 13482-13483.

335 Karageorgiou, V.; Kaplan, D., Porosity of 3D biomaterial scaffolds and osteogenesis. *Biomaterials* **2005**, 26(27), 5474-5491.

336 Hulbert, S. F.; Young, F. A.; Mathews, R. S.; J.J., K.; Talbert, C. D.; Stelling, F. H., Potential of ceramic materials as permanently implantable skeletal prostheses. *Journal of Biomedical Materials Research* **1970**, 4(3), 433-456.

337 Murphy, C. M.; Haugh, M. G.; O'Brien, F. J., The effect of mean pore size on cell attachment, proliferation and migration in collagen-glycosaminoglycan scaffolds for bone tissue engineering. *Biomaterials* **2010**, 31(3), 461-466.

338 Campbell, J. J.; Husmann, A.; Hume, R. D.; Watson, C. J.; Cameron, R. E., Development of three-dimensional collagen scaffolds with controlled architecture for cell migration studies using breast cancer cell lines. *Biomaterials* **2017**, 114, 34-43.

339 Muehleder, S.; Ovsianikov, A.; Zipperle, J.; Redl, H.; Holnthoner, W., Connections matter: channeled hydrogels to improve vascularization. *Frontiers in Bioengineering and Biotechnology* **2014**, 2, 52.

340 Stuckensen, K.; Gbureck, U.; Groll, J. Production of materials having an anisotropic structure. Patent No. EP2788171A2, **2012**.

341 Waschkies, T.; Oberacker, R.; Hoffmann, M. J., Control of Lamellae Spacing During Freeze Casting of Ceramics Using Double-Side Cooling as a Novel Processing Route. *Journal of the American Ceramic Society* **2009**, 92(1), S79-S84.

342 Waschkies, T.; Oberacker, R.; Hoffmann, M. J., Investigation of structure formation during freeze-casting from very slow to very fast solidification velocities. *Acta Materialia* **2011**, 59(13), 5135-5145.

343 Yin, K. Y.; Divakar, P.; Wegst, U. G. K., Freeze-casting porous chitosan ureteral stents for improved drainage. *Acta Biomaterialia* **2019**, 84, 231-241.

344 Florczyk, S. J.; Kim, D. J.; Wood, D. L.; Zhang, M. Q., Influence of processing parameters on pore structure of 3D porous chitosan-alginate polyelectrolyte complex scaffolds. *Journal of Biomedical Materials Research Part A* **2011**, 98a(4), 614-620.

345 Francis, N. L.; Hunger, P. M.; Donius, A. E.; Riblett, B. W.; Zavaliangos, A.; Wegst, U. G. K.; Wheatley, M. A., An ice-templated, linearly aligned chitosan-alginate scaffold for neural tissue engineering. *Journal of Biomedical Materials Research Part A* **2013**, 101(12), 3493-3503.

346 Nematollahi, Z.; Tafazzoli-Shadpour, M.; Zamanian, A.; Seyedsalehi, A.; Mohammad-Behgam, S.; Ghorbani, F.; Mirahmadi, F., Fabrication of Chitosan Silk-based Tracheal Scaffold Using Freeze-Casting Method. *Iranian Biomedical Journal* **2017**, 21(4), 228-239.

347 Christiansen, C. D.; Nielsen, K. K.; Bjork, R., Novel freeze-casting device with high precision thermoelectric temperature control for dynamic freezing conditions. *Review of Scientific Instruments* **2020**, 91(3), 033904.

348 Yin, K.; Divakar, P.; Hong, J.; Moodie, K. L.; Rosen, J. M.; Sundback, C. A.; Matthew, M. K.; Wegst, U. G. K., Freeze-cast Porous Chitosan Conduit for Peripheral Nerve Repair. *MRS Advances* **2018**, 3(30), 1677-1683.

349 Seifert, A.; Groll, J.; Weichhold, J.; Boehm, A. V.; Müller, F. A.; Gbureck, U., Phase Conversion of Ice-Templated alpha-Tricalcium Phosphate Scaffolds into Low-Temperature Calcium Phosphates with Anisotropic Open Porosity. *Advanced Engineering Materials* **2021**, 23(5), 2001417.

350 Weiner, S.; Traub, W.; Wagner, H. D., Lamellar bone: Structure-function relations. *Journal of Structural Biology* **1999**, 126(3), 241-255.

351 Weiner, S.; Traub, W., Bone-Structure - from Angstroms to Microns. *Faseb Journal* **1992**, 6(3), 879-885.

352 Hannink, G.; Arts, J. J. C., Bioresorbability, porosity and mechanical strength of bone substitutes: What is optimal for bone regeneration? *Injury-International Journal of the Care of the Injured* **2011**, 42, S22-S25.

353 Madrid, A. P. M.; Vrech, S. M.; Sanchez, M. A.; Rodriguez, A. P., Advances in additive manufacturing for bone tissue engineering scaffolds. *Materials Science & Engineering C-Materials for Biological Applications* **2019**, 100, 631-644.

354 Gbureck, U.; Hoelzel, T.; Biermann, I.; Barralet, J. E.; Grover, L. M., Preparation of tricalcium phosphate/calcium pyrophosphate structures via rapid prototyping. *Journal of Materials Science-Materials in Medicine* **2008**, 19(4), 1559-1563.

355 Gbureck, U.; Vorndran, E.; Muller, F. A.; Barralet, J. E., Low temperature direct 3D printed bioceramics and biocomposites as drug release matrices. *Journal of Controlled Release* **2007**, 122(2), 173-180.

356 Habibovic, P.; Gbureck, U.; Doillon, C. J.; Bassett, D. C.; van Blitterswijk, C. A.; Barralet, J. E., Osteoconduction and osteoinduction of low-temperature 3D printed bioceramic implants. *Biomaterials* **2008**, 29(7), 944-953.

357 Khalyfa, A.; Vogt, S.; Weisser, J.; Grimm, G.; Rechtenbach, A.; Meyer, W.; Schnabelrauch, M., Development of a new calcium phosphate powder-binder system for the 3D printing of patient specific implants. *Journal of Materials Science-Materials in Medicine* **2007**, 18(5), 909-916.

358 Lee, J. Y.; Choi, B.; Wu, B.; Lee, M., Customized biomimetic scaffolds created by indirect three-dimensional printing for tissue engineering. *Biofabrication* **2013**, 5(4), 045003.

References

359 Richter, R. F.; Ahlfeld, T.; Gelinsky, M.; Lode, A., Development and Characterization of Composites Consisting of Calcium Phosphate Cements and Mesoporous Bioactive Glass for Extrusion-Based Fabrication. *Materials* **2019**, 12(12), 2022.

360 Detsch, R.; Uhl, F.; Deisinger, U.; Ziegler, G., 3D-Cultivation of bone marrow stromal cells on hydroxyapatite scaffolds fabricated by dispense-plotting and negative mould technique. *Journal of Materials Science-Materials in Medicine* **2008**, 19(4), 1491-1496.

361 Fernandez, E.; Gil, F. J.; Ginebra, M. P.; Driessens, F. C. M.; Planell, J. A.; Best, S. M., Calcium phosphate bone cements for clinical applications - Part I: Solution chemistry. *Journal of Materials Science-Materials in Medicine* **1999**, 10(3), 169-176.

362 Galea, L.; Alexeev, D.; Bohner, M.; Doebelin, N.; Studart, A. R.; Aneziris, C. G.; Graule, T., Textured and hierarchically structured calcium phosphate ceramic blocks through hydrothermal treatment. *Biomaterials* **2015**, 67, 93-103.

363 Galea, L. G.; Bohner, M.; Lemaitre, J.; Kohler, T.; Muller, R., Bone substitute: Transforming beta-tricalcium phosphate porous scaffolds into monetite. *Biomaterials* **2008**, 29(24-25), 3400-3407.

364 Ritman, E. L., Current Status of Developments and Applications of Micro-CT. *Annual Review of Biomedical Engineering* **2011**, 13, 531-552.

365 Zhang, L.; Liu, X. S.; Deb, A.; Feng, G., Ice-Templating Synthesis of Hierarchical and Anisotropic Silver-Nanowire-Fabric Aerogel and Its Application for Enhancing Thermal Energy Storage Composites. *Acs Sustainable Chemistry & Engineering* **2019**, 7(24), 19910-19917.

366 Bahari, L.; Bein, A.; Yashunsky, V.; Braslavsky, I., Directional freezing for the cryopreservation of adherent mammalian cells on a substrate. *Plos One* **2018**, 13(2), 0192265.

367 Qu, H. W.; Fu, H. Y.; Han, Z. Y.; Sun, Y., Biomaterials for bone tissue engineering scaffolds: a review. *Rsc Advances* **2019**, 9(45), 26252-26262.

368 Abbasi, N.; Hamlet, S.; Love, R. M.; Nguyen, N. T., Porous scaffolds for bone regeneration. *Journal of Science-Advanced Materials and Devices* **2020**, 5(1), 1-9.

369 Kim, T. W.; Ryu, S. C.; Kim, B. K.; Yoon, S. Y.; Park, H. C., Porous hydroxyapatite scaffolds containing calcium phosphate glass-ceramics processed using a freeze/gel-casting technique. *Metals and Materials International* **2014**, 20(1), 135-140.

370 Kim, J. H.; Lee, J. H.; Yang, T. Y.; Yoon, S. Y.; Kim, B. K.; Park, H. C., TBA-based freeze/gel casting of porous hydroxyapatite scaffolds. *Ceramics International* **2011**, 37(7), 2317-2322.

371 Fu, Q.; Rahaman, M. N.; Dogan, F.; Bal, B. S., Freeze casting of porous hydroxyapatite scaffolds. II. Sintering, microstructure, and mechanical behavior. *Journal of Biomedical Materials Research Part B-Applied Biomaterials* **2008**, 86b(2), 514-522.

372 Monmaturapoj, N.; Soodsawang, W.; Thepsuwan, W., Porous hydroxyapatite scaffolds produced by the combination of the gel-casting and freeze drying techniques. *Journal of Porous Materials* **2012**, 19(4), 441-447.

373 Carrodeguas, R. G.; De Aza, S., alpha-Tricalcium phosphate: Synthesis, properties and biomedical applications. *Acta Biomaterialia* **2011**, 7(10), 3536-3546.

374 Karashima, S.; Takeuchi, A.; Matsuya, S.; Udoh, K.; Koyano, K.; Ishikawa, K., Fabrication of low-crystallinity hydroxyapatite foam based on the setting reaction of alpha-tricalcium phosphate foam. *Journal of Biomedical Materials Research Part A* **2008**, 88a(3), 628-633.

375 Guo, H.; Su, J. C.; Wei, J.; Kong, H.; Liu, C. S., Biocompatibility and osteogenicity of degradable Ca-deficient hydroxyapatite scaffolds from calcium phosphate cement for bone tissue engineering. *Acta Biomaterialia* **2009**, 5(1), 268-278.

376 Ioku, K.; Kawachi, G.; Sasaki, S.; Fujimori, H.; Goto, S., Hydrothermal preparation of tailored hydroxyapatite. *Journal of Materials Science* **2006**, 41(5), 1341-1344.

377 Kamitakahara, M.; Ohtsuki, C.; Kawachi, G.; Wang, D.; Ioku, K., Preparation of hydroxyapatite porous ceramics with different porous structures using a hydrothermal

treatment with different aqueous solutions. *Journal of the Ceramic Society of Japan* **2008**, 116(1349), 6-9.

378 Poinern, G. E.; Brundavanam, R. K.; Mondinos, N.; Jiang, Z. T., Synthesis and characterisation of nanohydroxyapatite using an ultrasound assisted method. *Ultrasonics Sonochemistry* **2009**, 16(4), 469-474.

379 Kniep, R.; Simon, P., Fluorapatite-gelatine-nanocomposites: Self-organized morphogenesis, real structure and relations to natural hard materials. *Biomineralization I: Crystallization and Self-Organization Process* **2007**, 270, 73-125.

380 Kniep, R.; Simon, P., "Hidden" hierarchy of Microfibrils within 3D-periodic fluorapatite-gelatine nanocomposites: Development of complexity and form in a biomimetic system. *Angewandte Chemie-International Edition* **2008**, 47(8), 1405-1409.

381 Tlatlik, H.; Simon, P.; Kawska, A.; Zahn, D.; Kniep, R., Biomimetic fluorapatite-gelatine nanocomposites: Pre-structuring of gelatine matrices by ion impregnation and its effect on form development. *Angewandte Chemie-International Edition* **2006**, 45(12), 1905-1910.

382 Simon, P.; Schwarz, U.; Kniep, R., Hierarchical architecture and real structure in a biomimetic nano-composite of fluorapatite with gelatine: a model system for steps in dentino- and osteogenesis? *Journal of Materials Chemistry* **2005**, 15(47), 4992-4996.

383 Göbel, C.; Simon, P.; Buder, J.; Tlatlik, H.; Kniep, R., Phase formation and morphology of calcium phosphate gelatine-composites grown by double diffusion technique: the influence of fluoride. *Journal of Materials Chemistry* **2004**, 14(14), 2225-2230.

384 Apelt, D.; Theiss, F.; El-Warrak, A. O.; Zlinszky, K.; Bettschart-Wolfisberger, R.; Bohner, M.; Matter, S.; Auer, J. A.; von Rechenberg, B., In vivo behavior of three different injectable hydraulic calcium phosphate cements. *Biomaterials* **2004**, 25(7-8), 1439-1451.

385 Oberle, A.; Theiss, F.; Bohner, M.; Müller, J.; Kastner, S. B.; Frei, C.; Zlinszky, K.; Wunderlin, S.; Auer, J. A.; von Rechenberg, B., Investigation about the clinical use of brushite-and hydroxylapatite-cement in sheep. *Schweizer Archiv Fur Tierheilkunde* **2005**, 147(11), 482-490.

386 Theiss, F.; Apelt, D.; Brand, B. A.; Kutter, A.; Zlinszky, K.; Bohner, M.; Matter, S.; Frei, C.; Auer, J. A.; von Rechenberg, B., Biocompatibility and resorption of a brushite calcium phosphate cement. *Biomaterials* **2005**, 26(21), 4383-4394.

387 Sheikh, Z.; Zhang, Y. L.; Grover, L.; Merle, G. E.; Tamimi, F.; Barralet, J., In vitro degradation and in vivo resorption of dicalcium phosphate cement based grafts. *Acta Biomaterialia* **2015**, 26, 338-346.

388 Tamimi, F.; Le Nihouannen, D.; Eimar, H.; Sheikh, Z.; Komarova, S.; Barralet, J., The effect of autoclaving on the physical and biological properties of dicalcium phosphate dihydrate bioceramics: Brushite vs. monetite. *Acta Biomaterialia* **2012**, 8(8), 3161-3169.

389 An, Y. H. in *Mechanical Testing of Bone and the Bone-Implant Interface* (eds Y.H. An & R.A. Draughn) 41-64 (CRC Press, 2000).

390 Gerhardt, L. C.; Boccaccini, A. R., Bioactive Glass and Glass-Ceramic Scaffolds for Bone Tissue Engineering. *Materials* **2010**, 3(7), 3867-3910.

391 Rezwan, K.; Chen, Q. Z.; Blaker, J. J.; Boccaccini, A. R., Biodegradable and bioactive porous polymer/inorganic composite scaffolds for bone tissue engineering. *Biomaterials* **2006**, 27(18), 3413-3431.

392 Weiss, G.; Schaible, U. E., Macrophage defense mechanisms against intracellular bacteria. *Immunological Reviews* **2015**, 264(1), 182-203.

393 Brinkmann, V.; Reichard, U.; Goosmann, C.; Fauler, B.; Uhlemann, Y.; Weiss, D. S.; Weinrauch, Y.; Zychlinsky, A., Neutrophil extracellular traps kill bacteria. *Science* **2004**, 303(5663), 1532-1535.

394 Papayannopoulos, V., Neutrophil extracellular traps in immunity and disease. *Nature Reviews Immunology* **2018**, 18(2), 134-147.

References

395 Daniel, C.; Leppkes, M.; Munoz, L. E.; Schley, G.; Schett, G.; Herrmann, M., Extracellular DNA traps in inflammation, injury and healing. *Nature Reviews Nephrology* **2019**, 15(9), 559-575.

396 Abaricia, J. O.; Shah, A. H.; Olivares-Navarrete, R., Substrate stiffness induces neutrophil extracellular trap (NET) formation through focal adhesion kinase activation. *Biomaterials* **2021**, 271, 120715.

397 Sperling, C.; Fischer, M.; Maitz, M. F.; Werner, C., Neutrophil extracellular trap formation upon exposure of hydrophobic materials to human whole blood causes thrombogenic reactions. *Biomaterials Science* **2017**, 5(10), 1998-2008.

398 Peng, H. H.; Liu, Y. J.; Ojcius, D. M.; Lee, C. M.; Chen, R. H.; Huang, P. R.; Martel, J.; Young, J. D., Mineral particles stimulate innate immunity through neutrophil extracellular traps containing HMGB1. *Scientific Reports* **2017**, 7, 16628.

399 Loureiro, A.; Pais, C.; Sampaio, P., Relevance of Macrophage Extracellular Traps in C. albicans Killing. *Frontiers in Immunology* **2019**, 10, 2767.

400 Mantovani, A.; Biswas, S. K.; Galdiero, M. R.; Sica, A.; Locati, M., Macrophage plasticity and polarization in tissue repair and remodelling. *Journal of Pathology* **2012**, 229(2), 176-185.

401 Giannoudis, P. V.; Dinopoulos, H.; Tsiridis, E., Bone substitutes: An update. *Injury-International Journal of the Care of the Injured* **2005**, 36, 20-27.

402 Humbert, P.; Brennan, M. A.; Davison, N.; Rosset, P.; Trichet, V.; Blanchard, F.; Layrolle, P., Immune Modulation by Transplanted Calcium Phosphate Biomaterials and Human Mesenchymal Stromal Cells in Bone Regeneration. *Frontiers in Immunology* **2019**, 10.

403 Stevens, B.; Yang, Y.; Mohandas, A.; Stucker, B.; Nguyen, K. T., A review of materials, fabrication methods, and strategies used to enhance bone regeneration in engineered bone tissues. *J Biomed Mater Res B Appl Biomater* **2008**, 85(2), 573-582.

404 Magri, A. M. P.; Parisi, J. R.; de Andrade, A. L. M.; Renno, A. C. M., Bone substitutes and photobiomodulation in bone regeneration: A systematic review in animal experimental studies. *Journal of Biomedical Materials Research Part A* **2021**, 109(9), 1765-1775.

405 Lichte, P.; Pape, H. C.; Pufe, T.; Kobbe, P.; Fischer, H., Scaffolds for bone healing: Concepts, materials and evidence. *Injury-International Journal of the Care of the Injured* **2011**, 42(6), 569-573.

406 Baldwin, P.; Li, D. J.; Auston, D. A.; Mir, H. S.; Yoon, R. S.; Koval, K. J., Autograft, Allograft, and Bone Graft Substitutes: Clinical Evidence and Indications for Use in the Setting of Orthopaedic Trauma Surgery. *Journal of Orthopaedic Trauma* **2019**, 33(4), 203-213.

407 Tylek, T.; Schilling, T.; Schlegelmilch, K.; Ries, M.; Rudert, M.; Jakob, F.; Groll, J., Platelet lysate outperforms FCS and human serum for co-culture of primary human macrophages and hMSCs. *Scientific Reports* **2019**, 9, 3533.

408 Mastronarde, D. N., Automated electron microscope tomography using robust prediction of specimen movements. *Journal of Structural Biology* **2005**, 152(1), 36-51.

409 Ryma, M.; Tylek, T.; Liebscher, J.; Blum, C.; Fernandez, R.; Bohm, C.; Kastenmuller, W.; Gasteiger, G.; Groll, J., Translation of Collagen Ultrastructure to Biomaterial Fabrication for Material-Independent but Highly Efficient Topographic Immunomodulation. *Advanced Materials* **2021**, 33(33), 2101228.

410 Schamel, M.; Barralet, J. E.; Groll, J.; Gbureck, U., In vitro ion adsorption and cytocompatibility of dicalcium phosphate ceramics. *Biomaterials Research* **2017**, 21, 10.

411 Peng, H. H.; Martel, J.; Lee, Y. H.; Ojcius, D. M.; Young, J. D., Serum-derived nanoparticles: de novo generation and growth in vitro, and internalization by mammalian cells in culture. *Nanomedicine* **2011**, 6(4), 643-658.

412 Peng, H. H.; Wu, C. Y.; Young, D.; Martel, J.; Young, A.; Ojcius, D. M.; Lee, Y. H.; Young, J. D., Physicochemical and Biological Properties of Biomimetic Mineralo-Protein Nanoparticles Formed Spontaneously in Biological Fluids. *Small* **2013**, 9(13), 2297-2307.

413 Akiyama, M.; Kawasaki, S., Novel grout material comprised of calcium phosphate compounds: In vitro evaluation of crystal precipitation and strength reinforcement. *Engineering Geology* **2012**, 125, 119-128.

414 Burnouf, T.; Strunk, D.; Koh, M. B. C.; Schallmoser, K., Human platelet lysate: Replacing fetal bovine serum as a gold standard for human cell propagation? *Biomaterials* **2016**, 76, 371-387.

415 Eisinger, F.; Patzelt, J.; Langer, H. F., The Platelet Response to Tissue Injury. *Frontiers in Medicine* **2018**, 5, 317.

416 Kloc, M.; Uosef, A.; Kubiak, J. Z.; Ghobrial, R. M., Macrophage Proinflammatory Responses to Microorganisms and Transplanted Organs. *International Journal of Molecular Sciences* **2020**, 21(24), 9669.

417 Sadowska, J. M.; Wei, F.; Guo, J.; Guillem-Marti, J.; Lin, Z. M.; Ginebra, M. P.; Xiao, Y., The effect of biomimetic calcium deficient hydroxyapatite and sintered beta-tricalcium phosphate on osteoimmune reaction and osteogenesis. *Acta Biomaterialia* **2019**, 96, 605-618.

418 Warnatsch, A.; Ioannou, M.; Wang, Q.; Papayannopoulos, V., Inflammation. Neutrophil extracellular traps license macrophages for cytokine production in atherosclerosis. *Science* **2015**, 349(6245), 316-320.

419 Tylek, T.; Blum, C.; Hrynevich, A.; Schlegelmilch, K.; Schilling, T.; Dalton, P. D.; Groll, J., Precisely defined fiber scaffolds with 40 µm porosity induce elongation driven M2-like polarization of human macrophages. *Biofabrication* **2020**, 12(2), 025007.

420 Taskin, M. B.; Tylek, T.; Blum, C.; Bohm, C.; Wiesbeck, C.; Groll, J., Inducing Immunomodulatory Effects on Human Macrophages by Multifunctional NCO-sP(EO-stat-PO)/Gelatin Hydrogel Nanofibers. *Acs Biomaterials Science & Engineering* **2021**, 7(7), 3166-3178.

421 DeMerlis, C. C.; Schoneker, D. R., Review of the oral toxicity of polyvinyl alcohol (PVA). *Food Chem Toxicol* **2003**, 41(3), 319-326.

422 Mitchell, D. E.; Fayter, A. E. R.; Deller, R. C.; Hasan, M.; Gutierrez-Marcos, J.; Gibson, M. I., Ice-recrystallization inhibiting polymers protect proteins against freeze-stress and enable glycerol-free cryostorage. *Materials Horizons* **2019**, 6(2), 364-368.

423 Bhakta, A.; Ruckenstein, E., Ostwald Ripening - a Stochastic Approach. *Journal of Chemical Physics* **1995**, 103(16), 7120-7135.

424 Bachtiger, F.; Congdon, T. R.; Stubbs, C.; Gibson, M. I.; Sosso, G. C., The atomistic details of the ice recrystallisation inhibition activity of PVA. *Nature Communications* **2021**, 12(1), 1323.

425 Huang, J.; Guo, J.; Zhou, L.; Zheng, G.; Cao, J.; Li, Z.; Zhou, Z.; Lei, Q.; Brinker, C. J.; Zhu, W., Advanced Nanomaterials-Assisted Cell Cryopreservation: A Mini Review. *ACS Applied Bio Materials* **2021**, 4(4), 2996-3014.

426 Hedir, G.; Stubbs, C.; Aston, P.; Dove, A. P.; Gibson, M. I., Synthesis of Degradable Poly(vinyl alcohol) by Radical Ring-Opening Copolymerization and Ice Recrystallization Inhibition Activity. *ACS Macro Letters* **2017**, 6(12), 1404-1408.

427 Inada, T.; Lu, S. S., Inhibition of recrystallization of ice grains by adsorption of poly(vinyl alcohol) onto ice surfaces. *Crystal Growth & Design* **2003**, 3(5), 747-752.

428 Meneghel, J.; Kilbride, P.; Morris, G. J., Cryopreservation as a Key Element in the Successful Delivery of Cell-Based Therapies-A Review. *Frontiers in Medicine* **2020**, 7, 592242.

429 Qi, B.; Ji, Q. S.; Hou, G. H.; Li, L.; Cao, X. F.; Wu, J., Comparison of conventional and directional freezing for the cryopreservation of human umbilical vein endothelial cells. *International Journal of Ophthalmology* **2014**, 7(5), 768-772.

430 Arav, A.; Natan, D., Freeze Drying of Red Blood Cells: The Use of Directional Freezing and a New Radio Frequency Lyophilization Device. *Biopreservation and Biobanking* **2012**, 10(4), 386-394.

References

431 Notsu, H.; Kubo, W.; Shitanda, I.; Tatsuma, T., Super-hydrophobic/super-hydrophilic patterning of gold surfaces by photocatalytic lithography. *Journal of Materials Chemistry* **2005**, 15(15), 1523-1527.

432 Han, X.; Su, B.; Zhou, B.; Wu, Y. Z.; Meng, J. H., Soft lithographic fabrication of free-standing ceramic microparts using moisture-sensitive PDMS molds. *Journal of Micromechanics and Microengineering* **2019**, 29(3), 035002.

433 Ostrowski, N.; Roy, A.; Kumta, P. N., Magnesium Phosphate Cement Systems for Hard Tissue Applications: A Review. *Acs Biomaterials Science & Engineering* **2016**, 2(7), 1067-1083.

434 Haque, M. A.; Chen, B., Research progresses on magnesium phosphate cement: A review. *Construction and Building Materials* **2019**, 211, 885-898.

435 Kanter, B.; Vikman, A.; Brückner, T.; Schamel, M.; Gbureck, U.; Ignatius, A., Bone regeneration capacity of magnesium phosphate cements in a large animal model. *Acta Biomaterialia* **2018**, 69, 352-361.

436 de Grado, G. F.; Keller, L.; Idoux-Gillet, Y.; Wagner, Q.; Musset, A. M.; Benkirane-Jessel, N.; Bornert, F.; Offner, D., Bone substitutes: a review of their characteristics, clinical use, and perspectives for large bone defects management. *Journal of Tissue Engineering* **2018**, 9, 1-18.

Acknowledgements / Danksagung

An dieser Stelle möchte ich mich bei all denjenigen bedanken, die mich in den vergangenen vier Jahren auf verschiedenste Art und Weise unterstützt haben und ohne die die Entstehung meiner Dissertation in dieser Form nicht möglich gewesen wäre.

Zuallererst möchte ich mich sehr herzlich bei Prof. Dr. Jürgen Groll bedanken, der mir die Möglichkeit gab, meine Dissertation am FMZ anzufertigen und dabei thematisch an meine Masterarbeit anzuknüpfen. Durch das breit gefächerte Spektrum des Lehrstuhls konnte ich meine entwickelten Scaffolds sowohl materialwissenschaftlich als auch biologisch testen und dadurch mein Wissen kontinuierlich erweitern. Außerdem möchte ich mich für die nicht selbstverständliche Möglichkeit zur Teilnahme am PONTEA Seminar sowie an diversen wissenschaftlichen Konferenzen bedanken. Hierdurch konnte ich mich während meiner Promotion nicht nur fachlich, sondern auch persönlich weiterentwickeln.

Meinem Zweitbetreuer und Zweitgutachter Prof. Dr. Jens Pflaum möchte ich für die Begutachtung meiner Dissertation sowie die vielen wertvollen und hilfreichen Diskussionen, welche nicht nur im Rahmen der jährlichen GSLS Meetings stattfanden, danken. Durch einen physikalischen Blickwinkel auf meine Arbeiten kamen so einige neue und interessante Ideen und Fragestellungen auf.

Meinem Drittbetreuer Prof. Dr. Torsten Blunk danke ich für die Zeit, die er sich für die jährlichen GSLS Meetings genommen hat sowie die konstruktiven Diskussionen und neuen Denkanstöße, die daraus resultierten.

Prof. Dr. Uwe Gbureck möchte ich herzlichst dafür danken, dass er während meiner gesamten Promotion stets ein offenes Ohr für jegliche Probleme hatte und immer für eine Besprechung meiner Ergebnisse zur Verfügung stand. Außerdem danke ich ihm für das Korrekturlesen meiner Publikationen sowie dieser Dissertation. Darüber hinaus möchte ich mich aber auch für den ein oder anderen nicht-wissenschaftlichen Kaffeeklatsch sowie diverse Grillabende und -nachmittage im Hause Gbureck oder vor der Zahnklinik bedanken.

Außerdem geht mein Dank an Prof. Dr. Frank A. Müller und Anne V. Boehm von der Friedrich-Schiller-Universität Jena für die erfolgreiche Kooperation.

Bei Dr. Gudrun Reichenauer und Stephan Braxmeier vom Zentrum für angewandte Energieforschung (ZAE Bayern) möchte ich mich für die Stickstoffadsorptionsmessungen zur Bestimmung der spezifischen Oberfläche meiner Calciumphosphat-Proben bedanken.

Acknowledgements / Danksagung

Dr. Tomasz Jüngst danke ich für den Aufbau der Kooperation mit der UNSW in Sydney im Rahmen eines DAAD Programms, die zu wertvollem wissenschaftlichem Austausch und letztendlich zu einer gemeinsamen Publikation führte. Außerdem möchte ich mich für die äußerst hilfreichen Besprechungen zur Planung und Strukturierung meines Systematik-Papers bedanken.

Bei allen Bio-Kolleginnen und Kollgen, ob Doktorandinnen und Doktoranden, TAs oder Postdocs, möchte ich mich für die Hilfe bei sämtlichen biologischen Fragestellungen und der Versuchsplanung und Durchführung bedanken. Dr. Tatjana Schilling danke ich für die Besprechungen der geplanten Versuche und die Aufnahme in die Bio-Gruppe. Besonderer Dank geht aber an Dr. Tina Tylek und Dr. Carina Blum für die Einarbeitung und unermüdliche Hilfe bei der Durchführung meiner Makrophagen-Versuche.

Darüber hinaus möchte ich mich bei Harald Hümpfer und Anton Hofmann bedanken, die immer sofort zur Stelle waren, wenn die Gefrierstrukturierungsanlage mal wieder nicht so lief, wie sie sollte, es andere Kleinigkeiten zu reparieren gab oder ich Spezialanfertigungswünsche für meine Laborarbeit hatte. Bei Harald möchte ich mich insbesondere für den Bau der zweiten Gefrierstrukturierungsanlage und die kompetente Hilfe bei IT-Problemen aller Art bedanken. Toni gilt mein besonderer Dank für die zahlreichen Fahrten nach Wiesentheid, um mich mit Buffy-Coat-Nachschub zu versorgen.

Den „Zementis“, insbesondere Ib Holzmeister, Jan Weichhold und Friederike Kaiser, danke ich dafür, dass sie mich als „thematischen Sonderling“ mit offenen Armen in die Zementgruppe aufgenommen haben. Insbesondere die Reise zur Bioceramics nach New Orleans und der anschließende Kurzurlaub mit Ib und Jan werden mir noch lange in schöner Erinnerung bleiben. Darüber hinaus möchte ich mich auch noch herzlich bei Isabell Biermann für die Unterstützung und jederzeit vorhandene Hilfsbereitschaft bedanken.

Philipp Stahlhut und Judith Friedlein danke ich für die Einarbeitung am REM und die geduldige Hilfe bei allen kleineren und größeren Problemen, die bei der Aufnahme meiner Bilder auftauchten.

Tanja Dambach und Birgit Langner-Bischof danke ich für die Organisation und Koordination von Bestellungen und Chef-Terminen sowie sämtlichen anderen administrativen Dingen. Ohne Euren unermüdlichen Einsatz würde alles nicht mal halb so glatt laufen!

Bei den Mädels aus dem „Hühnerstall“, Franziska Weigl, Jessica Brand, Theresa Vogel, Dr. Carina Blum und der in unserem Büro aufgenommenen Johanna Lutz, möchte ich

mich für die schöne gemeinsame Zeit bedanken. Durch das angenehme Klima im Büro, die zahlreichen lustige Momente, Eure Unterstützung und aufbauenden Worte, die vielen fachlichen Diskussionen sowie die diversen eher weniger fachlichen Gespräche, habt ihr die Promotion für mich zu einer unvergesslichen Zeit gemacht!

Außerdem möchte ich mich bei den Büro-Mädels, aber auch bei Ilona Paulus, Viktoria Niklaus, Jan Weichhold, Ib Holzmeister, Friederike Kaiser, Junwen Shan, Christoph Böhm und Dr. Florian Pinzner für die gemeinsamen Mittags- und Kaffeepausen, Abendessen und allgemein die schöne Zeit bedanken.

Allen anderen nicht namentlich genannten „FMZlern“ danke ich für die gute Zusammenarbeit, das angenehme Arbeitsklima und die schöne Zeit, die ich während meiner Promotion am FMZ hatte.

Zu guter Letzt möchte ich mich von Herzen bei meiner Familie und meinen Freunden außerhalb des FMZs bedanken, die immer für mich da waren und ein offenes Ohr hatten. Danke Mama und Papa, dass ihr mir durch Eure mentale und finanzielle Unterstützung das Studium und dadurch letztlich auch diese Doktorarbeit ermöglicht habt, dass ihr immer hinter mir standet und stolz auf mich wart und seid. Meiner Schwester Franzi möchte ich dafür danken, mich über die gesamte Promotion hinweg sowohl in schönen als auch schwierigen Momenten begleitet und bei Bedarf immer wieder aufgebaut zu haben. Von Herzen bedanke ich mich auch bei Janosch für die viele Geduld und Unterstützung in den letzten Jahren und für das Verständnis, wenn wir unsere Planungen wegen Notfällen im Labor oder nahenden Deadlines mal wieder verschieben mussten. Danke, dass Du Dich immer für mich und mit mir freust, mich unterstützt und immer für mich da bist! ♥

Curriculum Vitae

Affidavit

I hereby confirm that my thesis entitled “Unidirectional freezing of soft and hard matter for biomedical applications” is the result of my own work. I did not receive any help or support from commercial consultants. All sources and / or materials applied are listed and specified in the thesis.

Furthermore, I confirm that this thesis has not yet been submitted as part of another examination process neither in identical nor in similar form.

Würzburg,

Place, Date

Signature

Eidesstattliche Erklärung

Hiermit erkläre ich an Eides statt, die Dissertation „Unidirektionales Gefrieren von weichen und harten Materialien für biomedizinische Anwendungen“ eigenständig, d.h. insbesondere selbständig und ohne Hilfe eines kommerziellen Promotionsberaters, angefertigt und keine anderen als die von mir angegebenen Quellen und Hilfsmittel verwendet zu haben.

Ich erkläre außerdem, dass die Dissertation weder in gleicher noch in ähnlicher Form bereits in einem anderen Prüfungsverfahren vorgelegen hat.

Würzburg,

Ort, Datum

Unterschrift